Characterisation of optimum devices and parameters for enhanced optical frequency comb generation

Mohab Nabil Hammad

B. Eng., M. Sc.

A dissertation submitted in fulfilment of the
requirements for the award of
Doctor of Philosophy (Ph.D.)

School of Electronic Engineering

Faculty of Engineering and Computing

Dublin City University

Supervisor: Dr. Prince Anandarajah

Co-Supervisor: Dr. Pascal Landais

April 2022

Declaration

I hereby certify that this material, which I now submit for assessment on the programme of study leading to the award of Doctor of Philosophy is entirely my own work, and that I have exercised reasonable care to ensure that the work is original, and does not to the best of my knowledge breach any law of copyright, and has not been taken from the work of others save and to the extent that such work has been cited and acknowledged within the text of my work.

Signed:
ID No.: 17212427
Date: /4/2022

To my parents, brother

"When everything goes to hell, the people who stand by you without flinching – they are your family." – Jim Butcher

Acknowledgements

Firstly, I would like to thank all the people who contributed and helped me both professionally and personally during the last four years period. I would like to personally thank my supervisor Dr.Prince Anandarajah for initially giving me the opportunity and the trust to join his research group to pursue my PhD. Throughout all the PhD journey, he provided me with his support and expertise on all professional and personal levels. His inspiring dedication, enthusiasm and understanding have motivated me even during the most tough parts of the PhD. I will always be grateful for him. I would also like to thank my co-supervisor Dr.Pascal Landais for his help and guidance during my PhD. His valuable comments and suggestions substantially improved my work. He was always willing to sharing his expertise and knowledge with me. Also, thanks to Dr.Aleksandra Kaszubowska for always being there for supporting me and giving me ideas to improve my research skills. Throughout our years together, their kindness and understanding had me consider them as not only my mentors but as a part of my extended family.

Special thanks go to my dear friend Prajwal. He was always a supportive person, who is willing to help in whatever way he can. I would like also to thank Dr.Eamonn Martin for his patient guidance and lab mentorship and training during the early days of my PhD. My appreciation also goes to all my friends who has played an important role in giving me a great time during my stay in Ireland and helped me in many ways throughout my PhD journey: Gaurav, Ankit, Devika, Amol, Syed, Manas, Eric, Blas.

I would like to express my greatest gratitude and appreciation to my parents and my brother. Their unconditional love has always been one of the most important assets in my life. They have always been supportive and encouraging about my education. I owe them everything.

Table of contents

List of Tables

List of Figures

List of Acronyms

APD	Avalanche Photo Diode
APSK	Amplitude Phase Shift Keying
AR	Anti-Reflection
ASE	Amplified Spontaneous Emission
AWG	Array Waveguide Grating
B2B	Back-To-Back
BER	Bit Error Rate
C-Band	Conventional Band
CLP	Comb Line Power
CPR	Carrier Photon Resonance
CW	Continuous Wave
DBR	Distributed Bragg Reflector
DCF	Dispersion Compensating Fibre
DCI/Ns	Data Centre Interconnects/Networks
DD	Dual Drive
DFB	Distributed Feedback Laser
DM	Discrete Mode
DMT	Discrete Multi-Tone
DP	Dual Polarisation
DSF	Dispersion Shifted Fibre
DSP	Digital Signal Processing
DWDM	Dense Wavelength Division Multiplexing
EAM	Electro-Absorption Modulator
ED	Error Detector
EDFA	Erbium Doped Fibre Amplifiers
EON	Elastic Optical Networks
ER	Extinction Ratio
ESA	Electrical Spectrum Analyser
FDM	Frequency Division Multiplexing
FEC	Forward Error Correction

FM	Frequency-Modulated
FP	Fabry Pérot
FSR	Free Spectral Range
FWM	Four-Wave Mixing
HR	High Reflection
I	In-Phase
ICI	Inter-Carrier Interference
IFB	Integrated Feedback
IL	Injection-Locked
In	Indium
InP	Indium Phosphide
IRSN	injection Recombination Shot Noise
ISI	Inter-Symbol Interference
ITU	International Telecommunication Union
L-band	Long Band
LD	Laser Driver
LFF	Low-Frequency Fluctuation
LIDAR	Light Detection and Ranging
LO	Local Oscillator
LPF	Low Pass Filter
MBW	Modulation Bandwidth
MG	Master Gain
MLL	Mode Locked Laser
MMF	Multimode Fibre
MPI	Multi-Path Interference Noise
MPN	Mode Partition Noise
MR	Master Reflector
MRR	Micro-Ring Resonator
MS-SOA	Multi-Section SOA
MZI	Mach-Zehnder Interferometer
MZM	Mach-Zehnder Modulator
NF	Noise Figure
NRZ	Non-Return to Zero

OBPF Optical Band-Pass Filter

OCDMA Optical Code-Division Multiple Access

OCNR Optical Carrier to Noise Ratio

OFC Optical Frequency Comb

OFDM Orthogonal Frequency Division Multiplexing

OIL Optical Injection Locking

OOK On-Off Keying

OPEX Lower Operational Expenditure

OSA Optical Spectrum Analyser

OSNR Optical Signal to Ratio

PAM Pulse Amplitude Modulation

PCB Printed Circuit Board

PDM Polarisation Division Multiplexing

PFL Passive Feedback Laser

PIC Photonic Integrated Circuit

PM Polarisation Multiplexed

PMF Polarisation-Maintaining Fibre

PON Passive Optical Network

PPG Pulse Pattern Generator

PPR Photon Photon Resonance

PRBS Pseudo Random Bit Sequence

PSD Power Spectral Density

Q Quadrature

QAM Quadrature Amplitude Modulation

QD Quantum Dot

QPSK Quadrature Phase Shift Keying

QW Quantum Well

RF Radio Frequency

RHS Right-Hand Side

RIN Relative Intensity Noise

ROF Relaxation Oscillation Frequency

ROP Received Optical Power

RRC Root Raised Cosine

RTS Real-Time Scope

RZ-DPSK Return To Zero Differential Phase Shift Keyed

SA Saturable Absorber
S-band Short- Band
SDM Space Division Multiplexing
SG Slave Gain
Si Silicon
SMF Single Mode Fibre
SMSR Side-Mode Suppression Ratio
SNR Signal To Noise Ratio
SOA Semiconductor Optical Amplifier
SOH Silicon Organic Hybrid
SR Slave Reflector
SSG Small Signal Gain

TDM Time Division Multiplexing
TEC Thermoelectric Cooler
TW Travelling Wave

UDWDM Ultra-Dense Wavelength Division Multiplexing Modulation

VCSEL Vertical Cavity Surface Emission Laser
VNA Vector Network Analyser
VOA Variable Optical Attenuator

WDM Wavelength Division Multiplexing
WSS Wavelength Selective Switch

Characterisation of optimum devices and parameters for enhanced optical frequency comb generation

By Mohab Nabil Mohamed Fathy Hammad

Abstract

The Internet has become an irreplaceable aspect of our daily life. It is used every day by billions of people around the world for various functions such as business, study, and entertainment. Hence, an unabated rise in the demand for higher and faster data traffic has been experienced through the last few decades. This demand for bandwidth is further fuelled by the introduction of bandwidth intensive applications such as ultra-high-definition video streaming, real time online gaming and cloud services making the realization of higher capacity and performance optical networks a necessity.

Today's telecommunication systems are static, with pre-provisioned links requiring an expensive and time-consuming reconfiguration process. The state-of-the-art approach (wavelength division multiplexing - WDM), entailing multiple lasers emitting differing wavelengths (each modulated) multiplexed together (on a 50 GHz grid), cannot meet the growing demands. Hence, future networks need to be flexible and programmable, allowing for resources to be directed, where the demand exists, thus improving network efficiency. A cost-effective solution is to utilise the legacy fibre infrastructure more efficiently by reducing the size of the guard bands and allowing closer optical carrier spacing, thereby increasing the overall spectral efficiency. However, such a scheme imposes a stringent transmitter requirement in terms of wavelength stability, noise properties and cost-efficiency, which would not be met with the incumbent laser-array based transmitters. An attractive alternative would be to employ an optical frequency comb (OFC), which generates multiple phase-correlated optical carriers with a precise frequency separation. The reconfigurability of such a multi-carrier transmitter would enable tuning of channel spacing, number of carriers and emission wavelengths, according to the dynamic network demands.

This thesis focusses on the externally injected gain-switched laser-based OFC (GSL-OFC) technique. Advances to the state of the art are achieved via a detailed static and dynamic characterisation of lasers, which is then used for enhancing the comb generation process. Specifically, initial efforts are devoted to the use of different laser structures for OFC generation. This aspect is then furthered by incorporating the concept of photonic integration to reduce the cost, power consumption and footprint of the multi-carrier transmitter. Self and externally seeded photonic integrated circuits are used to generate combs that are then fully characterized to verify their employability in optical networks.

Motivation and main contributions

Digitalisation has become a global trend and a growth factor of the modern societies. The integration of digital technologies in almost all aspects of our daily life has created an ever-increasing demand for high-speed internet. The introduction of bandwidth hungry applications such as high-quality video streaming and conferencing, real time online gaming and video calls and high-speed cloud services has even put more pressure on currently deployed optical networks to evolve towards higher speeds and bandwidth.

Wavelength division multiplexing (WDM) has enabled the transmission of multiple wavelengths using a single fibre, which opened the door for implementation of higher capacity transmission systems. WDM has been successfully implemented in commercial optical networks during the last 30 years. However, with the development and wide spread of internet services all over the world, not only there exists an ever-increasing demand for higher bandwidth but also this traffic demand is very dynamic. This is due to the reason that there are multiple users with diverse needs that also changes over time. In order to cater for this, the introduction of more advanced solutions is required allowing more flexibility and reconfigurability. Some of the proposed techniques are the utilisation of higher order modulation formats, that provides multi-level encoding of data onto the optical carriers and the employment of multicarrier modulation techniques in which the spectral efficiency is enhanced as a result of the bandwidth usage minimisation by the usage of tightly packed optical channels.

Advanced modulation formats are prevalent in today's networks. However, to further enhance the spectral efficiency, the usage of proposed techniques a reliable optical carrier source that generates multiple stable and closely spaced optical carriers is required. Multicarrier optical sources enable denser channel spacing and potentially the technology of super channels. Optical frequency combs (OFCs) can be considered as an attractive solution for the generation of multiple phase-correlated optical carriers. It has attracted a lot of attention recently as an appealing replacement for a bank of semiconductor lasers, providing a more compact and a simpler solution. Furthermore, it provides a stable and a fixed spacing among the multiple carriers, that overcomes the drift and interference between the different optical channels over time. This results in the reduction or the elimination of the guard bands

between these channels, enhancing the overall spectral efficiency of the communication system.

Next generation optical networks would favour an OFC that provides good inherent spectral characteristics such as narrow linewidth, low relative intensity noise (RIN), high optical carrier to noise ratio (OCNR) and wide bandwidth. Furthermore, it should provide tunability in terms of free spectral range (FSR) and emission wavelength to allow dynamic spectrum allocation and bit rate variation according to the variable traffic demand of the network. Finally, it should be as compact as possible or even integrated thus providing a lower footprint solution.

There exist various techniques for generating an OFC. Gain switching technique is one of the attractive generation techniques, which provides simplicity, cost efficiency and the prospect for photonic integration. Thus, the focus of this thesis is to identify the optimum laser parameters and operating conditions for generation of an enhanced OFC using this technique. In this thesis, investigation of the various laser parameters that have an impact on the quality of the generated gain switched OFC is shown. This is carried out for different types of laser structures using simulation models and mostly via experimental characterisation.

Main contributions

The main contributions of this work can be outlined as below:

- Investigation of laser parameters influence on the laser output. This is done using a simulation model based on the rate equations to study the semiconductor laser dynamics and give optimum laser parameters. Experimental full characterisation of different laser structures that can be effectively used for gain switching were carried out to support the simulated results.
- Demonstration of a gain switched externally injected vertical cavity surface emission laser (VCSEL) based OFC that exhibits remarkable spectral properties such as high OCNR, low phase noise and low relative intensity noise (RIN). The positive impact of the external injection on the OFC spectral properties is clearly highlighted.
- Introduction of a novel multi-section photonically integrated device to realise optical injection locking (OIL) which addresses problems with direct modulation. Detailed static and dynamic characterisation of the device were carried out and the results were shared with the device manufacturer to serve as feedback for an improved

design. A simulation model backing up the experimental results was constructed, which also gave an insight on the device physical parameters and how to optimise it.

- Demonstration of a simple, cost-effective method for expansion of the generated OFC by gain switching an integrated two section passive feedback laser (PFL). Optimisation of the operating parameters of the PFL two sections results in an outstanding enhancement of the modulation bandwidth of the laser as a result of the photon-photon resonance (PPR) effect. Hence, a remarkable expansion in the gain switched OFC bandwidth and number of tones is demonstrated.
- Report of an integrated multi-section semiconductor optical amplifier (SOA) as a compact, simple solution for optical signal amplification applications for short reach optical networks. The device is demonstrated to give flexibility to dynamically achieve either a low noise figure or a high saturation power according to the required application by simply tuning the bias of the different sections.

Thesis structure

This thesis is structured as follows:

Chapter 1 describes the evolution of optical communications during the different stages of its development with a particular attention to the introduction of WDM. The different challenges, because of the ever-increasing demand for bandwidth, are highlighted and different capacity scaling solutions to overcome this need are discussed. The main techniques discussed are the usage of advanced modulation formats and multicarrier modulation techniques to improve the spectral efficiency of the network. Eventually, OFCs are proposed as an attractive solution for generation of multiple optical carriers in a simple and easy manner, which qualify it to be a key enabling technology for next generation optical networks employing super channels.

Chapter 2 provides a literature review of the popular techniques of OFCs generation, highlighting the main merits and drawbacks of each technique. Subsequently, a special focus on gain switching technique is drawn due to its simplicity, cost effectiveness and the prospect for photonic integration. A Matlab model is presented based on rate equation to study the semiconductor laser dynamics, in order to tweak different laser parameters for generating an OFC using gain switching technique.

Chapter 3 presents a static and dynamic characterisation of different laser structures with a primary aim to identify optimised driving parameters for gain switching technique to

generate an enhanced OFC. A full study of two different VCSEL devices is shown. The full study resulted in the generation of (to the best of our knowledge, for the first time) an externally injected gain switched VCSEL based OFC, that demonstrates high OCNR, low phase noise and low RIN. Furthermore, a brief study of the VCSEL polarization dynamics and how it can be used to further enhance the generated OFC is also shown.

Chapter 4 introduces a novel photonic integrated multi-section laser device that realises OIL to tackle problems associated with direct modulation. The master-slave configuration of the device allows the in-chip optical injection to improve various spectral characteristics of the device such as linewidth, RIN and modulation bandwidth. This leads to generation of an enhanced OFC in terms of number of lines and bandwidth. A VPI simulation model is presented to support the experimental results and to study the effect of variation of the different laser parameters on the output. Providing these results to the company who fabricated the first device for feedback on an upgraded design has resulted in the production of an updated version of the device. The new device is characterized and demonstrated to have more accurate control on the injection parameters, resulting in an enhancement in the injection locking procedure of the device.

Chapter 5 shows the detailed characterisation of another two-section integrated device. It is a PFL that allows for on-chip optical feedback (self-seeding). The accurate optimisation of the bias configurations applied to both sections result in an outstanding enhancement of the modulation bandwidth of the device. The latter allows for the generation of an OFC with an expanded bandwidth and higher number of comb tones under the influence of optimised on-chip optical feedback. A VPI simulation model is introduced and provides similar results, which supports the output of the experimental characterisation.

Chapter 6 proposes a multi-section integrated SOA for amplification purposes in short reach optical networks. The device is characterised and demonstrated to generate either a low noise figure or a high saturation power according to the bias configuration applied to its different sections. This allows for adaptation of the device to a specified application. Moreover, the device was shown to be implemented successfully in a system experiment employing OOK and PAM-4 modulation formats. The potential of the device to be integrated with a gain switched OFC in a single chip provides a potentially exceptional multi-carrier transmitter solution with a high output power.

Chapter 7 provides a brief summary of the research highlighting some important output results. Moreover, it gives a summary of the future prospects of the same research line.

Chapter 1

Optical fibre communication

1.1 Introduction

Since the beginning of civilisations, communication has always played a crucial part in shaping the history and culture of humankind. It all started with basic communication methods such as rudimentary hand movements or simple verbal expressions and evolving towards more advanced techniques with the invention of languages and written scripts. Communication methods have evolved at a fast pace in order to keep track of the developments in the civilizations. In a typical modern communication system, transfer of data is accomplished by modulation (superimposing) of the desired information onto a carrier. A transmission medium is then used as a mean of transporting the modulated carrier to its eventual destination. The original data is recovered by being processed and demodulated at the destination. Co-axial cables were used initially as a transfer medium where electromagnetic waves were employed as a carrier of data. Several efforts were exerted to improve the system capacity. However, the amount of transferred data was still limited by the carrier frequency. Nowadays, a massive amount of data is transferred between various parts of the world with rapid speeds and very low latency, thanks to the invention of optical fibres [1]. Optical networks have become a crucial part of our daily life, since internet and data transfer are used in almost all aspects of life. The ever-increasing demand for faster and cheaper data traffic has led to an urgent need for improvements in the currently existing optical networks. With the current optical networks experiencing a capacity crunch due to the exponential growth of data traffic and the introduction of several advanced bandwidth-intensive applications, the need for more advanced and efficient optical networks that can cater for such high bandwidth demands has become unavoidable.

1.2 Evolution of optical fibre communication

Optical fibre communication has been introduced in the second half of the twentieth century to cater for the need for a quicker and more reliable technique to transfer large amounts of data all over the world [2]. The introduction of optical fibres in 1966, preceded by the invention of semiconductor laser diodes in 1960 laid the foundation for the development of today's optical networks [3]. However, the main breakthrough was achieved in 1970 [4], when Corning Glass Works designed and manufactured the first optical fibre that was capable of maintaining the strength of laser light signals over significant distances with relatively low transmission loss (attenuation of 17 dB/km). This opened the door for optical fibres to be implemented as a real-life technology, which is able to increase the capacity of the transmission systems by several times. Early optical networks operated at a very low data rates (45 Mb/s in the 1980s) [5]. The continuous efforts in technological developments led to a moderate rate of increase of bit rate in the single optical channel supported on these systems. One of the other changes that supported the bit rate increment is the change of the optical frequency transmission window from 800 nm to 1300 nm and finally to 1550 nm [6]. However, it was not until the late 1980s when Erbium doped fibre amplifiers (EDFA) were introduced to optical networks that led to the rapid growth in the capacity of the data transfer rate [7].

Evolution of optical fibre communication over time can be split into several discernible phases as shown in Figure 1.1(a,b). The main criterion of the evolution is the bit rate distance product (*BL*), where *B* is the bit rate achieved and *L* is the achievable distance. This product is a count for the number of repeaters required for a given transmission [8]. The first generation of optical fibre communication used graded-index multimode fibre (MMF) and GaAs semiconductor materials at an operating wavelength of 800 nm as optical sources to achieve a bit rate of 45 Mb/s as previously mentioned [9]. It had a repeater spacing of only 10 km. As per the figure, the *BL* product for the first generation is in the order of less than 10 Gb/s.km. Shifting the operation lower loss wavelength (with respect to 800 nm) of 1300 nm opened the door for implementation of the second generation of optical fibre communication. Semiconductor laser sources and detectors were developed to operate in the 1300 nm region, where both fibre loss (1 dB/km) and dispersion are low. For further improvement of the *BL* product and reduction of dispersion, the attention was targeted towards the single mode fibre (SMF) to replace the MMF. SMF provides much lower dispersion compared to MMF.

Both low transmission loss and low dispersion figures resulted in the achievement of systems operating at bit rates up to 2 Gb/s with an extended repeater spacing of 50 km [11], leading to an improvement of the *BL* product to approach 100 Gb/s.km.

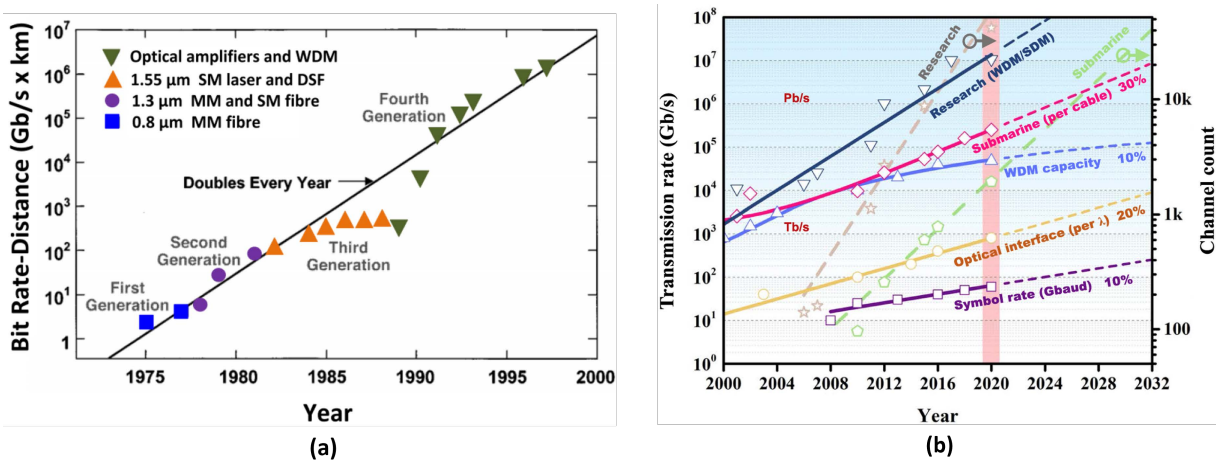

Figure 1.1: (a) Evolution of BL product over the period between 1975 and 2000 through distinct generations of optical fibre communications. Source: [8], (b) Evolution of fibre-optic transmission capacity through the period between 2000 and 2032 [10].

Further advancements took place to achieve better *BL* product for the third generation (in the order of 1000 Gb/s.km). The operating wavelength shifted again to a lower loss window (at 1.55 µm). This was mainly driven by the leap forward of achieving a much lower fibre transmission loss (0.2 dB/km) at 1.55 µm in 1979 [12]. However, another issue emerged as the SMF suffers from higher dispersion values at 1550 nm. Several efforts were devoted to counter this issue, which led to the introduction of dispersion-shifted fibre (DSF) [13], designed to have lower dispersion at 1.55 µm operating wavelength in the link. Successful implementation of this solution has resulted in the achievement of a transmission with a bit rate of 4 Gb/s for a distance exceeding 100 km in 1985 [14]. Dispersion compensating fibres (DCFs) were also introduced as an alternative lower cost solution for compensating the dispersion of the existing SMFs. Replacing millions of kilometres of the conventional SMFs with DSFs would involve huge costs. DCFs have a very large negative dispersion coefficients that can compensate for the positive dispersion coefficients of the SMFs. Introduction of a few hundred meters to a kilometre of DCFs, can compensate for dispersion over tens of kilometres of the conventional SMFs, which provides a more economical solution.

The advent of both EDFAs and the wavelength division multiplexing (WDM) [15] has marked the revolutionary start of the fourth generation of optical fibre communication. WDM has allowed the explosive increase in the transmission capacity, which resulted in the doubling of the *BL* product each year as shown in Figure 1.1, to approach a *BL* product in the order of 1×10^{7} by the 2000s. WDM is a technique that allows the transmission of multiple optical channels on different carrier wavelengths over a single optical fibre. EDFAs are used to extend the distance between the different regenerators by amplifying the optical signal to compensate for the signal attenuation occurring during propagation through the optical fibre [7]. The emergence of internet and the exponential growth in demand for transmission of a massive amount of data over long-haul distances have

promoted and pushed the development of WDM systems forward. This has resulted in the introduction of the fifth generation of optical fibre communication by introduction of both dense wavelength division multiplexing (DWDM) (which will be explained in detail later in this chapter) and space division multiplexing (SDM) in order to make WDM system more efficient spectrally. In this generation, a bit rate of 40 Gb/s and a repeater spacing of more than 100 km can be achieved. Moreover, the concept of optical solitons, which are pulses that can preserve their shape by counteracting the negative effects of dispersion [16] is being explored as a part of this generation to further enhance the efficiency of the optical networks. Figure 1.1(b) gives a more-in depth analysis of the currently used technologies with a future forecast of both the transmission rate and the channel count. Coherent receivers (which will be explained later in details) that are capable of detecting both the amplitude and phase of an optical signal were developed soon after the year 2000. Their commercial availability has allowed system designers to employ advanced modulation formats in which information is encoded using both the amplitude and phase of an optical carrier [10]. The development efforts have resulted in achieving bit rates up to 10 Tb/s and a regenerating spacing of more than 100,000 km, announcing the beginning of a new era for optical fibre communication. Being currently in the fifth generation of the optical fibre communication, the increasing development in enhancing the transmission capacity is faced by the ever-increasing demand for internet bandwidth. As the capacity of WDM systems approached 10 Tb/s, researchers have begun to think about the ultimate information capacity of a single-mode fibre. Shannon limit first introduced in 1948, shows that the optical signal to noise ratio (OSNR) sets the fundamental limit for any linear communication channel. The latter in principle, can be increased indefinitely by sending more and more powerful signals over the channel to increase the OSNR. Unfortunately, this conclusion does not hold for optical fibres that are inherently nonlinear and affect the bit stream propagating through them in a nonlinear fashion [3]. For the future, Next-generation fibre-optic communication systems bit rate is expected to exceed 1 (Tb/s) per wavelength. An ultrahigh-capacity transmission system exceeding petabits-per-second (Pb/s) will comprise a vast number of wavelength-spatial channels on the 10,000 scale (e.g., 100+ wavelengths times 10+ spatial paths as shown in Figure 1.1(b)) [10]. This will result in a huge increase in the complexity that cannot be obtained using discrete optical components [10]. Photonic integrated circuits (which will be discussed in detail in this thesis) provide a promising solution to resolve the dilemma of scaling system complexity while reducing the cost per bit.

In the next section, WDM technique is investigated as one of the main techniques currently applied for improving the transmission capacity of the optical network.

1.3 Transmission capacity enhancement (Information age)

1.3.1 Wavelength division multiplexing

The internet evolution and the start of alteration of the transmitted data types from plain text to videos and multimedia contents have urged the need for a higher transmission capacity. Multiplexing has been developed as a mean of sending multiple data streams using a common medium at the same time. In case of optical communications, multiple optical signals are multiplexed into a single signal that is transmitted through one optical fibre. The signal is then demodulated at the receiver, where the original data are recovered from it and is available for processing. There exist different types of multiplexing that employs several degrees of freedom such as frequency division multiplexing (FDM) [17], time division multiplexing (TDM) [18], SDM [19], polarisation division multiplexing (PDM) [20] and WDM. The latter is the multiplexing technique that will be adopted and discussed in this work.

For example, enhancement of the transmission capacity can be achieved employing PDM, where different chunks of data can be conveyed within the two orthogonal polarisation modes. This results in doubling of the transmission capacity leading to an overall improvement in the spectral efficiency (which will be defined later in Section 1.3.3.1). All modulation formats can be incorporated with PDM to enhance the spectral efficiency and the aggregate data rate. PDM has been used in conjunction with higher order modulation formats (which will be discussed in more detail in the next section) such as differential quadrature phase shift keying (DQPSK) and quadrature amplitude modulation (QAM) to push the achieved single channel bit rate to higher values reaching 100 Gb/s [21] and even 400 Gb/s [22] .

The technology of WDM has catered for the early part of the exponential increase in the demand for bandwidth. It entails the employment of multiple carrier wavelengths for the transmission of data in which each wavelength can be considered as an individual channel. This results in maximising the usage of available resources, as the multiple wavelengths (channels) can be transmitted through a single optical fibre where they are separated by a specific frequency spacing.

Figure 1.2 shows a schematic of a generic WDM architecture. At the transmitter side, each transmission channel incorporates a single mode laser source which emits a light signal that can be considered as an optical carrier. Each laser emits at a specific wavelength, and it can be modulated

(with data) either directly (as shown in Figure 1.2) or externally. All the channels are then combined together using a multiplexer to be transmitted through a single optical fibre. At intermediate points in the transmission stage, the optical signal can be amplified using EDFAs to compensate for the attenuation. Moreover, specific channels can be added or removed according to need through an optical add/drop multiplexer. On the receiver side, the different channels are separated using a demultiplexer to be routed to the desired destinations, where they are detected using a photodetector and demodulated. The original transmitted data can then be recovered from the demodulated data.

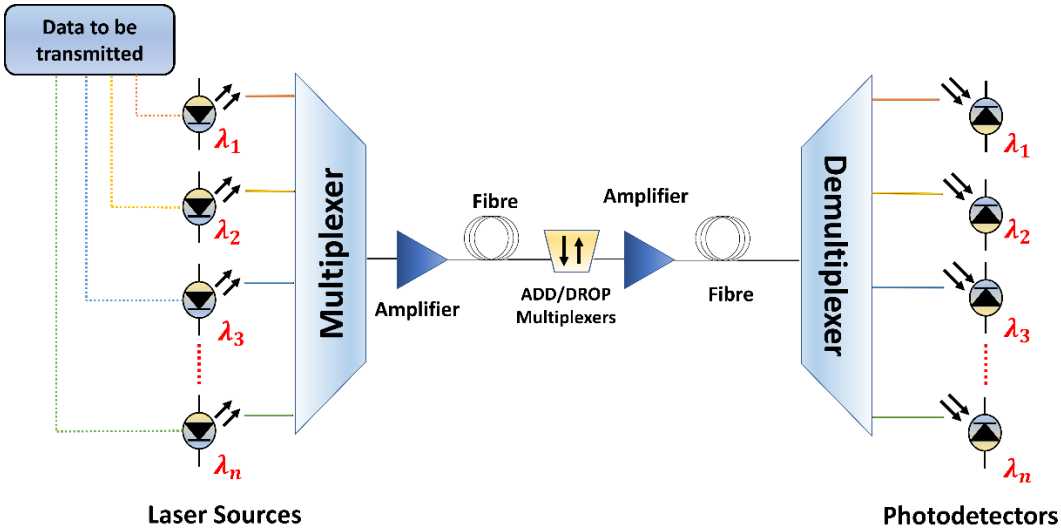

Figure 1.2: Generic WDM architecture.

In an WDM architecture, the transmitted carriers are typically separated by an allocated amount of frequency bandwidth called channel spacing. The used frequency grid for fibre-optic communication for channel spacing at wavelengths around 1550 nm is defined by International Telecommunication Union (ITU) G.694.1 standard [23]. The grid was previously defined relative to 193.1 THz and extends from 191.7 THz to 196.1 THz (1528.77 nm to 1563.86 nm) with a channel spacing of 100 GHz (~0.8 nm). In the meantime, ITU has standardised a 50 GHz reduced grid channel spacing, which is used by the currently deployed optical networks, and is referred to as DWDM [23]. Furthermore, ultra-dense wavelength division multiplexing (UDWDM) was introduced by ITU-T recommendation [23] to accommodate even lower grid channel spacing of 25 and 12.5 GHz. The channel spacing typically comprises both the bandwidth of the encoded data to be transmitted and the guard bands. Although not carrying any kind of transmissible data, it is crucial to insert the latter between adjacent channels to avoid any kind of undesired interference among them. Cross-channel interference among neighbouring channels can occur due to various reasons such as wavelength drift of the laser devices and non-ideal response of the demultiplexer [24]. Despite their importance, the guard bands are

generically considered a waste of the network resources (the available bandwidth) as they do not carry transmitted data. Several efforts have been devoted towards decreasing the size of the implemented guard bands or alleviating it, which will be discussed in detail later in this chapter.

The number of channels that can be implemented in an optical network is governed by several factors that can be classified into three main categories (spectral efficiency, multiplexing/demultiplexing optical components bandwidth limitations and amplifiers):

1) **Spectral efficiency:**

The primary factor is the capacity and the bit rates that each channel can achieve. This can be quantitatively measured using the spectral efficiency, which is defined as the ratio of an individual channel bit rate to the frequency spacing between the WDM channels [25]. In a typical short reach network employing basic modulation formats such as on-off keying (OOK), a 100 GHz grid channel spacing is required to avoid any cross-channel interference among channels employing a bit rate of 40 Gb/s each to generate a spectral efficiency of 0.4 (*bit/s)/Hz* [26]. Further enhancement of spectral efficiency can be achieved by employing advanced modulation formats, in which transmitted data can be encoded in both the amplitude and the phase of the optical carrier, resulting in multiplication of the transmission capacity [27]. Furthermore, spectral efficiency enhancement can also be achieved by employing much lower required channel spacing, that is as low as 12.5 GHz [23]. Lower channel spacing maximises the benefit of the available bandwidth by using more individual wavelengths for transmission, which in turn facilitates the accommodation of a higher number of end users of the network.

2) **Multiplexing/demultiplexing optical components bandwidth limitations:**

The bandwidth limitation of the optical components used in the multiplexing and the demultiplexing processes is also an important factor in defining the lowest achievable channel spacing. An array waveguide grating (AWG) is a typical component used for these functions. For demultiplexing, it works on the principle of multi-mode interference in a free-space propagation region, which induces different phase shifts in each channel, leading to the separation of the channels at different output ports, thus performing the demultiplexing operation [28]. Moreover, it can be used in a reverse manner to achieve multiplexing. However, the precise need of a specific channel spacing of an AWG-based multiplexer/demultiplexer means that the AWG has to be tailor made to operate on a given WDM grid [29]. This results in an additional cost for fabrication and implementation. The currently deployed AWGs typically operate with a spacing of 100GHz and 50GHz contributing to an opposing force towards movements to smaller grid sizes (25 and

12.5GHz). Research efforts are looking for alternative technologies allowing for more reconfigurability such as wavelength selective switch (WSS), which have been proposed to tackle the lower bandwidth limitation issue [30].

3) **Amplifiers:**

They represent a crucial part of a WDM system. As previously mentioned, they are used to amplify the signal propagating through the fibre, compensating for any attenuation or losses occurring during the transmission process. EDFAs are the most commonly used amplifiers in fibre optic links, ensuring sufficient power for each channel to be transmitted. Despite this important function, the EDFAs impose a limitation on the system, as each EDFA operates over a specified limited wavelength range, around the conventional band (C–band) (1525nm–1565nm) or the long band (L–band) (1570nm–1610nm), which results in the limitation of the WDM system to that specific operation wavelength range. In recent years, the focus has been on enhancing the transmission capacity of the WDM systems. One of the main methods of achieving this is through extending the operational wavelength of WDM beyond the C-band to both L-band and short- band (S-band) (1460 nm- 1525 nm) in order to accommodate a larger number of optical channels. Raman amplification [31] can be used as an alternative technique to EDFA, as the former can operate in all the three mentioned wavelength bands.

1.3.1.1 Development of WDM systems

Figure 1.3 shows the estimation and the prediction of the global internet traffic by connected devices through the period of years (2017- 2022) [32]. Despite considering only a span of five years, the global internet traffic by 2022 is expected to be approximately four times (≈ 400 Exabytes per month) of what it was in 2017 (≈110 Exabytes per month). This is primarily driven by the massive increase in number of users of smart internet-connected devices and gadgets such as smartphones and tablets. Furthermore, the introduction of bandwidth-hungry applications such as real-time online gaming, high-definition video and cloud services has contributed to a remarkable increase in the required bandwidth for internet traffic. The unabating increase in demand for bandwidth and internet traffic, and with the optical communication technologies reaching their maturity stages in the last decade, fears are growing of the occurrence of a capacity crunch. The latter means that the technology will not be able to be ahead of the required internet traffic usage and it will reach its limits, which will result in the optical networks not being able to respond to the required bandwidth demand leading to poor service to the end user [33] [34]. To avoid this, more creative solutions have to be introduced to provide the optical networks with a better performance and a higher spectral efficiency [35].

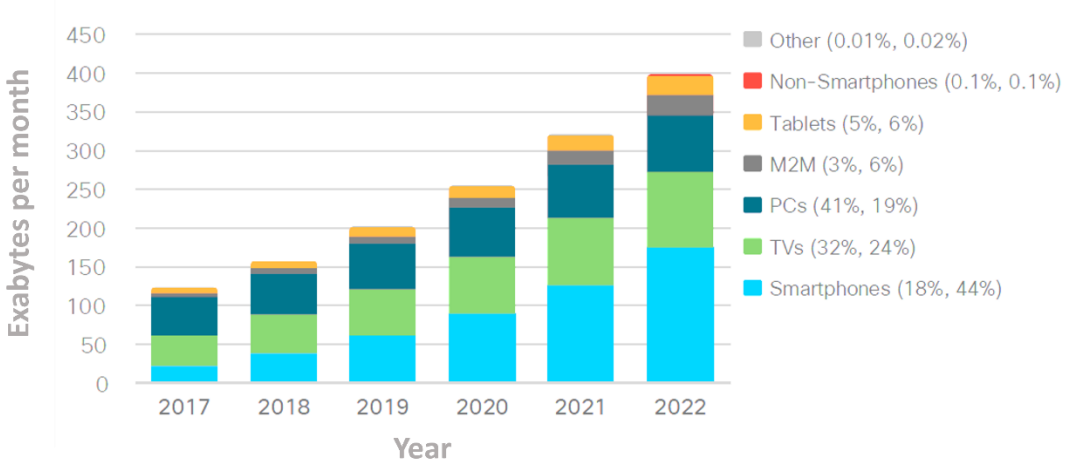

Figure 1.3: Global Internet traffic growth by year through the period (2017-2022). Source: [32].

There exist several methods that aim towards achieving higher spectral efficiency such as the usage of efficient advanced modulation techniques and enhancing the occupied bandwidth. However, in this section, the focus will be about two main methods:

- Increasing the modulation order (number of bits per transmitted symbol) which enhances the usage of the available spectrum. This requires the usage of advanced modulation formats which make use of the phase. Phase noise is an important aspect that will be discussed later in details in this thesis.
- Increasing the number of optical channels through reduction of the size of the guard bands among them, allowing for the implementation of densely packed optical channels.

Since their first implementation, WDM systems have had great breakthroughs which allowed for a massive increase in the achievable transmission capacity to be able to counter the ever-increasing demand for bandwidth. In [36], the authors demonstrate transmission capacities of 34.9 Tb/s over 6375 km based on Gaussian-like dual polarisation amplitude phase shift keying (DP-64APSK) and 33.3 Tb/s over 6800 km using DP-32 QAM modulation formats. The technological breakthroughs of the various aspects of the WDM systems, have resulted in a massive boost of the *BL* product, opening new horizons for optical fibre communications to establish itself as the primary method of transferring data all over the world.

Early commercial WDM systems employed a simple 2-level amplitude modulation format (OOK) which encodes one bit per symbol. In 1995, the first commercial WDM system was introduced to transmit data with a total bit rate of 340 Gb/s (17 communication channels with a bit rate of 20 Gb/s each) over 150 km fibre with an amplifier spacing of 50 km [37]. Over time, channel bit rates improved up to 40 Gb/s employing OOK modulation [38]. Nevertheless, basic amplitude formats such as OOK has their own limitations in terms of achievable bit rate and transmission distance [39]. On the other hand,

advanced modulation formats can be utilised to encode information in both the phase and the amplitude of an optical carrier (coherent communication) [27]. Additionally, lasers emitting in dual polarisation modes offer the possibility of utilising the two polarisation modes for encoding the data [40]. The usage of advanced modulation formats has allowed the emergence of coherent optical networks [41]. In the early stage of the development of coherent communications, a channel bit rate of 40 Gb/s was achievable using DQPSK, leading to a doubling in the spectral efficiency compared to the conventional OOK [42]. Soon after that, a higher channel bit rate of 100 Gb/s was introduced employing advanced modulation formats with a channel spacing of 50 GHz to achieve a high spectral efficiency of 2 *(bit/s)/Hz* [43] which is 10 times the initial spectral efficiency provided by the early WDM systems. Continuous research efforts were exerted to push the channel bit rate to even higher values up to 400 Gb/s and 1 Tb/s (namely coherent super-channel) to be used with next generation optical networks [44].

1.3.2 Role of optical amplifiers

The invention and implementation of optical amplifiers had revolutionised the fibre optic communication systems a few decades ago. Since then, optical amplifiers have become crucial and indispensable components of fibre optic communication systems. Currently deployed optical networks consist of lossy elements such as SMF, connectors/adapters, modulators, splitters etc. Hence, amplification of the optical signal at intermittent points of the optical network, depending on its topology, is vital. The essential properties of amplifiers, apart from amplification and power scaling, are bandwidth of operation, noise figure (NF), energy efficiency, and integrability. Several kinds of optical amplifiers have been implemented, as discussed below. The choice of the optimum-performing amplifier is made based on the above-mentioned parameters, which are imposed by the system requirements.

The placement of the amplifier in the network defines its specific function. If it is placed directly after the transmitter, it is called “booster amplifier”. Placing it between the SMF spans makes it an “in-line amplifier”, while if placed before the receiver, it is referred to as “pre-amplifier”. An amplifier is expected to have a high gain and a low NF when employed as a pre-amplifier, but it typically generates a low output power as the input optical signal is already low in power, distorted, and noisy. On the other hand, boosters, and in-line amplifiers generate a higher output power and have a high saturation power, but at the expense of having a higher NF.

There exist different types of optical amplifiers. However, the focus on this work will be on three main types that have attracted more attention due to their advantageous properties such as ease of

implementation, cost efficiency and extended wavelength region. The three types are: Raman amplifiers, EDFA and semiconductor optical amplifier (SOA).

Raman amplifiers: The main advantage of Raman amplifiers is their extended wavelength operation range, as they exhibit a wide gain bandwidth of ~100 nm around the 1550 nm wavelength [45]. The Raman amplification process utilises the transmission fibres themselves as a gain medium. Its operation is based on the transfer of energy between the pump and the optical signal through the inelastic scattering process of the pump photon in the non-linear regime of the medium [46]. Raman gain arises from the transfer of power from one optical carrier to another that is downshifted in frequency by an amount corresponding to the energy of an optical phonon [45]. However, Raman amplifiers require a high-power laser pump, which is a limiting factor. Hence, they are usually employed in long haul core networks as an in-line amplifier.

EDFA: Is the most commonly used type of amplifiers in optical networks due to its outstanding inherent characteristics in terms of gain due to the usage of a rare earth element [47]. According to the optical network requirements, an EDFA can be employed as either a booster, in-line or pre-amplifier, with the respective gain and noise characteristics [48]. As previously stated, the operating wavelength of EDFAs are one of their limitations, EDFAs employed as preamplifiers use pump lasers at a wavelength of 980 nm, while booster and in-line EDFAs usually use pumps at 1480 nm [7] [49]. Even though EDFAs are the most commonly used optical amplifier type, they suffer from some drawbacks such as: possessing a bulky structure and being costly to manufacture. Additionally, due to the optical pumping of the gain medium, EDFAs have low energy efficiency [50]. Finally, they do not have the capability of being photonically integrated, unlike SOAs.

SOA: Another alternative to the EDFAs is the SOA which provides several advantages over the former. It has a similar structure to that of the semiconductor laser except that it does not have a laser cavity where the amplification of the optical signal is achieved through stimulated emission [51]. SOAs are typically utilised as booster amplifiers or pre-amplifiers but rarely used as an-inline amplifier, as they have a lower gain, lower output saturation power and a higher NF compared to EDFAs. However, SOAs possess an attractive property, which is their ability to be integrated with other optical components such as lasers, modulators and optical detectors on the same chip, providing a lower cost and footprint solution. SOA also provides a simple mean of analysing dynamics in semiconductor materials. Chapter 6 in this thesis will be dedicated to a detailed characterisation of an integrated multi-section SOA which has the potential to provide low NF or high saturation power depending on the bias configuration applied to its different sections.

1.3.3 Modulation of an optical carrier

As aforementioned, the most basic transmission scenario is modulating a single optical carrier with data and transmit it through a single channel.

Modulation of an optical carrier is the process of imposing the desired data on the laser light signal. As previously mentioned, several laser signal characteristics can be employed for that purpose such as amplitude, phase, and polarisation.

The electric field of the output signal of a typical laser diode can be described using the following equation:

$$E(t) = A(t).\, e^{j(\omega_o t + \varphi(t))} \tag{1.1}$$

where $E(t)$ is the electric field, $A(t)$ is the amplitude, ω_o is the angular frequency and φ is the phase of the generated electric field. It is evident from the equation, that the output represents both the amplitude and phase of the laser signal and can be resolved into real and imaginary components. These two components can be represented as In-phase (I) and quadrature (Q) components correspondingly. Figure 1.4 shows several examples of I-Q constellations representing different types of modulation formats. The amplitude is depicted by the length between the origin point and each point of the constellation diagram (blue circles) while the phase is represented by the angular component.

The optical signal needs to be detected after being transmitted through the optical fibre, and the transmitted data needs to be demodulated to recover the desired information from the optical carrier. There exist two main methods for detection, direct detection, and coherent detection. In the direct detection, a photodiode is employed to detect the optical signal and generate an output photocurrent, which is directly proportional to the power of the received optical signal. Direct detection receivers are mainly affected by the intensity noise of the optical signal [52]. Despite being a simple and a cost-effective technique, direct detection is limited to recovering of intensity modulated signals as it is phase independent.

For phase modulated optical signals, more complex detectors are required which are called coherent detectors. The phase variations of the incident modulated signal are converted into intensity changes by coupling the modulated optical signal with a reference signal, known as local oscillator (LO), creating constructive or destructive interferences depending on the relative phase differences [53].

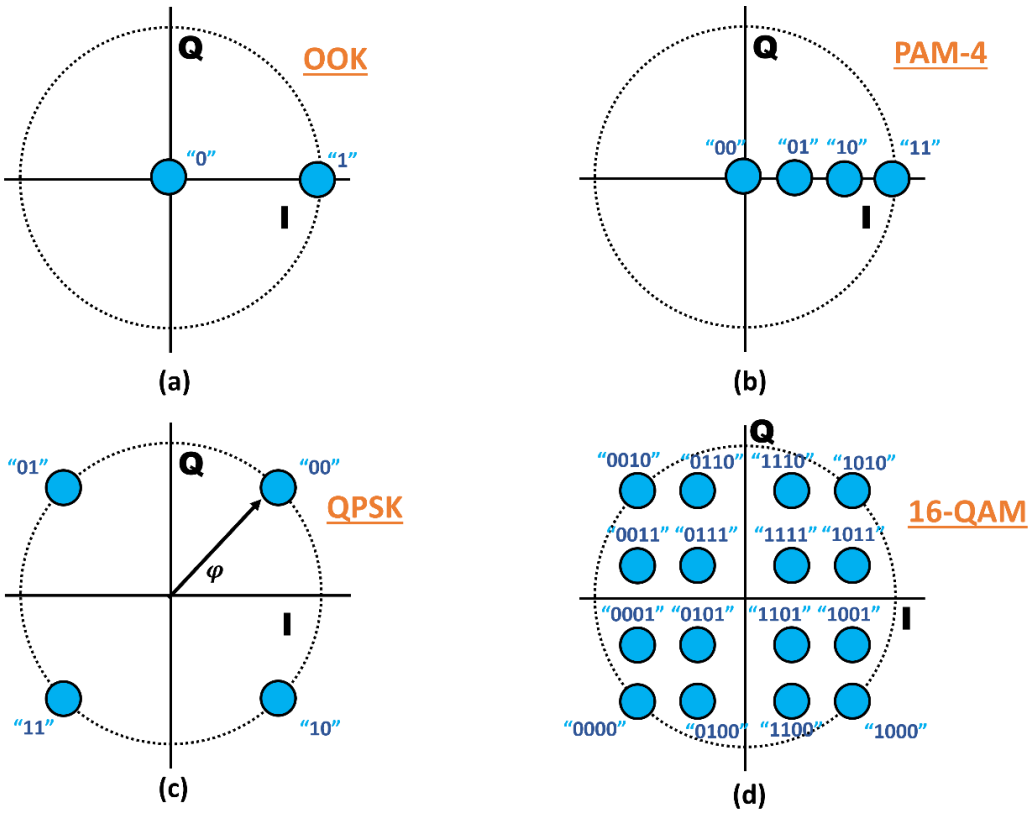

Figure 1.4: Constellation diagrams for the following modulation formats: (a) OOK, (b) PAM-4, (c) QPSK and (d) 16-QAM.

The simplest modulation format to be used with WDM systems is the OOK format, depicted by the constellation in Figure 1.4(a). It is a 2-level intensity modulation format. The laser diode is simply turned on and off to represent levels '1' and '0' respectively. In the constellation diagram, the '0' (first) symbol is represented by the symbol at the axes' origin. On the other hand, the '1' (second) symbol is represented by the amplitude of the electric field vector at the I-axis. There is no angular component entailing there is no phase modulation. In OOK, one bit is represented by one symbol. Hence, the bit rate and symbol rate (baud rate) are equal to each other.

1.3.3.1 Advanced modulation formats

In order to respond to the unabating demand for transmission capacity growth, it was crucial to look into improving the spectral efficiency. Hence, the advanced modulation formats were introduced to be used with WDM systems, where number of encoded bits per symbol could be increased. This entails the transmission of a larger amount of data using the same symbol rate resulting in an overall enhancement of the spectral efficiency. The latter is defined as the total data rate that can be transmitted over a given bandwidth. Its unit is (bit/s)/Hz and can be calculated using the following formula:

$$Spectral\ efficiency = \frac{Data\ rate}{channel\ bandwidth} \quad (1.2)$$

The introduction of multi-level amplitude modulation allowed the transfer of a higher number of bits per symbol. The simplest form of applying this technique is the pulse amplitude modulation (PAM). PAM-4 entails the usage of four different pulse amplitude levels to encode the transmitted data. The usage of the four levels results in the possibility of enhancing the spectral efficiency by transmitting two bits per symbol. In comparison with OOK, PAM-4 provides double the transmission capacity. The constellation diagram showing the four different amplitude levels of PAM-4 is shown in Figure 1.4(b). The current research interest for PAM-4 is focused on implementation in short reach networks and data centres [54].

The relationship between the number of optical symbols and optical bits is portrayed by the following equation [55]:

$$M = log_2(m) \quad (1.3)$$

where m is the number of the available symbols in the modulation format, and M is the number of bits per symbol. The modulation order can be defined as the number of the different symbols that a modulation format is capable of transmitting.

Employing phase modulation is another technique to extend the transmission capacity of the network. QPSK is a form of phase modulation with the constellation diagram shown in Figure 1.4(c), in which, the amplitude is kept constant, and each symbol corresponds to a different phase value that is imposed on the optical carrier. QPSK provides a symbol rate of 2 bits per symbol, as four different phase values can be transmitted. This once again results in doubling of the transmission capacity obtained in comparison with the OOK format.

A further advanced step is employing the encoding of the data in both amplitude and phase of the laser in order to provide a better transmission capacity. QAM is another modulation format, that embeds transmitted data within both the laser amplitude and phase. Such modulation formats are referred to as m-QAM where m is the total number of symbols. The constellation diagram for 16-QAM format is shown in Figure 1.4(d). Each symbol represents a distinctive state of amplitude and phase values. 16-QAM provides the prospect of transmitting four different bits per symbol, resulting in multiplying the system transmission capacity by 4 times compared to the OOK on the same time interval [56]. Higher order QAM such as 32-QAM [57] and 64-QAM [58] have been introduced to further improve the transmission capacity and the spectral efficiency of the network.

Despite the fact that augmenting the symbol size by introducing higher order advanced modulation formats that allow the inclusion of higher number of bits per symbol has a positive impact on the transmission capacity and the spectral efficiency of the network [59], it also introduces more stringent requirements on the optical carrier. An optical carrier with a higher OSNR and a much lower phase noise/optical linewidth is required for such implementations [60]. In such regard, usage of 64-QAM in place of 16-QAM would facilitate the encoding of two more bits per symbol, thus improving the spectral efficiency. However, it would require an optical carrier with an OSNR higher by ~6 dB [60].

The most straightforward method to improve the OSNR values is to increase the optical power launched from the laser into the optical fibre. However, there exist limitations on the maximum peak power that can be launched into the fibre to avoid the manifestation of optical nonlinearities in fibre which can cause distortion of the transmitted optical signal [61].

Another consequence of increasing the modulation order is the augmented sensitivity of the system to the noise. It is due to the fact that including more symbols in the modulation format populates the constellation diagram more densely, thus resulting in a significant challenge in distinguishing the adjacent symbols in the receiver after the transmission [60]. The usage of an optical source with lower intensity noise and phase noise can be considered as a critical solution to tackle this issue and to extend the reach of optical networks employing coherent solutions [62].

To conclude, advanced modulation formats can be considered as one of the essential means of achieving a better spectral efficiency. However, for high bit rates (> 100 Gb/s), the increase in the modulation order is limited by the achievable transmission distance due to the introduced noise and distortion effects in the fibre. Furthermore, the usage of narrow spectral width optical sources with advanced modulation formats would result in an unnecessary waste and ineffective usage of the available bandwidth of the ITU-50 GHz grid due to the necessity of implementation of guard bands. As previously mentioned, the bandwidth demand keeps increasing. Hence, the usage of single carrier transmitters with advanced modulation formats will struggle to satisfy this demand. This is because of the wavelength instability suffered by lasers which makes the use of guard bands mandatory. The usage of reliable multi-carrier transmitter sources in conjunction with advanced modulation formats has gained a lot of attention recently to mitigate these drawbacks by further enhancement of utilisation of the available bandwidth. Employing multi-carrier transmitter sources results in decreasing the size of guard bands, allowing the fitting of more optical channels in the same spectral bandwidth, and hence, further improving the overall spectral efficiency of the system [63]. To further enhance the spectral efficiency, flexible grid and gridless technologies are introduced. Flexible grid employs much lower granularity frequency grid, while gridless cross out the use of any specified grids

which results in an enhanced usage of the available bandwidth. This will be discussed in more detail in the Section 1.4 below.

1.4 Towards flexible and elastic networks

The unpreceded acceleration in demand for higher bandwidth of data transfer has put a lot of pressure on optical networks to evolve towards higher transmission capacities. However, this capacity improvement needs to be met with improved use of the available spectrum (enhanced spectral efficiency). Figure 1.5 shows a comparison of three different suggested scenarios for transmitting 1 terabit of data in a single cycle [64]. In “option 1”, a single carrier operating at 1 Tpbs is employed, here the optical transmitter is operating at a really high bit rate. However, electronics that operate at 320 Gbaud rate will be required which is not currently available in the market.

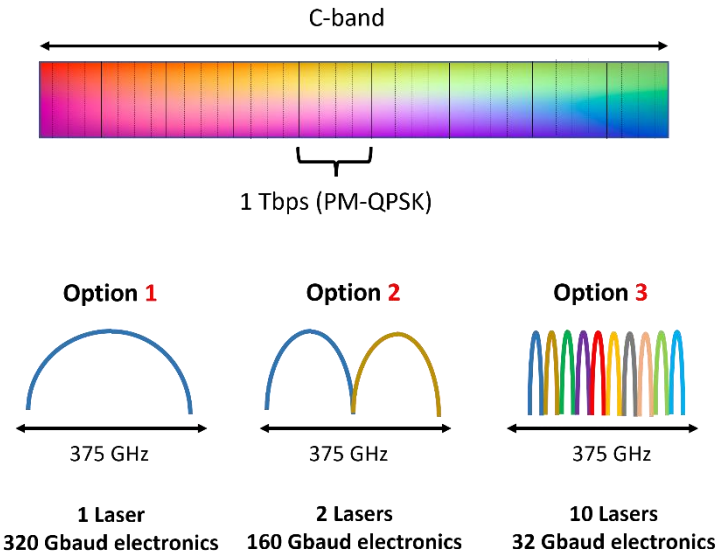

Figure 1.5: Spectral efficiency comparison for a single carrier, two carriers super-channel and 10 carriers super-channel.

In “option 2”, a super-channel (which will be defined later) of two 500 Gb/s optical carriers is employed. Although the electronics rate is now halved to 160 Gbaud, it is still not available in the market for usage. The third scenario “option 3” uses also super-channel concept, but this time with 10 different carriers each operating at 37.5 Gb/s. This requires electronics operating at 32 Gbaud, which is already available in the market. However, implementing 10 different channels in compliance with the ITU-T G.694.1 recommendation, which forces a fixed grid spacing (several spacing including 25 and 50 GHz) would mean an inefficient use of the available spectrum leading to a decrease in the spectral efficiency. In the presented scenario (Option 3), assuming the usage of a 10-carrier super-channel of 100G per subcarrier, using polarisation multiplexed (PM)-QPSK, then the carrier width is

about 37 GHz. On one hand, the carrier width will be too wide and will not fit in a 25 GHz fixed grid. On the other hand, using of a fixed 50 GHz grid will mean wasting of around 13 GHz (>25%) of the available spectrum. Flexible grids with a lower granularity are needed to tackle this issue.

The development of more flexible and elastic networks has become a necessity for enhancing the spectral efficiency. The optical networks have to employ grids with lower frequency granularities or even to go beyond that to a more flexible solution that does not use any specified grids (gridless) [65]. For this purpose, ITU-T has also proposed the implementation of a much lower granularity frequency grid (12.5 GHz) in their G.694.1 recommendation [23]. This gives the ability to define super-channels (defined as an advanced evolution of the DWDM where multiple coherent optical carriers are combined to create a unified channel of a higher data rate which leads to the achievement of higher bit rates) with a spectral width that is equal to multiples of 12.5 GHz. It improves the spectral efficiency of the installed optical fibres by reducing the frequency spacing between the adjacent optical channels through the usage of a finer granularities. Combining this with technologies that allow reduction of the size of the guard bands (discussed in detail in Section 1.4.3) results in an enhancement of the usage of the available optical bandwidth and an overall improved spectral efficiency [83].

Elastic optical network (EON) is a term that is used to refer to a flexible network, employing the 12.5 GHz flexible grid [66]. Typical 50 GHz grid can satisfy the requirement for transmission systems using 100 Gb/s bit rates. However, there is a rising interest in moving towards higher bit rates beyond the 100 Gb/s and reaching 400 Gb/s or even 1 Tb/s. Fitting the broad spectral width of a 400 Gb/s signal into the 50 GHz grid is a challenging task and a higher modulation format (with enhanced spectral efficiency) would be required. However, it is well known, that the higher order formats place a stringent requirement on the linewidth and OSNR, thereby limiting the reach of the system [66]. On the other hand, EONs can provide a better solution by flexible allocation of different grid sizes according to the need for transmission at a particular instant. An optimised spectral efficiency and network performance can be achieved through the dynamic adjustment of several transmission parameters such as information rates, channel bandwidths, and modulation formats depending on the available bandwidth, required capacity, optical link reach or any other required specifications [67].

Figure 1.6 shows a schematic example of the aggregate spectral saving that the system can benefit of when employing the concept of 12.5 GHz flexible grid and gridless technologies in place of the typical 50 GHz grid. It is important to note that the grid-less technologies are still futuristic and research efforts are being conducted to overcome the different challenges facing it such as inter channel interference [68].

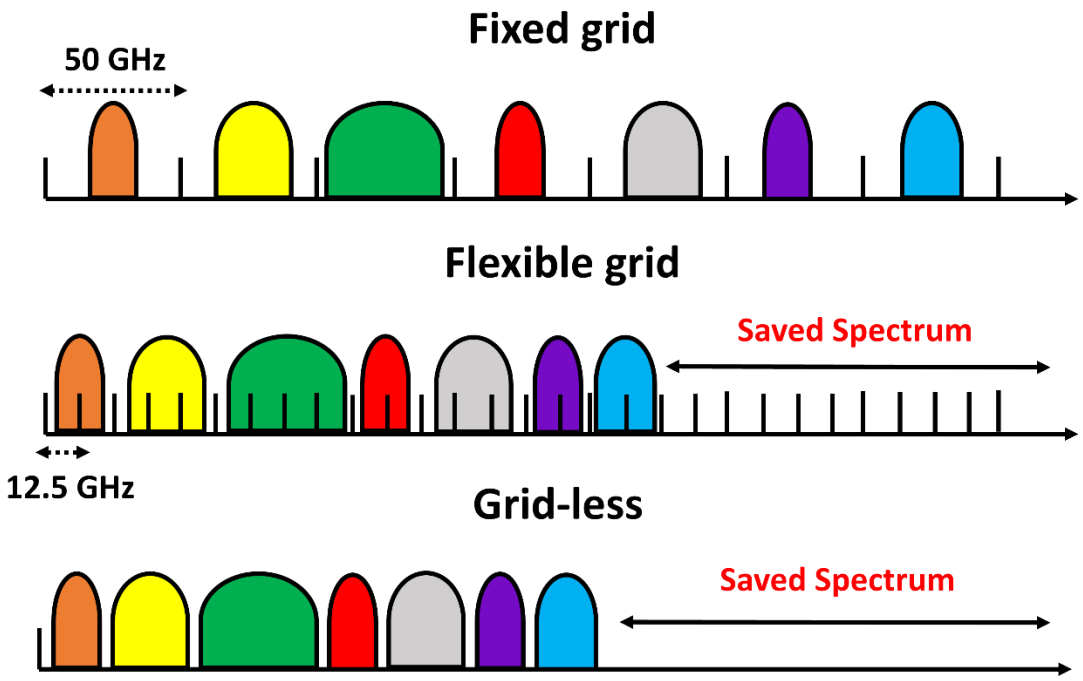

Figure 1.6: Comparison of the spectral occupancy of 50 GHz fixed grid, 12.5 GHz flexible grid and gridless configurations.

1.4.1 Signal shaping enabling technologies

Signal shaping is a term that refers to the modification of the spectral and temporal shape of the pulses carrying the transmitted data. This helps in allowing the dense packing of optical channels together in the available frequency spectrum, hence improving the overall spectral efficiency. The main motivation for the introduction of signal shaping in optical communications systems was to reduce the amount of inter-symbol interference (ISI) [69], where the transmitted signal is distorted due to the interference of adjacent symbols. ISI is caused as a result of reduction of the channel spacing, which also results in inter-carrier interference (ICI) or crosstalk between the adjacent communication channels, thus reducing the transmission capacity of the system [70]. In this work, orthogonal frequency division multiplexing (OFDM) and Nyquist WDM are the two used signal shaping techniques for reduction of ISI and ICI and to enhance the spectral efficiency of the network.

1.4.1.1 Orthogonal frequency division multiplexing

OFDM can be considered as a derivative of FDM where an optical channel uses multiple sub-carriers located at adjacent frequencies [71]. Furthermore, it comprises spectrally overlapped optical channels to maximise the usage of the available spectrum. Typically, the overlapped channels would have interference with each other due to the crosstalk occurring among them. However, using OFDM, the adjacent sub-carriers (channels) are ensured to be precisely orthogonal to each other [17]. This

ensures that the channels may overlap together without interfering with each other. Hence, OFDM offers the capability of enhancing spectral efficiency without causing interference. Figure 1.7(a) shows a frequency domain schematic representation of an OFDM system. It clearly shows the size of spectral saving that OFDM systems can achieve in comparison with the traditional 50 GHz fixed grid.

OFDM technique entails the temporal shaping of the transmitted signal. The transmitted pulses in time domain are ideal rectangular pulses. This corresponds to a sinc shaped spectral functions in the frequency domain. These shaped spectra are precisely spaced at multiples of the inverse of the pulse period. The neighbouring spectra strongly overlap in the frequency domain. However, their orthogonalisation prevents the interference among them. The peak of each sub-carrier coincides with the null of adjacent sub-channels as shown in Figure 1.8.

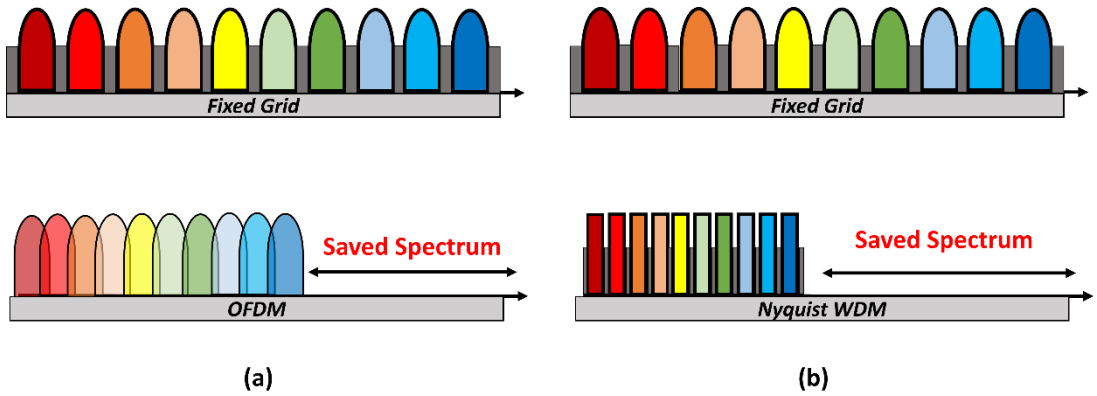

Figure 1.7: Illustration of the schematic architecture for: (a) OFDM, (b) Nyquist WDM.

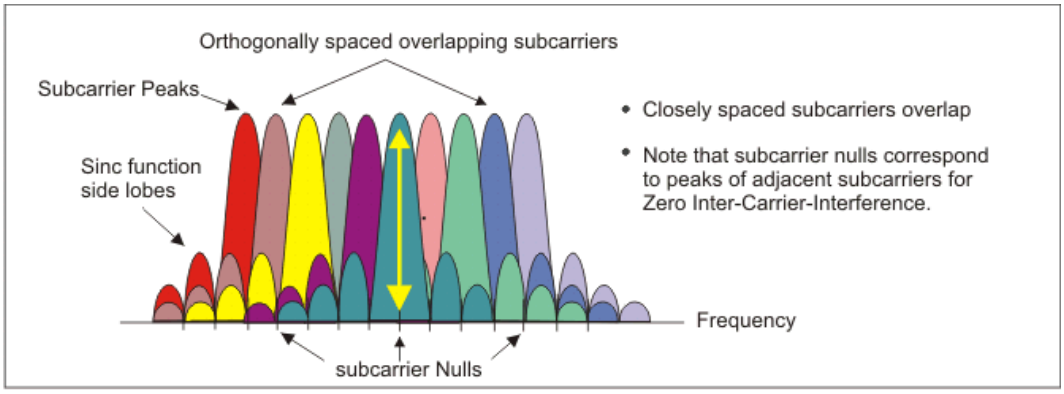

Figure 1.8: OFDM spectrum with overlapped sinc functions. source: [72].

OFDM systems suffer from crosstalk effects among its channels due to them being overlapped together. To mitigate and eliminate these effects, the different sub-carriers should have a strong phase correlation, which allows the phase noise to be cancelled out at the receiver [73]. Conversely, the arbitrary phase noise of the sub carriers would translate into frequency noise, causing the subchannels to interfere together [74].

1.4.1.2 Nyquist WDM

Nyquist pulse shaping is another well-established spectral shaping technique, where each sub-channel is spectrally shaped to a rectangular shape to occupy the minimum possible spectral width or bandwidth that ensures that ICI does not occur. This process is decided by the Nyquist-ISI criterion and coincides with the symbol rate [75]. Nyquist shaping allows the sub-channels to be placed in a very compact manner, which allows the reduction of the size of channel spacing and guard bands without having ISI effects at the receiver [76].

Figure 1.7(b) shows an ideal spectrum of optical channels employing Nyquist WDM. The various channels are rectangular shaped and densely packed but do not overlap. This optical spectrum corresponds to a series of sinc pulses in the time domain.

To implement the ideal shape of Nyquist WDM signals, a precise rectangular shape filter is needed at the transmitter. Nonetheless, it is hard to realise perfect sinc pulses physically in the time domain. An alternative solution is to use a root raised cosine (RRC) filter for Nyquist pulse shaping in addition to matched filters at the receiver to reduce the ISI effects due to the implemented narrow filtering. After shaping the sub-channels individually, they are multiplexed to realise a super-channel with reduced guard bands. For successful employment of Nyquist WDM, the used sub-carriers should offer a good level of wavelength stability and low phase noise in order to avoid drift, fluctuations and interference between the different sub channels.

Spectral efficiency enhancement can be achieved using Nyquist WDM, due to the minimisation of the sub-channel spectral occupancy and reduction of the size of guard bands between the different sub-channels.

Multiple optical carriers are an attractive solution for implementing super-channels. As is the case with the rest of WDM systems, to generate super-channels employing advanced modulation formats, a reliable optical source with the capability of producing a stable and closely frequency-spaced optical carrier is desired. The latter can be sourced either from an array of lasers or an OFC. In the next section, a discussion about an array of lasers which is the currently employed multi-carrier optical sources in WDM networks, will be presented showing their limitations and relevant challenges. Furthermore, a more promising alternative to achieve super-channels, which is the optical frequency combs (OFCs), will be introduced. The latter is the focus of this thesis and will be discussed in full detail in the next chapter.

1.4.2 Bank of lasers

The current technology used to realise multiple optical carriers entails the employment of a bank or an array of single mode lasers [77]. Each laser is designed to emit at a certain wavelength to maintain the desired frequency spacing and to satisfy the requirements of the ITU-T 50 GHz grid.

Figure 1.9(a) shows an illustration of an array of single mode lasers. One of the main challenges faced by the use of a bank of single mode lasers, is to keep the frequency spacing between the optical carriers constant. Normally, a drift of the emission wavelength of the laser is expected over time. This wavelength drift can cause a serious problem when the frequency spacing between the adjacent channels is small, or even worse if the guard-bands are eliminated.

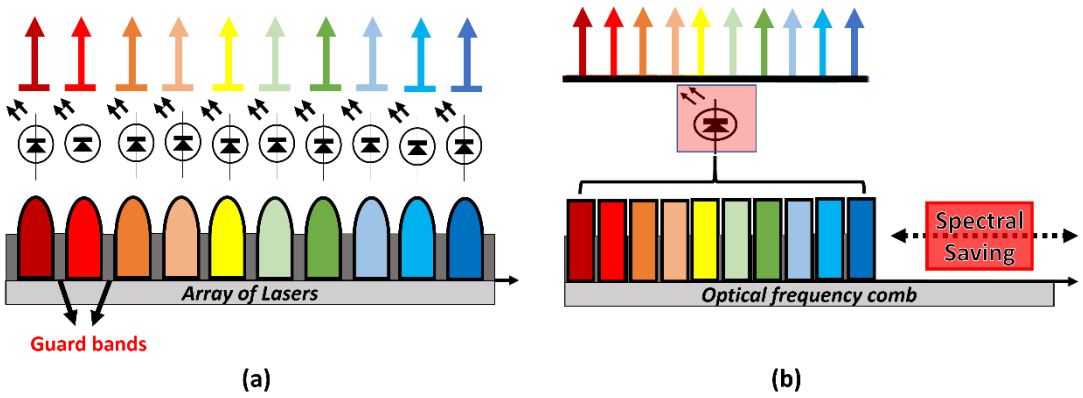

Figure 1.9: Illustration of: (a) Fixed grid with an array of lasers, (b) Flexible grid with an optical frequency comb.

In such cases, an undesired interference between adjacent channels can take place. Control mechanisms such as the use of an optical interferometer or a digital feedback loop have been proposed to stabilise the emission wavelengths of multiple laser sources at the same time [78] [79]. However, usage of such methods increases the complexity, cost, and power consumption of the optical network.

Another drawback of usage of bank of lasers as a multi-carrier optical source is the lack of phase correlation among the optical carriers as they are generated from different laser sources. As mentioned before, phase correlation is a desired property for optical systems employing OFDM. Furthermore, having phase correlation relaxes the digital signal processing (DSP) requirements, resulting in lower complexity and a reduction of the power consumption [80].

1.4.3 Optical frequency combs

An OFC can be considered to be a ruler of equidistant spectral lines, each of which can be used as a distinct sub-carrier [81]. OFC offers a precise free spectral range (FSR) amongst its lines. In [82], the authors show that the individual lines of the OFC can be quantum-mechanically entangled to form complex optical states. Energy-time entangled quantum OFCs is considered as an attractive source to enable a unique, practical and scalable framework for quantum signal and information processing [83].

The merits of OFCs have led to a wide variety of applications such as THz and millimetre wave generation [84], spectroscopy [85], and most importantly as an efficient optical source for next generation optical network [86] [87], which is the main focus of this thesis.

An OFC can be used as an efficient replacement of the bank of semiconductor lasers currently used as a transmitter in optical networks. It offers a simpler, more compact, cheaper, and lower power consumption solution when compared to an array of traditional lasers. Figure 1.9(b) shows an illustration of an OFC and its spectral occupancy compared to the traditional laser array. The inherent precise and stable frequency spacing between the different OFC spectral lines (tones) allows the reduction or even the elimination of guard bands between them.

The tunability in both the frequency spacing and emission wavelength is another attractive feature that OFCs offer. This allows the OFC to be used as a flexible optical source for EONs that can be simply tuned to meet the requirements of the traffic demands in terms of symbol rate and range of wavelength operation [88].

Advanced modulation formats, discussed earlier in this chapter, have shown their potential to increase the optical network capacities by substantially increasing spectral efficiency and maximising the benefits of usage of the existing resources. At the same time, the usage of a reliable multi-carrier optical source that can accommodate these advanced modulation formats while increasing the spectral efficiency is crucial. OFC is an attractive candidate for this due to its precise FSR which results in the decrease of the guard bands size and improving the spectral efficiency. An optimum OFC is expected to give a high number of optical carriers with good spectral flatness (in terms of peak power difference among its tones) and a precise and stable frequency spacing among them. Furthermore, the OFC tones should possess low phase noise, low relative intensity noise (RIN) and a strong phase correlation among them. An OFC with these spectral characteristics has the potential to be an attractive optical multicarrier source that can be used in an optical network that employs DWDM and super-channels.

In the next chapter, a detailed study of an OFC is presented. This includes definition and explanation of the various spectral characteristics that are used to describe the OFC. Furthermore, a study of the different semiconductor laser-based OFC generation techniques such as mode locked lasers (MLL), electro-optic modulator-based combs, micro-ring resonators (MRR) and gain switching will be given. The advantages and disadvantages of each technique will be illustrated. A special focus will be placed on the gain switching as it the main OFC generation technique that will be used in this thesis.

1.5 Conclusions

The last decades have witnessed a revolutionary development of optical communication networks, as it has evolved from bit rates of “Mb/s” to “Tb/s” thanks to a series of technological breakthroughs improving different components and parts of the network. However, the introduction of bandwidth-hungry applications such as real-time online gaming and ultra-high-definition video streaming has resulted in a persistent demand for more bandwidth and transmission capacity putting more pressure on the currently deployed networks.

As an immediate response to these challenges, advanced modulation formats and multi-carrier modulation have been proposed to tackle the increasing bandwidth demands. Higher order modulation formats such as QPSK and QAM imply multi-level data encoding in the amplitude, phase and even polarisation state of the carrier to increase the spectral efficiency and the transmission capacity of the network. At the same time, the multi-carrier modulation techniques such as OFDM and Nyquist WDM result in the reduction of the size of guard bands inserted between the adjacent channels, reducing the channel spacing which enhances the usage of the available bandwidth. Using these technologies in conjunction with the concept of WDM super-channels allows the achievement of higher data rate going beyond Tb/s. To achieve super-channels with an optimum use of the available spectrum, a migration from the fixed 50 GHz grid to a flexible 12.5 GHz grid is discussed. An OFC instead of an array of lasers as a source of multiple optical carriers is then discussed as a perfect candidate to be used with next generation optical networks employing the flexible 12.5 GHz gird. It provides efficiency, stability, flexibility, and cost-efficiency. It is used for generation of multiple stable optical carriers that are phase correlated from a single laser source. It also offers a precise FSR amongst its lines.

References

[1] J.-P. Uzan and B. Leclercq, The Natural Laws of the Universe: Understanding Fundamental Constants, New York: Springer , 2010.

[2] J. Ballato and P. Dragic, “Glass: The Carrier of Light - A Brief History of Optical Fiber,” *International Journal of Applied Glass Science,* vol. 7, no. 4, pp. 413-422, 2016.

[3] G. P. Agrawal, Fiber-Optic Communication Systems, Fourth Edition, John Wiley & Sons, 2010.

[4] J. Hecht, “The Breakthrough Birth of Low-Loss Fiber Optics,” 1 March 2020. [Online]. Available: https://www.osa-opn.org/home/articles/volume_31/march_2020/features/the_breakthrough_birth_of_low-loss_fiber_optics/. [Accessed 4 July 2021].

[5] G. P. Agrawal, “Optical Communication: Its History and Recent Progress,” in *Optics in Our Time*, Springer Link, 2016.

[6] R.-J. Essiambre and R. W. Tkach, “Capacity Trends and Limits of Optical Communication Networks,” *Proceedings of the IEEE ,* vol. 10, no. 5, pp. 1035-1055, 2012.

[7] P. Becker, N. Olsson and J. Simpson, Erbium-Doped Fiber Amplifiers Fundamentals and Technology, Elsevier Inc, 1999.

[8] H. Kogelnik, “High-capacity optical communications: personal recollections,” *IEEE Journal of Selected Topics in Quantum Electronics,* vol. 6, no. 6, pp. 1279-1286, 2000.

[9] T. Li, “Advances in lightwave systems research,” *AT&T Technical Journal,* vol. 66, no. 1, pp. 5 - 18, 1987.

[10] Wei Shi, Ye Tian and Antoine Gervais, “Scaling capacity of fiber-optic transmission systems via silicon photonics,” *Nanophotonics*, vol.9, no.4, 309, 2020.

[11] J. Yamada, S. Machida and T. Kimura, “2 Gbit/s optical transmission experiments at 1.3 µm with 44 km single-mode fibre,” *Electronics Letters,* vol. 17, no. 13, p. 479 – 480, 1981.

[12] T. Miya, Y. Terunuma, T. Hosaka and T. Miyashita, “Ultimate low-loss single-mode fibre at 1.55 µm,” *Electronics Letters ,* vol. 15, no. 4, p. 106 – 108, 1979.

[13] V. A. Bhagavatula, M. S. Spotz and W. F. Love, “Dispersion-shifted segmented-core single-mode fibers,” *Optics letters,* vol. 9, no. 5, pp. 186-188, 1984.

[14] A. Gnauck, B. Kasper, R. Linke, R. Dawson, T. Koch, T. Bridges, E. Burkhardt, R. Yen, D. Wilt, J. Campbell, K. Nelson and L. Cohen, “4-Gbit/s transmission over 103 km of optical fiber using a novel electronic multiplexer/demultiplexer,” *Journal of Lightwave Technology,* vol. 3, no. 5, pp. 1032 - 1035, 1985.

[15] H. Ishio, J. Minowa and K. Nosu, “Review and status of wavelength-division-multiplexing technology and its application,” *Journal of Lightwave Technology,* vol. 2, no. 4, pp. 448 - 463, 1984.

[16] L. F. Mollenauer and J. P. Gordon, Solitons in Optical Fibers: Fundamentals and Applications, Academic Press, 2006.

[17] J. Armstrong, “OFDM for Optical Communications,” *Journal of Lightwave Technology ,* vol. 27, no. 3, pp. 189-204, 2009.

[18] H.-G. Weber, R. Ludwig, S. Ferber, C. Schmidt-Langhorst, M. Kroh, V. Marembert, C. Boerner and C. Schubert, “Ultrahigh-Speed OTDM-Transmission Technology,” *Journal of Lightwave Technology,* vol. 24, no. 12, pp. 4616-4627, 2006.

[19] D. J. Richardson, J. M. Fini and L. E. Nelson, “Space Division Multiplexing in Optical Fibres,” *Nature Photonics,* vol. 7, p. 354–362, 2013.

[20] P. J. Winzer, A. H. Gnauck, C. R. Doerr, M. Magarini and L. L. Buhl, “Spectrally Efficient Long-Haul Optical Networking Using 112-Gb/s Polarization-Multiplexed 16-QAM,” *Journal of Lightwave Technology,* vol. 28, no. 4, pp. 547-556, 2010.

[21] S. Yamamoto, T. Inui, H. Kawakami, S. Yamanaka, T. Kawai, T. Ono, K. Mori, M. Suzuki, A. Iwaki, T. Kataoka, M. Fukutoku, T. Nakagawa, T. Sakano, M. Tomizawa, Y. Miyamoto, S. Suzuki, K. Murata, T. Kotanigawa and A. Maeda, “Hybrid 40-Gb/s and 100-Gb/s PDM-QPSK DWDM transmission using real-time DSP in field testbed,” in *OFC/NFOEC*, Los Angeles, CA, USA, 2012.

[22] D. Mongardien, C. Bastide, B. Lavigne, S. Etienne and H. Bissessur, “401 km unrepeatered transmission of dual-carrier 400 Gb/s PDM-16QAM mixed with 100 Gb/s channels,” in *39th European Conference and Exhibition on Optical Communication (ECOC)*, London, United Kindgom, 2013.

[23] I. T. U. (ITU), “G.694.1 spectral grids for WDM applications: DWDM frequency grid”, Series G: Transmission Systems and Media, Digital Systems and Networks,” 1 2021. [Online]. Available: https://www.itu.int/rec/T-REC-G.694.1-202010-I/en. [Accessed 7 2021].

[24] E. Connolly, A. Kaszubowska-Anandarajah and L. P. Barry, “Cross Channel Interference due to Wavelength Drift of Tuneable Lasers in DWDM Networks,” in *International Conference on Transparent Optical Networks*, Nottingham, United Kingdom , 2006.

[25] P. J. Winzer, D. T. Neilson and A. R. Chraplyvy, “Fiber-optic transmission and networking: the previous 20 and the next 20 years [Invited],” *Optics Express,* vol. 26, no. 18, pp. 24190-24239, 2018.

[26] J. Yu, Z. Jia, M.-F. Huang, M. Haris, P. N. Ji, T. Wang and G.-K. Chang, “Applications of 40-Gb/s Chirp-Managed Laser in Access and Metro Networks,” *Journal of Lightwave Technology ,* vol. 27, no. 3, pp. 253 - 265, 2009.

[27] P. Winzer and R.-J. Essiambre, “Advanced Optical Modulation Formats,” *Proceedings of the IEEE ,* vol. 94, no. 5, pp. 952 - 985, 2006.

[28] I. P. Kaminow, T. Li and A. E. Willner, Optical Fiber Telecommunications Volume A: Components and Subsystems, Elsevier Inc., 2008.

[29] B. Pulikkaseri, “Filter bandwidth definition of the waveshaper S-series programmable optical processor, White paper,” 2012. [Online]. Available: https://teracomm.com/newsite/wp-content/uploads/2015/02/WaveShaper_Filter_Bandwidth_Defn.pdf. [Accessed 31 7 2021].

[30] A. Sano, H. Masuda, E. Yoshida, T. Kobayashi, E. Yamada, Y. Miyamoto, F. Inuzuka, Y. Hibino, Y. Takatori, K. Hagimoto, T. Yamada and Y. Sakamaki, “30 x 100-Gb/s all-optical OFDM transmission over 1300 km SMF with 10 ROADM nodes,” in *33rd European Conference and Exhibition of Optical Communication (ECOC)*, Berlin, Germany, 2007.

[31] J. Bromage, “Raman amplification for fiber communications systems,” *Journal of Lightwave Technology ,* vol. 22, no. 1, pp. 79-93, 2004.

[32] CISCO, “Cisco Visual Networking Index: Forecast and Trends, 2017–2022,” March 2020. [Online]. Available: https://www.cisco.com/c/en/us/solutions/collateral/executive-perspectives/annual-internet-report/white-paper-c11-741490.html. [Accessed July 2021].

[33] A. D. Ellis, N. M. Suibhne, D. Saad and D. N. Payne, “Communication networks beyond the capacity crunch,” *Philosophical Transactions of the Royal Society: A Mathematical, Physical and Engineering Sciences,* vol. 374, no. 2062, 2016.

[34] E. B. Desurvire, “Capacity Demand and Technology Challenges for Lightwave Systems in the Next Two Decades,” *Journal of Lightwave Technology,* vol. 24, no. 12, pp. 4697-4710, 2006.

[35] A. A. Saleh and J. M. Simmons, “Technology and architecture to enable the explosive growth of the internet,” *IEEE Communications Magazine ,* vol. 49, no. 1, pp. 126 - 132, 2011.

[36] S. Zhang, F. Yaman, Y.-K. Huang, J. D. Downie, D. Zou, W. A. Wood, A. Zakharian, R. Khrapko, S. Mishra, V. Nazarov, J. Hurley, I. B. Djordjevic, E. Mateo and Y. Inada, “Capacity-approaching transmission over 6375 km at spectral efficiency of 8.3 bit/s/Hz,” in *Optical Fiber Communications Conference and Exhibition (OFC)*, Anaheim, CA, USA, 2016.

[37] A. Chraplyvy, A. Gnauck, R. Tkach, R. Derosier, E. Giles, B. Nyman, G. Ferguson, J. Sulhoff and J. Zyskind, “One-third terabit/s transmission through 150 km of dispersion-managed fiber,” *IEEE Photonics Technology Letters,* vol. 7, no. 1, pp. 98 - 100, 1995.

[38] M. Birk, D. Fishman and P. Magill, “Field trial of end-to-end OC-768 transmission using 9 WDM channels over 1000 km of installed fiber,” in *Optical Fiber Communications Conference (OFC)*, Atlanta, GA, USA, 2003.

[39] R. Agalliu and M. Lucki, “Benefits and Limits of Modulation Formats for Optical Communications,” *Advances in electrical and electronic engineering,* vol. 12, no. 2, pp. 160-167, 2012.

[40] P. J. Winzer and R.-J. Essiambre, “Advanced Modulation Formats for High-Capacity Optical Transport Networks,” *Journal of Lightwave Technology ,* vol. 24, no. 12, pp. 4711 - 4728, 2006.

[41] K. Kikuchi, “Fundamentals of Coherent Optical Fiber Communications,” *Journal of Lightwave Technology,* vol. 34, no. 1, pp. 157-179, 2016.

[42] R. Griffin and A. Carter, “Optical differential quadrature phase-shift key (oDQPSK) for high capacity optical transmission,” in *Optical Fiber Communication Conference and Exhibit (OFC)*, Anaheim, CA, USA, 2002.

[43] P. J. Winzer, G. Raybon, H. Song, A. Adamiecki, S. Corteselli, A. H. Gnauck, D. A. Fishman, C. R. Doerr, S. Chandrasekhar, L. L. Buhl, T. J. Xia, G. Wellbrock, W. Lee, B. Basch, T. Kawanishi, K. Higuma and Y. Painchaud, “100-Gb/s DQPSK Transmission: From Laboratory Experiments to Field Trials,” *Journal of Lightwave Technology,* vol. 26, no. 20, pp. 3388 - 3402, 2008.

[44] J. Yu and X. Zhou, “Ultra-High-Capacity DWDM transmission system for 100G and beyond,” *IEEE Communications Magazine,* vol. 48, no. 3, pp. S56-S64, 2010.

[45] M. N. Islam, “Raman amplifiers for telecommunications,” *IEEE Journal of Selected Topics in Quantum Electronics,* vol. 8, no. 3, pp. 548-559, 2002.

[46] Z. Zalevsky and I. Abdulhalim, Integrated Nanophotonic Devices: 2nd edition, William Andrew, 2014.

[47] M. Yamada, A. Mori, K. Kobayashi, H. Ono, T. Kanamori, K. Oikawa, Y. Nishida and Y. Ohishi, “Gain-flattened tellurite-based EDFA with a flat amplification bandwidth of 76 nm,” *IEEE Photonics Technology Letters,* vol. 10, no. 9, pp. 1244-1246, 1998.

[48] J. Putrina, S. Olonkins and V. Bobrovs, “Investigation of EDFA positioning impact on the quality of the amplified signal in DWDM transmission systems,” in *Electronics*, Palanga, Lithuania, 2017.

[49] R. M. Schmogrow, Real-time Digital Signal Processing for Software-defined Optical Transmitters and Receivers, Karlsruhe Scientific Publishing, 2014.

[50] L. Lundberg, P. A. Andrekson and M. Karlsson, “Power Consumption Analysis of Hybrid EDFA/Raman Amplifiers in Long-Haul Transmission Systems,” *Journal of Lightwave Technology ,* vol. 35, no. 11, pp. 2132-2142, 2017.

[51] M. J. Connelly, Semiconductor Optical Amplifiers, Springer US, 2002.

[52] B. J. C. Schmidt, A. J. Lowery and J. Armstrong, “Experimental Demonstrations of Electronic Dispersion Compensation for Long-Haul Transmission Using Direct-Detection Optical OFDM,” *Journal of Lightwave Technology,* vol. 26, no. 1, pp. 196-203, 2008.

[53] Y. Yamamoto and T. Kimura, “Coherent optical fiber transmission systems,” *IEEE Journal of Quantum Electronics ,* vol. 17, no. 6, pp. 919-935, 1981.

[54] E. El-Fiky, M. Chagnon, M. Sowailem, A. Samani, M. Morsy-Osman and D. V. Plant, “168-Gb/s Single Carrier PAM4 Transmission for Intra-Data Center Optical Interconnects,” *IEEE Photonics Technology Letters,* vol. 29, no. 3, pp. 314-317, 2017.

[55] G. Kaiser, Optical Fiber Communications, McGraw-Hill Education, 2008.

[56] P. J. Winzer, A. H. Gnauck, C. R. Doerr, M. Magarini and L. L. Buhl, “Spectrally Efficient Long-Haul Optical Networking Using 112-Gb/s Polarization-Multiplexed 16-QAM,” *Journal of Lightwave Technology,* vol. 28, no. 4, pp. 547 - 556, 2010.

[57] P. J. Winzer, A. H. Gnauck, S. Chandrasekhar, S. Draving, J. Evangelista and B. Zhu, “Generation and 1,200-km transmission of 448-Gb/s ETDM 56-Gbaud PDM 16-QAM using a single I/Q modulator,” in *36th European Conference and Exhibition on Optical Communication*, Turin, Italy, 2010.

[58] F. Buchali, F. Steiner, G. Böcherer, L. Schmalen, P. Schulte and W. Idler, “Rate Adaptation and Reach Increase by Probabilistically Shaped 64-QAM: An Experimental Demonstration,” *Journal of Lightwave Technology ,* vol. 34, no. 7, pp. 1599 - 1609, 2016.

[59] P. J. Winzer, “High-Spectral-Efficiency Optical Modulation Formats,” *Journal of Lightwave Technology,* vol. 30, no. 24, pp. 3824 - 3835, 2012.

[60] R.-J. Essiambre, G. Kramer, P. J. Winzer, G. J. Foschini and B. Goebel, “Capacity Limits of Optical Fiber Networks,” *Journal of Lightwave Technology,* vol. 28, no. 4, pp. 662-701, 2010.

[61] S. Singh and N. Singh, “Nonlinear Effects in Optical Fibers: Origin, Management and Applications,” *Progress in Electromagnetic research,* vol. 73, pp. 249-275, 2007.

[62] K. Kikuchi, “Fundamentals of Coherent Optical Fiber Communications,” *Journal of Lightwave Technology ,* vol. 34, no. 1, pp. 157-179, 2016.

[63] T. Ohara, H. Takara, T. Yamamoto, H. Masuda, T. Morioka, M. Abe and H. Takahashi, “Over-1000-channel ultradense WDM transmission with supercontinuum multicarrier source,” *Journal of Lightwave Technology,* vol. 24, no. 6, pp. 2311-2317, 2006.

[64] Infinera, “Super-channels and the Future of Optical Networks,” 2015. [Online]. Available: https://www.yumpu.com/en/document/read/31845460/super-channels-and-the-future-of-optical-networks-infinera. [Accessed 21 8 2021].

[65] N. Amaya, I. Muhammad, G. S. Zervas, R. Nejabati, D. Simeodinou, Y. R. Zhou and A. Lord, “Experimental demonstration of a gridless multi-granular optical network supporting flexible spectrum switching,” in *Optical Fiber Communication Conference and Exposition and the National Fiber Optic Engineers Conference*, Los Angeles, CA, USA, 2011.

[66] O. Gerstel, M. Jinno, A. Lord and S. B. Yoo, “Elastic optical networking: a new dawn for the optical layer?,” *IEEE Communications Magazine,* vol. 50, no. 2, pp. S12-S20, 2012.

[67] M. Jinno, H. Takara, B. Kozicki, Y. Tsukishima, Y. Sone and S. Matsuoka, “Spectrum-efficient and scalable elastic optical path network: architecture, benefits, and enabling technologies,” *IEEE Communications Magazine,* vol. 47, no. 11, pp. 66-73, 2009.

[68] I. Tomkos, E. Palkopoulou and M. Angelou, “A survey of recent developments on flexible/elastic optical networking,” in *14th International Conference on Transparent Optical Networks (ICTON)*, Coventry, United Kingdom, 2012.

[69] T. Wong and T. Lok, “Chapter 4: Intersymbol Interference and Equalization,” in *Theory of Digital Communications*, 2000.

[70] J. Pan, C. Liu, T. Detwiler, A. J. Stark, Y.-T. Hsueh and S. E. Ralph, “Inter-Channel Crosstalk Cancellation for Nyquist-WDM Superchannel Applications,” *Journal of Lightwave Technology,* vol. 30, no. 24, pp. 3993-3999, 2012.

[71] G. Zhang, M. D. Leenheer, A. Morea and B. Mukherjee, “A Survey on OFDM-Based Elastic Core Optical Networking,” *IEEE Communications Surveys & Tutorials,* vol. 15, no. 1, pp. 65-87, 2013.

[72] K. Technologies, “Concepts of Orthogonal Frequency Division Multiplexing (OFDM) and 802.11 WLAN,” [Online]. Available: https://rfmw.em.keysight.com/wireless/helpfiles/89600B/WebHelp/Subsystems/wlan-ofdm/Content/ofdm_basicprinciplesoverview.htm. [Accessed 21 August 2021].

[73] D. Petrovic, W. Rave and G. Fettweis, “Effects of Phase Noise on OFDM Systems With and Without PLL: Characterization and Compensation,” *IEEE Transactions on Communications ,* vol. 55, no. 8, pp. 1607 - 1616, 2007.

[74] P. Robertson and S. Kaiser, “Analysis of the effects of phase-noise in orthogonal frequency division multiplex (OFDM) systems,” in *Proceedings IEEE International Conference on Communications ICC*, Seattle, WA, USA, 1995.

[75] G. Bosco, A. Carena, V. Curri, P. Poggiolini and F. Forghieri, “Performance Limits of Nyquist-WDM and CO-OFDM in High-Speed PM-QPSK Systems,” *IEEE Photonics Technology Letters ,* vol. 22, no. 15, pp. 1129-1131, 2010.

[76] G. Bosco, V. Curri, A. Carena, P. Poggiolini and F. Forghieri, “On the Performance of Nyquist-WDM Terabit Superchannels Based on PM-BPSK, PM-QPSK, PM-8QAM or PM-16QAM Subcarriers,” *Journal of Lightwave Technology ,* vol. 29, no. 1, pp. 53-61, 2011.

[77] H. Oohashi, T. Kurosaki, M. Okayasu, Y. Kawaguchi, Y. Kondo and Y. Tohmori, “1550-nm spot-size converter integrated DFB lasers for low-cost single-mode optical sources,” in *IEEE Lasers and Electro-Optics Society Annual Meeting (LEOS)*, Rio Grande, PR, USA, 2000.

[78] K. Igarashi, T. Tsuritani, I. Morita, K. Katoh and K. Kikuchi, “Frequency stabilization of multiple semiconductor lasers for Nyquist-WDM transmission systems,” in *Optical Fiber Communication Conference and Exposition and the National Fiber Optic Engineers Conference (OFC/NFOEC)*, Anaheim, CA, USA, 2013.

[79] P. K.J.Park, S.K.Shinl, H.C.Ji and Y.C.Chung, “Frequency stabilization of multiple semiconductor lasers using digital feedback loop,” *Optics Communications,* vol. 272, no. 1, pp. 217-220, 2007.

[80] J. Zhao, Y. Liu and T. Xu, “Advanced DSP for Coherent Optical Fiber Communication,” *Applied Sciences,* vol. 9, no. 19, p. 4192, 2019.

[81] P. Delfyett, S. Gee, M.-T. Choi, H. Izadpanah, W. Lee, S. Ozharar, F. Quinlan and T. Yilmaz, “Optical frequency combs from semiconductor lasers and applications in ultrawideband

signal processing and communications," *Journal of Lightwave Technology,* vol. 24, no. 7, pp. 2701-2719, 2006.

[82] C. Reimer, M. Kues, P. Roztocki, B. Wetzel and R.Morandotti, "Generation of multiphoton entangled quantum states by means of integrated frequency combs," *Science* , vol. 351, pp. 1176-1180, 2016.

[83] M. Kues, C. Reimer, J. M. Lukens, W. J. Munro, A. M. Weiner, D. J. Moss and R. Morandotti, "Quantum optical microcombs," *Nature Photonics ,* vol. 13, pp. 170-179, 2019.

[84] A. R. Criado, C. d. Dios, E. Prior, P. Acedo, M. Ortsiefer and P. Meissner, "Photonic generation of CW sub-THz and THz waves using an efficient Gain-Switching based VCSEL optical frequency comb," in *38th International Conference on Infrared, Millimeter, and Terahertz Waves (IRMMW-THz)*, Mainz, Germany, 2013.

[85] P. Martin-Mateos, M. Ruiz-Llata, J. Posada-Roman and P. Acedo, "Dual-Comb Architecture for Fast Spectroscopic Measurements and Spectral Characterization," *IEEE Photonics Technology Letters,* vol. 27, no. 12, pp. 1309-1312, 2015.

[86] P. M. Anandarajah, R. Maher, Y. Q. Xu, S. Latkowski, J. O'Carroll, S. G. Murdoch, R. Phelan, J. O'Gorman and L. P. Barry, "Generation of Coherent Multicarrier Signals by Gain Switching of Discrete Mode Lasers," *IEEE Photonics Journal ,* vol. 3, no. 1, pp. 112-122, 2011.

[87] S. Bennett, B. Cai, E. Burr, O. Gough and A. Seeds, "1.8-THz bandwidth, zero-frequency error, tunable optical comb generator for DWDM applications," *IEEE Photonics Technology Letters ,* vol. 11, no. 5, pp. 551-553, 1999.

[88] M. Wang and J. Yao, "Tunable Optical Frequency Comb Generation Based on an Optoelectronic Oscillator," *IEEE Photonics Technology Letters ,* vol. 25, no. 21, pp. 2035-2038, 2013.

[89] T. Itoi, K. Fukuchi and T. Kasamatsu, "Enabling technologies for 10 Tb/s transmission capacity and beyond," in *27th European Conference on Optical Communication (ECOC)*, Amsterdam, Netherlands, 2001.

[90] J. Prat, I. N. Cano, M. Presi, I. Tomkos, D. Klonidis, G. Vall-llosera, R. Brenot, R. Pous, G. Papastergiou, A. Rafel and E. Ciaramella, "Technologies for Cost-Effective udWDM-PONs," *Journal of Lightwave Technology,* vol. 34, no. 2, pp. 783 - 791, 2016.

[91] J. Rahn, S. Kumar, M. Mitchell, H. Sun, K.-T. Wu, G. Goldfarb, M. Kato, D. Krause, R. Nagarajan, F. Kish and D. Welch, "Super-channels: DWDM transmission beyond 100 Gb/s," in *IEEE Photonics Conference* , Burlingame, CA, USA, 2012.

[92] M. Mazur, M.-G. Suh, A. Fülöp, J. Schröder, V. Torres-Company, M. Karlsson, K. Vahala and P. Andrekson, "High Spectral Efficiency Coherent Superchannel Transmission With Soliton Microcombs," *Journal of Lightwave Technology,* vol. 39, no. 13, pp. 4367 - 4373, 2021.

[93] A. H. Gnauck, G. Charlet, P. Tran, P. J. Winzer, C. R. Doerr, J. C. Centanni, E. C. Burrows, T. Kawanishi, T. Sakamoto and K. Higuma, "25.6-Tb/s WDM Transmission of Polarization-

Multiplexed RZ-DQPSK Signals," *Journal of Lightwave Technology,* vol. 26, no. 1, pp. 79-84, 2008.

[94] M. Morsy-Osman, M. Chagnon, M. Poulin, S. Lessard and D. V. Plant, "224-Gb/s 10-km Transmission of PDM PAM-4 at 1.3 µm Using a Single Intensity-Modulated Laser and a Direct-Detection MIMO DSP-Based Receiver," *Journal of Lightwave Technology ,* vol. 33, no. 7, pp. 1417 - 1424, 2015.

[95] R. Soref, "The Past, Present, and Future of Silicon Photonics," *IEEE Journal of Selected Topics in Quantum Electronics,* vol. 12, no. 6, pp. 1678-1687, 2006.

[96] E. Temprana, E. Myslivets, B.-P. Kuo, L. Liu, V. Ataie, N. Alic and S. Radic, "Overcoming Kerr-induced capacity limit in optical fiber transmission," *Science ,* vol. 348, no. 6242, pp. 1445-1448, 2015.

[97] F. O. Components, "What is the Meaning of 100G Channels Networks to Service Providers," 2014. [Online]. Available: https://www.fiber-optic-components.com/what-is-the-meaning-of-100g-channels-networks-to-service-providers.html. [Accessed 8 2021].

Chapter 2

Generation of optical frequency combs

2.1 Introduction

An OFC source is considered to be a highly promising alternative to the bank of lasers that is currently employed in optical networks. As previously mentioned, such a source can generate multiple phase coherent optical tones/carriers with a highly stable frequency spacing. Hence, it can be considered as one of the key technologies to achieve spectrally efficient optical networks employing super-channels and multi-carrier modulation techniques. The precise and stable frequency spacing between the OFC-generated tones allows the reduction or even the elimination of guard bands between the communication channels. In addition, the OFC can offer the tunability of the FSR leading to simple adaptation of the individual OFC tones to different modulation formats and bit rates [1].

This chapter gives a general discussion about OFCs and the key parameters that define their quality and suitability for implementation in next generation optical networks. Following that, various OFC generation techniques are discussed, and their characteristics and advantages are discussed. In addition, a detailed comparison of the techniques is provided. The selected generation techniques for discussion in this work are as follow: MLL, opto-electric modulators, Kerr effects in MRR, parametric techniques and finally gain switching. The scope of this work is limited to semiconductor based OFCs, as they can be photonically integrated. Photonic integration (which will be discussed in detail in the next chapters) can provide major advantages for next-generation optical networks in terms of compactness, low power consumption and low footprint.

2.2 Optical frequency combs

2.2.1 OFC history and definition

While OFCs were first introduced in the 60s and 70s [2], it was not until 2005 and after John L. Hall and Theodor W. Hänsch were jointly awarded the Nobel Prize in physics for their pioneering work on OFCs for spectroscopy applications [3], that the research community realised the potential of the OFC. Currently, OFCs are used in a wide variety of applications such as millimetre wave and terahertz signal generation [4], spectroscopy [5], metrology [6] , Light detection and ranging (LIDAR) [7] and next next-generation spectrally efficient optical networks [8].

Several techniques have been proposed to generate OFCs. The choice of the suitable generation technique depends mainly on the desired application that the OFC will be used for. There is no single technique that can be labelled as the 'optimum' one. Depending on the required applications, the desired comb characteristics would be defined and then the most suitable generation technique would be chosen. Gain switched laser based OFCs portray attractive advantages compared to the other generation techniques. It is a simple and a cost-effective technique, that can be used with any traditional off-the shelf semiconductor laser. Moreover, it provides simple FSR tunability. Hence, this technique has been chosen to be the main cornerstone of my study and is the generation technique that is used in the different results presented later in this work.

2.2.2 OFC characteristics

As previously described, an OFC consists of comb tones or lines with equal and precise frequency spacing. Since the comb lines are generated from the same laser source, they are phase correlated. To implement an OFC as a multicarrier transmitter within an optical network, it has to satisfy a series of requirements. Figure 2.1 shows an illustration of an OFC spectrum depicting some of its important characteristics. OFCs are characterised using various parameters such as the generated number of tones, FSR and its tunability, tunability of the central emission wavelength, optical linewidth, optical carrier to noise ratio (OCNR), and amplitude stability and flatness of the optical OFC lines. A detailed discussion of each of these parameters characterising an OFC is itemised below.

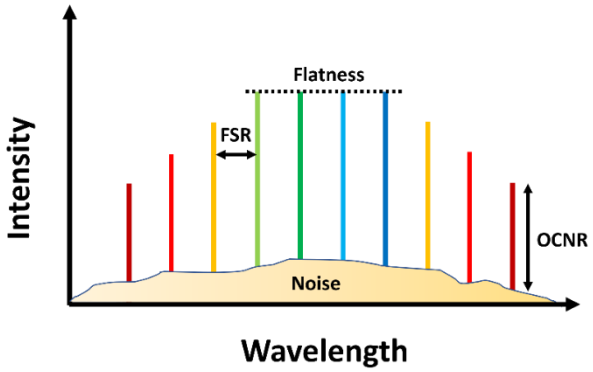

Figure 2.1: Schematic diagram of a typical OFC spectrum.

- **Spectral flatness:** The spectral flatness (amplitude ripple) describes the power variation between several contiguous comb tones around the tone with the highest power. A flat comb is expected to possess tones that have almost the same level of power. Typically, the power of the individual comb lines is not constant across the comb spectrum. A flat power distribution across the comb tones is important to ensure a similar level of performance between the various channels and avoids the need for utilization of equalisation techniques. When the comb tones are used as individual carriers, they should exhibit similar or the same levels of power. The biggest deviation acceptable is a power level that is no more than 3 dB lower than the power of the highest single peak.

- **Frequency spectral range**: It is the frequency difference/spacing between two adjacent OFC tones. OFC tones are usually equidistant i.e., have a constant frequency spacing between them. Some OFCs (based on the generation technique) also provide the advantage of tunability of the FSR, which is considered as a crucial parameter for next generation flexible optical networks. The tunability allows one to dynamically adapt the frequency spacing to different bit/baud rates and modulation formats according to the need of the network.

- **Occupied optical bandwidth:** It can be defined as the total optical spectral width that the OFC occupies. It is usually defined in terms of the number of comb tones with power within a certain threshold power level relative (in dB, i.e., 3 dB or 20 dB) to the peak power of the comb. The OFC bandwidth is an important parameter for optical communications as it determines the number of comb tones that can be utilised as optical carriers to carry information through the network.

- **RIN:** It is defined as the laser intensity noise normalised to the average power level. The RIN refers to the fluctuations in the optical power of a laser. This is mainly caused by the spontaneous emission which produces fluctuations of amplitude, frequency, and phase in the laser output. Each photon emitted due to the spontaneous emission process adds a small component with random phase that can causes perturbation in the amplitude of the laser, leading to intensity noise in the output spectrum of the laser. The RIN is usually described using a power spectral density function which depends on the noise amplitude. It is usually represented in a logarithmic scale and its unit is dB/Hz. It is also important to note that extra care should be taken while measuring RIN as the measured RIN value depends strongly on the current noise and the quality of the measurement setup.

- **Optical linewidth:** As mentioned before, the spontaneous emission of the laser produces random phase fluctuations, which corresponds to frequency variations. These frequency fluctuations prevent the comb tones to be strictly monochromatic, thus resulting in spectral width broadening. This spectral width is usually called the optical linewidth. Thus, the linewidth of a comb tone is directly related to the phase noise. It is considered as a vital parameter for advanced modulation formats that modulate the carrier phase.

- **Phase correlation:** It is an indication of the quality of phase relationship between the different tones of an OFC. It can be measured through the observation of the linewidth of the radio frequency (RF) beat tone produced from the detection of an OFC using a high-speed photodiode. This RF tone is generated at the frequency that corresponds to the frequency spacing between the adjacent OFC tones. It consists of the combination of the phase noise of the detected comb tones. So, in the presence of a strong phase correlation, the optical phase noise should be cancelled out [9]. In other words, the linewidth of the RF-tone generated is low when the phase correlation between the measured comb tones is high.

- **Optical carrier to noise ratio:** This parameter can be defined as the ratio between the power of a given comb tone and the noise level surrounding that comb tone, measured at a given spectral resolution. The OCNR is crucial for next generation optical networks, as a high OCNR would mean increase in the information rate that can be transmitted in an optical network, which allows the use of higher order advanced modulation formats [10].

- **Optical power:** The optical power of an OFC is usually represented by the optical power per comb line. It is important to note that a higher optical power will alleviate the need for amplification. In general, the power from an OFC source is low. This is due to the fact that all the OFC tones are generated from a single laser source, and the total optical power is

distributed over several tones. The relatively low power of the individual OFC tones is a major challenge that needs to be overcome before OFCs are adopted as transmitters to be used in next generation optical networks. A high optical power at the transmitter would enable longer reach transmission whilst achieving a relatively lower cost and power consumption in comparison to an amplified system. As it is well known that the commonly used optical amplifiers (EDFAs) are usually bulky and costly and contribute to the degradation of the OSNR or the OCNR (in the case of an OFC). As previously mentioned, SOAs can be integrated with other optical components in a single chip which can assist with a reduced footprint and power consumption. However, the challenge of reducing the NF of such amplifiers needs to be tackled (usually SOAs portray a higher NF than EDFAs). In chapter 6 of this thesis, an integrated multi-section SOA, which reduces the NF) is introduced and characterised in the context of short reach optical networks.

To conclude, an ideal OFC would need to portray good spectral flatness (low spectral ripple), a high number of usable OFC tones that can be employed as carriers, FSR and wavelength tunability, a wide bandwidth, a high OCNR (>40 dB), a low RIN (<-120 dB/Hz) and a narrow linewidth (~ 100's of kHz), and a strong phase correlation. Moreover, it should be stable in terms of wavelength, amplitude, frequency spacing and optical power. An OFC which presents such optimum spectral characteristics can be a strong potential candidate, to replace an array of lasers.

2.3 Semiconductor based OFC generation techniques

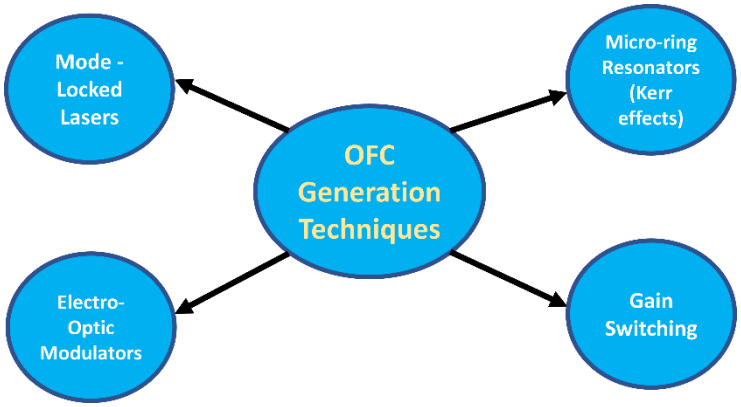

Figure 2.2: Different OFC generation techniques.

There exists a wide range of semiconductor device-based OFC generation techniques. In order to choose the most suitable one, the strengths and weaknesses of each technique, and its suitability for employment in different applications is studied. Although an extensive variety of generation techniques exists, this section will focus on ones that have a high potential of being employed in

optical communications networks. Figure 2.2 highlights the selected OFC generation techniques to be discussed in the upcoming sections. A comparative study between these techniques will also be presented.

2.3.1 Mode locked lasers

Mode locking of semiconductor lasers is one of the well-known OFC generation techniques. Previous reports have shown that MLL based OFCs can be used in optical networks employing WDM technologies [8] [11].

Mode locking can be defined as the process of generation of pulsed radiation through the locking of multiple axial modes in a laser cavity, which enforces the coherence between the phases of the different modes of the laser cavity [12]. Typically, in a conventional semiconductor laser cavity, no fixed phase relationship exists between the various modes resulting in the different longitudinal modes oscillating independently. This causes a random variation of their phases. These modes interfere in the cavity and averages to a near-constant intensity power, similar to a combined set of independent lasers emitting at different frequencies. Inducing a fixed phase relationship between these various modes, results in a constructive and periodic interference inside the cavity which produces a train of pulses as the laser output. At this stage, the laser is considered to be mode locked. Using a relatively weak modulation synchronous with the roundtrip time of radiation circulating in the laser, the pulse can be made shorter on every pass through the resonator. The shortening process continues until the pulse becomes very short and its spectrum so wide that pulse lengthening mechanisms or spectrum narrowing processes spring into action, such as finite bandwidth of the gain [12]. The resultant train of pulses in the temporal domain is translated to the frequency domain as an OFC with equidistant tones, the spacing of which is determined by the spacing between the longitudinal modes of the laser cavity. The latter is determined originally by the length of the laser cavity.

Figure 2.3 shows the temporal and spectral output of a laser that is mode locked. Figure 2.3(a) shows the spectral output while Figure 2.3(b) shows the corresponding train of short pulses in the time domain. Typically, mode locking technique allows the generation of pulses with a duration between nano- and pico-seconds [13].

MLLs can be based on either semiconductor [15] or fibre laser sources [16]. Within the context of this thesis, the focus will be on the semiconductor lasers, due to their potential for use in next generation optical networks. The mode locking of semiconductor lasers can be classified into 3 major categories: passive mode locking [17], active mode-locking [18] and hybrid mode-locking [14].

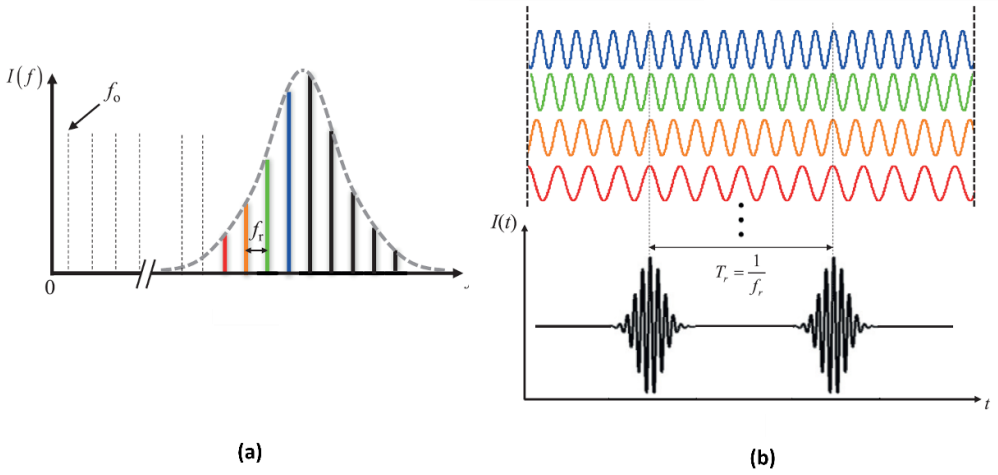

Figure 2.3: MLL based OFC output in: (a) Optical comb in the frequency domain, (b) Pulse train in the time domain. [14].

Active mode locking implies the utilisation of a modulator placed in the laser cavity that is driven by an external signal. This is used for the periodic modulation of the round-trip phase change [19]. The modulation can be realised with the use of a semiconductor electro-absorption modulator (EAM), an acousto-optic modulator or a Mach-Zehnder modulator (MZM) [20] or with the modulating signal applied directly to a custom designed semiconductor laser [18]. The modulating frequency has to be synchronised with the round-trip time of the resonator (the spacing between the longitudinal modes) in order to establish a fixed phase relationship among the modes of the laser [12]. The modulation signal would result in each longitudinal mode producing side bands that coincide with the adjacent modes. The side bands then act as phase locking signals for the adjacent modes of the cavity, thereby leading to mutual synchronisation and phase correlation [21]. The process then repeats itself in each round-trip, resulting in the emission of a train of short pulses in the time domain which corresponds to an OFC in the spectral domain.

The passive mode locking technique does not involve the use of a modulator inside the laser cavity. Instead, it employs nonlinear optical effects [17]. In this technique, the laser device is usually composed of two different sections, an SOA as the gain section, and the other laser section has to act as a saturable absorber (SA) [22]. In the SA section, the light is absorbed until a saturation point is reached, beyond which the SA allows the light to pass through and provides high transparency, resulting in the transmission of a high-intensity incident light. It is simple to understand the pulse-formation mechanism due to saturable absorption. The generated light (noise due to ASE) inside the cavity undergoes amplification over several roundtrips in the cavity until its power reaches the saturation point of the SA. The SA, having intensity-dependent transmission, offers a higher attenuation to the lower intensity regions of the noise waveform, and vice versa, thus acting as a gate for the peaks of noise waveforms and suppressing the low-intensity regions. The process repeats itself

over several roundtrips, eventually leading to a train of ultrashort pulses being produced, and in turn the laser getting mode locked. One of the main advantages of this method is that it does not require an external RF source which leads to a lower power consumption. Passive mode locking can be attributed to the nonlinearities in the semiconductor active region, mainly sustained by four wave mixing processes [23].

Hybrid mode locking techniques employs both the passive and active mode locking methods in the same system [24]. The pulses are generated the same way as the passive mode locking method, and they are synchronised using an external electrical signal, that is similar to the same technique implemented in the active mode locking.

MLL based OFC characteristics

One of the main strengths of mode locking technique is their capability to generate an OFC with a broad spectrum that spans over tens of nanometres with a reasonably good spectral flatness from a single laser source [25]. Furthermore, it can lend itself to monolithic integration which results in a lower power consumption and a smaller footprint [26]. On the other hand, a main drawback of the MLL-based OFCs is the lack of tunability of its FSR. This is due to the reason that the frequency spacing between the adjacent comb tones depends on the cavity length which cannot be tuned easily. This limits the application of MLL based OFCs in next generation networks, where the flexibility of the comb source is crucial as previously explained. Piezoelectric effects [27] can be employed as a potential solution for cavity length tuning. A certain value of voltage is imposed to cause a small alternation on the cavity length. However, this technique requires the application of a high voltage resulting in higher energy consumption. Moreover, the applied high voltage would result in a raise in the temperature of the device leading to instabilities. The piezoelectric effect may result in mechanical changes causing defects in the laser structure [28]. In addition to that, achieving an accurate very small variation in the laser cavity length is not an easy task. Another disadvantage of passively mode locked lasers is that the comb tones typically have a relatively large optical linewidth (in the range of several MHz) [29]. External optical injection can be used to improve the spectral characteristics of MLL based OFCs. A significant linewidth narrowing and a phase locking of the injected quantum dash-MLL slave laser to the master laser was shown in [30]. Another technique for achieving a narrow linewidth OFC tone with a wide frequency tuning within the locking range for a single and a two-section 21 GHz quantum dash MLLs was shown in [31] , where a dual-mode optical injection locking (OIL) of the device was employed. However, using OIL results in narrowing the advantageous emission span of the MLLs.

Another disadvantage with MLLs is mode partition noise (MPN), which is generated by the power

fluctuations among the different longitudinal modes forming the overall MLL spectrum while competing for a common injected-carrier population [32]. MPN can degrade the RIN of individual tones of the MLL.

2.3.2 Electro-optic modulators

The employment of EOMs that are driven by a large amplitude RF signal to generate multi-carrier laser sources was introduced in 1972 [33]. The developments achieved over time in improving the EOMs characteristics such as, reduction of the required driving voltage and improvement of bandwidth have enabled the generation of an OFC using a single or multiple modulators [34]. Moreover, the advancements in the performance of RF amplifiers have enabled the simple generation of a large amplitude RF signal that is used to drive the EOMs. One of the attractive selling points of this generation technique is that the phase noise properties of the generated OFC is determined by the laser feeding light and operating in continuous wave (CW). Hence, the use of a narrow linewidth input seed laser would result in the generation an OFC with narrow linewidth tones.

OFC generation using this method is driven mainly by the nonlinear properties of the EOMs, where the large signal modulation caused by the RF signal introduces higher order modulation harmonics of the driving RF signal which is centred around the emission optical wavelength of the input laser [35]. Hence, the various spectral properties of the tones of generated OFC such as the output power, OCNR, intensity and phase noise are governed by the characteristics of the several components used in the system such as the input laser, the modulators, the sinusoidal RF signal and the RF amplifier.

Various EOMs configurations utilising a single modulator [36] [37] or a series of cascaded modulators [38] [39] can be employed to generate an OFC. Figure 2.4 shows different configurations of employing MZMs for generation of an OFC. Figure 2.4(a) shows the use of a single MZM, which will introduce the advantage of simplicity and cost-effectiveness, but it does not produce a satisfactory level of spectral flatness across the generated comb. This happens because the generated higher order harmonics do not usually have a regular amplitude distribution among them, since the variation of the amplitude is governed by the Bessel functions [34]. Another downside to using a single modulator is that it does not result in the generation of a wide bandwidth OFC. According to S. Ozharar et al. [40], the flatness can be improved by using a single-phase modulator which is driven by combined RF signals with different amplitudes and frequencies.

Figure 2.4(b) shows a dual drive (DD) MZM configuration. By careful adjustment of amplitudes, frequencies, and phases of the modulating signal, it allows the optical non-flat spectra obtained from each phase modulator in the interferometric arms inside the MZM to combine together and form a combined flat optical comb spectrum as shown in [41].

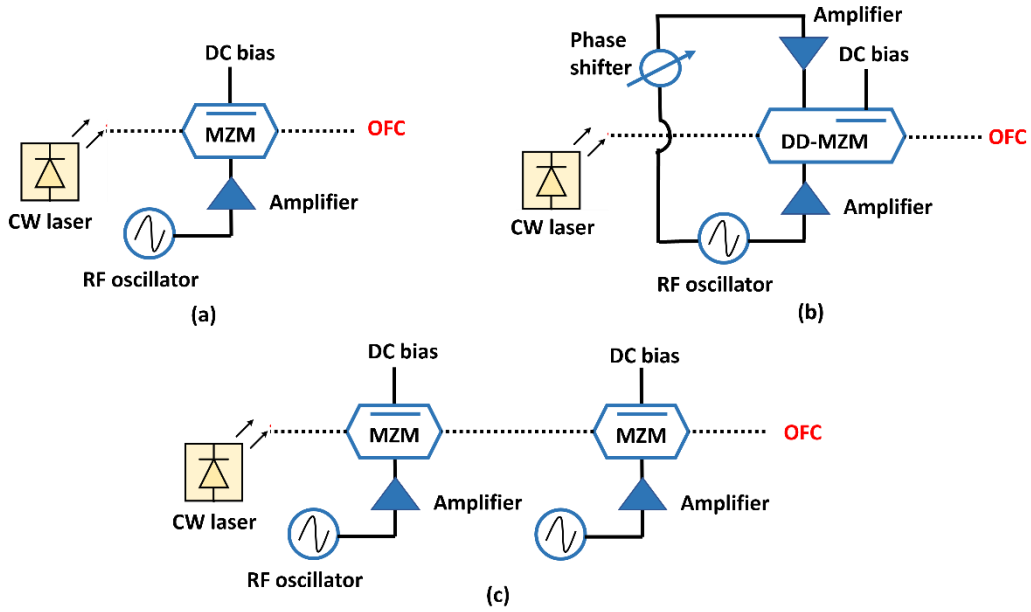

Figure 2.4: Different configurations for electro-optic modulators-based OFC generation: (a) Single MZM, (b) Dual drive MZM, and (c) Cascaded MZMs.

By cascading multiple MZMs as shown in Figure 2.4(c), an OFC with a better flatness and a higher number of comb tones can be generated [42]. Using a series of cascaded phase modulators would introduce more complexity to the system but will generate a larger number of OFC spectral tones with an improved flatness [38]. A hybrid combination of both intensity and phase modulators can be considered as the most balanced solution in terms of the output OFC flatness, complexity, and tuning flexibility [43] [44]. IQ modulators can also be employed to generate an EO-based OFC [45] [46].

EOM based OFC characteristics

The EOM based OFCs give a high degree of tunability and flexibility, as the central wavelength, the phase noise and the RIN of the generated OFC depend mainly on the properties of the input seed laser. Furthermore, the FSR can be easily tuned by changing the modulation frequency of the RF signal(s) applied to the modulator(s). The FSR is only limited by the maximum electrical bandwidth of the EOMs, and the RF amplifiers used for the generation process. Recent research efforts have shown the potential of integration of EOM based OFCs by using Indium Phosphide (InP) [47] [48] and silicon organic hybrid (SOH) based modulators [49] [50]. The limited bandwidth of the generated OFC is one of the downsides of this generation technique. To generate a wide bandwidth OFC with good spectral flatness, a series of cascaded modulators must be used. However, this results in a higher complexity and insertion loss (for example ≈21 dB for SOH based modulators in [51]). Several techniques have been proposed to improve the stability of the EO based OFCs such as feedback control loops [52]. However, this again results in an additional complexity.

2.3.3 Micro-ring resonators

OFC generation using an MRR has attracted a lot of attention recently since it can generate ultra-broadband coherent OFCs with comb tones of low linewidth [53]. OFC generation in the MRR relies on the optical Kerr non-linear effect when a high-power optical signal is launched into it [54]. When this optical signal is confined inside the MRR, it leads to the generation of a multi-carrier optical signal. This takes place because the optical signal is trapped in a tiny volume, which in turn leads to an enhancement in the intensity of light and consequently non-linear interactions. The optical Kerr effect consists of a variation in the refractive index of the resonator material proportional to the confined pump intensity [55].

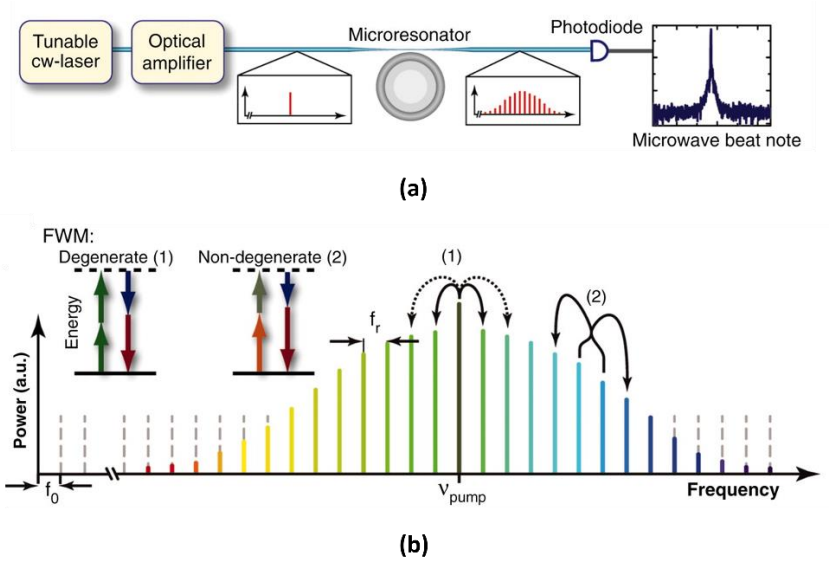

Figure 2.5: (a) Experimental setup diagram for generation of micro resonator-based Kerr OFC, (b) Demonstration of cascaded FWM phenomenon in the micro resonator [53].

This allows the optical signal to generate side modes through the four-wave mixing (FWM) phenomena [56] [57] where a pump photon at the original frequency is scattered elastically into a pair of photons that are up and downshifted in frequency [58]. This results in what can be called cascaded FWM, where the generated side modes interact with the original MRR cavity modes and among themselves to produce new optical tones, enhancing the nonlinear process, which eventually leads to the generation of an ultra-wide OFC. Figure 2.5(a) shows a schematic that could be used to generate an OFC using the MRR Kerr effect-based technique. Figure 2.5(b) illustrates the non-linear process that takes place inside the MRR to produce a series of side bands that interact with the cavity modes to generate an OFC.

MRR based OFC characteristics

The MRR based OFC generates a large number of tones that can cover multiple telecommunication bands [C and L bands], which is considered to be one of major attributes. In [56], the authors demonstrate the data transmission of 50 Tb/s over 75 km enabled by the utilisation of a single MRR based OFC. The MRR based OFCs possess good OCNR, phase correlation [59] and offers low phase noise inherited from the input laser used [57].

One of the main challenges facing this technique is the generated OFC characteristics and phase noise depend mainly on the pump conditions, i.e., on polarisation and power of the pump laser, and on its wavelength detuning with respect to the pumped resonance, which have to be carefully adjusted to obtain maximum frequency conversion efficiency and optimum phase correlation [60]. The wavelength tuning has to be finely adjusted in order to obtain the maximum frequency conversion efficiency [60]. Therefore, sophisticated pumping schemes are required to obtain the optimum phase correlation and frequency conversion.

Another downside associated with this technique is that the generated OFC FSR is fixed (not tunable), as it is determined by the length of the resonator cavity. It is also quite challenging to integrate OFC sources based on MRR. Although the microresonators are compact tiny components, the strong optical input pump power required for generating the OFC (>30 dBm) presents a serious challenge for monolithic integration of the optical pump laser and the microresonator on the same single chip.

2.3.4 Gain switching

Gain switching is a simple and cost-effective technique that can be used for the generation of OFCs. It entails the generation of periodic optical pulses, by directly modulating a commercially available off-the-shelf standard semiconductor laser with a large amplitude RF signal at the desired frequency [61] [62]. The most attractive features of the gain switching technique is its outstanding simplicity, stability and cost-efficiency while providing FSR tunability. Hence, the work on the thesis will be focused on this technique. The next sections below will initially give a detailed explanation of the operating principle of the gain switching. After that, a simulation model will be presented providing a theoretical and simulation analysis of a semiconductor laser. This model can be used to have more understanding about the different laser parameters, which can be then later used to enhance the operating parameters of the laser during the gain switching process. Eventually, optical injection is presented and explained in detail as a complementary process to the gain switching, which improves different spectral properties of the generated OFC such as the RIN and the phase noise of the OFC tones.

2.3.4.1 Operating principle

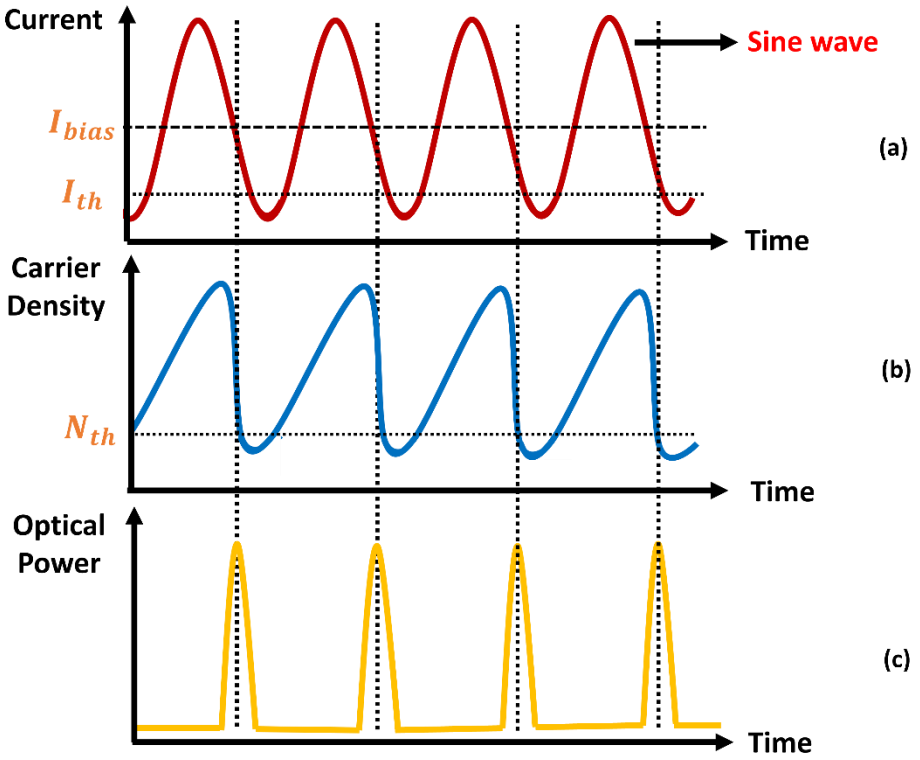

Figure 2.6: Illustration of time evolution of: (a) Applied bias, (b) Carrier density, and (c) Optical power of a gain switched semiconductor laser.

In this technique, the laser is forced to work in a non-linear regime continuously, where it is switched below and above threshold in a fast manner. In this case, the laser is usually driven around the relaxation oscillation frequency (ROF) [63] (frequency when the laser relaxes to its stable state), where the large modulating RF signal is cut before the second oscillation spike of the laser emission appears, enabling only the first spike of the relaxation oscillation to be excited [64]. Repeating this process leads to the generation of a train of periodic optical pulses at the rate of the modulating RF signal frequency with a short pulse width.

Figure 2.6 illustrates in detail the operating principle of the gain switching technique. A large RF-signal is applied to a semiconductor laser which is biased above threshold (I_{th}) as shown in Figure 2.6(a). The increase in the sine wave amplitude (from the trough to the crest) applied to the laser leads to a sudden rise in the carrier density within the laser cavity above the carrier density threshold (N_{th}) where lasing occurs, as shown in Figure 2.6(b). When N_{th} is reached, the photon density starts to increase. The rapid increase in the photon density population through recombination, results in the depletion of the carrier density. This in turn causes a reduction of the photon density leading to the emission of a short optical pulse. The duration of the modulation applied to the laser, where it is

operated below threshold results in preventing the excitation of the second and the subsequent spikes of the ROF. The repetition of this process leads eventually to the generation of a train of periodic optical pulses at the laser output shown in Figure 2.6(c).

Gain switching was initially considered as a technique for optical pulse generation. However, the increasing demand for spectral efficiency enhancement due to the vast increase in the data traffic has fuelled the extensive need for low-cost multi-carrier transmitters. This has led to the proposal of gain switching as an OFC generation technique. The first report of a gain switched OFC was in 2009 [65], where it was successfully implemented in a return to zero differential phase shift keyed (RZ-DPSK) system through fine filtering of individual comb tones and encoding them with DPSK for transmission over standard SMF.

Figure 2.7(a) shows a typical experimental setup for gain switching a single-longitudinal mode laser to generate an OFC. The laser is driven by an amplified 6.25 GHz RF-signal in conjunction with a DC bias through a bias tee. This generates an OFC with a corresponding FSR of 6.25 GHz whose optical spectrum is shown in Figure 2.7(b). The generated OFC has 5 different comb tones within 3 dB from the spectral peak and a free spectral range (same as the repetition rate of the optical pulses) that depends on the frequency of the modulating amplified RF-signal.

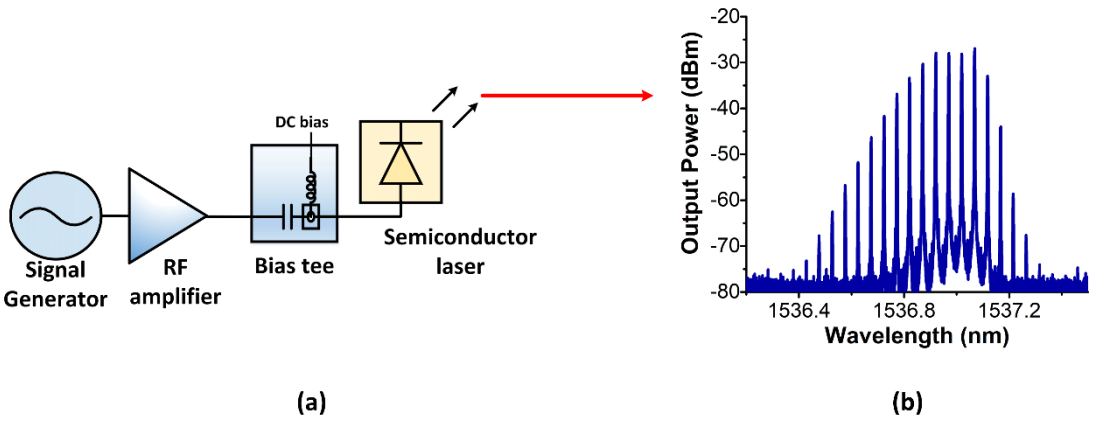

Figure 2.7: (a) Setup diagram for gain switching a semiconductor laser diode, (b) An example of an output OFC optical spectrum.

2.3.4.1.1 Theoretical and simulation analysis of a semiconductor laser

As the gain switching technique is the main focus of this thesis, a basic theoretical analysis of the transient response of semiconductor lasers is presented in the following section. This will give a deeper insight into the operational principle of the laser being gain switched.

This section will provide a semiconductor laser simulation model based on rate equations and will give an insight on the different physical parameters that affects the laser performance. Moreover, a study of the laser emission stability around the steady state is presented using Jacobian matrix. Eventually, the effect of different parameters on the power spectral density (PSD) of the frequency noise is shown and explained. These theoretical study serves as an important mean of understanding the semiconductor laser dynamics and their operation, which have a positive impact on having deeper understanding of the laser gain switching process. The latter, as aforementioned, is the focus of this thesis.

As is well known, the semiconductor laser dynamics can be described using a set of non-linear rate equations that describe the creation and the transformation (time evolution of the carrier and photon densities and the modal phase inside the laser cavity. The three basic rate equations can be defined as follows in the next page [66]:

$$\begin{cases} \dfrac{dN}{dt} = \dfrac{I}{eV} - \gamma_e(N) - G_N(N - N_O)P + F_N & (2.1) \\ \dfrac{dP}{dt} = (\Gamma_F G_N(N - N_O)P - \dfrac{P}{\tau_p} + \Gamma_F R_{sp} + F_P & (2.2) \\ \dfrac{d\phi}{dt} = \dfrac{\alpha}{2}\cdot\left(\Gamma_F G_N(N - N_O) - \dfrac{1}{\tau_p}\right) + F_\phi & (2.3) \end{cases}$$

$\gamma_e(N) = AN + BN^2 + CN^3$ where A is the non-linear recombination coefficient due to defects in the active material, B is the radiative recombination coefficient and C is the Auger recombination coefficient.

$R_{sp} = \beta BN^2$ where β is the fraction of spontaneous emission coupled to the mode.

F_N , F_P and F_ϕ are the noise sources added to the carrier density, photon density and modal phase respectively. They are represented by Langevin forces (defined as complementary forces pushing the Brownian particle around in the velocity space). Langevin equations are used as stochastic motion differential equations to describe the time evolution of a subset of degrees of freedom for slowly relaxing (macroscopic) variables and the rapidly relaxing (microscopic) variables. This results in an equation with a stochastic nature.

The different symbols are defined as follows:

Symbol	Definition
N	Carrier density
P	Photon density
ϕ	Phase of the lasing mode
V	Volume of the active layer
e	Elementary charge
γ_e	Carrier recombination rate (lifetime)
G_N	Differential gain
N_O	Carrier density at transparency
Γ_F	Confinement factor
τ_p	Photon lifetime
R_{sp}	Spontaneous emission rate
α	Linewidth enhancement factor

Table 2.1: Rate equations simulation parameter definitions.

Equations 2.1,2.2 and 2.3 represent the set of rate equation, and can be explained physically in the following way:

- Equation 2.1 determines the time evolution of the carrier density. The first term on the right-hand side (RHS) describes the injection of carriers by the current into the volume of interest. The second term shows the decay of carriers (carrier depletion rate) due to the different recombination process mechanisms as a result of the spontaneous emission. The third term (-ve sign) defines the losses of the carrier density as a result of the stimulated emission and absorption and the last term represents the added noise to the carrier density represented by the Langevin force F_N .

- Equation 2.2 defines the time evolution of the photon density. The first term on the RHS defines the photon density generated by the stimulated emission process while the second term shows the losses of the photon density due to the losses in the cavity (including the output coupling losses). The third term dictates the portion of the spontaneously emitted photons that are coupled to the laser output. The last term represents the added noise to the photon density represented by the Langevin force F_P and associated with spontaneous emission.

- Equation 2.3 defines the time evolution of the modal phase. The first term indicates the influence of the stimulated emission process on the time evolution of the laser phase while the second term indicates the influence of the spontaneous emission on the same. The last term again represents the Langevin force F_ϕ generated as a result of the spontaneous emission.

To study the stability around the steady state, the set of the rate equations can be analysed in the stationary case where the equations can be converted into the following Jacobian matrix with the Eigen value (λ). Please note that the Langevin forces are neglected at this time for simplicity.

$$\begin{pmatrix} -(\gamma_e' + \mathrm{G_N\,P} + \lambda) & -\mathrm{G} & 0 \\ \Gamma_\mathrm{F}\,\mathrm{G_N\,P} + 2\Gamma_\mathrm{F}\beta\,\mathrm{BN} & -\lambda & 0 \\ \frac{\alpha}{2}\Gamma_\mathrm{F}\mathrm{G_N} & 0 & -\lambda \end{pmatrix} \tag{2.4}$$

This matrix implies that there is no fluctuations and *N, P* and *Φ* have reached a steady state. The determinant is calculated to be $\lambda^2 + (P+P_s)\,G_N\,\lambda + G G_N\left(P + n_{sp}\right) = 0$

where $P_s = \frac{\gamma_e'}{G_N}$, $n_{sp} = \frac{2\beta BN}{G_N G}$.

If we consider that $2\,\Gamma_r = (P+P_s)G_N$ and $\Delta^2 = \Gamma_F G(G_N P + 2\,\beta BN^2)$, then the equation can be written as:

$$\lambda^2 + 2\,\Gamma_r\lambda + \Delta^2 = 0 \tag{2.5}$$

The solution for λ can be written as $\lambda = -\Gamma_r \pm \Omega_r$ where Γ_r is the damping factor and Ω_r is the term for the relaxation oscillation frequency.

Figure 2.8 shows the generated plot for the time evolution of λ where the envelope of the generated oscillation is $e^{-\Gamma_r t}$. It can be concluded that as we move on time, the oscillation is damped where in the end it reaches a steady-state, and the system is considered to be stable. This means that if the laser goes into instability state, it will eventually return to the stable steady state. The speed of this process depends on the damping factor value.

To confirm the stability of the system, small signal analysis around the steady state is carried out. The perturbations are limited to first order only which means that δN, $\delta P, \delta\Phi$ are added to *N, P,* ϕ respectively.

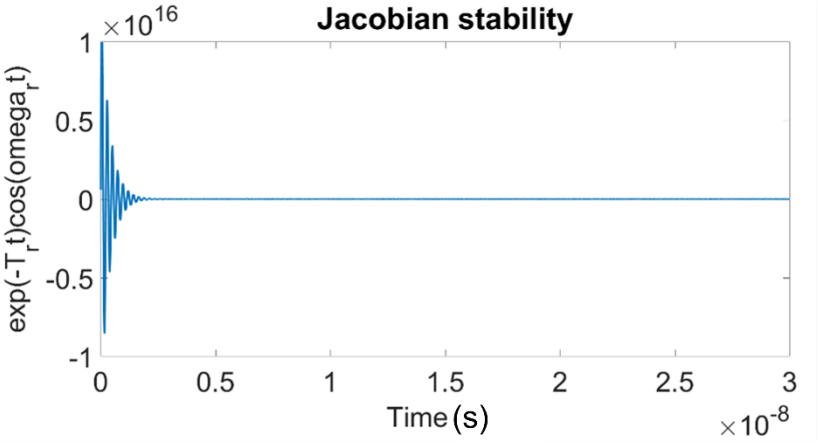

Figure 2.8: Jacobian stability of a single mode laser.

The temporal dependence of δN, δP and $\delta\phi$ can then be given by the following set of equations:

$$\begin{aligned}\frac{d\delta N}{dt} &= -(\gamma_e'(N) + G_N P)\delta N - G\delta P + F_N \\ \frac{d\delta P}{dt} &= \left(\Gamma_f G_N P + 2\beta BN\right)\delta N + \left(\Gamma_F \mathrm{G}(N - N_O) - \frac{1}{\tau_p}\right)\delta P + F_P \\ \frac{d\delta\phi}{dt} &= \frac{\alpha}{2}\Gamma_f G_N \delta N + F_\phi\end{aligned} \qquad (2.6)$$

With $\gamma_e'(N) = A + 2BN + 3CN^2$.

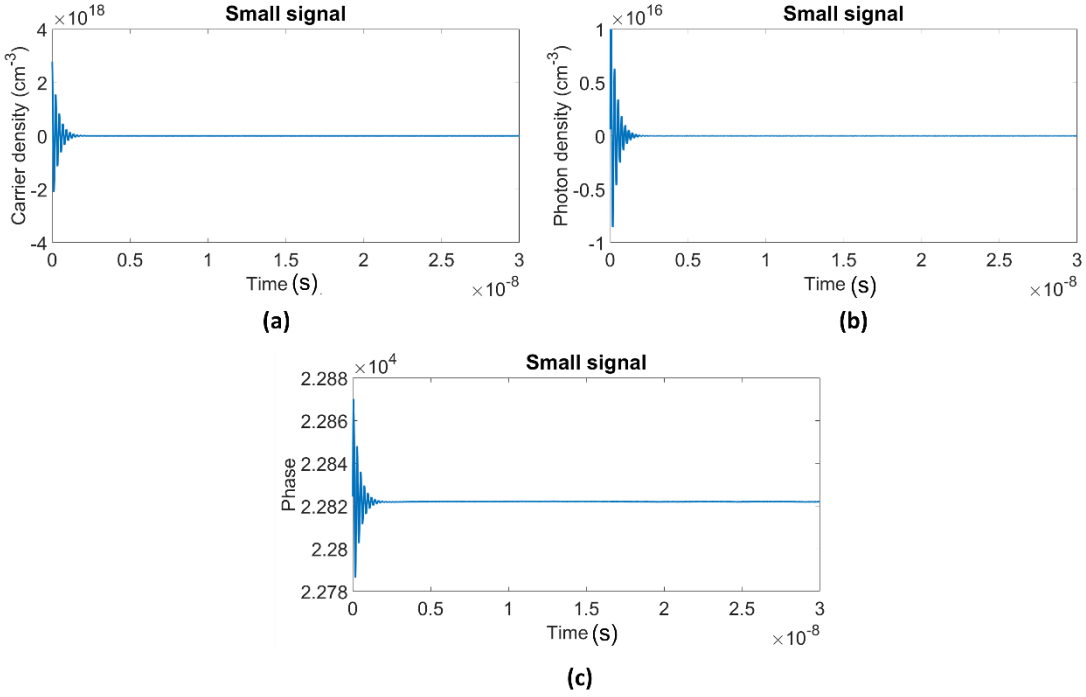

Figure 2.9: Time evolution of: (a) Carrier perturbation, (b) Photon perturbation, and (c) Phase perturbation around steady state.

These equations can be solved using the Runge-Kutta method in Matlab to give the time evolution of the different perturbations.

Figure 2.9(a, b & c) show the time evolution of the carrier density, photon density and modal phase respectively. The figures confirm that even with small-signal perturbation, the laser tends to return to the steady-state after a short time, which confirms the stability of the laser. As mentioned before this mainly depends on the value of the damping factor and ROF.

By performing a Fourier transform of the set of equations of the small-signal analysis, the following set of equations can be derived:

$$\begin{aligned} j\Omega\,\widetilde{\delta}\,N &= -(\grave{\gamma_e}(N)+G_N\,P)\widetilde{\delta}\,N - G\widetilde{\delta}\,P + \widetilde{F_N} \\ j\Omega\,\widetilde{\delta}\,P &= \left(\Gamma_f G_N\,P + 2\,\beta\,BN\right)\widetilde{\delta}\,N + \left(\Gamma_F\,G(N-N_O) - \frac{1}{\tau_p}\right)\widetilde{\delta}\,P + \widetilde{F_P} \\ j\Omega\,\widetilde{\delta}\,\phi &= \frac{\alpha}{2}\Gamma_f G_N\,\widetilde{\delta}\,N + \widetilde{F_\phi} \end{aligned} \tag{2.7}$$

Set of equations (2.7) can be expressed as a matrix equation considering that the gain will be equal to the losses as follows in the next page:

$$\begin{pmatrix} j\Omega + \gamma'_e(N) + G_N\,P & G & 0 \\ -\left(\Gamma_f G_N\,P + 2\,\beta\,BN\right) & \mathrm{j}\Omega & 0 \\ -\frac{\alpha}{2}\Gamma_f G_N & 0 & \mathrm{j}\Omega \end{pmatrix} X \begin{pmatrix} \widetilde{\delta}\,N \\ \widetilde{\delta}\,P \\ \widetilde{\delta}\,\phi \end{pmatrix} = \begin{pmatrix} \widetilde{F_N} \\ \widetilde{F_P} \\ \widetilde{F_\phi} \end{pmatrix} \tag{2.8}$$

F_N , F_p , F_ϕ are the Langevin forces of the carrier, photon number and phase respectively and can be calculated using the following set of equations:

$$\langle F_N(t)F_N(\grave{t})\rangle = 2(R_{sp}P+\gamma_e(N)/V)\,\delta(t-\grave{t}) \tag{2.9}$$

$$\langle F_p(t)\,F_p(\grave{t})\rangle = 2(R_{sp}P)\,\delta(t-\grave{t}) \tag{2.10}$$

$$\langle F_\phi(t)\,F_\phi(\grave{t})\rangle = 2\left(\frac{R_{sp}}{4p}\right)\delta(t-\grave{t}) \tag{2.11}$$

For easier representation, this set of equations can then be transformed into matrix form with the following labels:

$$\begin{pmatrix} a & b & 0 \\ d & e & 0 \\ g & 0 & i \end{pmatrix} X \begin{pmatrix} \widetilde{\delta}\,N \\ \widetilde{\delta}\,P \\ \widetilde{\delta}\,\phi \end{pmatrix} = \begin{pmatrix} \widetilde{F_N} \\ \widetilde{F_P} \\ \widetilde{F_\phi} \end{pmatrix} \tag{2.12}$$

$\tilde{\delta}\phi$ can then be expressed as a function of the Langevin forces by inverting the matrix where it will be equal to:

$$\widetilde{\delta}\,\phi = \frac{-eg}{det}\widetilde{F_N} + \frac{bg}{det}\widetilde{F_P} + \frac{ae-bd}{det}\widetilde{F_\phi} \tag{2.13}$$

With $det = a(ei) - b(di)$

By solving this while considering

$$det = j\Omega(j\Omega(j\Omega + \gamma_e'(N) + G_N P) + G(\Gamma_f G_N P + 2\beta BN)) \tag{2.14}$$

Then $\tilde{\delta}\phi$ can be expressed as:

$$\tilde{\delta}\phi = \frac{j\Omega\frac{\alpha}{2}\Gamma_F G_N \widetilde{F_N}}{det} - \frac{\frac{\alpha}{2}\Gamma_F G_N G\widetilde{F_P}}{det} + \frac{(j\Omega(j\Omega+\gamma_e'(N)+G_N P)+G(\Gamma_F G_N P+2\beta BN))\widetilde{F_\Phi}}{det} \tag{2.15}$$

In this case, this equation is a sum of $\widetilde{F_N}$, $\widetilde{F_P}$ and $\widetilde{F_\phi}$. Then S_ϕ which is the power spectral density of the phase noise can be considered as a contribution of three sources of noise expressed by $\widetilde{F_\phi}$. If we can consider the contribution of F_N , and F_P as negligible, then the PSD of the frequency modulation noise S_{fm} can be calculated according to the following equation and by using Fourier transform properties:

$$S_{fm} = \Omega^2 S_\phi \tag{2.16}$$

$$S_\phi = < \delta\phi, \delta\phi^* > \tag{2.17}$$

$$S_{fm} = \frac{R_{sp}}{2P} + \frac{\left(\frac{\alpha G_N}{2}\right)^2}{\left(\Omega^2 - {\Omega_r}^2\right)^2 + (2\Gamma\Omega)^2}\left(2\Omega^2\left(R_{sp}P + \gamma_e N\right) + 2R_{sp}PG\right) \tag{2.18}$$

where the first term is a result of the phase noise, second term is a result of the carrier noise, and the last term is a result of the photon noise.

Figure 2.10 shows the PSD of the small signal analysis of the frequency modulation noise. Using this plot, it is possible to extract the value of the linewidth of the laser using the flat part. Moreover, the small peak after the flat region is considered as the ROF of the laser.

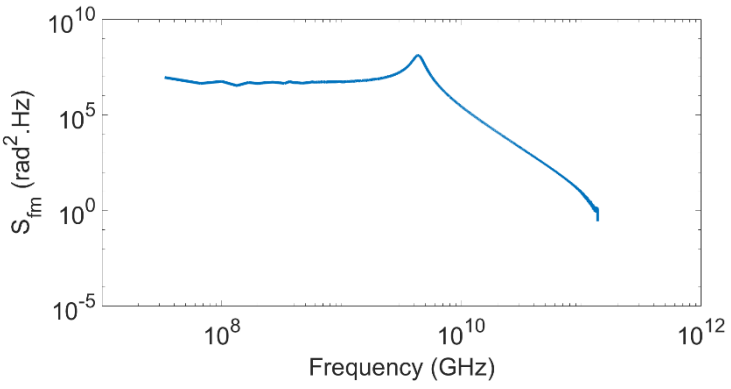

Figure 2.10: Power spectral density of frequency noise.

Similarly, to S_ϕ, the dominant contribution to S_{fm} is from the phase noise as depicted in Figure 2.11(a). The phase noise is independent of the observation frequency, while the photon noise and carrier noise peak at the ROF.

At Ω=0, S_{fm} can be approximated by $\frac{\Gamma_f R_{sp}}{4P}\ (1+\alpha^2)$ (2.19)

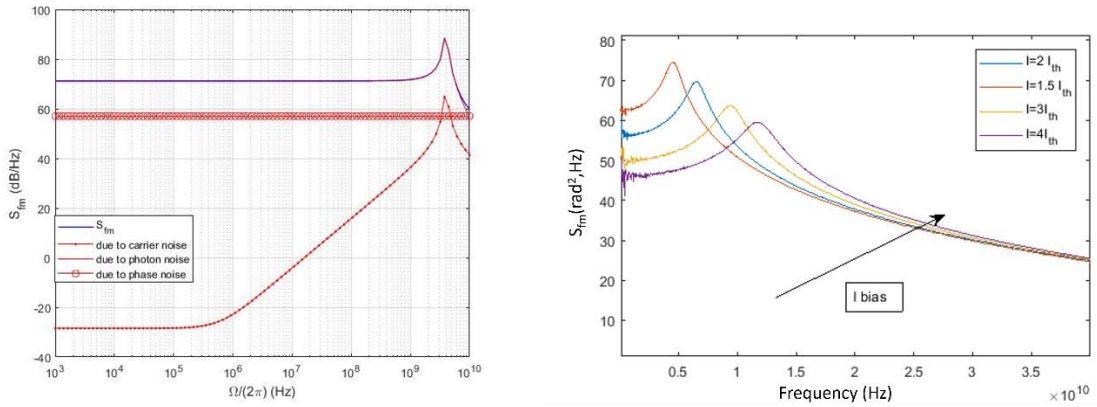

Figure 2.11: (a) Dependence of PSD of frequency noise on different parameters, (b) S_{fm} for different bias currents.

Figure 2.11(b) shows the dependence of S_{fm} on the bias current applied to the laser at a device length

of 450 µm. It can be observed that the ROF is directly proportional to the applied bias current. Moreover, the linewidth of the mode defined by $S_{fm}\ (0)$ decreases as the current increases due to the increase in the photon density.

It is worth noting that this model can be expanded to include the case of injection into one mode of the laser. This can be done by including injection terms in the rate equations and then solving these equations according to the previously explained methods in this section which will be discussed later in this chapter.

2.3.4.2 OFC characteristics

The most attractive characteristic of a gain-switched OFC is the ultimate simplicity, stability, and cost effectiveness it offers. Furthermore, it provides simple tuning of FSR.

Unlike the EOM technique, gain switching eliminates the need for bulky, lossy, and expensive optical components required for the generation of OFCs. At the same time, it generates a comparable number of comb tones with high power per comb tone (>0 dBm), as the gain-switched laser power gets distributed between the different comb tones without the need of use of any lossy components.

The central wavelength of the comb is determined by the central emission wavelength of the gain-switched laser source and a limited tunability of around 2 nm can be achieved through fine control of DC bias and temperature of the laser source. In addition to that, the gain switched OFCs provide inherent stability without the need for any complicated bias control or feedback loops [67].

On the other hand, there are some major shortcomings with the gain switching technique. As it is a technique based on the direct modulation of laser, the gain-switched pulses suffer from frequency chirp caused by the time-varying carrier density (hence refractive index) in the laser active region [68]. Furthermore, the generated pulses are also penalised with a large timing jitter caused by the random spontaneous emission contribution as a result of the laser turn-on (switching of the gain) event [69]. Specifically, bringing the laser below threshold during each cycle of the gain switching process increases the phase noise and broadens the linewidth of the generated OFC tones to levels that are higher than the CW laser case [70]. Another limitation that the gain switched OFC sources possess, is its dependence on the intrinsic modulation bandwidth (MBW) of the laser. Most commercially available semiconductor lasers exhibit a MBW of 15 GHz and lower, which limits the maximum FSR of the gain switched comb to a maximum of such a frequency. Finally, if a single mode semiconductor laser is used tunability of the OFC's central wavelength is limited to about 1-2 nm (temperature tuning of the laser). However, all these shortcomings can be overcome by applying optical injection to the gain switched laser [71]. It offers many benefits to the generated OFC, which will be discussed in detail in the next section.

2.3.4.3 Optical injection

Optical injection [72] can be considered as a complementary yet essential part of the gain switching OFC generation technique. It can enhance the MBW of the gain switched laser leading to the generation of an OFC with a larger span or overall bandwidth [73], decrease the noise (amplitude and phase), reduce the frequency chirp [71] and offer centre wavelength tunability (when a Fabry Pérot (FP) laser is used) [74]. Optical injection can be achieved in two different ways, external optical injection, and self-optical injection. Both techniques are discussed in detail below.

2.3.4.3.1 External optical injection

External optical injection process entails coupling the light coming out of an external laser source (master laser) into the cavity of another laser (slave laser), which improves the performance of the slave laser. The injected light from the master laser oscillates inside the cavity of the slave laser leading to interaction between both laser's fields. These interactions vary based on the wavelength difference

between the master and the slave lasers, and the level of injected power. It starts with nonlinear processes such as FWM, and then leads to an OIL state, where the master laser field takes control and locks the slave laser mode to its central emission wavelength. At this state, the slave laser inherits the frequency and phase of the master laser. Moreover, the slave laser inherits the noise properties of the master laser when it is injection locked to it. This can help in improving the noise properties of the slave laser by using a master laser with high spectral (phase noise) and amplitude purity, which will be in turn transferred to the slave laser via OIL.

Figure 2.12 shows the setup diagram of a typical optical injection process into a gain switched semiconductor laser. A wavelength tunable (master) laser is used to inject light into the cavity of another laser diode (slave) through a passive optical circulator.

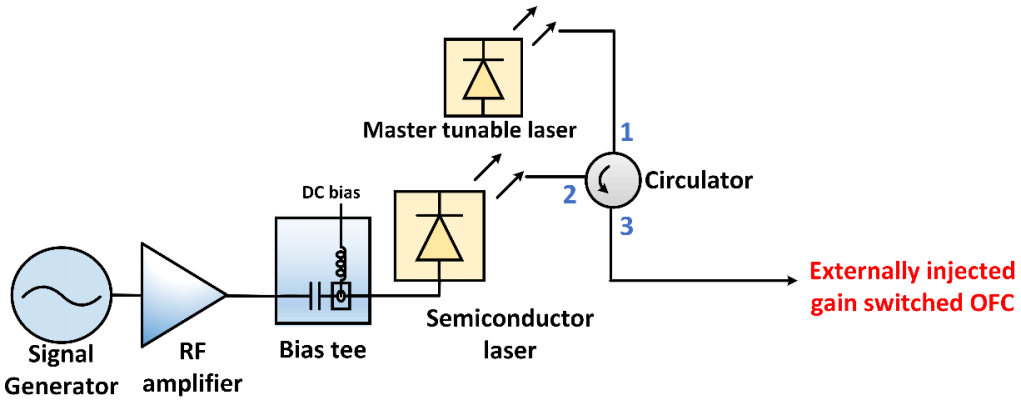

Figure 2.12: Setup diagram of gain switching an externally injected semiconductor laser diode.

The main parameters that control the different interactions between the master and slave laser fields inside the slave laser cavity are, the injection ratio (R) and the detuning range $(\Delta\omega)$. R can be defined as the power ratio between the injection master laser and the injected slave laser, while $\Delta\omega$ is the difference between the emission frequencies of the master and slave lasers. An OIL range can be defined as the zone where both the injection ratio and the detuning range satisfy a stable injection locking state condition, at which the slave laser frequency tracks that of the master laser and locks to it [75] [76]. In the injection locking range, the slave laser inherits the master noise properties, and its emission frequency shifts to the master laser emission frequency. Injection power and detuning frequency are interlinked, as the injection power determines the detuning frequency and vice versa. Decreasing the injection power or increasing the detuning range would mean going out of the injection locking range to the region where several non-linear processes such as FWM take place as a result of the interaction between the two lasers [77].

The traditional method of achieving OIL via external injection, entails using a setup that comprises various discrete passive and active optical components, such as circulators, polarisation controllers,

isolators, master, and slave lasers. Such a setup suffers from instabilities due to polarisation dependence in case of employing SMF and temperature variation in the injection path. One method to overcome the polarisation dependence problem is to use polarisation-maintaining fibre (PMF) based components. Even though this solves the problem with polarisation, the external passive components introduce insertion losses and may still suffer from temperature variations. An on-chip (integrated) optical injection solution can provide the same advantages as the discrete setup, whilst offering a simpler, cheaper, smaller footprint, and polarisation independent operation which results in better overall efficiency of the system [78].

Different research reports have shown the possibility of achieving an on-chip optical injection locking resulting in improving the various spectral characteristics of the slave laser. In [78], the authors show that the on-chip internal injection (without the need of an external source), from the master laser to the slave laser, enhances the slave's side-mode suppression ratio (SMSR) from 30 dB to over 50 dB and reduces its RIN from about -129.3 dB/Hz to -142.6 dB/Hz. Subsequent dynamic characterisation also shows that the MBW of the slave laser is improved via injection to about three times the inherent free-running bandwidth. Another report [79] demonstrates by showing the frequency response curve that on-chip optical injection can result in the expansion of the 3-dB MBW of a discrete mode (DM) laser. This improves the performance of the integrated device when employed in a direct modulation OFDM system due to the capability of handling higher bit rates. In [80], the authors demonstrate that optical injection locking of an integrated distributed feedback (DFB) laser results in the enhancement of the laser ROF to 23 GHz from an initial value of 11 GHz, and the suppression of nonlinear distortions by more than 15 dB.

A photonically integrated laser device employing optical injection will be characterised and presented in detail in chapter 4 of this thesis. This device makes use of the master-slave configuration to improve the different parameters of the slave laser such as the linewidth, RIN and MBW. The injection also results in a reduction of the chirp value when the device is employed as a directly modulated transmitter, leading to a better transmission performance in terms of bit error rate (BER) [81].

2.3.4.3.2 Self optical injection

Self-optical injection entails the use of a wavelength selective external cavity, to inject a selected fraction of the laser output light back into its own cavity. The optical self-feedback delay has to be adjusted so that the re-injected optical signal arrives at the same time of the build up of an optical pulse inside the laser cavity. This synchronisation would result in the generation of an optimum optical pulse with enhanced spectral characteristics. Large SMSR value can be also obtained if the reflected

pulse is fed back to the laser cavity during a narrow time window (between the time the electrical pulse is initiated but before the carrier density reaches threshold). A single mode output with a high SMSR value is obtained as a result of this optimised feedback causing the dominant mode to be initially well excited above the spontaneous emission noise level [82]. Typically, a small amount (0.2 – 6 %) of the optical output power of the laser is being fed back into the active layer of the laser diode to improve the spectral characteristics of the generated OFC.

Self-seeding can be considered as one of the simplest and most reliable techniques available to generate enhanced gain switched based OFCs. In a typical FP laser cavity, self-seeding can be used to obtain lasing on a single longitudinal cavity mode [83]. Moreover, self-seeding provides reduction in timing jitter for both DFB and FP gain-switched systems [84].

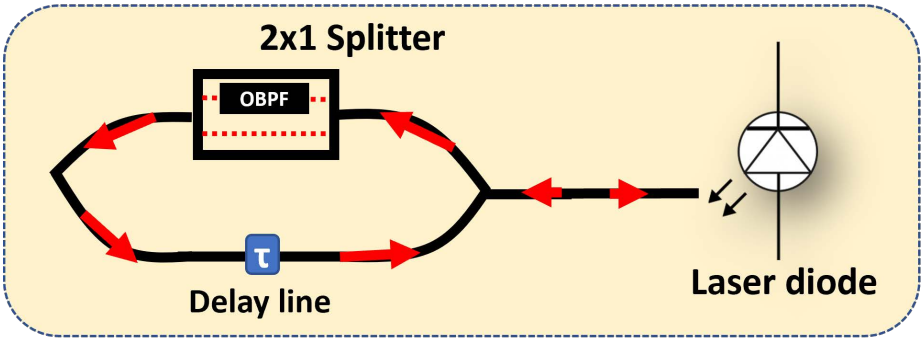

Figure 2.13: Schematic setup diagram of self-seeding of a semiconductor laser.

Figure 2.13 shows a setup diagram of a typical self-seeding of a semiconductor laser process. The laser output signal is injected into one arm on the RHS of a 2×1 splitter. On the left-hand side of the coupler, there exists two paths for the optical signal, either through an OBPF to filter a specific desired part of the signal or directly through a connector to allow the path of all the signal without any filtering. After that, the signal passes through a tunable optical delay line. The latter is used for accurate control and tuning of the delay that the optical signal experiences during its self-injection path to the laser. The delay is needed to synchronise the phase of the feedback signal with that of the main laser signal in order to have a constructive interference, which leads to improvement in the spectral characteristics of the laser. The other arm on the right-hand side (which serves as both input and output as shown in the figure) is connected to the laser to complete the self-injection path.

A photonically integrated laser device employing self-optical injection will be characterised and presented in detail in chapter 5 of this thesis. This device employs an on-chip self-feedback injection to improve the slave laser characteristics and to have an expansion in the bandwidth of the generated OFC when applying the gain switching technique.

2.3.4.3.3 Optical injection advantages

As mentioned before, optical injection can offer many advantages to the gain switched OFC by enhancing several parameters of the utilised laser such as the following:

- **MBW and resonance frequency enhancement:** The relaxation oscillation takes place during the turn-on action of a laser, where interactions between the carrier and photon densities take place. The resonance frequency and strength of oscillation are determined using various basic parameters of the laser device such as intracavity power, resonator losses and the round-trip time of the resonator [85]. Depending on these parameters, the peak of the ROF can be either suppressed or enhanced. Both cases can be useful for different applications. For example, the gain switching technique favours a high ROF peak [86], while for broadband digital modulation, the ROF peak can degrade the system performance and a flat frequency response (3-dB MBW) is more important [87]. Optical injection with high powers has been shown to be capable of pushing the ROF and the MBW to much higher values compared to the original values of the free-running laser. Resonance frequency enhancement in excess of 100 GHz in semiconductor lasers and intrinsic 3-dB MBW improvement up to 80 GHz as a result of optical injection has been shown in [86]. Research work in [87] has also shown MBW enhancement as high as 3.7 times the original value as a result of the strong optical injection.

- **Phase noise reduction:** The main source of noise in a semiconductor laser source is the random spontaneous emission process [88], which leads to intensity noise and phase noise. When a laser is gain switched, it is turned “ON” and “OFF” at each cycle. When the laser is turning ON from the OFF state, the optical pulses build up from the random spontaneous emission, which reduces the correlation between each pulse and thereby increases the phase noise. In external optical injection, a large number of photons are continuously injected from the master laser into the cavity of the slave laser which keeps the photon density within the cavity high. Hence, in an externally injected gain switched laser, the pulses are built up from the stimulated emission process. This ensures the coherence between the successive pulses, as they now are phase locked to the master laser and have a constant delay between them [89]. This leads eventually to a reduction in phase noise levels of the generated OFC. These results have been proven experimentally in some research work where the external optical injection has resulted in the reduction of phase noise and the emission linewidth [90] [91].

- **Intensity noise reduction:** One of the main parameters of the intensity noise of semiconductor lasers is the RIN. External OIL (from a low RIN master) can reduce the carrier

and photon densities fluctuations, hence reducing the level of RIN [92]. Another source of intensity noise in lasers is the MPN which is caused by the competition of the several modes inside the laser cavity for the gain [93]. The continuous competition for gain inside the laser cavity can cause fluctuations in the power level of each comb tone, which affects the stability of the OFC. OIL has been shown to reduce MPN level [94].

- **Wavelength tunability:** Optical injection can provide central wavelength tunability for gain switched OFCs (when an FP laser is used). This can be achieved when the wavelength of the light injected by the master laser coincides with one of the longitudinal modes of the slave laser. The injected mode dominates by taking all the gain and suppressing all the other longitudinal modes in the cavity [95]. This results in a single mode operation of the slave laser. By tuning the wavelength of the master laser to coincide with different longitudinal modes of the slave laser, discrete wavelength tunability of the slave can be achieved. It is worth noting that this tuning is only limited to the wavelengths of the slave laser longitudinal modes and the small locking range around it. However, by temperature tuning the slave laser, quasi-continuous wavelength tunability can be achieved.

In order to understand more about the optical injection process and its influence on the semiconductor laser parameters, the MATLAB simulation model will be enhanced to include injection into the slave laser and will be discussed in detail in the next section

2.3.4.3.4 Theoretical and simulation analysis of a semiconductor laser

Using the same simulation model presented previously in Section 2.3.4.1.1 and with adding some additional terms to the rate equations, the model can be upgraded to represent a semiconductor laser subjected to optical injection. The rate equations are updated to be as follow:

$$\frac{dN}{dt} = \frac{I}{eV} - \gamma_e(N) - G_N(N - N_O)P + F_N \quad (2.20)$$

$$\frac{dP}{dt} = (\Gamma_F G_N(N - N_O)P - \frac{P}{\tau_p} + \Gamma_F R_{sp} + \mathbf{2\kappa\sqrt{P_i P}\cos(\theta)} + F_P \quad (2.21)$$

$$\frac{d\phi}{dt} = \frac{\alpha}{2}.(\Gamma_F G_N(N - N_O) - \frac{1}{\tau_p}) - \boldsymbol{\kappa\sqrt{\frac{P_i}{P_o}}\sin(\theta)} - (\boldsymbol{d\omega - d\omega_c}) + F_\Phi \quad (2.22)$$

Where $d\omega_c = (\Omega_{FP} - \omega)$, $d\omega = (\omega_i - \omega)$ and $\theta = (\phi - \phi_{inj})$.

The additional terms of the injection are bolded in the rate equations definition above and are defined below:

Symbol	Definition
κ	Coupling coefficient
Ω_{FP}	Laser FP resonances
ω	Lasing angular frequency
$d\omega_c$	Detuning between the laser FP resonances and the lasing angular frequency
$d\omega$	Detuning between the angular frequency of the injected mode and the lasing angular frequency
P_i	Injected photon density
θ	Phase difference between ϕ and the phase of the injected mode

Table 2.2: Injected mode rate equations simulation parameters definitions.

The locking range can be obtained by assuming a first approximation that the laser reaches a steady state which means $\frac{d}{dt} = 0$. Moreover, the spontaneous emission terms can be neglected. The locking range can then be defined as the maximum value of the detuning range $(d\omega - d\omega_c)$ and will be called $\Delta\omega_l$ where

$$\Delta\omega_l = -\kappa\sqrt{\frac{P_i}{P_o}}\sqrt{1+\alpha}\,sin(\theta + arctan(\alpha)) \tag{2.23}$$

This shows that the injection locking range increases with the increase in the square root of the injected power. Moreover, it is also directly proportional to the linewidth enhancement factor.

To study the effect of applying injection on the slave laser phase noise, a comparison between the slave and master phase noises is shown in Figure 2.14. It shows the injection locking case where the injected slave laser phase is following the master laser phase. This means that the slave is injection locked to the master and inherits its noise properties.

As aforementioned, use of a pure master laser would mean an enhancement of the spectral properties of the slave laser. Furthermore, it shows that by the time when the detuning between both lasers exceeds the locking range, the slave starts to retain its own phase and get out of the injection locking regime to be a free running laser again. This proves that optical injection with a pure master laser can play an important role in enhancing the phase noise (linewidth) of the gain switched based OFC tones.

As aforementioned, OFC tones with narrower linewidth are a desired property that allows the OFC to be used as a multi-carrier source in coherent optical networks.

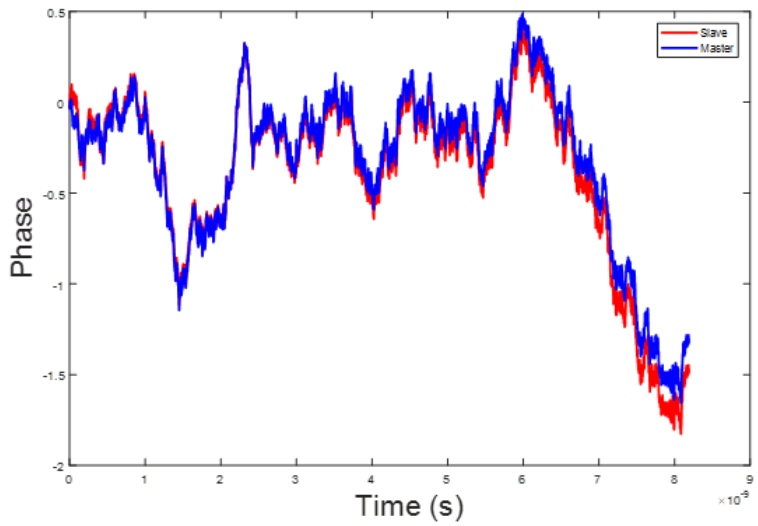

Figure 2.14: Evolution of slave and master lasers phase with time showing the injection locking regime.

Figure 2.15(a)&(b) show the output optical spectra of a simulated gain switched semiconductor laser generating an OFC for the cases without and with optical injection respectively. It is clear that the optical injection has improved different parameters of the generated OFC such as the OCNR and the number of lines within a given power bandwidth. Before injection, the gain switched OFC tones have an OCNR of ~35 dB, which improves to be ~65 dB after applying injection. Within 3-dB power bandwidth, the number of OFC tones increases to be 8 with applying injection, in place of only 3 lines when the laser is only gain switched without injection.

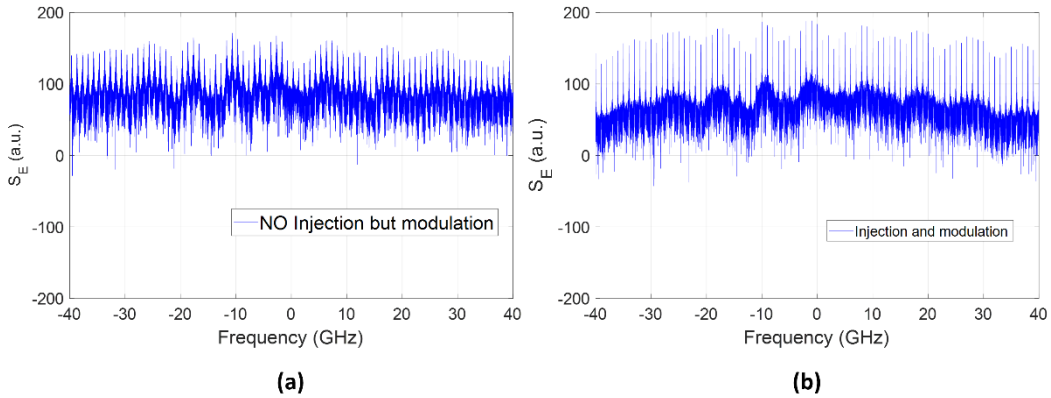

Figure 2.15: Simulated optical spectrum: (a) Non-injected gain switched OFC, (b) Injected gain switched OFC.

2.4 Conclusion

This chapter has introduced the OFC as an attractive transmitter solution for next generation optical networks. The various characteristics that are used to define and determine the quality of an OFC such

as the number of generated comb tones and the total OFC bandwidth have been introduced and explained in detail. These characteristics are important as an indicator parameter for the capability of implementation of OFC in different next generation optical networks.

Furthermore, a comparative review of various OFC generation techniques has been introduced, by highlighting the merits and drawbacks of each technique, and their different features that are crucial for their employment in spectrally efficient flexible optical networks. Depending on the network requirement, the most suited technique can be chosen according to its own characteristics and limitations.

MLLs and Kerr MRR based combs have the ability to generate an OFC with large number of tones that extends over a large wavelength span. On the other hand, MLLs and micro resonator based OFCs do not offer FSR tunability. Moreover, passively mode locked MLLs suffer from large levels of phase noise and RIN. EO modulators based OFCs present more flexibility, but still suffers from high cost and power consumption due to the use of cascaded modulators in order to achieve a wide bandwidth OFC. Gain switching, which is proven to be a simple and a cost-effective technique is the focus of this thesis. It provides FSR tunability, strong phase correlation among the different OFC tones and lends itself to photonic integration. Furthermore, optical injection can be used as a complementary technique to overcome the limitations of gain switching and generate a wider bandwidth OFC with better noise characteristics.

In the next chapter, gain switching of various laser structures such as FP, DFB and Vertical cavity surface emission laser (VCSEL) will be presented highlighting the positive influence of optical injection on the spectral characteristics of the generated OFC experimentally. The subsequent chapters will present two different photonically integrated devices that can also be gain switched to generate an OFC providing a lower cost, power consumption and footprint which are all desirable requirements for next generation optical networks. The focus of all the next chapters will be upon studying and identifying the optimum laser parameters and operating conditions for generation of an enhanced OFC using gain switching technique. This will be carried out for various types of laser structures using simulation models and mostly via experimental characterisation.

References

[1] P. Zhu, J. Li, L. Niu, Y. Xu, Y. Chen, X. Xie, X. Chen, B. Guo, Z. Chen and Y. He, "Optical comb-enabled cost-effective ROADM scheme for elastic optical networks," in *Optical Fiber Communications (OFC)*, San Francisco, CA, USA, 2014.

[2] J. Hall, "Optical frequency measurement: 40 years of technology revolutions," *IEEE Journal of Selected Topics in Quantum Electronics ,* vol. 6, no. 6, pp. 1136 - 1144, 2000.

[3] T. W. Hänsch, "A Passion for Precision," in *The European Conference on Lasers and Electro-Optics (ECOC)* , Munich, Germany, 2007.

[4] T. Shao, H. Shams, P. M. Anandarajah, M. J. Fice, C. C. Renaud, F. v. Dijk, A. J. Seeds and L. P. Barry, "Phase Noise Investigation of Multicarrier Sub-THz Wireless Transmission System Based on an Injection-Locked Gain-Switched Laser," *IEEE Transactions on Terahertz Science and Technology,* vol. 5, no. 4, pp. 590-597, 2015.

[5] B. Jerez, P. Martín-Mateos, E. Prior, C. d. Dios and P. Acedo, "Dual optical frequency comb architecture with capabilities from visible to mid-infrared," *Optics Express,* vol. 24, no. 13, pp. 14986-14994, 2016.

[6] J. Ye, H. Schnatz and L. Hollberg, "Optical frequency combs: from frequency metrology to optical phase control," *IEEE Journal of Selected Topics in Quantum Electronics,* vol. 9, no. 4, pp. 1041 - 1058, 2003.

[7] L.-Y. Chen, A. K. Vinod, J. F. McMillan, H. Liu, H. Yang, C.-K. K. Yang and C. W. Wong, "A Pulsed-Coherent Lidar System with a Chip Based Optical Frequency Comb," in *Conference on Lasers and Electro-Optics (CLEO)*, San Jose, CA, USA, 2021.

[8] Y. B. M'Sallem, Q. T. Le, L. Bramerie, Q.-T. Nguyen, E. Borgne, P. Besnard, A. Shen, F. Lelarge, S. LaRochelle, L. A. Rusch and J.-C. Simon, "Quantum-Dash Mode-Locked Laser as a Source for 56-Gb/s DQPSK Modulation in WDM Multicast Applications," *IEEE Photonics Technology Letters ,* vol. 23, no. 7, pp. 453 - 455, 2011.

[9] F. Kéfélian, R. Gabet and P. Gallion, "Characteristics of the phase noise correlation of injection locked lasers for RF signal generation and transmission," *Optical and Quantum Electronics,* vol. 38, pp. 467-468, 2006.

[10] R. Maher, A. Alvarado, D. Lavery and P. Bayvel, "Increasing the information rates of optical communications via coded modulation: a study of transceiver performance," *Scientific reports,* vol. 6, no. 21278, 2016.

[11] V. Vujicic, P. M. Anandarajah, C. Browning and L. P. Barry, "WDM-OFDM-PON Based on Compatible SSB Technique Using a Mode Locked Comb Source," *IEEE Photonics Technology Letters ,* vol. 25, no. 21, pp. 2058-2061, 2013.

[12] H. Haus, “Mode-locking of lasers,” *IEEE Journal of Selected Topics in Quantum Electronics,* vol. 6, no. 6, pp. 1173-1185, 2000.

[13] R. Maldonado-Basilio, S. Latkowski, S. Philippe and P. Landais, “Experimental investigation of harmonic and subharmonic synchronization of 40 GHz mode-locked quantum-dash laser diodes,” *Optics Letters,* vol. 36, no. 9, pp. 1569-1571, 2011.

[14] J. Jin, “Dimensional metrology using the optical comb of a mode-locked laser,” *Measurement Science and Technology,* vol. 27, 2016.

[15] J. Parra-Cetina, J. Luo, N. Calabretta, S. Latkowski, H. J. S. Dorren and P. Landais, “Subharmonic All-Optical Clock Recovery of up to 320 Gb/s Signal Using a Quantum Dash Fabry–Pérot Mode-Locked Laser,” *Journal of Lightwave Technology,* vol. 31, no. 19, pp. 3127-3134, 2013.

[16] W.-W. Hsiang, C.-H. Chang, C.-P. Cheng, H.-C. Su, S. Tsau, C. Hu and Y. Lai, “Passive synchronization between self-similar Yb-Fiber and stretched-pulse Er-fiber mode-locked lasers,” in *Conference on Lasers and Electro-Optics (CLEO)*, Baltimore, MD, USA, 2009.

[17] R. Koumans and R. V. Roijen, “Theory for passive mode-locking in semiconductor laser structures including the effects of self-phase modulation, dispersion, and pulse collisions,” *IEEE Journal of Quantum Electronics,* vol. 32, no. 3, pp. 478-492, 1996.

[18] K. Y. Lau, “Direct modulation and active mode-locking of ultrahigh-speed GaAIAs lasers at frequencies up to 18 GHz,” in *Optical Fiber Communication Conference (OFC)*, San Diego, California, United States, 1985.

[19] L. Kuznetsova, C. Y. Wang, V. M. Gkortsas, L. Diehl, F. Kartner, M. A. Belkin, A. Belyanin, X. Li, D. Ham, H. Schneider, H. C. Liu and F. Capasso, “Mode-locking via active gain modulation in quantum cascade lasers,” in *Conference on Lasers and Electro-Optics (CLEO)*, Baltimore, MD, USA, 2009.

[20] K. Lau, “Narrow-band modulation of semiconductor lasers at millimeter wave frequencies (>100 GHz) by mode locking,” *IEEE Journal of Quantum Electronics,* vol. 26, no. 2, pp. 250-261, 1990.

[21] M. I. o. Technology, “Ultrafast Optics Course, Chapter 5: Active Mode-locking,” 2005. [Online]. Available: https://ocw.mit.edu/courses/electrical-engineering-and-computer-science/. [Accessed 22 7 2021].

[22] V. Moskalenko, J. Koelemeij, K. Williams and E. Bente, “Study of extra wide coherent optical combs generated by a QW-based integrated passively mode-locked ring laser,” *Optics Letters,* vol. 42, no. 7, pp. 1428-1431, 2017.

[23] J. Javaloyes, J. Mulet, M. Giudici and S. Balle, “Passive mode-locking of lasers by crossed-polarization gain modulation,” in *European Conference on Lasers and Electro-Optics and the International Quantum Electronics Conference*, Munich, Germany, 2007.

[24] K.-H. Lee, W.-Y. Choi, Y. A. Leem, K.-S. Choi, H. Ko and K. H. Park, “Harmonic Signal Generation and Frequency Up-Conversion Using a Hybrid Mode-Locked Multisection DFB Laser,” *IEEE Photonics Technology Letters ,* vol. 19, no. 12, pp. 901-903, 2007.

[25] P. Delfyett, S. Gee, M.-T. Choi, H. Izadpanah, W. Lee, S. Ozharar, F. Quinlan and T. Yilmaz, “Optical frequency combs from semiconductor lasers and applications in ultrawideband signal processing and communications,” *Journal of Lightwave Technology,* vol. 24, no. 7, pp. 2701-2719, 2006.

[26] Y. Barbarin, E. Bente, M. Heck, J. d. Besten, G. Guidi, Y. Oei, J. Binsma and M. Smit, “Realization and modeling of a 27-GHz integrated passively mode-locked ring laser,” *IEEE Photonics Technology Letters ,* vol. 17, no. 11, pp. 2277-2279, 2005.

[27] V.K.Dugaev, O.A.Mironov and S.V.Kosyachenko, “Piezoelectric effect in p-Si/SiGe/(001)Si modulation doped heterostructures,” *Condensed Matter Physics,* vol. 3, no. 4, p. 835–844, 2000.

[28] F. Li, T. Shen, C. Wang, Y. Zhang, J. Qi and H. Zhang, “Recent Advances in Strain-Induced Piezoelectric and Piezoresistive Effect-Engineered 2D Semiconductors for Adaptive Electronics and Optoelectronics,” *Nano-Micro Letters,* vol. 12, no. 106, 2020.

[29] T. Habruseva, S. O’Donoghue, N. Rebrova, F. Kéfélian, S. P. Hegarty and G. Huyet, “Optical linewidth of a passively mode-locked semiconductor laser,” *Optics Letters,* vol. 34, no. 21, pp. 3307-3309, 2009.

[30] E. Sooudi, S. Sygletos, A. D. Ellis, G. Huyet, J. G. McInerney, F. Lelarge, K. Merghem, R. Rosales, A. Martinez, A. Ramdane and S. P. Hegarty, “Optical Frequency Comb Generation Using Dual-Mode Injection-Locking of Quantum-Dash Mode-Locked Lasers: Properties and Applications,” *IEEE Journal of Quantum Electronics ,* vol. 48, no. 10, pp. 1327-1338, 2012.

[31] T. Habruseva, S. O'Donoghue, N. Rebrova, D. Rachinskii, S. Hegarty and G. Huyet, “Linewidth narrowing and phase locking of quantum-dot mode-locked lasers employing single- and dual-mode injection locking,” in *European Conference on Lasers and Electro-Optics and the European Quantum Electronics Conference (CLEO/Europe - EQEC)*, Munich, Germany, 2009.

[32] G. P. Agrawal, “Mode-partition noise and intensity correlation in a two-mode semiconductor laser,” *Phys. Rev. A,* vol. 37, no. 7, pp. 2488-2494, 1988.

[33] T. Kobayashi and T. Sueta, “High-repetition-rate optical pulse generator using a Fabry-Perot electro-optic modulator,” *Applied Physics Letters,* vol. 21, no. 8, pp. 341-343, 1972.

[34] A. Chiba, N. Kobayashi, Y. Moteki, T. Sakamoto and K. Takada, “Generation of wide frequency-spacing optical frequency comb composed of odd/even multiple harmonics,” in *Conference on Lasers and Electro-Optics Pacific Rim (CLEO-PR)*, Singapore, 2017.

[35] T. Sakamoto, T. Kawanishi and M. Izutsu, “Optoelectronic oscillator using a LiNbO3 phase modulator for self-oscillating frequency comb generation,” *Optics Letters,* vol. 31, no. 6, pp. 811-813, 2006.

[36] T. Sakamoto, T. Kawanishi and M. Izutsu, “Asymptotic formalism for ultraflat optical frequency comb generation using a Mach–Zehnder modulator,” *Optics Letters,* vol. 32, no. 11, pp. 1515-1517, 2007.

[37] T. Yamamoto, K. Hitomi, W. Kobayashi and H. Yasaka, “Optical Frequency Comb Block Generation by Using Semiconductor Mach–Zehnder Modulator,” *IEEE Photonics Technology Letters,* vol. 25, no. 1, pp. 40-42, 2013.

[38] J. Zhang, N. Chi, J. Yu, Y. Shao, J. Zhu, B. Huang and L. Tao, “Generation of coherent and frequency-lock multi-carriers using cascaded phase modulators and recirculating frequency shifter for Tb/s optical communication,” *Optics Express,* vol. 19, no. 14, pp. 12891-12902, 2011.

[39] J. Zhang, J. Yu, N. Chi, Z. Dong, X. Li, Y. Shao, J. Yu and L. Tao, “Flattened comb generation using only phase modulators driven by fundamental frequency sinusoidal sources with small frequency offset,” *Optics Letters,* vol. 38, no. 4, pp. 552-554, 2013.

[40] S. Ozharar, F. Quinlan, I. Ozdur, S. Gee and P. J. Delfyett, “Ultraflat Optical Comb Generation by Phase-Only Modulation of Continuous-Wave Light,” *IEEE Photonics Technology Letters ,* vol. 20, no. 1, pp. 36-38, 2008.

[41] T. Sakamoto, T. Kawanishi and M. Izutsu, “Widely wavelength-tunable ultra-flat frequency comb generation using conventional dual-drive Mach-Zehnder modulator,” *Electronics Letters ,* vol. 43, no. 19, pp. 1039-1040, 2007.

[42] B. Das, K. Mallick, P. Mandal, B. Dutta, C. Barman and A. S. Patra, “Flat optical frequency comb generation employing cascaded dual-drive Mach-Zehnder modulators,” *Results in Physics,* vol. 17, p. 103152, 2020.

[43] M. Fujiwara, M. Teshima, J. Kani, H. Suzuki, N. Takachio and K. Iwatsuki, “Optical carrier supply module using flattened optical multicarrier generation based on sinusoidal amplitude and phase hybrid modulation,” *Journal of Lightwave Technology,* vol. 21, no. 11, pp. 2705-2714, 2003.

[44] R. Wu, V. R. Supradeepa, C. M. Long, D. E. Leaird and A. M. Weiner, “Highly flat and stable optical frequency comb generation using intensity and phase modulators employing quasi-quadratic phase modulation,” in *IEEE International Topical Meeting on Microwave Photonics*, Montreal, QC, Canada, 2010 .

[45] J. Li, H. Ma, Z. Li and X. Zhang, “Optical Frequency Comb Generation Based on Dual-Polarization IQ Modulator Shared by Two Polarization-Orthogonal Recirculating Frequency Shifting Loops,” *IEEE Photonics Journal ,* vol. 9, no. 5, 2017.

[46] A. Parriaux, K. Hammani and G. Millot, “Electro-optic frequency combs,” *Advances in Optics and Photonics,* vol. 12, no. 1, pp. 223-287, 2020.

[47] R. Slavík, S. G. Farwell, M. J. Wale and D. J. Richardson, “Compact Optical Comb Generator Using InP Tunable Laser and Push-Pull Modulator,” *IEEE Photonics Technology Letters ,* vol. 27, no. 2, pp. 217-220, 2015.

[48] T. Cassese, N. Andriolli, M. Chiesa, A. R. Criado and G. Contestabile, “InP Photonic Integrated Comb Generator made by a cascade of Optical Modulators,” in *Optical Fiber Communications Conference and Exposition (OFC)*, San diego, CA, USA, 2018.

[49] L. Alloatti, R. Palmer, S. Diebold, K. P. Pahl, B. Chen, R. Dinu, M. Fournier, J.-M. Fedeli, T. Zwick, W. Freude, C. Koos and J. Leuthold, “100 GHz silicon–organic hybrid modulator,” *Light: Science & Applications ,* vol. 3, no. 173, 2014.

[50] C. Weimann, S. Wolf, D. Korn, R. Palmer, S. Koeber, R. Schmogrow, P. C. Schindler, L. Alloatti, A. Ludwig, W. Heni, D. Bekele, D. L. Elder, H. Yu, W. Bogaerts, L. R. Dalton, W. Freude, J. Leuthold and C. Koos, “Silicon-organic hybrid (SOH) frequency comb source for data transmission at 784 Gbit/s,” in *39th European Conference and Exhibition on Optical Communication (ECOC)*, London, United Kingdom, 2013.

[51] C. Weimann, P. C. Schindler, R. Palmer, S. Wolf, D. Bekele, D. Korn, J. Pfeifle, S. Koeber, R. Schmogrow, L. Alloatti, D. Elder, H. Yu, W. Bogaerts, L. R. Dalton, W. Freude, J. Leuthold and C. Koos, “Silicon-organic hybrid (SOH) frequency comb sources for terabit/s data transmission,” *Optics Express,* vol. 22, no. 3, p. 3629–3637, 2014.

[52] T. Healy, F. C. G. Gunning, A. D. Ellis and J. D. Bull, “Multi-wavelength source using low drive-voltage amplitude modulators for optical communications,” *Optics Express,* vol. 15, no. 6, pp. 2981-2986, 2007.

[53] T. J. Kippenberg, R. Holzwarth and S. A. Diddams, “Microresonator-Based Optical Frequency Combs,” *Science,* vol. 332, no. 6029, pp. 555-559, 2011.

[54] P. Del’Haye, A. Schliesser, O. Arcizet, T. Wilken, R. Holzwarth and T. J. Kippenberg, “Optical frequency comb generation from a monolithic microresonator,” *Nature,* vol. 450, p. 1214–1217, 2007.

[55] J. Pfeifle, V. Brasch, M. Lauermann, Y. Yu, D. Wegner, T. Herr, K. Hartinger, P. Schindler, D. Hillerkuss, R. Schmogrow, R. Holzwarth, W. Freude, J. Leuthold, T. J. Kippenberg and C. Koos, “Coherent terabit communications with microresonator Kerr frequency combs,” *Nature Photonics ,* vol. 8, p. 375–380 , 2014.

[56] P. Marin, J. Pfeifle, M. Karpov, P. Trocha, R. Rosenberger, K. Vijayan, S. Wolf, J. Kemal, A. Kordts, M. Pfeiffer, V. Brasch, W. Freude, T. J. Kippenberg and C. Koos, “50 Tbit/s massively parallel WDM transmission in C and L band using interleaved cavity-soliton Kerr combs,” in *Conference on Lasers and Electro-Optics (CLEO)*, San Jose, CA, USA, 2016.

[57] P. Liao, C. Bao, A. Kordts, M. Karpov, M. H. P. Pfeiffer, L. Zhang, A. Mohajerin-Ariaei, Y. Cao, A. Almaiman, M. Ziyadi, S. R. Wilkinson, M. Tur, T. J. Kippenberg and A. E. Willner, “Dependence of a microresonator Kerr frequency comb on the pump linewidth,” *Optics Letters,* vol. 42, no. 4, pp. 779-782, 2017.

[58] F. Yaman, Q. Lin and G. P. Agrawal, “Fiber Optic Parametric Amplifiers for Lightwave Systems,” University of Rochester, New York, USA, 2005.

[59] J. Li, H. Lee, T. Chen and K. J. Vahala, “Low-Pump-Power, Low-Phase-Noise, and Microwave to Millimeter-Wave Repetition Rate Operation in Microcombs,” *Phys. Rev. Lett. ,* vol. 109, no. 23, p. 233901, 2012.

[60] J. Pfeifle, M. Lauermann, D. Wegner, J. Li, K. Hartinger, V. Brasch, T. Herr, D. Hillerkuss, R. Schmogrow, T. Schimmel, R. Holzwarth, T. Kippenberg, J. Leuthold, W. Freude and C. Koos, “Microresonator-based frequency comb generator as optical source for coherent WDM transmission,” in *Optical Fiber Communication Conference and Exposition and the National Fiber Optic Engineers Conference (OFC/NFOEC)*, Anaheim, CA, USA, 2013 .

[61] P. Torphammar and S. Eng, “Picosecond pulse generation in semiconductor lasers using resonance oscillation,” *Electronics Letters ,* vol. 16, no. 15, p. 587 – 589, 1980.

[62] S. Tarucha and K. Otsuka, “Response of semiconductor laser to deep sinusoidal injection current modulation,” *IEEE Journal of Quantum Electronics ,* vol. 17, no. 5, pp. 810-816, 1981.

[63] P. Paulus, R. Langenhorst and D. Jager, “Generation and optimum control of picosecond optical pulses from gain-switched semiconductor lasers,” *IEEE Journal of Quantum Electronics ,* vol. 24, no. 8, pp. 1519 - 1523, 1988.

[64] R. Zhou, “Optical Frequency Comb Source for Next Generation Access Networks,” Dublin, Ireland, 2014.

[65] P. M. Anandarajah, K. Shi, J. O’Carroll, A. Kaszubowska, R. Phelan, L. P. Barry, A. D. Ellis, P. Perry, D. Reid, B. Kelly and J. O’Gorman, “Phase shift keyed systems based on a gain switched laser transmitter,” *Optics Express,* vol. 17, no. 15, pp. 12668-12677, 2009.

[66] P. Paulus, R. Langenhorst and D. Jager, “Generation and optimum control of picosecond optical pulses from gain-switched semiconductor lasers,” *IEEE Journal of Quantum Electronics ,* vol. 24, no. 8, pp. 1519 - 1523, 1988.

[67] M. D. G. Pascual, R. Zhou, F. Smyth, P. M. Anandarajah and L. P. Barry, “Software reconfigurable highly flexible gain switched optical frequency comb source,” *Optics Express,* vol. 23, no. 18, pp. 23225-23235, 2015.

[68] S. P. Ó. Dúill, R. Zhou, P. M. Anandarajah and L. P. Barry, “Analytical Approach to Assess the Impact of Pulse-to-Pulse Phase Coherence of Optical Frequency Combs,” *IEEE Journal of Quantum Electronics ,* vol. 51, no. 11, 2015.

[69] J. Dellunde, M. Torrent, J. Sancho and M. S. Miguel, “Frequency dynamics of gain-switched injection-locked semiconductor lasers,” *IEEE Journal of Quantum Electronics,* vol. 33, no. 9, pp. 1537-1542, 1997.

[70] E. K. Lau, L. J. Wong and M. C. Wu, “Enhanced Modulation Characteristics of Optical Injection-Locked Lasers: A Tutorial,” *IEEE Journal of Selected Topics in Quantum Electronics,* vol. 15, no. 3, pp. 618-633, 2009.

[71] T. Simpson, J. Liu and A. Gavrielides, “Bandwidth enhancement and broadband noise reduction in injection-locked semiconductor lasers,” *IEEE Photonics Technology Letters,* vol. 7, no. 7, pp. 709-711, 1995.

[72] R. Lang and K. Kobayashi, “External optical feedback effects on semiconductor injection laser properties,” *IEEE Journal of Quantum Electronics,* vol. 16, no. 3, pp. 347-355, 1980.

[73] R. Zhou, S. Latkowski, J. O'Carroll, R. Phelan, L. P. Barry and P. Anandarajah, “40nm wavelength tunable gain-switched optical comb source,” in *37th European Conference and Exhibition on Optical Communication (ECOC)*, Geneva, Switzerland, 2011 .

[74] L. Barry, P. Anandarajah and A. Kaszubowska, “Optical pulse generation at frequencies up to 20 GHz using external-injection seeding of a gain-switched commercial Fabry-Perot laser,” *IEEE Photonics Technology Letters,* vol. 13, no. 9, pp. 1014-1016, 2001.

[75] A. Murakami, K. Kawashima and K. Atsuki, “Cavity resonance shift and bandwidth enhancement in semiconductor lasers with strong light injection,” *IEEE Journal of Quantum Electronics ,* vol. 39, no. 10, pp. 1196-1204, 2003.

[76] Z. Liu and R. Slavík, “Optical Injection Locking: From Principle to Applications,” *Journal of Lightwave Technology,* vol. 38, no. 1, pp. 43-59, 2020.

[77] C. Henry, N. Olsson and N. Dutta, “Locking range and stability of injection locked 1.54 μm InGaAsp semiconductor lasers,” *IEEE Journal of Quantum Electronics ,* vol. 21, no. 8, pp. 1152-1156, 1985.

[78] P. M. Anandarajah, S. Latkowski, C. Browning, R. Zhou, J. O'Carroll, R. Phelan, B. Kelly, J. O'Gorman and L. P. Barry, “Integrated Two-Section Discrete Mode Laser,” *IEEE Photonics Journal,* vol. 4, no. 6, pp. 2085 - 2094, 2012.

[79] C. Browning, K. Shi, S. Latkowski, P. M. Anandarajah, F. Smyth, B. Cardiff and L. P. Barry, “Increased Bit Rate Direct Modulation AMO-OFDM Transmission by Optical Injection Using Monolithically Integrated Lasers,” *IEEE Photonics Technology Letters ,* vol. 24, no. 11, pp. 879-881, 2012.

[80] H.-K. Sung, T. Jung, M. Wu, D. Tishinin, T. Tanbun-Ek, K. Liou and W. Tsang, “Modulation bandwidth enhancement and nonlinear distortion suppression in directly modulated monolithic injection-locked DFB lasers,” in *International Topical Meeting on Microwave Photonics (MWP)*, Budapest, Hungary, 2003.

[81] S. Hwang and J. Tian, “Chirp reduction in directly-modulated semiconductor lasers subject to external optical injection,” in *IEEE LEOS Annual Meeting Conference Proceedings*, Sydney, NSW, Australia, 2005.

[82] D. N. Wang and X. Fang, “Generation of electrically wavelength-tunable optical short pulses using a Fabry–Perot laser diode in an external-injection seeding scheme with improved side mode suppression ratio,” *IEEE Photon. Technol. Lett.,* vol. 15, no. 1, pp. 123 - 125, 2003.

[83] D. Seo, H. Liu, D. Y. Kim and D. D. Sampson, “Injection power and wavelength dependence of an external-seeded gain-switched fabry-perot laser,” *Appl. Phys. Lett.,* vol. 67, p. 1503–1505, 1995.

[84] M. Poelker, “High power gain-switched diode laser master oscillator and amplifier,” *Appl. Phys. Lett.,* vol. 67, p. 2762–2764, 1995.

[85] H. Ghafouri-Shiraz, Principles of Semiconductor Laser Diodes and Amplifiers: Analysis and Transmission Line Laser Modelling, Imperial College Press, 2003.

[86] E. K. Lau, X. Zhao, H.-K. Sung, D. Parekh, C. Chang-Hasnain and M. C. Wu, "Strong optical injection-locked semiconductor lasers demonstrating >100-GHz resonance frequencies and 80-GHz intrinsic bandwidths," *Optics Express,* vol. 16, no. 9, pp. 6609-6618, 2008.

[87] X. JunMeng, T. Chau and M. C.Wu, "Experimental demonstration of modulation bandwidth enhancement in distributed feedback lasers with external light injection," *Electronics Letters,* vol. 34, no. 21, pp. 2031-2032, 1998.

[88] N. Schunk and K. Petermann, "Noise analysis of injection-locked semiconductor injection lasers," *IEEE Journal of Quantum Electronics,* vol. 22, no. 5, pp. 642-650, 1986.

[89] N. Schunk and K. Petermann, "Noise analysis of injection-locked semiconductor injection lasers," *IEEE Journal of Quantum Electronics ,* vol. 22, no. 5, pp. 642 - 650, 1986.

[90] F. Mogensen, H.Olesen and G.Jacobsen, "FM noise suppression and linewidth reduction in an injection-locked semiconductor laser," *Electronics Letters ,* vol. 21, no. 16, pp. 696-697, 1985.

[91] R. Zhou, T. N. Huynh, V. Vujicic, P. M. Anandarajah and L. P. Barry, "Phase noise analysis of injected gain switched comb source for coherent communications," *Optics Express,* vol. 22, no. 7, pp. 8120-8125, 2014.

[92] G. Yabre, H. D. Waardt, H. v. d. Boom and G.-D. Khoe, "Noise characteristics of single-mode semiconductor lasers under external light injection," *IEEE Journal of Quantum Electronics ,* vol. 36, no. 3, pp. 385 - 393, 2000.

[93] J. Law and G. Agrawal, "Mode-partition noise in vertical-cavity surface-emitting lasers," *IEEE Photonics Technology Letters,* vol. 9, no. 4, pp. 437 - 439, 1997.

[94] K. Iwashita and K. Nakagawa, "Suppression of Mode Partition Noise by Laser Diode Light Injection," *IEEE Transactions on Microwave Theory and Techniques ,* vol. 30, no. 10, pp. 1657-1662, 1982.

[95] M. D. G. Pascual, R. Zhou, F. Smyth, P. M. Anandarajah and L. P. Barry, "Software reconfigurable highly flexible gain switched optical frequency comb source," *Optics Express,* vol. 23, no. 18, pp. 23225-23235, 2015.

[96] V. Vujicic, A. P. Anthur, A. Saljoghei, V. Panapakkam, R. Zhou, Q. Gaimard, K. Merghem, F. Lelarge, A. Ramdane and L. P. Barry, "Mitigation of relative intensity noise of quantum dash mode-locked lasers for PAM4 based optical interconnects using encoding techniques," *Optics Express,* vol. 25, no. 1, pp. 20-29, 2017.

[97] J. Renaudier, G.-H. Duan, P. Landais and P. Gallion, "Phase Correlation and Linewidth Reduction of 40 GHz Self-Pulsation in Distributed Bragg Reflector Semiconductor Lasers," *IEEE Journal of Quantum Electronics ,* vol. 43, no. 2, pp. 147-156, 2007.

[98] T. Habruseva, N. Rebrova, T. Piwonski, J. Pulka, S. P. Hegarty, D. A. Reid, L. P. Barry and G. Huyet, “Stabilization of quantum-dot mode-locked lasers via optical injection,” in *CLEO/QELS: Laser Science to Photonic Applications*, San Jose, CA, USA, 2010.

[99] S. Gee, F. Quinlan, S. Ozharar and P. Delfyett, “Optical comb frequencies stabilization and super mode noise suppression of harmonically modelocked semiconductor ring laser using a single etalon,” in *The 17th Annual Meeting of the IEEELasers and Electro-Optics Society (LEOS)*, Rio Grande, PR, USA, 2004.

[100] Y. Cheng, J. Yan, Z. Zheng and S. Zhao, “Tunable Parametric Optical Frequency Combs Generation based on an Electroabsorption Modulated Laser,” in *Conference on Lasers and Electro-Optics (CLEO)*, San Jose, CA, USA, 2019.

[101] V. Ataie, E. Temprana, L. Liu, E. Myslivets, B. P.-P. Kuo, N. Alic and S. Radic, “Flex-grid compatible ultra wide frequency comb source for 31.8 Tb/s coherent transmission of 1520 UDWDM channels,” in *OFC* , San Francisco, CA, USA, 2014.

[102] V. Ataie, E. Myslivets, B. P.-P. Kuo, N. Alic and S. Radic, “Spectrally Equalized Frequency Comb Generation in Multistage Parametric Mixer With Nonlinear Pulse Shaping,” *Journal of Lightwave Technology ,* vol. 32, no. 4, pp. 840-846, 2014.

[103] B. P.-P. Kuo, E. Myslivets, N. Alic and S. Radic, “Wavelength Multicasting via Frequency Comb Generation in a Bandwidth-Enhanced Fiber Optical Parametric Mixer,” *Journal of Lightwave Technology ,* vol. 29, no. 23, pp. 3515-3522, 2011.

[104] B. P.-P. Kuo, E. Myslivets, V. Ataie, E. G. Temprana, N. Alic and S. Radic, “Wideband Parametric Frequency Comb as Coherent Optical Carrier,” *Journal of Lightwave Technology,* vol. 31, no. 21, pp. 3414-3419, 2013.

[105] V. Ataie, E. Temprana, L. Liu, E. Myslivets, B. P.-P. Kuo, N. Alic and S. Radic, “Flex-grid compatible ultra wide frequency comb source for 31.8 Tb/s coherent transmission of 1520 UDWDM channels,” in *OFC*, San Francisco, CA, USA, 2014.

[106] E. Temprana, V. Ataie, B. P.-P. Kuo, E. Myslivets, N. Alic and S. Radic, “Low-noise parametric frequency comb for continuous C-plus-L-band 16-QAM channels generation,” *Optics Express,* vol. 22, no. 6, pp. 6822-6828, 2014.

[107] K. Y. Lau, “Gain switching of semiconductor injection lasers,” *Applied Physics Letters,* vol. 52, no. 4, p. 257, 1988.

[108] M. D. G. Pascual, V. Vujicic, J. Braddell, F. Smyth, P. M. Anandarajah and L. P. Barry, “InP photonic integrated externally injected gain switched optical frequency comb,” *Optics Letters,* vol. 42, no. 3, pp. 555-558, 2017.

[109] C.-W. Tseng, C.-W. Tsai, K.-C. Lin, M.-C. Lee and Y.-J. Chen, “Study of coupling loss on strongly-coupled, ultra compact microring resonators,” *Optics Express,* vol. 21, no. 6, pp. 7250-7257, 2013.

[110] J. G. Proakis, “Chapter 9,” in *Digital Communications, 3rd Edition*, John G. Proakis, 1995.

[111] C.-H. Chang, L. Chrostowski and C. Chang-Hasnain, “Injection locking of VCSELs,” *IEEE Journal of Selected Topics in Quantum Electronics,* vol. 9, no. 5, pp. 1386-1393, 2003.

Chapter 3

Optimum operating parameters for generation of optical frequency combs

3.1 Introduction

In the previous chapter, various techniques for OFC generation were introduced, showing the strengths and the weakness of each technique and the applications they are suited for. As previously mentioned, focus will be directed towards the gain switching technique due to its simplicity and cost-effectiveness. It was already stated that gain switching can be applied to any commercially available off-the-shelf semiconductor laser. At the same time, it is crucial to pick the most suitable laser type for the desired application. Different applications impose diverse requirements and specifications according to the network topology that it will be used in. Access and short-reach networks, for example, have stringent requirements on cost.

This chapter presents the static and dynamic characterisations of various traditional laser structures. The primary goal is to identify the optimised driving parameters for each different laser structure to be used with the gain-switching technique in order to generate an enhanced OFC in terms of larger optical bandwidth, optical flatness and OCNR. Both FP and DFB laser structures are characterised for the generation of an OFC. External optical injection is also presented as an essential technique that is complementary to the gain switching process to improve the spectral characteristics of the generated OFC. As previously explained, this is achieved by locking the frequency, phase, and polarization of the slave laser to the spectrally purer master laser. A full study of two different VCSEL devices is presented

where the motivation and several advantages over the traditional edge-emitting laser structures are explained. The VCSEL device parameters are also examined and optimised to generate an enhanced OFC. In addition, the positive impact of external optical injection on the characteristics of the generated OFC is highlighted through a series of different characterisations. Eventually, the polarisation dynamics of VCSEL structures are explained and discussed. Finally, a discussion on how the polarisation dynamics could be utilised (expand the generated OFC) is included.

In summary, this chapter provides a gateway to characterisation and optimisation of different laser structures driving parameters to be gain-switched to generate an OFC with enhanced spectral parameters.

3.2 Fabry Pérot laser diodes

FP lasers are one of the well-known semiconductor laser structures [1], that were typically used for short-distance light wave telecommunication systems [2]. Their popularity stems from the simplicity and cost-effectiveness of their manufacturing process. An FP laser is an edge-emitting laser, where two flat cleaved surfaces are placed at either side of the gain medium as reflectors [3]. A resonator cavity is formed by these reflectors, where light reflections take place only at the end of the cavity and not within the gain medium as opposed to a DFB laser. In the resonator cavity, the light reinforces itself at only the frequencies satisfying the condition for which the distance between the two ends is an integral multiple of half wavelengths. Such frequencies are supported by the cavity, since they undergo constructive interference over one round-trip, and are referred to as the resonant frequencies (or wavelengths) of the cavity. However, the non-resonant wavelengths suffer from destructive interference over one round-trip in the cavity and are not supported. The two reflectors cause the light inside the cavity to propagate back and forth in the active region forming a standing wave. Thus, the two reflecting surfaces are responsible for creating the suitable condition for the lasing to happen, by supporting only specific wavelengths that undergo constructive interference to form standing waves. These wavelengths or frequencies supported by the cavity are called the longitudinal modes of the FP laser diode.

The longitudinal mode separation is dependent on the length of the laser cavity according to the following equation [4]:

$$\Delta V = \frac{C}{2nL} \tag{3.1}$$

Where ΔV is the FSR between the laser longitudinal modes, C is the speed of light, n is the refractive index and L is the laser cavity length. The frequency selectivity is decided by the FSR which in turn sets

the cavity length. Consequently, FP lasers have a relatively short cavity length to the filter and select a specific range of wavelengths. A long laser cavity would correspond to a smaller FSR and would result in a large number of longitudinal modes in a given wavelength range, thereby compromising the wavelength selectivity of the laser cavity. However, selective filtering of a single longitudinal mode is not possible due to restrictions on the laser cavity length. Sufficient laser cavity length is required for stimulated emission to occur and to amplify the light wave signal, as we are limited by the amount of power that we can be delivered to a small area. A tunable single-mode operation of the FP cavity can be achieved by coupling it with a very-short cavity with selective optical feedback as shown in [5]. The short cavity length of the FP structures also results in the widening of the generated linewidth [6], as the linewidth is directly proportional to the square of the resonator bandwidth. The latter in turn is inversely proportional to the length of the laser cavity. The laser cavity length is inversely proportional to the mode spacing.

3.2.1 FP laser structure

As mentioned before, the FP laser is an edge-emitting laser. A typical structure of an FP laser is shown in Figure 3.1**.** The two main elements forming the structure are the gain element, which is the active region that provides optical gain [7], and the two cleaved surfaces at the end of the laser forming a cavity. The resonator is formed as a consequence of the discrepancy between refractive indices that occurs at the interface between the semiconductor device structure and air, resulting in reflectance without the need of any additional measures.

The active gain region is formed by applying current to a lower band gap active layer that is surrounded by higher bandgap materials, which confines the electron and holes into a small volume. The injected current causes the movement of electrons from the lower energy valence band (energy state) to the higher energy conduction band. As electrons from the conduction band fall back to the valence band, they lose energy in the form of photons (emitted light) as shown by Figure 3.2(a).

The frequency of the emitted photon f depends on the the difference in energy E between the higher energy level E_2 and the lower energy state E_1 and can be calculated according to the following equation:

$$E = E_2 - E_1 = hf \tag{3.2}$$

Where h is the Planck's constant.

The emission process can take place in two different ways, the first by spontaneous emission in which the electron returns to the lower energy state in a random manner.

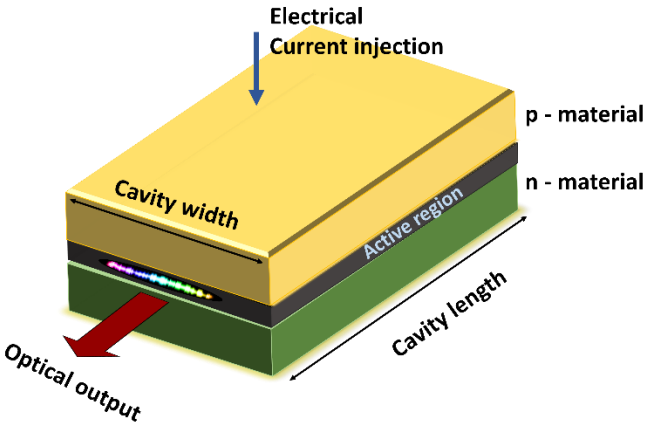

Figure 3.1: Schematic structure of an FP laser.

The second case is by stimulated emission, when a photon having an energy that is equal to the energy difference between two energy states ($E_2 - E_1$) interacts with an electron in the higher energy state, leading to its return to the lower energy state with the creation of a second photon. Having this process repeating itself would result in the photons generated by the stimulated emission having an identical energy to the one which caused it, which results in the light signal associated with them generated at the same frequency. Moreover, the light signal is in phase and has the same polarisation [8].

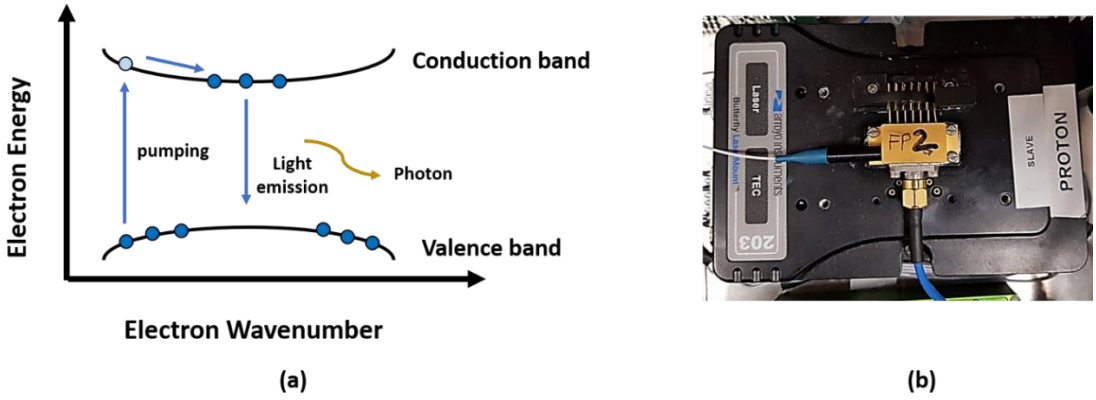

Figure 3.2: (a) FP laser emission mechanism, (b) FP packaged laser on a mount.

In the next section, a brief static characterisation of an FP device is presented. Moreover, gain switching with external injection of the device results are shown.

3.2.2 FP static characterisation

The FP laser is packaged into a 7-pin butterfly package that has an integrated TEC for ease of use and handling and an integrated lens for providing an optimised coupling between the laser and the output fibre as shown in Figure 3.2(b). The laser package is placed on a laser mount which facilitates the control of the bias current and the temperature of the laser using an LD driver and TEC controller.

The generated L-I curves of the laser for different temperatures (16, 21, 25, and 30 °C) is shown in Figure 3.3(a). It shows that at all temperatures, the optical output power increases with the increase of the bias current. This is due to the fact that increasing the bias current results in the injection of a larger number of free carriers inside the laser cavity which increases the gain. The increase of the latter results in the increase of number of photons inside the cavity, and thus, increasing the output power. This dependence has been explained in more details using the semiconductor laser rate equations in Section 2.3.4.1.1 in Chapter 2. With low values of bias, the generated gain cannot overcome the losses inside the cavity where the spontaneous emission is dominating. This happens until we reach a bias point, where the gain inside the cavity is equal to the losses. At this point, the laser threshold is reached, beyond which the stimulated emission dominates the spontaneous one and keeps increasing the laser output power with the increase in the bias supplied [9]. At 16 °C, the laser yields a threshold current of 6.5 mA. The laser threshold bias value has a direct proportional relationship with the temperature of the laser. When the temperature increases inside the laser cavity, the intrinsic losses (mainly recombination rates due to defects in the active region material) increase due to shifting of the exponential absorption edge to lower energies faster than the emission peak [10]. The difference between the two shifts is nearly linear with temperature. Moreover, the gain also decreases as increasing the temperature can lead to narrowness of the laser bandgap. It is known that the motion of carriers (electrons and holes) becomes intensive in the region of PN junction of laser diode with increase of working temperature, which results in more remarkable non-irradiative recombination process. Therefore, the outer quantum efficiency decreases rapidly. As a result, the output power inevitably decreases [11]. Hence, more carriers are needed to reach the threshold condition, as the gain is less efficient. It is important also to note that there is no exciton at room temperature for this laser.

Figure 3.3(b) shows the dependence of central emission wavelength of the device on the temperature. Using an optical spectrum analyser (OSA), the central emission wavelength at different values of temperature is recorded. At this point, the laser bias is kept constant at 17 mA. The figure shows that increasing the temperature results in the central emission wavelength experiencing a red shift where it moves to a higher wavelength. The wavelength of the laser diode shifts about 1.5 nm with every 10 degrees rise in temperature which agrees with the direct proportionality relationship between the temperature and the central emission wavelength of the laser, as the emission wavelength of the laser depends on its refractive index, which in turn is dependent on the temperature [12].

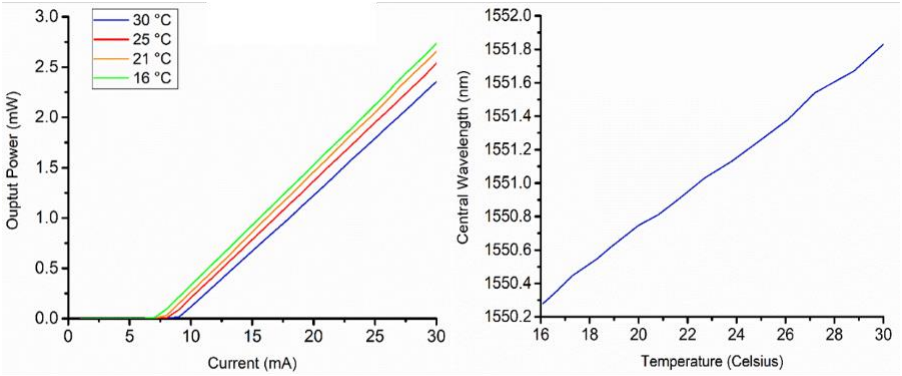

Figure 3.3: (a) L-I curve of the FP laser at different temperatures, (b) Wavelength temperature dependence curve of the FP laser.

3.2.3 FP Gain switching

Being one of the most common types of semiconductor laser structures used with short-reach optical networks, the FP laser can be gain-switched to generate an OFC. However, one of the initial steps in the generation of an OFC using FP lasers entails the use of external optical injection. This results in concentrating all the gain in a single longitudinal mode, after which gain switching is achieved by directly modulating the injected FP laser using an amplified RF signal. Figure 3.4(a) shows the setup diagram of gain switching an externally injected temperature controlled (20°C) FP laser. The laser is initially DC biased to set the operating point of the laser at about 35 mA, which is almost 5 times the threshold value. Gain-switching is achieved by directly modulating the optically injected FP laser with an amplified 6.25 GHz (corresponding to ITU.T definition of flexible grid granularity) sinusoidal RF signal using the integrated RF connector in the laser package. A signal generator is used to generate a pure 6.25 GHz sinusoidal RF signal, which is then amplified using an RF amplifier to have an amplitude of 24 dBm. The RF signal is then combined with the DC bias using a bias tee. The combined signal is then used to directly modulate the injection locked FP laser, that is locked using a tunable continuous wave master laser at a wavelength of 1545.4 nm for locking the FP mode at this particular wavelength. The optical output of the laser is then connected to a high resolution OSA (20 MHz) in order to capture the optical spectrum.

The optical spectrum of the free running (DC biased without optical injection) FP laser is shown in Figure 3.4(b). The FP centre emission wavelength is around 1545 nm and the several FP longitudinal modes with mode spacing of 1.37 nm (corresponding to frequency separation of approximately 175 GHz) can be seen. Figure 3.4(c) shows the optical spectrum of the injection locked FP using a tunable master laser emitting at 1545.4 nm. The central emission wavelength can be tuned by tuning the master (external) laser to coincide with one of the FP modes. Thus, this particular mode dominates

over all the other longitudinal modes in the cavity by suppressing the gain in them [13]. Figure 3.4(d) shows the spectrum of the generated OFC which exhibits 15 OFC tones within 3-dB from the spectral peak and an OCNR of around 50 dB. Choosing a multimode laser over a single mode laser would be based on the wavelength tunability that can be achieved [14].

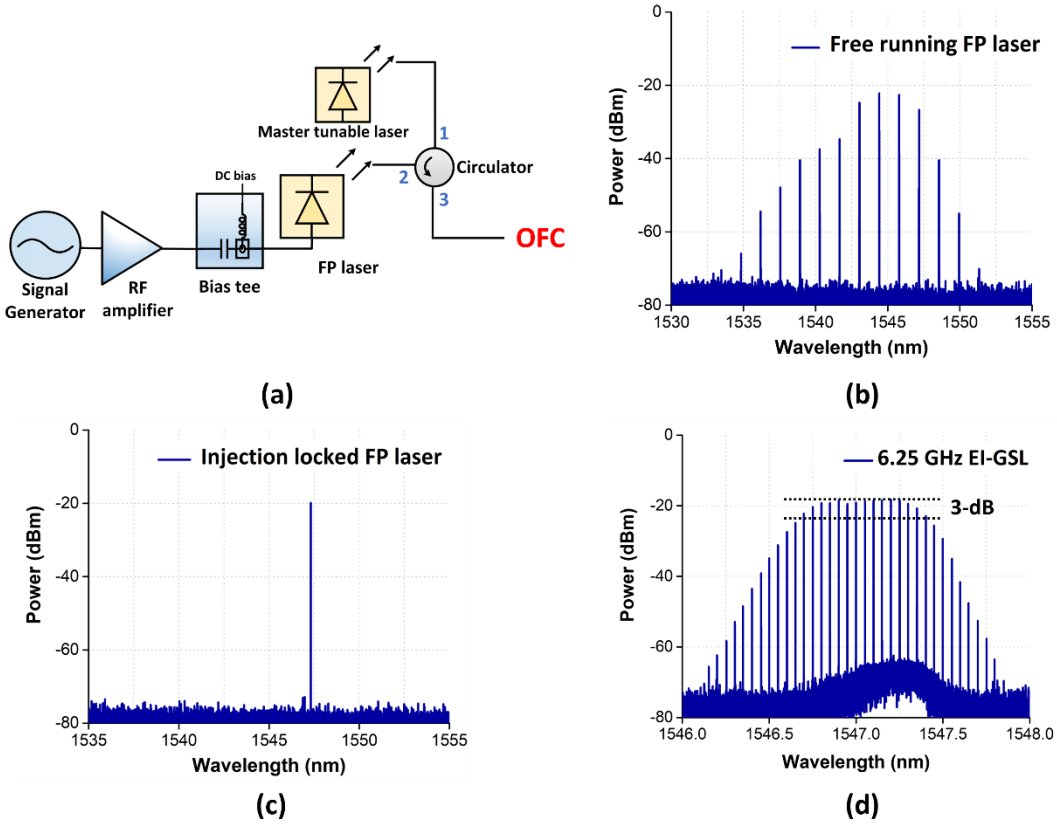

Figure 3.4: (a) Setup diagram for gain switching an externally injected FP laser, (b) Optical spectrum of free running FP laser, (c) Optical spectrum of injection locked FP laser, and (d) Optical spectrum of the gain-switched FP laser.

There have been previous demonstrations of FSR and wavelength tunability of externally injection-locked FP lasers, where quasi-continuous wavelength tunability over the C-band (30 nm) and FSR tunability ranging from 6 GHz to 14 GHz have been demonstrated [15]. Moreover, an OFC based on gain switching of an externally injected FP laser has been used as a transmitter in a simple and low-cost uplink transmission scheme for coherent optical code-division multiple access (OCDMA) passive optical networks (PONs) as shown in [16], where the authors demonstrate the simplicity and the cost-effectiveness of their scheme compared with a transmitter based on a conventional MLL. In addition to that, a broadband OFC has been shown based on simultaneous injection locking of two longitudinal modes of a gain-switched FP laser [17]. The generated OFC exhibits an overall width of 325 GHz within 6 dB occupied optical bandwidth and offers tunability of both wavelength and FSR. The demonstrated results show the potential of FP based gain-switched OFC to be employed in several telecommunication applications such as next-generation elastic optical networks and millimetre/THz wave generation [18].

3.3 DFB lasers

3.3.1 DFB laser structure

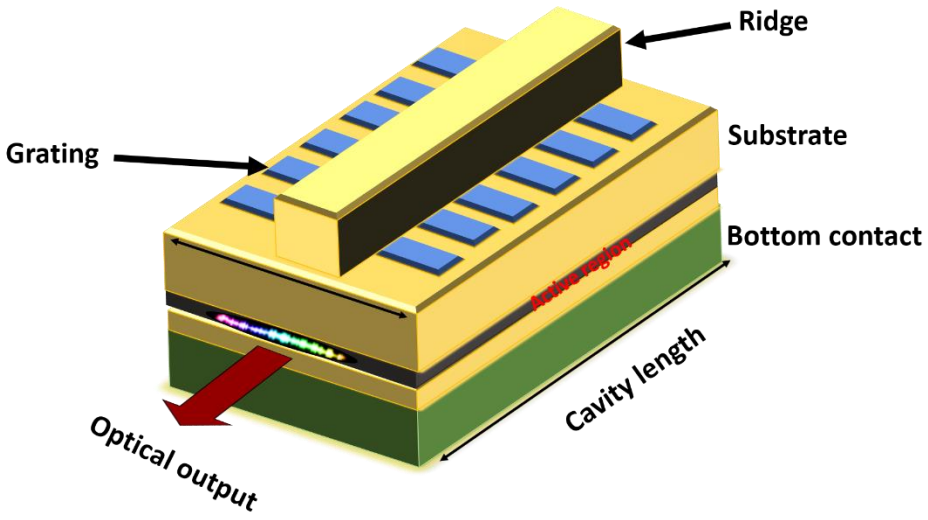

Figure 3.5: Schematic structure of a DFB laser.

A DFB is another well-known type of semiconductor laser. Its structure is very similar to that of an FP laser with the addition of a Bragg reflector that is placed near the active region [19] as shown in Figure 3.5. The main function of this Bragg reflector is to select a single longitudinal mode in the laser output as it provides periodic variation in the refractive index along the laser waveguide in the direction of the light wave propagation [8]. In a FP laser cavity, the feedback is the same for all modes, while in a DFB laser, the feedback is frequency dependant. This results in the cavity losses not being the same for all the longitudinal modes leading eventually to emission of a single longitudinal mode that is supported by both the cavity and the Bragg reflector. The latter is used to select the desired output mode. The other longitudinal modes experiencing higher losses are suppressed from oscillation inside the cavity. Using long cavity DFBs that have high coupling coefficients results in achieving narrow linewidths (less than 1 MHz) [20].

3.3.2 DFB static characterisation

In our work, we have used an InGaAsP/InP multi-quantum well DFB laser diode that is manufactured by Gooch&Housego (G&H). The device is mounted in a 7-pin k-package where it contains a TEC,

thermistor, back facet monitor detector, and a bias tee as specified by the manufacturer. Figure 3.6(a) shows a picture of the physical packaged device, while the measured L-I curve at 20°C temperature is shown in Figure 3.6(b). The threshold current is measured to be 12 mA. The direct proportional relationship between the threshold value and the laser package temperature shown previously for the FP laser applies to the DFB lasers also.

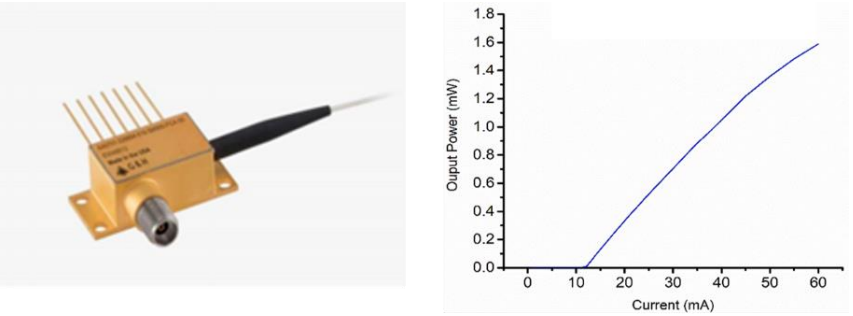

(a) **(b)**

Figure 3.6: (a) 7-pin packaged DFB laser, (b) L-I curve of the DFB laser.

3.3.3 DFB gain switching

To gain switch the DFB laser, the same setup diagram as Figure 3.4(a) is used (FP laser replaced by the G&H DFB laser). Figure 3.7(a) shows the optical spectrum of the free running DFB laser when biased at 47.78 mA (around 4 times the threshold current). Different bias current values result in the variation of the OFC characteristics due to variations in the gain inside the laser cavity [21]. Relating to the simulation analysis conducted in Section 2.3.4.1.1 in Chapter 2, the increase in bias value would result in the increase in the laser MBW value due to the decrease in the carrier lifetime [22]. The increase in the laser MBW leads to generation of a wide bandwidth OFC that accommodates a greater number of comb lines depending on the driving RF signal frequency. Moreover, since for gain switching, the laser needs to be driven by a large sinusoidal RF signal, the laser bias needs to be optimised that the RF signal results in the laser being turned off for only a short period of time. This is to avoid coupling of more spontaneous emission noise to the laser output and to protect it from damage. Hence, the mentioned bias is chosen for the generation of an optimised OFC. The spectrum of the DFB laser is single moded and centred at 1550 nm as shown by the figure. A 6.25 GHz amplified sinusoidal signal is then applied to the DFB laser in conjunction with the DC bias which results in gain switching the device and generating the output shown in Figure 3.7(b). However, the generated output shows a clear broadening in the output of the laser and an absence of discernible OFC tones. The overlapping of the broadened modes prevents the side mode being distinguished from the main mode [23]. The broadening is due to two main reasons, firstly the large timing jitter induced in the pulses of gain

switched DFB laser [24]. This is related to the gain switching process explained in Section 2.3.4.1 in Chapter 2, Applying an amplified sinusoidal modulation to a laser causes the carrier concentration to increase rapidly. Once the carrier concentration reaches the threshold condition, the photon population also rises rapidly and depletes the carrier concentration. If the laser gain is cut off (alternate half cycle of the modulation sinusoid) is applied at the appropriate time, as the photon and electron densities are decreasing from their peak values, there would not be sufficient gain for the second oscillation peak to form. This results in the photon density decaying to zero leading to the creation of a short optical pulse. The increase in the injected current results in recovering the laser gain and formation of a successive pulse is formed. The process repeats resulting in a train of short optical pulses. The large timing jitter stems from the random delay in the build-up of successive pulses caused by the fluctuation in the photon density during the build-up of the optical pulse [25]. the fluctuation in photon density is caused by random spontaneous emission [26]. Secondly, the time variation of the carrier density in the active region of the device due to the direct modulation applied on the laser, resulting in the variation of the laser output signal wavelength which causes the broadening [25]. The absence of the discernible OFC tones is due to the absence of the pulse-to-pulse phase coherence, as the previous pulses do not seed the successive pulses [27]. External injection (EI) is then introduced to the setup as shown in Figure 3.7(c) where the output of a master tunable laser emitting at 1549.7 nm is injected into the cavity of the DFB slave laser through a circulator to injection lock it. Injection locking results in the generation of the OFC shown in Figure 3.7(d), where clear discrete OFC tones can be observed. With EI, the pulse-to-pulse phase coherence is established, as the EI from a master laser stabilises the phase of the slave laser thereby allowing for an OFC to be created [27]. Furthermore, EI leads to reduction in the timing jitter of the gain switched pulses. applying EI leads to a constant rate of photons much larger than the number of spontaneously emitted photons to be injected into the cavity. This leads to each pulse being built up from a constant number of photons each time, resulting in timing jitter reduction because of the constant delay between the creation of each pulse [27]. Moreover, EI results in the phase of the successive pulses to be locked to the master laser thus ensuring pulse-to-pulse phase coherence. Also, the master laser wavelength should be tuned in order to injection lock the higher power OFC tones (the ones that are near to the central emission wavelength of the OFC). An injection into the lower power OFC tones would result in not achieving a proper injection locking. This is due to the reason that the beating between the low power comb tones and the nearest modulated fields (due to gain switching) of the injected master being insufficient to lock the OFC [28]. The generated injection locked OFC exhibits 14 lines within 3-dB from the spectral peak (as indicated by the dotted lines) and an OCNR of ≈49 dB.

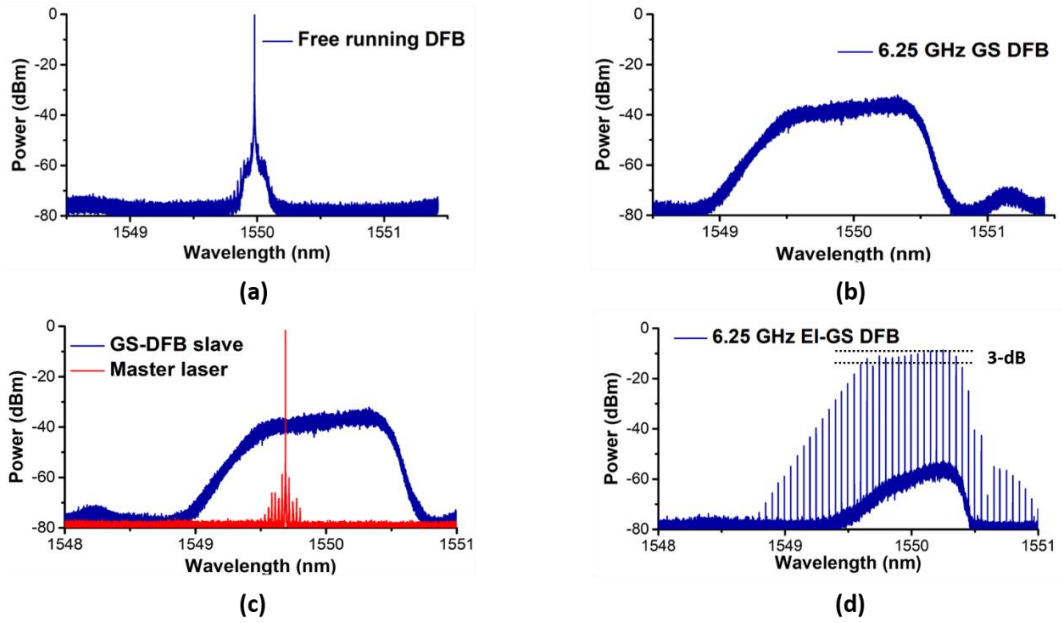

Figure 3.7: Optical spectrum of: (a) Free-running DFB laser, (b) Gain-switched DFB laser, (c) Master laser output emission with the gain-switched DFB laser, and (d) Externally injected gain-switched DFB laser.

OFCs based on gain-switched DFB lasers have shown the potential to be used in a wide variety of applications. In [29], the authors demonstrate a high stability 100 Gb/s multicarrier THz wireless transmission system based on an externally injected gain-switched DFB laser source. Another 25-Gb/s OFDM 60-GHz radio over fibre transmission system employing a gain-switched DFB laser for millimetre-wave generation is demonstrated [30]. The authors achieve a transmission performance below the 7% forward error correction (FEC) limit over 25 km of SMF. Moreover, gain-switched DFB based OFCs have shown the capability of achieving a 10 Gb/s all-optical 3R regeneration and format conversion as shown in [31] where the authors show the reamplification, retiming and reshaping of a poor-quality non-return to zero (NRZ) data signal at 10 Gb/s.

3.4 VCSEL devices

VCSELs were originally developed as a low-cost alternative to FP and DFB lasers [32]. The VCSELs are somehow different from the traditional edge-emitting lasers [33]. Unlike edge-emitting lasers, in which the light propagates in a direction along the axis of the laser waveguide and is emitted out at the edge, VCSELs emit coherent light in a direction perpendicular to the top plane of the semiconductor substrate [34].

3.4.1 VCSEL device structure and advantages

As a vertical short cavity laser, the VCSEL has a different physical structure than the traditional edge-emitting lasers. The VCSEL is formed by the surfaces of epitaxial layers and the optical output is taken from one of the mirror surfaces [35]. Compared to the average length of FP or DFB laser cavities (in the range of 300 µm), the VCSEL cavity is shorter (typically $\lambda/3$ of the emitted electromagnetic wave) [36]. The short cavity length limits the value of the gain that can be generated out of the active region.

Figure 3.8 shows a schematic diagram of a VCSEL structure, where the active region is sandwiched between two highly reflective mirrors formed of distributed Bragg reflectors (DBRs) [37]. The main purpose of the high reflectivity of the mirrors order is to allow the short and low gain cavity to achieve threshold [38]. It is important to note that the cavity emits only a single longitudinal mode, because of the short distance between the two mirrors inherited from the overall short length of the laser cavity.

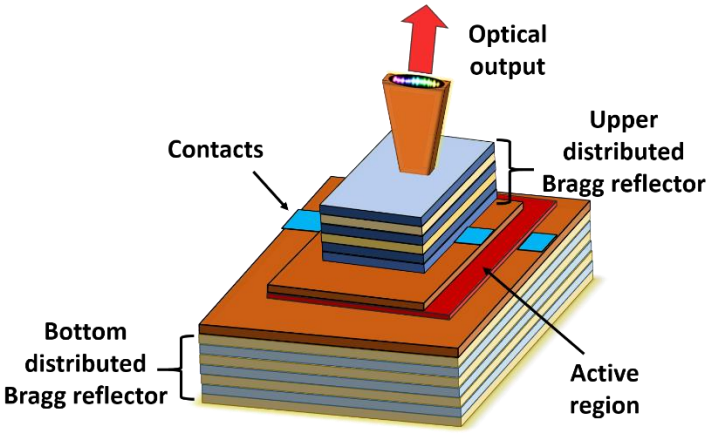

Figure 3.8: Schematic structure of a VCSEL device.

One of the major advantages of VCSELs is its lower overall cost of fabrication compared to the traditional edge-emitting lasers, due to its ease of fabrication and simpler packaging [39]. Furthermore, VCSELs offers the advantage of testing capability on the wafer itself before implementation into manufactured devices saving time and cost [40]. This is possible because of the special nature of VCSELs, where it emits from the top surface of the chip. In addition to that, ease of coupling into fibres and higher coupling efficiencies can be achieved with VCSELs, as the divergence angle of their output light beam is lower owing to the larger output apertures compared to the edge-emitting lasers [41].

Another major advantage is the relatively low threshold bias values of VCSELs compared to the typical threshold values of the edge-emitting lasers. This is mainly due to the high reflectivity of the mirrors [42]. Lower threshold values translate into lower power consumption, which is a very attractive

feature for next generation optical networks [43], especially with the current interest in greener optical networks [44]. In addition, the lower power consumption leads to a lower operational expenditure (OPEX).

The most common emission wavelength of VCSELs is in the range of 750–980 nm (often around 850 nm). However, longer wavelengths of 1300 nm - 1550 nm (most widely used for optical communications due to the absorption characteristics of the glass material used in fibres [45]) or even beyond 2000 nm can be obtained using devices based on Indium Phosphide (InAlGaAsP on InP) [46].

Different tuning mechanisms can be used to select a particular wavelength within the gain band of the active region. One of the most common techniques is through using a Bragg grating [47]. It is a temperature dependent structure, where the change in temperature would cause a change in the refractive index of the material. Hence, by varying the temperature, the transmission wavelength of the VCSEL can be tuned [48].

3.4.2 VCSEL static characterisation

In this work, characterisation of two different VCSEL devices that emit in the range of 1550 nm are presented. VCSEL devices emitting at that wavelength range are still at a relatively early development stage. However, they provide an attractive alternative to the traditional edge-emitting lasers due to the several advantages (mentioned above) they offer [49] [50].

The first VCSEL device to be characterised for generation of an OFC using the gain switching technique, is a VCSEL from VERTILAS that emits around the 1550 nm window. The device is custom packaged to have an integrated optical isolator that prevents backwards reflection to the cavity. Absence of backward reflections is beneficial for the stability of the device output. On the other hand, it prevents the implementation of external optical injection. Several attempts to inject the device with high optical power were carried out in vain as the isolation seemed to be as high as 50 dB. For ease of reference, the VERTILAS VCSEL will be hereinafter referred to as "VCSEL_1". VCSEL_1 L-I curve at 20 °C is shown in Figure 3.9(a) where the device exhibits a threshold current of around 6 mA. The corresponding output optical spectrum of VCSEL_1 where the device is biased at 12.5 mA and its temperature is kept constant at 20 °C is presented in Figure 3.9(b). It generates a single mode output with a central emission wavelength of 1548.75 nm.

The second device presented in this work is a VCSEL that also emits around the 1550 nm window. It is a single mode semiconductor laser supplied by VIS photonics. The laser does not have an integrated optical isolator which allows external optical injection. This device will be hereinafter referred to as "VCSEL_2".

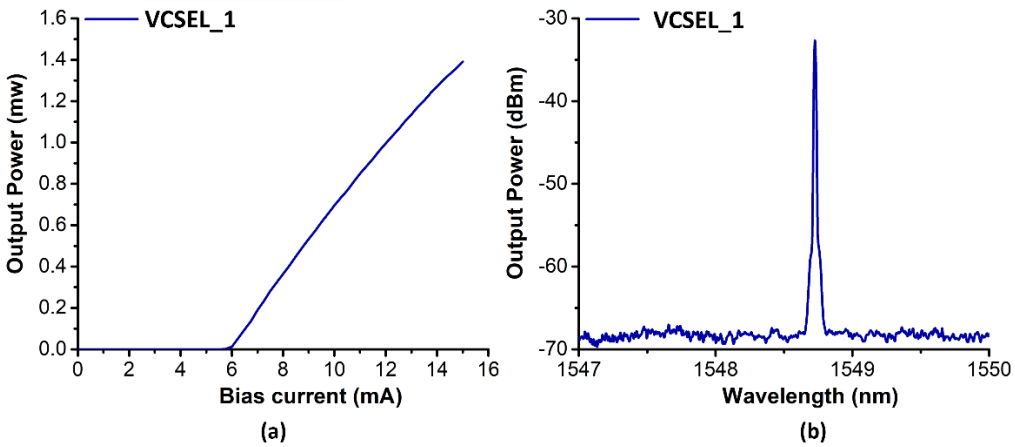

Figure 3.9: (a) L-I curve of VCSEL_1, (b) Optical spectrum of free-running VCSEL_1 biased at 12.5 mA.

VCSEL_2 has an RF connector which can be used to supply the laser with both the DC bias current and the RF modulation signal. On the other hand, the package does not have an integrated temperature controller. In order to tackle this, a specifically designed aluminium plate was used to mount the device, where a thermoelectric cooler (TEC) (the feedback loop is controlled in a PID configuration) and a thermistor is used underneath the laser package (as shown in Figure 3.10(a)). This is to ensure the stable operation of the device (minimise the temperature induced wavelength drift) and to limit the operating temperatures within its safety limits.

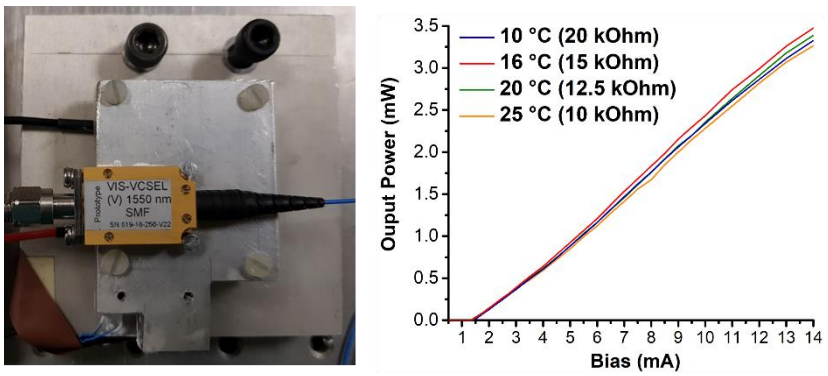

Figure 3.10: (a) Packaged VCSEL_2 device with a custom almunium mount, (b) L-I curve of VCSEL_2 at different values of temperature.

Figure 3.10(b) shows the L-I curve of VCSEL_2 recorded at different values of temperature (10°C, 16°C, 20°C, 25°C). The laser threshold is almost the same for the different temperature values and is equal to 1.35 mA. Although the value of the threshold does not change with varying the temperature, the L-I curve slope varies slightly, and the laser gives a slightly enhanced optical output power at a

temperature of ~16.1 °C. The threshold value of VCSEL_2 is much lower than that of VCSEL_1 indicating lower resonator losses and higher gain efficiency for this device [51].

Figure 3.11(a) & (b) show the output optical spectrum (resolution bandwidth: 312.5 MHz) of VCSEL_2 recorded for different values of bias currents and temperatures of 10°C and 25°C, respectively. From the figures, it can be observed that increasing the bias value results in a redshift in the emission wavelength of the VCSEL device. This is expected as in typical semiconductor lasers, the wavelength increases when the bias current increases [52]. Moreover, by observing both plots, it can be concluded that there is a blue shift of about 1.5 nm when decreasing the temperature of the laser package from 25 °C to 10 °C which corresponds to a typical blue shift of 0.1 nm for each 1 °C reduction. This again confirms the relationship between the temperature and the central emission wavelength (directly proportional) of a laser as discussed previously in the FP laser section.

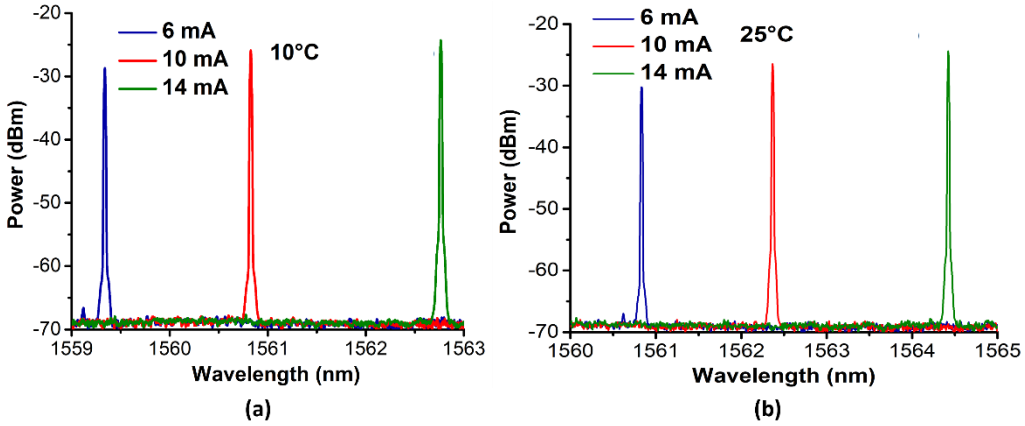

Figure 3.11: Optical output spectrum of VCSEL_2 at different bias values and at a temperature of: (a) 10 °C, and (b) 25 °C.

3.4.2.1 Linewidth characterisation

In the previous chapter, narrow optical linewidth of the generated tones was identified as a desired property of an optimised OFC. The linewidth is a critical parameter for VCSELs to be employed in next-generation coherent optical networks [53]. The phase noise of the laser results in a finite linewidth, hence the linewidth characterisation is an indication about the laser phase noise.

The delayed self-heterodyne (DSH) technique [54] with a resolution of 30 kHz is used to measure the linewidth values of the free running VCSEL_2 under different bias scenarios. The temperature of the VCSEL is kept constant at 20 °C throughout these measurements. The DSH setup diagram is shown in Figure 3.12 where the laser output signal is injected into a 50-50 coupler, which is used to split the signal into two different paths. The first half of the signal (top path) is sent through a phase modulator that is driven by a 2 GHz RF signal. The main purpose of this is to have all the signal components shifted

away from DC by 2 GHz. In the lower path, the second half of the signal passes through a 25 km standard single mode fibre which serves as a delay that decorrelates the two signals. Polarisation controllers are used in the two paths for matching the polarisation state of both signals. The two signals are then recombined using a 50-50 coupler in a single path and sent to a 20 GHz photodiode, where they beat together. The signal is offset at 2 GHz by the modulation in one arm. The RF (beat) signal is then observed using an electrical spectrum analyser (ESA), where it can be analysed to measure the value of the linewidth.

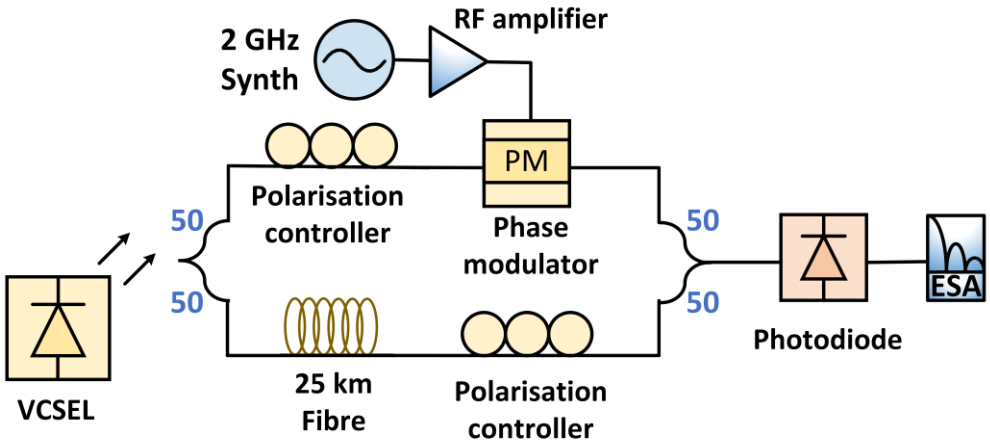

Figure 3.12: Setup diagram of the delayed self-hetrodyne technique for measuring the linewidth of a laser.

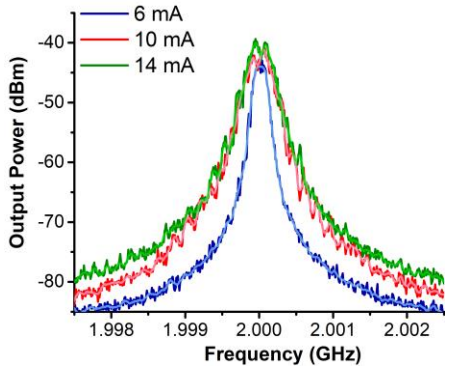

Bias	Measured Linewidth using Lorentzian fit
6 mA	86 kHz
10 mA	186 kHz
14 mA	157 kHz

Table 3.1: Linewidth values of VCSEL_2 at different bias values.

Figure 3.13: Electrical spectrum of measured linewidths of VCSEL_2 at 20°C for different bias values (6,10,14 mA).

Figure 3.13 shows the output electrical spectrum of the DSH setup when VCSEL_2 was used as the source under characterisation. Table 3.1 shows the measured 3-dB linewidth values at different bias current values of 6, 10, and 14 mA. The linewidth of the device gets narrower for lower bias values. This is contrary to theory [55] , as in semiconductor lasers, the linewidth should get narrower with higher bias values due to the increase in stimulated emission rate and the decrease in the frequency fluctuations caused by the spontaneous emission of the laser. This unexpected result is attributed to

the presence of reflections that are sent back to the laser cavity, causing instability in the emission of the laser [56]. This is one of the disadvantages of not having an optical isolator inside the laser package.

The 3-dB linewidth values shown in the table were measured using a Lorentzian fit on the generated spectrum and are found to be in the range of ~100-200 kHz. Same linewidth measurements were repeated at different values of temperatures where no remarkable change in the values obtained was noticed.

3.4.2.2 RIN characterisation

RIN is another important parameter of an optical transmitter. It quantifies the intensity fluctuations in the laser output signal [57], which in turn determines the potential of the device to be used in intensity modulated systems especially those employing multi-level intensity modulation formats such as PAM4/8 [58]. Typically, a low RIN (<-120 dB/Hz) is required.

Figure 3.14 shows the setup used for the RIN measurement. The optical output signal of the laser is passed through a variable optical attenuator (VOA) in order to control the power injected into a 20 GHz photodiode. The signal with both AC and DC components is then sent to a bias tee (through the RF+DC port). The DC signal is connected to a multimeter to measure the output voltage while the AC signal is amplified using an RF amplifier and sent to an ESA for capturing the spectrum of the intensity fluctuations.

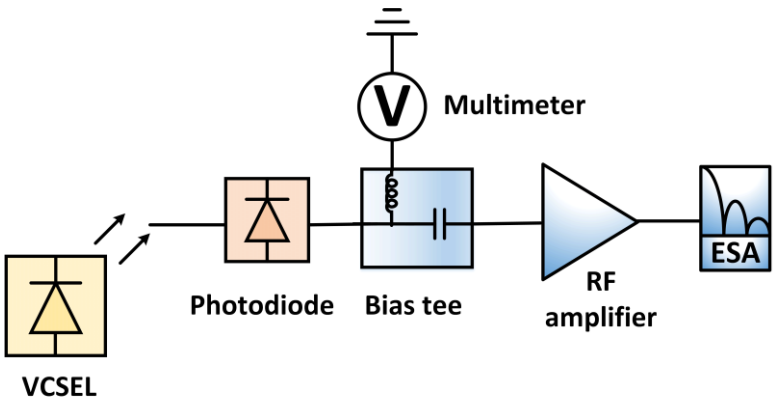

Figure 3.14: Schematic of the setup diagram used to measure RIN.

Offline processing is then used to compute the RIN values. The RIN value can be computed using both the AC spectrum obtained from the ESA and the voltage value obtained from the multimetre, using the equation below [59]:

$$RIN = \frac{\Delta P_E}{P_{EO}} \tag{3.3}$$

where ΔP_E is the overall noise of the laser (AC component) while P_{EO} is the average electrical power (DC component). ΔP_E can be computed using the following equation:

$$\Delta P_E = N_L - N_{th} - N_q \tag{3.4}$$

where N_L is the noise of the laser itself, N_{th} is the thermal noise of the photodiode, and N_q is the shot noise also of the photodiode. The thermal noise N_{th} can be measured using the ESA spectrum showing the fluctuations of different components in the setup diagram when there is no optical signal from the laser going into the setup. The shot noise N_q can be computed using the following equation:

$$N_q = 2 * q * I_{DC} * R_L \tag{3.5}$$

where q is the elementary charge, I_{DC} is the photocurrent at the load resistance R_L . This can be measured from the voltage value obtained from the multimetre.

Figure 3.15 shows the electrical spectrum of intensity fluctuation of VCSEL_1 biased at 12 mA and VCSEL_2 biased at the same bias values used in the linewidth measurements shown in Section 3.4.2.1. The measurements are taken at a constant laser temperature of 20°C. Table 3.2 shows the computed value of the averaged RIN (DC to 10 GHz) for all the cases.

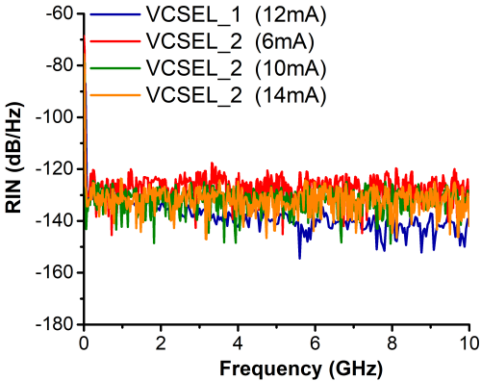

Figure 3.15: Electrical spectrum of measured VCSEL_1 and VCSEL_2 RIN.

Device	Bias	Averaged RIN (dB/Hz)
VCSEL_1	12 mA	-138.33
VCSEL_2	6 mA	-127.52
VCSEL_2	10 mA	-132.51
VCSEL_2	14mA	-132.278

Table 3.2: Averaged RIN values (DC-10GHz) of VCSEL_2 at different bias values.

For VCSEL_1, the obtained averaged RIN value is -138.33 dB/Hz, while for VCSEL_2, the obtained averaged RIN value is around the -130 dB/Hz range. Both VCSELs generate low enough RIN values. The same measurements were repeated for different values of laser temperatures, and there was no remarkable difference reported.

3.4.2.3 External optical injection

The next aspect of the VCSEL static characterisation is to study the external optical injection to the device with different cases of positive and negative detuning. The detuning is defined as the difference in frequency between the injection master laser and injected slave laser modes. The main aim is to

identify various locking regimes, and to show the effect of using injection at different detuning on the output of the laser. This part of the characterisation was conducted only with VCSEL_2 and not VCSEL_1 due to the presence of an isolator on the latter as discussed before.

A tunable master laser is used to inject light into VCSEL_2 via a 3-port circulator. A polarisation controller is placed on the injection path for aligning the polarisation of the master laser signal with that of the VCSEL.

Figure 3.16(a) shows the case of positive detuning. At a detuning of +10 GHz and +30 GHz, injection locking [60] is not achieved despite several attempts of polarisation optimisation and variation of injection power. While for +20 GHz detuning case, where the slave laser (VCSEL_2) central emission frequency is at 192.135 THz and the tunable master laser emission frequency is at 192.155 THz (marked by the green dotted line in Figure 3.16(a)), a single mode emission is achieved after very careful optimisation of the polarisation. This result does not follow typical behaviour as injection locking is likely to occur at a lower detuning (+10 GHz) where the master laser would have a stronger influence on the slave laser. Hence, a more detailed and thorough investigation was carried out by zooming (smaller span) into the optical spectrum. This led to the observation of multiple modes being emitted by the VCSEL contrary to the previous result in Figure 3.11. Hence, in the case of +20 GHz detuning, the master laser emission frequency actually coincides with the frequency of one of the weaker side modes of the slave (VCSEL). Injection locking of this particular mode causes it to draw all the gain and be more prominent than the main mode in the free running case. A confirmation of this case can also be seen from the figure, where the emission frequency of the injection-locked laser changes by approximately 21 GHz when injecting at this detuning value.

The case shown in Figure 3.16(b) indicates the negative detuning (master laser injection frequency is lower than that of the main mode of the slave) experiment. At a detuning of -10 GHz, the slave central emission frequency is at 192.135 THz and the master laser central emission frequency is at 192.125 THz (marked by dotted yellow line), injection locking is achieved. Although using the same value of detuning as before but with a different sign, the injection locked is achieved only for the negative detuning which can be attributed to the asymmetry of the locking range. This is due to the slave laser having to reduce its gain (or carrier number) to achieve a steady state that locks to the master laser. The nonzero linewidth enhancement factor α, which describes the amplitude phase coupling (i.e., phase change due to the change of carrier density dependent refractive index) leads to the cavity mode being red shifted (negative frequency detuning), which causes the asymmetry of the locking range [61]. For the two other cases of detuning (-20 GHz, -30 GHz), injection locking is not achieved

despite efforts of polarisation optimisation. This follows the same expected behaviour of the injection locking process as explained in the case of positive detuning.

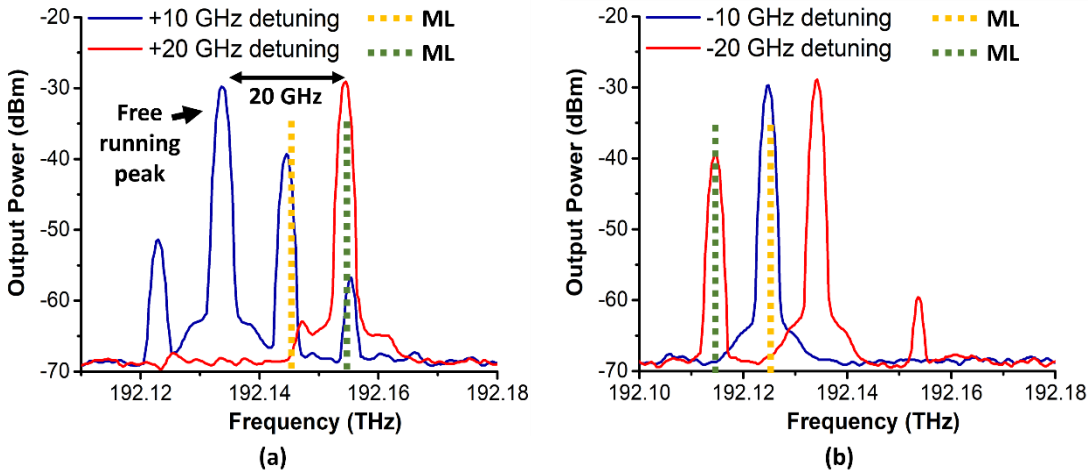

Figure 3.16: Optical spectrum of external injection of VCSEL_2 with : (a) +ve detuning values, (b) -ve detuning values. ML: master laser.

Linewidth and RIN measurements are conducted again to see the influence of injection locking on both parameters. The goal would be to achieve a transfer of the pure spectral characteristics from the master laser to the slave [62] [63].

Figure 3.17(a) shows the linewidth measurement conducted using the DSH technique for both the positive and negative detuning cases of injection locking. The injection locked slave laser shows a narrower linewidth (around 30 kHz for the negative detuning and 45 kHz for the positive detuning cases). The difference between the obtained values in this case can be considered within the measurement setup error tolerance. However, generally, the difference in linewidth between the positive and negative detunings cases can be attributed to the difference in phase noise transfer efficiency. The results show that the master tunable laser has transferred its better spectral characteristics to the slave laser, which confirms the importance of the injection locking and its capability to improve the transmitter performance resulting in a better performance of the whole system. It should also be mentioned that when OIL is achieved, the RF beat tone (from the DSH) is purer and does not show the repetitive ripples. All other measurements, with and without injection, exhibited ripples in the electrical spectrum of the RF beat tone. This behaviour can be attributed to the back reflections (shown in Figure 3.13).

RIN measurements for the injection locked cases are shown in Figure 3.17(b). Firstly, the averaged RIN value (DC to 10 GHz) of the master laser is measured to be -132.5 dB/Hz. This measurement was carried out at different emission wavelengths and at an output power of 5.5 dBm. The injection locked VCSEL biased at 6 mA shows an averaged RIN value of -132.49 dB/Hz. As previously mentioned in Section 3.4.2.2, free running VCSEL_2 has an averaged RIN value of -127.52 dB/Hz when biased at 6

mA. The decrease in the RIN value after applying injection suggests that the injection locked slave laser has inherited the RIN characteristics of the master laser.

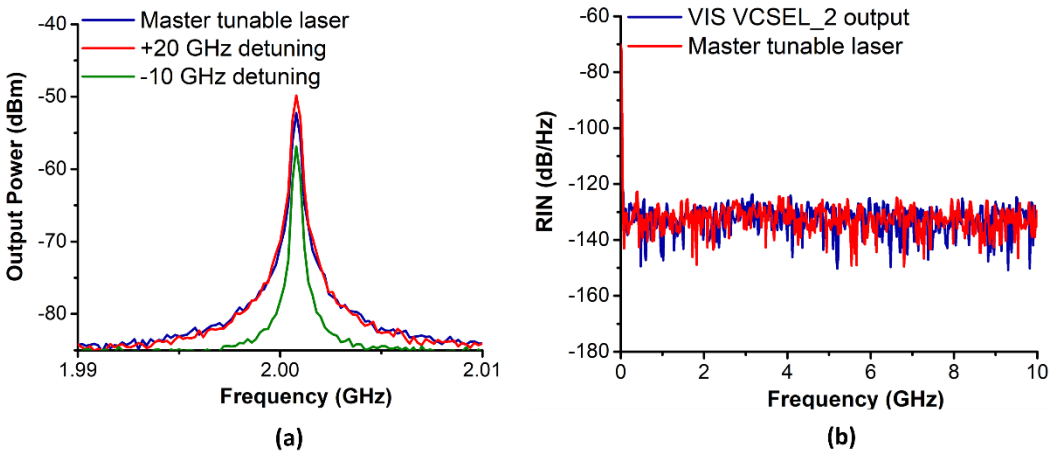

Figure 3.17: Electrical spectrum of (a) Measured linewidth of master laser and injection locked VCSEL_2 with different detunings, (b) RIN of master laser and injection locked VCSEL_2.

3.4.3 VCSEL dynamic characterisation

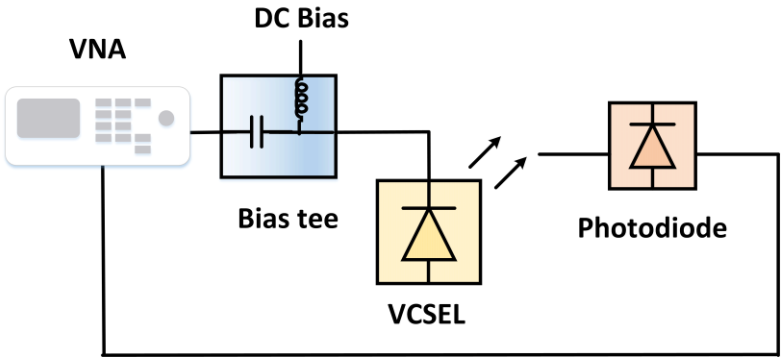

Figure 3.18: Setup diagram used for the frequency response measurement.

One of the main dynamic measurements to be conducted on a laser for it to be used as a directly modulated laser or be gain switched, is the frequency response measurement [64]. The setup diagram to measure frequency response of VCSEL device is shown in Figure 3.18.

A 50 GHz vector network analyser (VNA) is used to directly modulate the VCSEL with a small signal that sweeps from 0 to 10 GHz in conjunction with a DC bias via a bias tee through the RF connector attached to the device. The optical output of the laser is then detected by a high-speed photodiode of bandwidth 20 GHz. The electrical signal then directed back to the second port of the VNA, so that the S parameters (S_{21}) can be measured.

We start off by measuring the free running VCSEL_2 frequency response when it is biased at different current values.

Figure 3.19 and Table 3.3 show the dependence of the 3-dB MBW and the ROF peak power on the applied bias. The 3-dB MBW is enhanced with the bias increase. This follows the analytical analysis presented in [65] showing that the MBW is determined by the relaxation frequency and damping rate of laser oscillation and increases with the bias current. Moreover, there is no clear occurrence of ROF peaks. This can be attributed to the presence of back reflections that affects the emission of the laser as a result of absence of an optical isolator as explained before. Furthermore, the ROF frequency value and peak is directly related to the optical injection as shown in [66] and in this case, there is absence of optical injection. The next step is to study the effect of optical injection on the frequency response of VCSEL_2. This study is carried out by varying two different injection parameters (injection power and the detuning parameters). Two parameters of interest to extract from the frequency response curves in this case, are the laser 3- dB MBW and the ROF dependency on the injection parameters (power and detuning). For ease of representation, the bias scenarios and the obtained 3-dB MBW and ROF values will be presented in a table that will accompany the resultant plots.

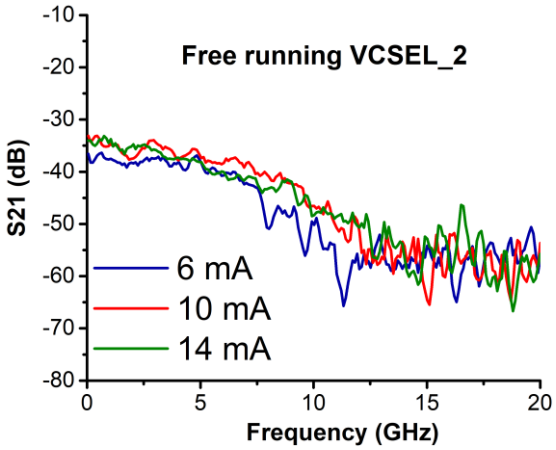

Figure 3.19: Measured small signal frequency response (S_{21}) of free running VCSEL_2 dc biased at 6,10 and 14 mA.

Slave bias	3-dB MBW
6 mA	5.33 GHz
10 mA	5.95 GHz
14 mA	6.23 GHz

Table 3.3: Measured 3-dB MBW for free running VCSEL_2 at bias currents of 6, 10, 14 mA.

Next step is to keep VCSEL_2 bias constant at 6 mA while varying the injection conditions as per Figure 3.20. Table 3.4 show the obtained 3-dB MBW and ROF peak values for the same bias and injection conditions. The blue plot in Figure 3.20 shows the frequency response of VCSEL_2 biased at 6 mA and without any optical injection applied to it. In this case, the laser shows a 3-dB MBW of 5.33 GHz, and it does not show a prominent ROF peak due to the reasons explained earlier in this section. After that, optical injection is applied to the device with an injection power of -3 dBm and detuning value of +2 GHz as shown in the red plot of Figure 3.20. The 3-dB MBW is enhanced to be 9.72 GHz in this case

(almost double the initial value in the case of no injection. Moreover, due to the presence of injection, there is a pronounced ROF peak at -19.86 dB. Next, the injection power in increased to be 1 dBm. The frequency response in this case is demonstrated by the green plot in Figure 3.20, where the 3-dB MBW is now enhanced to be 11.52 GHz. The results prove that an optimised external optical injection results in the enhancement of the frequency response of the laser extending its 3-dB MBW.

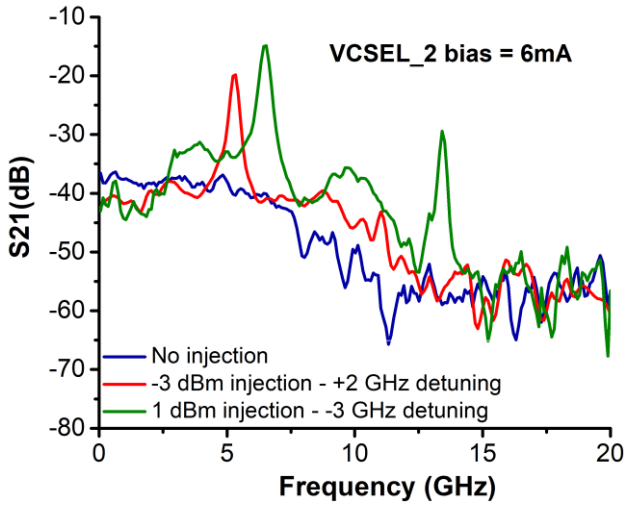

Figure 3.20: Measured small signal frequency response (S_{21}) of VCSEL_2 dc biased at 6mA using different injection powers and detuning.

Slave bias	Injection power	Detuning	3-dB MBW	ROF peak
6 mA	No Injection	-	5.33 GHz	-
6 mA	-3 dBm	+2 GHz	9.72 GHz	-19.86 dB
6 mA	1 dBm	-3 GHz	11.52 GHz	-14.35 dB

Table 3.4: Measured 3-dB MBW and ROF peak values for VCSEL_2 bias of 6mA, with different injection powers and detuning.

Furthermore, in this VCSEL_2 bias case, increasing the injection power from -3 dBm to 1 dBm also results in the enhancement of the 3-dB MBW by approximately 2 GHz. It is important to note that some of the more interesting injection conditions were chosen to be displayed and discussed here.

Next, VCSEL_2 DC bias was increased and sweep of a couple of injection conditions were examined in order to study the influence of VCSEL_2 DC bias on the measured frequency response curve. Figure 3.21 shows the small signal response of VCSEL_2 when it is DC biased at 10 mA for the free running case and for two different injection conditions.

A 5.95 GHz 3-dB MBW is obtained with no ROF peak. As explained earlier in this section, enhancement of the 3-dB MBW value is expected with increasing the laser bias. Next, a -3 dBm external injection is applied to the laser with a detuning of +2 GHz. This results in the enhancement of the 3-dB MBW to be 9.42 GHz as shown by the red plot in Figure 3.21 as a direct result of applying injection. This has been explained in detail in Chapter 2 in Section 2.3.4.3. The green plot in Figure 3.21 shows another

injection condition, where the injection power is increased to be 0 dBm and with a detuning of +3 GHz. In this case, a 3-dB MBW of 8.73 GHz is obtained with the presence of an ROF peak of -11.96 dB. The measured results show that both injection cases have resulted in the enhancement of the 3-dB MBW and occurrence of a pronounced ROF peak. However, in the case of VCSEL_2 biased at 10mA, the injection power is not directly proportional to the enhancement of the 3-dB MBW. This can be attributed to having a better injection locking conditions in terms of injection power and detuning for the first case (-3 dBm, +2 GHz) than the second case (0 dBm, +3 GHz) [67].

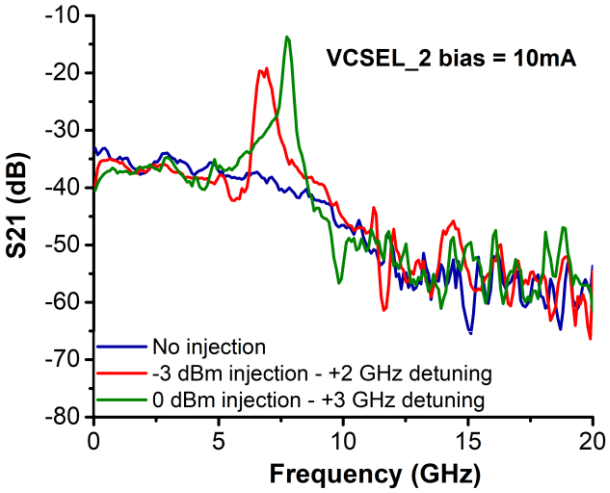

Figure 3.21: Measured small signal frequency response (S_{21}) of VCSEL_2 dc biased at 10mA using different injection powers and detuning.

Slave bias	Injection power	Detuning	3-dB MBW	ROF peak
10 mA	No injection	-	5.95 GHz	-
10 mA	-3 dBm	+2 GHz	9.42 GHz	-19.63 dB
10 mA	0 dBm	+3 GHz	8.73 GHz	-11.96 dB

Table 3.5: Measured 3-dB MBW and ROF peak values for VCSEL_2 bias of 10mA, with different injection powers and detuning.

The blue plot in Figure 3.21 shows the case where there is no injection applied to VCSEL_2. Again, the effect of varying VCSEL_2 bias on the MBW and ROF values is being examined. Figure 3.22 shows the small signal response of the VCSEL laser when the VCSEL bias is set to 14 mA.

The blue plot in the figures show the free running case, where the 3-dB MBW is measured to be 6.23 GHz. This value is higher than the free running case when the VCSEL_2 is biased at 6 mA and 10 mA. It is an expected behaviour as explained earlier in this section due to enhancement of relaxation frequency and damping rate of laser oscillation leading to an increase in the MBW. The red plot in Figure 3.22 shows the case when VCSEL_2 is injected with a -2 dBm signal and a detuning of -15 GHz. The 3-dB MBW slightly decrease compared to the free running case to be 5.83 Ghz. This decrease can be attributed to the non-achievement of the injection locking case using these particular values of

injection power and detuning. However, for the green plot where VCSEL_2 is injected by a higher power signal of 0 dBm and detuning of -18 GHz, the 3-dB MBW is enhanced to be 8.92 GHz. This enhancement is expected and following the same behaviour of the previously shown results.

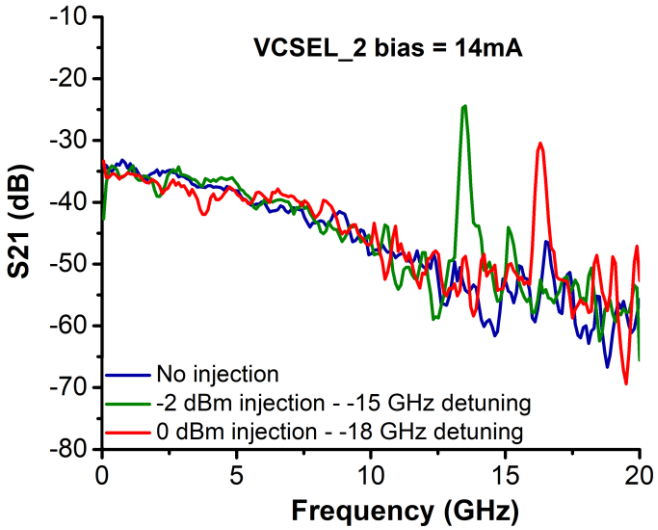

Figure 3.22: Measured small signal frequency response (S_{21}) of VCSEL_2 dc biased at 14mA using different injection powers and detuning.

Slave bias	Injection power	Detuning	3-dB MBW	ROF peak
14 mA	No injection	-	6.23 GHz	-
14 mA	-2 dBm	-15 GHz	5.83 GHz	-16.4 dB
14 mA	0 dBm	-18 GHz	8.92 GHz	-21.73 dB

Table 3.6: Measured 3-dB MBW and ROF peak values for VCSEL_2 bias of 14mA, with different injection powers and detuning.

Having shown the main highlights of the dynamic characterisation of VCSEL_2, several findings can be extracted from the obtained results. Firstly, following the typical behaviour of semiconductor lasers, increasing VCSEL_2 laser bias results in the enhancement of the 3-dB MBW. This follows the expected behaviour of semiconductor laser as explained in detail by the analytical analysis in [65]. Secondly, applying an external injection with optimised conditions (in terms of power and detuning) results in the enhancement of the 3-dB MBW of VCSEL_2. Several reports have shown the positive influence of an optimised optical injection on the enhancement of the MBW [68] [69]. Finally, the injection conditions have to be carefully optimised to achieve an injection locking case that results in the enhancement of the MBW. Otherwise, the injection (if not properly optimised in terms of power and detuning) can result in deterioration of the 3-dB MBW as shown by the first injection case in Figure 3.22 where the laser is injected by a -2 dBm signal and a detuning of -15 GHz, which results in a slight decrease of the laser MBW.

For gain switching, the laser bias, injection power and detuning should be adjusted in order to obtain a high ROF peak at the largest frequency possible. Biasing VCSEL_2 at 14 mA and injecting it with a -2

dBm signal and a detuning of -15 GHz results in the generation of an ROF peak at -16.4 dB and at a frequency of 13.46 GHz. The obtained results show that VCSEL_2 can be gain switched using this bias point and injection condition to generate an enhanced OFC. In the next sub-section, gain switching of both VCSEL devices will be presented for both cases of injection and without injection. Furthermore, the characterisation of the generated comb tones in terms of linewidth and RIN will be presented.

3.4.3.1 VCSEL Gain switching

As discussed before, the VCSEL is an attractive alternative to edge-emitting lasers when used as a gain switched OFC source. The main advantage is the low threshold values of VCSELs due to its short cavity. This typically results in a power saving in the gain switching process [70].

First, VCSEL_1 is gain-switched to generate an OFC. Optimisation of several parameters such as the VCSEL bias and temperature and the RF signal frequency and amplitude is carried out in order to enhance the generated OFC in terms of the number of comb tones generated and its spectral flatness.

Figure 3.23(a) & (b) show the output optical spectra of the generated OFC with two different FSRs of 7.5 and 10 GHz respectively. For the first case shown in Figure 3.23(a), the VCSEL is biased at 13.77 mA at a constant temperature of 20 °C. The RF signal used for direct modulation of the laser has an amplitude of 3.4 dBm and a frequency of 7.5 GHz. The generated OFC has 8 comb tones within a 3-dB spectral window (referenced from the peak) and an OCNR of ~25 dB. This OCNR value does not qualify the generated OFC for use in coherent optical communication networks employing WDM due to performance reach limitation [71].

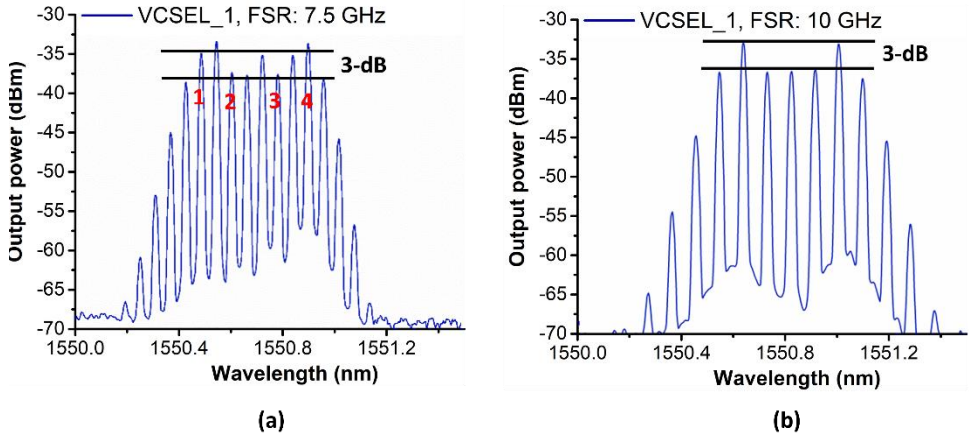

Figure 3.23: Optical spectrum of gain-switched VCSEL_1 at an FSR of: (a) 7.5 GHz, (b) 10 GHz.

Figure 3.23(b) shows the second case, where the VCSEL is biased at 12.81 mA (almost the double of its threshold) while keeping its temperature constant at 19 °C. The RF signal used for modulation has an amplitude of 8.4 dBm and a frequency of 10 GHz. It can be noticed that the total number of

generated comb tones has decreased. Moreover, the number of comb tones within the 3-dB window is now only 2. As shown in the previous section, the modulation bandwidth of the VCSEL is limited to 6 GHz in the free running case without applying injection. This limited MBW leads to decrease of the number of generated OFC tones with higher FSR values.

The generated OFC in Figure 3.23(a) is further characterised in terms of linewidth and RIN of the individual comb tones. The DSH technique is used for computing the linewidths of the tones. The same setup shown in Figure 3.12 is used, with the only addition of inserting a narrow optical band-pass filter (OBPF) at the input of the setup, which is used to filter the desired comb tone.

Figure 3.24 shows the Lorentzian fit of the obtained linewidth for 4 different OFC tones (taken at the middle and the two sides of the OFC and marked by the numbers in red font in Figure 3.23(a)). Each tone is filtered and sent through the DSH setup and detected using a 3 GHz ESA. Table 3.7 states the 3-dB linewidth measured values.

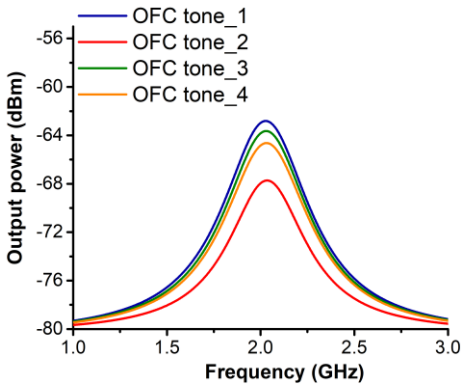

Comb tone	Estimated 3-dB linewidth
1	240 MHz
2	192 MHz
3	184 MHz
4	208 MHz

Table 3.7: Measured 3-dB linewidth values of filtered OFC tones of gain switched VCSEL_1.

Figure 3.24: Lorentzian fit of electrical spectrum of measured linewidth of filtered OFC tones of gain-switched VCSEL_1.

The generated comb tones have 3-dB linewidth varying from 184 to 240 MHz. The huge increase in the linewidth values can be related to the gain switching process. As previously explained in Section 3.3.3 in this chapter, the laser is forced to be switched off as a part of the gain switching process which leads to an increase in the phase noise due to the spontaneous emission being coupled into the main mode. Furthermore, at this case there is no external optical injection from a pure master laser. The presence of external optical injection would force the OFC tones to inherit the narrow linewidth [72]. The variation in the measured linewidth values can be related to the absence of the optical injection.

RIN is the next aspect of characterisation of the generated OFC tones. The main sources of RIN in lasers are the intrinsic optical phase and frequency fluctuations caused by spontaneous emission. RIN is characterised using the same setup shown in Figure 3.14, with the addition of OBPF which is used to filter out a single tone.

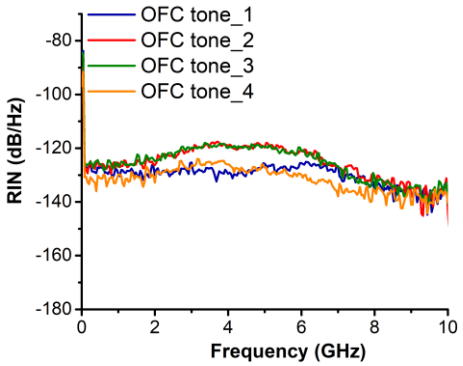

Comb tone	Averaged RIN (dB/Hz)
1	-134.839
2	-132.19
3	-134.552
4	-135.911

Table 3.8: Averaged RIN values (DC-10 GHz) of filtered OFC tones of gain switched VCSEL_1.

Figure 3.25: Electrical spectrum of measured RIN of filtered OFC tones of gain-switched VCSEL_1.

Figure 3.25 shows the generated RIN plots of the same OFC tones that were filtered out for the linewidth measurement. Table 3.8 states the measured averaged RIN values (DC-10 GHz) for the same. The averaged RIN values are approximately equal to -135 dB/Hz, which lies within the typical RIN values expected for semiconductor lasers. Although the OFC tones have a large linewidth, the relatively low RIN values make it an attractive multicarrier source. VCSEL_2 is also gain-switched to generate an OFC. In the case of this VCSEL, the positive impact of external optical injection on the characteristics of the generated OFC can be highlighted. Figure 3.4(a) shows the setup used for gain switching the externally injected VCSEL_2. It is important to note that an RF amplifier is not required here, unlike the case where a DFB or an FP is gain switched. This is due to the low threshold of the VCSEL, which results in a much lower power sinusoidal signal that is needed to gain switch the device.

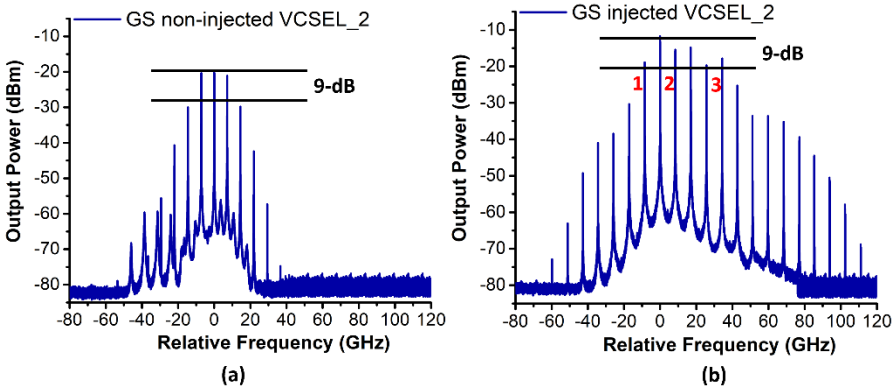

Figure 3.26: Optical spectrum of gain-switched VCSEL_2 : (a) Without injection, (b) With injection.

Several trials of directly modulating the VCSEL_2 device were carried out with different values of gain switching frequency and power, and injection power and detuning. This was done to obtain the optimum parameters for the generation of an enhanced OFC. Figure 3.26(a) shows the generated OFC without applying external injection. The RF modulating frequency is 6.25 GHz which is translated into a 6.25 GHz FSR based OFC. The generated OFC has only 3 tones, within a 9-dB spectral range (due to the reduced spectral flatness as a result of the limited MBW of the laser), each with an OCNR of ~40 dB. When applying external optical injection from a tunable master laser, the generated OFC spectrum

presented in Figure 3.26(b) now clearly shows an improvement in the number of OFC tones (6 tones, within a 9-dB spectral range) and an improvement of OCNR which is now ~55 dB. Furthermore, the generated OFC in case of injection has a much wider bandwidth than the non-injection case. These two plots confirm the enhancements that external optical injection can offer to the gain-switched OFC, as it can increase the number of comb tones generated due to the increase in the MBW as explained in detail in the dynamic characterisation of the device. The MBW is originally limited by the laser modulation bandwidth in case of gain switching without injection. Moreover, external optical injection enhances the bandwidth of the generated OFC. As previously shown in the various frequency response plots in Section 3.4.3, the external injection has a positive impact on enhancing the laser MBW. In this case, an injection power of 0 dBm was applied to the laser resulting in MBW enhancement, which clearly agrees with the previously presented frequency response curves.

The influence of the external injection on the characteristics of the generated OFC tones is then examined in terms of both the phase noise and the RIN. Even though linewidth measurement can give an indication about the phase noise, the measurement of FM-noise spectrum can give more detailed information about the different sources contributing to the phase noise. The phase noise measurement is conducted using a modified DSH method setup. Full details of the measurement can be obtained from [73]. The setup is similar to Figure 3.12, with the main difference being the use of a real-time scope (RTS) in place of the ESA. Offline DSP is done using the data obtained from the RTS to generate the frequency-modulated (FM) noise spectra shown below in Figure 3.27(a)&(b) which represents the frequency noise of the OFC tones. The 3-dB linewidth can be obtained from the same spectra.

The FM-noise spectrum of the master laser used to inject the VCSEL is shown in Figure 3.27(a). The latter is divided into 3 main parts which represents the three main regions of phase noise [74]. The first region is the 1/f region which can be considered as the flicker noise coming from active devices and electronics in the system due to the thermal noise at lower offsets. The second region is called the white noise region in which the noise is expected to be broad and flat. This region is important for studying the laser phase noise, as the 3-dB linewidth can be calculated from the average straight line in this region. These two kinds of noise cannot be avoided as they come from different sources in the system such as the laser diode under test, the measuring instrument (the RTS) and the different active components placed in the setup between the laser under test and the measuring instrument. The third part of the plot is referred to as high-frequency noise. It is also worth noting that the sharp cut-off of the plot at high frequencies is due to a digital filter implemented in the offline DSP code used for extracting the FM noise spectral plot. Figure 3.27(b) shows the comparison between the measured FM noise spectra for the master tunable laser, the injected comb tone, and the non-injected comb

tone. It is clear that the master tunable laser has a much lower phase noise than the non-injected comb tone. The tunable master laser should have good spectral characteristics so that it can pass it to the injected laser diode or comb tone when OIL takes place. This result is shown in the figure where the injected comb tone now has inherited the phase noise of the tunable master laser and is much lower than the initial noise value before injection.

As mentioned previously the 3-dB linewidth value can be extracted from the FM noise spectrum. It can be determined from the white noise region using the equation: $\Delta\nu = \pi(\frac{S_0}{2})$ where S_0 represents the averaged value of the white noise marked by the dotted line in Figure 3.27(a).

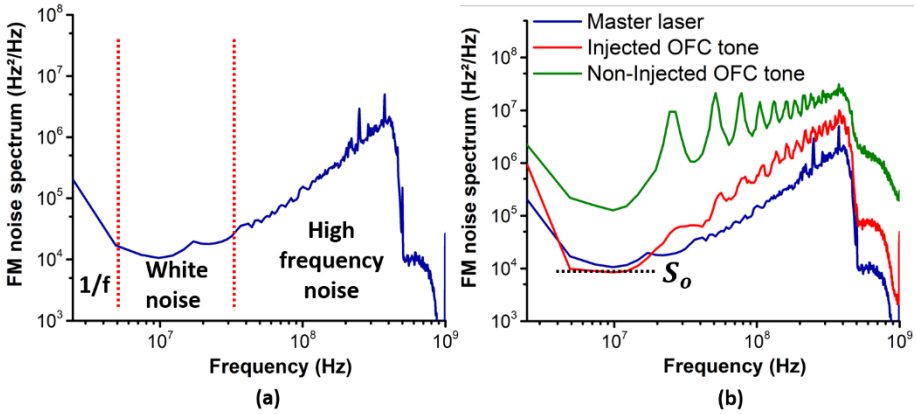

Figure 3.27: (a) FM noise spectrum different characterisation regions, (b) FM spectrum of the phase noise of master laser, injected and non -injected comb tones.

The measured 3-dB linewidths of the tunable master laser, non-injected comb tone, injected comb tone is ~15 kHz, ~234 kHz, ~14 kHz respectively. This result confirms the fact that the master laser has passed on its spectral properties to the injected comb tone.

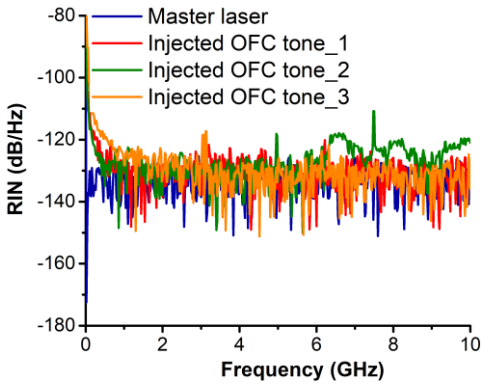

Figure 3.28: Electrical spectrum of measured RIN of master laser and three different filtered OFC tones.

For further characterisation of the generated comb tones, the RIN of three different OFC tones (centre and two sides of the OFC) is measured. RIN measurements were done using the same setup explained

previously in Section 3.4.2.2 in this chapter. Figure 3.28 shows the RIN measurements of the tunable master laser and three different injected comb tones.

The measured RIN values for the tunable master laser, and three different injected comb tones (1, 2 and 3) are -133.72 dB/Hz, -131.59 dB/Hz, -128.252 dB/Hz, -130.515 dB/Hz respectively. The results show that the injected comb tones have similar RIN values to the tunable master laser used for the injection, which also confirms that external optical injection has resulted in improving the RIN properties of the injected OFC through transferring the RIN characteristics of the master laser to the different comb tones.

3.4.4 VCSEL polarisation dynamics

One of the special characteristics of VCSELs is their ability to emit light at two different polarisations modes (X and Y). VCSELs are should ideally be single-longitudinal-mode devices and their output usually is divided into two linearly polarized modes with orthogonal polarisations [75]. Normally, the VCSELs are designed to minimise this polarisation duality by suppressing one of the polarisation modes to present a device with an SMSR of more than 30 dB. Hence, the device can be considered as a single mode one [76]. However, studies of polarisation dynamics of VCSELs under gain switching regime have shown that this dual mode property can be used to generate a wider span OFC. In [77], the authors show that the OFC generated using a gain switched VCSEL consists of two sub-combs with orthogonal polarisations, where the first OFC is generated from the main VCSEL mode, while the other is generated from the suppressed mode in the opposite polarisation. Moreover, it has been observed that these two orthogonally polarised combs are strongly phase correlated due to the gain switching process involving optical injection a master laser [77]. In another report [78], the authors make use of this property to demonstrate the generation of a wide bandwidth OFC of 70 GHz within a 10 dB spectral ripple (with reference to the spectral peak). The authors also show that the generated OFC tones possess a low single-sideband phase noise below -120.6 dBc/Hz at 10 kHz.

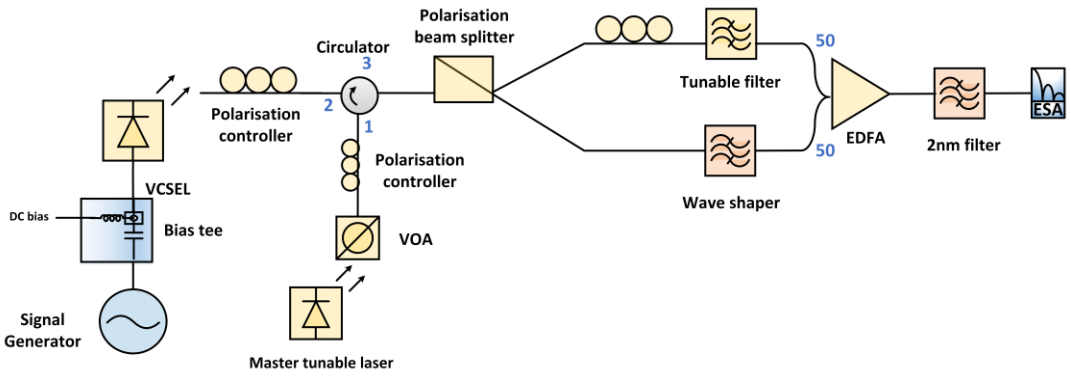

Figure 3.29: Setup diagram for examining the polarisation dynamics of VCSEL devices.

An experiment is conducted to characterise the polarisation dynamics of VCSEL_2 under the influence of gain switching and optical injection. The setup diagram used for this purpose is shown in Figure 3.29. VCSEL_2 is gain-switched using a sinusoidal signal at a frequency of 8.25 GHz and a power of 10 dBm in conjunction with a DC bias of 3 mA. Also, the device is externally injected using a master tunable laser source at 192.0099 THz and an injection power of 13 dBm.

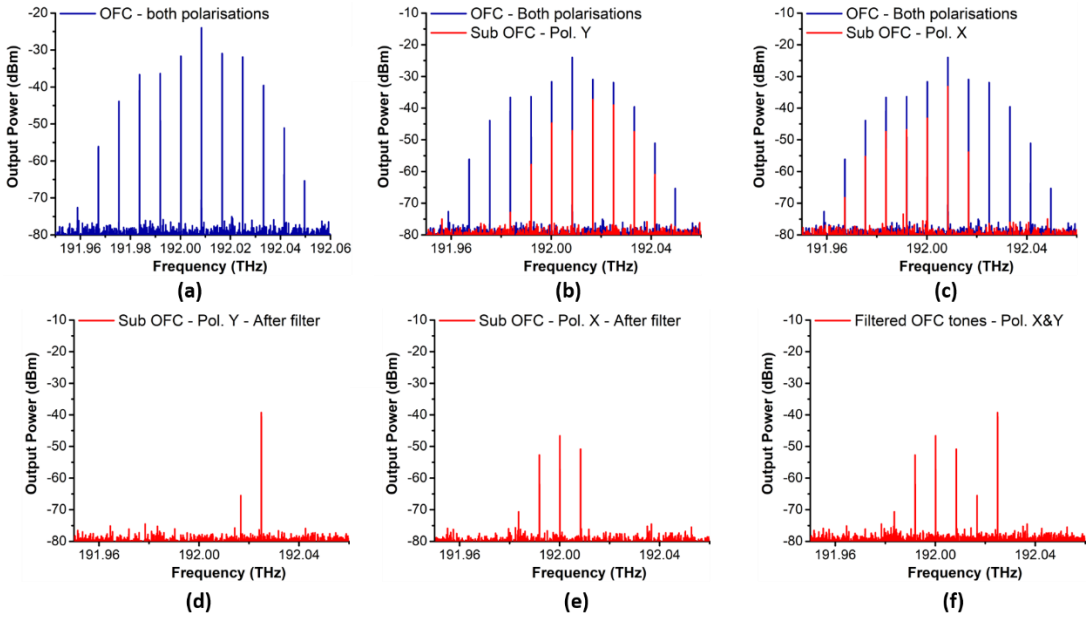

Figure 3.30: Optical spectrum of Gain swtiched VCSEL_2: (a) in both polarisation (Pol.) directions (X&Y), (b) In pol. Y, (c) In pol. X, (d) Filtered OFC tone of Pol. Y, (e) Filtered OFC tones of Pol. X , and (f) Combined filtered tones in both Pol. X & Y.

The generated OFC is shown in Figure 3.30(a). The generated OFC is then split into two OFCs in the two different polarisation directions using a polarisation splitter. Figure 3.30(b) shows the first sub-comb in polarisation Y, while Figure 3.30(c) shows the second sub-comb in polarisation X. This shows that the two sub-combs in both polarisations can be combined to form an expanded OFC simply by gain switching the VCSEL. A 6.25 GHz Yenista narrowband tunable optical filter is used in the top path to filter a single OFC tone out of the first sub-comb (polarisation Y) as shown in Figure 3.30(d). In the lower path, a reconfigurable wave shaper (WSS) is used to filter a single OFC tone out of the second sub-comb (polarisation X). It is important to note that due to the resolution limit of the WSS, it is not possible to filter just a single OFC tone. Instead, the lowest number of tones that could be filtered is three as shown in Figure 3.30(e). The filtered OFC tones from both paths are then combined as shown in Figure 3.30(f) and amplified using an EDFA. A 2 nm filter is then used to filter out the out of band ASE noise generated by the EDFA. The filtered output is then sent to a photodiode, where the different comb tones beat together. The RF output of the photodiode is then sent to an ESA for examination. As can be seen from Figure 3.30 (d)&(e), the frequency difference between the filtered OFC tones from the two sub-combs is approximately 24.75 GHz. The centre frequency of the ESA is set at the

same value. It is worth noting that in our case, it is not possible to combine tones from far sides of the two OFCs due to bandwidth limitations on the ESA.

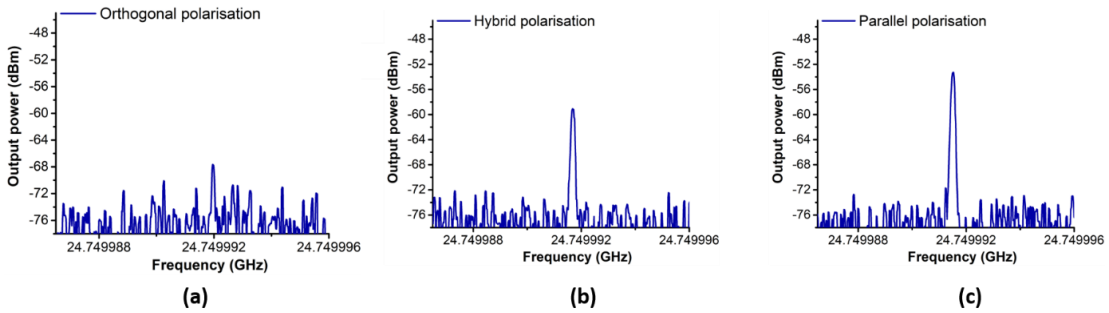

Figure 3.31: Electrical spectrum of the beat tone of filtered OFC tones in: (a) Orthognal Pol. case (b) Hybrid Pol. case, and (d) Parallel Pol. case.

Figure 3.31(a) shows the beat tone spectrum on the ESA, for the case when the two sub-combs are set to be orthogonal to each other. Hence, the filtered tones of the two sub-combs do not beat together to generate a beat tone as shown in the same figure. Figure 3.31(b) shows the case when the polarisation direction of a sub-comb is changed slightly using a polarisation controller placed in the top path. There is a slight beating between the filtered OFC tones, which results in the beat tone shown in the figure. A further variation of the polarisation direction of the top-path sub comb results in retaining a parallel polarisation between the two sub-combs, which in turn results in a relatively stronger beating of the filtered comb tones, to generate the beat tone shown in Figure 3.31(c). The results show that gain switching the VCSEL can generate two sub-combs in different polarisation states. Combining these two sub-combs would result in an expanded overall OFC. This OFC can find applications in various fields such as being employed in optical network using polarisation division multiplexing [79] and ultrafast laser dynamics [80].

3.5 Conclusions

Gain switching as a method of optical frequency comb generation has attracted a lot of attention recently due to its simplicity and the advantages it provides in terms of lower power consumption and cost. Compared to other generation techniques, gain switching can be used with any available traditional semiconductor laser source without any stringent or complicated requirements. Moreover, optical injection can be considered as a complementary part of the gain switching technique that further enhances the spectral characteristics of the generated OFC by transferring the better spectral characteristics from the purer master laser to the slave laser.

This chapter has started with the presentation of a gain switched FP at 6.25 GHz that generates an enhanced OFC that exhibits 15 OFC tones within 3-dB from the spectral peak and an OCNR of around

50 dB. The FP laser was characterised to optimise its operating parameters. Next, a DFB laser was characterised and had its operating parameters optimised to generate an enhanced OFC. The results show that with injection locking, the gain switched DFB at 6.25 GHz generates an OFC, which exhibits 14 lines within 3-dB from the spectral peak and an OCNR of ≈49 dB. A special focus was directed towards the characterisation of two different VCSEL devices for the generation of an OFC. VCSELs provide an attractive solution compared to edge emitting lasers in terms of cost efficiency, lower power consumption and simple manufacturing. Gain switching the first VCSEL device at 7.5 GHz while optimising its operating parameters results in the generation of an enhanced OFC of 8 tones within a 3-dB spectral window (referenced from the peak) and an OCNR of ≈25 dB. For the second VCSEL device, characterising the device (static and dynamic) in terms of linewidth, RIN and frequency response has resulted in obtaining the optimum operating parameters for generation of an enhanced OFC. Furthermore, injection has resulted in the generation of an OFC of 6 tones, within a 9-dB spectral range and also an OCNR of around 55 dB in place of an initial 3 tones with an OCNR of 40 dB. This clearly highlights the positive impact of optical injection in generating an enhanced OFC. Moreover, phase noise measurements of the filtered OFC tones have shown that they have inherited the superior phase noise characteristics of the purer master laser to possess a linewidth in the kHz range. Eventually, the polarisation dynamics of VCSEL_2 were characterised to show that the VCSEL emits at two different polarisation directions. The OFCs generated from gain switching the VCSEL results in the generation of two sub-combs, each in a different polarisation direction. The two sub-combs are then combined to generate an expanded overall OFC.

Further compactness and simplicity for gain-switched devices will be introduced in the next chapter, where a photonically integrated device consisting of two lasers to realise a master-slave configuration will be fully characterised for the generation of an OFC using the gain switching technique. Photonic integration provides a means for compact, lower power consumption and lower cost laser sources for next-generation optical networks.

References

[1] D. E. Dodds and M. J. Sieben, “Fabry—Perot Laser Diode Modeling,” *IEEE Photonics Technol. Lett.,* vol. 7, no. 3, pp. 254-256, 1995.

[2] J. Fu, Y. Xi, X. Li and W.-P. Huang, “Narrow Spectral Width FP Lasers for High-Speed Short-Reach Applications,” *Journal of Lightwave Technology,* vol. 34, no. 21, pp. 4898-4906, 2016.

[3] S. W. Corzine, R. S. Geels, J. W. Scott, R. H. Yan and L. A. Coldren, “Design of Fabry-Perot Surface-Emitting Lasers with a Periodic Gain Structure,” *EEE J. Quantum Electron.,* vol. 25, no. 6, pp. 1513-1524, 1989.

[4] C. Lin, C. Burrus and L. Coldren, “Characteristics of single-longitudinal-mode selection in short-coupled-cavity (SCC) injection lasers,” *Journal of Lightwave Technology,* vol. 2, no. 4, pp. 544-549, 1984.

[5] M. Al-Ghamdi, A. Bakry and M. Ahmed, “Inducing tunable single-mode operation of Fabry-Perot semiconductor laser coupled with very-short cavity with selective optical feedback,” *J. Eur. Opt. Soc.,* vol. 15, no. 22, 2019.

[6] C. Henry, “Theory of spontaneous emission noise in open resonators and its application to lasers and optical amplifiers,” *Journal of Lightwave Technology,* vol. 4, no. 3, pp. 288-297, 1986.

[7] M. J. Connelly, “Semiconductor Optical Amplifiers,” *Proc. IEEE,* vol. 80, no. 3, p. 308–316, 1992.

[8] J. M. Senior, Optical Fiber Communications: Principles and Practice, Pearson, 2008.

[9] H. Sun, “Laser Diode Basics,” in *Laser Diode Beam Basics, Manipulations and Characterizations*, Dordrecht, Netherlands, Springer, 2012, pp. 1-20.

[10] J. Pankove, “Temperature dependence of emission efficiency and lasing threshold in laser diodes,” *IEEE J. Quantum Electron.,* vol. 4, no. 4, pp. 119-122, 1968.

[11] S.-B. Xiang, X. Xiang and C.-G. Feng, “Effects of temperature on laser diode ignition,” *Optik,* vol. 120, no. 2, pp. 85-88, 2009.

[12] M. S. Mahdi, A. H. Ali, H. Alaa and M. H. Hussein, “Heat Effects on Data Transmission by Laser Diode and Light Emitted Diode for High Frequency Optical Communication Systems,” *J. Nanosci. Technol.,* vol. 2, no. 2, pp. 126-129, 2016.

[13] K. Iwashita and K. Nakagawa, “Suppression of Mode Partition Noise by Laser Diode Light Injection,” *IEEE Transactions on Microwave Theory and Techniques,* vol. 30, no. 10, pp. 1657-1662, 1982.

[14] P. M. Anandarajah, A. Kaszubowska-Anandarajah, R. Maher, K. Shi and L. P. Barry, "Characterization of wavelength tunable lasers for future optical communication systems," *J. Networks,* vol. 5, no. 2, pp. 152-157, 2010.

[15] M. Pascual, R. Zhou, F. Smyth, P. M. Anandarajah and L. P. Barry, "Software reconfigurable highly flexible gain switched optical frequency comb source," *Opt. Express,* vol. 23, pp. 23225-23235, 2015.

[16] J. Liu, Y. Lu, C. Guo, X. Hong, L. Xu and S. He, "Demonstration of Low-Cost Uplink Transmission in a Coherent OCDMA PON Using Gain-Switched Fabry–Pérot Lasers With External Injection," *IEEE Photonics Technology Letters,* vol. 22, no. 8, pp. 583-585, 2010.

[17] M. D. G. Pascual, R. Zhou, F. Smyth, T. Shao, P. M. Anandarajah and L. Barry, "Dual mode injection locking of a Fabry-Pérot laser for tunable broadband gain switched comb generation 2015 European Conference on Optical Communication (ECOC), 2," in *European Conference on Optical Communication (ECOC)*, Valencia, Spain, 2015.

[18] F. v. Dijk, B. Charbonnier, S. Constant, A. Enard, S. Fedderwitz, S. Formont, I. F. Lealman, F. Lecoche, F. Lelarge, D. Moodie, L. Ponnampalam, C. Renaud, M. J. Robertson, A. J. Seeds, A. Stöhr and M. Weiß, "Quantum dash mode-locked lasers for millimeter wave signal generation and transmission," in *23rd Annual Meeting of the IEEE Photonics Society*, Denver, CO, USA, 2010.

[19] W. Streifer, D. R. Scifres and R. D. Burnham, "Status of distributed feedback lasers," in *International Electron Devices Meeting*, Washington, DC, USA, 1976.

[20] K. Kojima, K. Kyuma and T. Nakayama, "Analysis of the spectral linewidth of distributed feedback laser diodes," *Journal of Lightwave Technology ,* vol. 3, no. 5, pp. 1048 - 1055, 1985.

[21] C. Wang, K. Schires, M. Osiński, P. J. Poole and F. Grillot, "Thermally insensitive determination of the linewidth broadening factor in nanostructured semiconductor lasers using optical injection locking," *Scientific Reports,* vol. 6, no. 27825, 2016.

[22] G. E. Shtengel, D. A. Ackerman, P. A. Morton, E. J. Flynn and M. S. Hybertsen, "Impedance-corrected carrier lifetime measurements in semiconductor lasers," *Applied Physics Letters,* vol. 67, no. 11, p. 1506, 1995.

[23] P. M. Anandarajah, C. Guignard, A. Clarke, D. Reid, M. Rensing, L. P. Barry, G. Edvell and J. D. Harvey, "Optimized Pulse Source Employing an Externally Injected Gain-Switched Laser Diode in Conjunction With a Nonlinearly Chirped Grating," *IEEE JOURNAL OF SELECTED TOPICS IN QUANTUM ELECTRONICS ,* vol. 12, no. 2, 2006.

[24] P. M. Anandarajah, K. Shi, J. O'Carroll, A. Kaszubowska, R. Phelan, L. P. Barry, A. D. Ellis, P. Perry, D. Reid, B. Kelly and J. O'Gorman, "Phase shift keyed systems based on a gain switched laser transmitter," *Optics Express,* vol. 17, no. 15, pp. 12668-12677, 2009.

[25] P. M. Anandarajah, S. P. Ó. Dúill, R. Zhou and L. P. Barry, "Enhanced Optical Comb Generation by Gain-Switching a Single-Mode Semiconductor Laser Close to Its Relaxation Oscillation

Frequency," *IEEE Journal of Selected Topics in Quantum Electronics,* vol. 21, no. 6, pp. 592-600, 2015.

[26] M. Jinno, "Correlated and uncorrelated timing jitter in gain-switched laser," *IEEE Photonics Technology Letters,* vol. 5, no. 10, pp. 1140-1143, 1993.

[27] S. P. Ó. Dúill, R. Zhou, P. M. Anandarajah and L. P. Barry, "Analytical Approach to Assess the Impact of Pulse-to-Pulse Phase Coherence of Optical Frequency Combs," *IEEE Journal of Quantum Electronics,* vol. 51, no. 11, pp. 1-8, 2015.

[28] S. P. Ó. Dúill, P. M. Anandarajah, R. Zhou and L. P. Barry, "Numerical investigation into the injection-locking phenomena of gain switched lasers for optical frequency comb generation," *Appl. Phys. Lett.,* vol. 106, no. 211105, 2015.

[29] H. Shams, T. Shao, M. J. Fice, P. M. Anandarajah, C. C. Renaud, F. V. Dijk, L. P. Barry and A. J. Seeds, "100 Gb/s Multicarrier THz Wireless Transmission System With High Frequency Stability Based on A Gain-Switched Laser Comb Source," *IEEE Photonics Journal,* vol. 7, no. 3, pp. 1-11, 2015.

[30] E. P. Martin, T. Shao, V. Vujicic, P. M. Anandarajah, C. Browning, R. Llorente and L. P. Barry, "25-Gb/s OFDM 60-GHz Radio Over Fiber System Based on a Gain Switched Laser," *Journal of Lightwave Technology,* vol. 33, no. 8, pp. 1635-1643, 2015.

[31] M. Owen, V. Saxena, R. V. Penty and I. H. White, "10-Gbits/s all-optical 3R regeneration and format conversion using a gain-switched DFB laser," in *Conference on Lasers and Electro-Optics (CLEO)*, San Francisco, CA, USA, 2000.

[32] L. A. Coldren, S. W. Corzine and M. L. Mašanović, Diode Lasers and Photonic Integrated Circuits, Second Edition, John Wiley & Sons, 2012.

[33] K. D. Croquette and H. Q. Hou, "Vertical-cavity surface emitting lasers: Moving from research to manufacturing," *Proceedings of the IEEE,* vol. 85, no. 11, p. 1730–1739, 1997.

[34] M.-C. Amann, "VCSEL structures and applications," in *IEEE/LEOS Winter Topicals Meeting Series*, Innsbruck, Austria, 2009.

[35] S. F. Yu, Analysis and Design of Vertical Cavity Surface Emitting Lasers, John Wiley & Sons, 2003.

[36] M. C. Amann, E. Wong and M. Mueller, "Energy-efficient high-speed short-cavity VCSELs," in *OFC/NFOEC*, Los Angeles, CA, USA, 2012.

[37] R. Jambunathan and J. Singh, "Design studies for distributed Bragg reflectors for short-cavity edge-emitting lasers," *IEEE Journal of Quantum Electronics,* vol. 33, no. 7, pp. 1180-1189, 1997.

[38] S. Murtaza, K. Anselm, A. Srinivasan, B. Streetman, J. Campbell, J. Bean and L. Peticolas, "High-reflectivity Bragg mirrors for optoelectronic applications," *IEEE Journal of Quantum Electronics,* vol. 31, no. 10, pp. 1819 - 1825, 1995.

[39] J. Jewell, J. Harbison, A. Scherer, Y. Lee and L. Florez, “Vertical-cavity surface-emitting lasers: Design, growth, fabrication, characterization,” *IEEE Journal of Quantum Electronics,* vol. 27, no. 6, pp. 1332 - 1346, 1991.

[40] F. Koyama, “Recent Advances of VCSEL Photonics,” *Journal of Lightwave Technology,* vol. 24, no. 12, pp. 4502 - 4513, 2006.

[41] J. Heinrich, E. Zeeb and K. J. Ebeling, “Butt-coupling efficiency of VCSEL’s into multimode fibers,” *IEEE Photonics Technol. Lett.,* vol. 9, no. 12, p. 1555–1557, 1997.

[42] K. Iga, “Surface-Emitting Laser—Its Birth and Generation of New Optoelectronics Field,” *IEEE Journal of Selected Topics in Quantum Electronics,* vol. 6, no. 6, pp. 1201 - 1215, 2000.

[43] J. Baliga, R. Ayre, K. Hinton, W. V. Sorin and R. S. Tucker, “Energy Consumption in Optical IP Networks,” *Journal of Lightwave Technology,* vol. 27, no. 13, pp. 2391-2403, 2009.

[44] R. S. Tucker, “Green optical communications—part I: Energy limitations in transport,” *IEEE J. Sel. Topics Quantum Electron.,* vol. 17, no. 2, p. 245–260, 2011.

[45] V. D. Silva, Y. Liu, A. Antos, G. Berkey and M. Newhouse, “Comparison of nonlinear coefficient of optical fibers at 1550 nm,” in *Optical Fiber Communications, OFC.*, San Jose, CA, USA, 1996.

[46] J.Pozo and E.Beletkaia, “VCSEL Technology in the Data Communication Industry,” *Photonics Views,* vol. 16, no. 6, pp. 21-23, 2019.

[47] T. Mizunami, T. Hamada and T. Yamamoto, “External-fiber-grating vertical-cavity surface-emitting lasers,” *IEEE Photonics Technology Letters,* vol. 12, no. 11, pp. 1558 - 1560, 2000.

[48] C. Chang-Hasnain, “Tunable VCSEL,” *IEEE Journal of Selected Topics in Quantum Electronics,* vol. 6, no. 6, pp. 978 - 987, 2000.

[49] T. N. Huynh, V. Vujicic, M. D. G. Pascual, P. M. Anandarajah and L. P. Barry, “Digital coherent communications with a 1550 nm VCSEL,” in *Optical Fiber Communications Conference and Exhibition (OFC)*, Los Angeles, CA, USA, 2015.

[50] R. Rodes, M. Mueller, B. Li, J. Estaran, J. B. Jensen, T. Gruendl, M. Ortsiefer, C. Neumeyr, J. Rosskopf, K. J. Larsen, M.-C. Amann and I. T. Monroy, “High-Speed 1550 nm VCSEL Data Transmission Link Employing 25 GBd 4-PAM Modulation and Hard Decision Forward Error Correction,” *Journal of Lightwave Technology ,* vol. 31, no. 4, pp. 689 - 695, 2013.

[51] Z. Toffano, “Investigation of threshold transition in semiconductor lasers,” *IEEE Journal of Selected Topics in Quantum Electronics,* vol. 3, no. 2, pp. 485 - 490, 1997.

[52] M. Funabashi, H. Nasu, T. Mukaihara, T. Kimoto, T. Shinagawa, T. Kise, K. Takaki, T. Takagi, M. Oike, T. Nomura and A. Kasukawa, “Recent advances in DFB lasers for ultradense WDM applications,” *IEEE Journal of Selected Topics in Quantum Electronics,* vol. 10, no. 2, pp. 312 - 320, 2004.

[53] R.-J. Essiambre, G. Kramer, P. J. Winzer, G. J. Foschini and B. Goebel, “Capacity Limits of Optical Fiber Networks,” *Journal of Lightwave Technology,* vol. 28, no. 4, pp. 662 - 701, 2010.

[54] L. Richter, H. Mandelberg, M. Kruger and P. McGrath, “Linewidth determination from self-heterodyne measurements with subcoherence delay times,” *IEEE Journal of Quantum Electronics,* vol. 22, no. 11, pp. 2070-2074, 1986.

[55] K. Kikuchi and H. Tomofuji, “Analysis of linewidth of separated-electrode DFB laser diode,” *Electron. Lett.,* vol. 25, no. 14, p. 6–8, 1989.

[56] K. Stubkjaer and M. Small, “Noise Properties of Semiconductor Lasers Due to Optical Feedback,” *IEEE J. Quantum Electron.,* vol. 20, no. 5, p. 472–478, 1984.

[57] R. Pillai, E. Garmire and P. Menendez-Valdes, “Relative intensity noise of laser-diode arrays,” *IEEE Photonics Technology Letters,* vol. 3, no. 11, pp. 968 - 970, 1991.

[58] V. Vujicic, A. P. Anthur, A. Saljoghei, V. Panapakkam, R. Zhou, Q. Gaimard, K. Merghem, F. Lelarge, A. Ramdane and L. P. Barry, “Mitigation of relative intensity noise of quantum dash mode-locked lasers for PAM4 based optical interconnects using encoding techniques,” *Optics Express,* vol. 25, pp. 20-29, 2017.

[59] E. Photonics, “Relative Intensity Noise of Distributed Feedback Lasers, Application note,” [Online]. Available: https://www.eagleyard.com/fileadmin/downloads/documents/eyP_App_Note_RIN__1-6.pdf. [Accessed 22 September 2019].

[60] C. Buczek, R. Freiberg and M. Skolnick, “Laser injection locking,” *Proceedings of the IEEE ,* vol. 61, no. 10, pp. 1411 - 1431, 1973.

[61] Z. Liu and R. Slavík, “Optical Injection Locking: From Principle to Applications,” *Journal of Lightwave Technology,* vol. 38, no. 1, pp. 43-59, 2020.

[62] L. Chrostowski, C.-H. Chang and C. Chang-Hasnain, “Reduction of relative intensity noise and improvement of spur-free dynamic range of an injection locked VCSEL,” in *Annual Meeting of the IEEE Lasers and Electro-Optics Society(LEOS)*, Tucson, AZ, USA, 2003.

[63] W. Ma, B. Xiong, C. Sun, X. Ke, J. Wang, Z. Hao, L. Wang, Y. Han, H. Li, J. Yu and Y. Luo, “Linewidth Narrowing of Mutually Injection Locked Semiconductor Lasers with Short and Long Delay,” *Applied Sciences,* vol. 9, no. 7, p. 1436, 2019.

[64] E. K. Lau, H. K. Sung and M. C. Wu, “Frequency response enhancement of optical iniection-locked lasers,” *IEEE J. Quantum Electron.,* vol. 44, no. 1, pp. 90-99, 2008.

[65] M. Ahmed and A. El-Lafi, “Analysis of small-signal intensity modulation of semiconductor lasers taking account of gain suppression,” *Journal of Physics - Pramana,* vol. 71, no. 1, 2008.

[66] Y. Hong and K. A. Shore, “Relaxation Oscillation Frequency Properties in Injection-Locked Semiconductor Lasers,” in *Advanced Semiconductor Lasers and Their Applications*, Santa Barbara, California United States, 1999.

[67] J. Wang, M. Haldar, L. Li and F. Mendis, “Enhancement of modulation bandwidth of laser diodes by injection locking,” *IEEE Photonics Technology Letters ,* vol. 8, no. 1, pp. 34-36, 1996.

[68] M. I. Memon, B. Li, G. Mezosi, Z. Wang, M. Sorel and S. Yu, “Modulation Bandwidth Enhancement in Optical Injection-Locked Semiconductor Ring Laser,” *IEEE Photonics Technology Letters,* vol. 21, no. 24, pp. 1792-1794, 2009.

[69] T. Simpson and J. Liu, “Enhanced modulation bandwidth in injection-locked semiconductor lasers,” *IEEE Photonics Technology Letters ,* vol. 9, no. 10, pp. 1322-1324, 1997.

[70] E. Prior, C. d. Dios, Á. R. Criado, M. Ortsiefer, P. Meissner and P. Acedo, “Expansion of VCSEL-Based Optical Frequency Combs in the Sub-THz Span: Comparison of Non-Linear Techniques,” *Journal of Lightwave Technology,* vol. 34, no. 17, pp. 4135 - 4142, 2016.

[71] P. Marin-Palomo, J. N. Kemal, T. J. Kippenberg, W. Freude, S. Randel and C. Koos, “Performance of chip-scale optical frequency comb generators in coherent WDM communications,” *Optics Express,* vol. 28, no. 9, pp. 12897-12910, 2020.

[72] P. Gallion, H. Nakajima, G. Debarge and C. Chabran, “Contribution of spontaneous emission to the linewidth of an injection-locked semiconductor laser,” *Electronics Letters ,* vol. 21, no. 14, p. 626 – 628, 1985.

[73] T. N. Huynh, L. Nguyen and L. P. Barry, “Delayed Self-Heterodyne Phase Noise Measurements With Coherent Phase Modulation Detection,” *IEEE Photonics Technology Letters,* vol. 24, no. 4, pp. 249 - 251, 2012.

[74] K. Technologies, “Understanding Phase Noise Needs and Choices in Signal Generation,” [Online]. Available: https://www.keysight.com/ie/en/assets/7018-03790/application-notes/5991-1744.pdf. [Accessed September 2018].

[75] J. Danckaert, B. Nagler, J. Albert, K. Panajotov, I. Veretennicoff and T. Erneux, “Minimal rate equations describing polarization switching in vertical-cavity surface-emitting lasers,” *Optics Communications,* vol. 201, no. 1-3, pp. Pages 129-137, 2002.

[76] E. Prior, C. D. Dios, M. Ortsiefer, P. Meissner and P. Acedo, “Understanding VCSEL-Based Gain Switching Optical Frequency Combs: Experimental Study of Polarization Dynamics,” *Journal of Lightwave Technology,* vol. 33, no. 22, pp. 4572-4579, 2015.

[77] E. Prior, C. d. Dios, R. Criado, M. Ortsiefer, P. Meissner and P. Acedo, “Dynamics of dual-polarization VCSEL-based optical frequency combs under optical injection locking,” *Optics Express,* vol. 41, pp. 4083-4086, 2016.

[78] H. Ren, L. F. N. Liu, Z. Wu and G. Xia, “Generation of Broadband Optical Frequency Comb Based on a Gain-Switching 1550 nm Vertical-Cavity Surface-Emitting Laser under Optical Injection,” *Photonics,* vol. 7, no. 4, 2020.

[79] A. D. Shiner, M. Reimer, A. Borowiec, S. O. Gharan, J. Gaudette, P. Mehta, D. Charlton, K. Roberts and M. O’Sullivan, “Demonstration of an 8-dimensional modulation format with reduced inter-channel nonlinearities in a polarization multiplexed coherent system,” *Optics Express,* vol. 22, no. 17, pp. 20366-20374, 2014.

[80] M. Brunel, J. Thévenin and M. Vallet, “Dual-polarization frequency comb from a diode-pumped solid-state laser,” in *CLEO*, San Jose, CA, USA, 2013.

[81] K. Kojima and K. Kyuma, “Analysis of the spectral linewidth of distributed feedback laser diodes,” *Electron. Lett.,* vol. 20, no. 21, p. 869, 2007.

[82] S. Saito, 0. Nilsson and Y. Yamamoto, “Oscillation center frequency tuning, quantum FM noise, and direct frequency modulation characteristics in external grating loaded semiconductor lasers,” *EEE J. Quantum Electron.,* vol. 18, no. 6, pp. 961-970, 1982.

[83] P. Qiao, K. T. Cook, K. Li and C. J. Chang-Hasnain, “Wavelength-Swept VCSELs,” *IEEE Journal of Selected Topics in Quantum Electronics,* vol. 23, no. 6, pp. 1-16, 2017.

[84] M. Sakib, B. Hraimel, X. Zhang, K. Wu, T. Liu, T. Xu and Q. Nie, “Impact of Laser Relative Intensity Noise on a Multiband OFDM Ultrawideband Wireless Signal Over Fiber System,” *IEEE/OSA Journal of Optical Communications and Networking,* vol. 2, no. 10, pp. 841 - 847, 2010.

[85] W. Streifer, D. Scifres and R. Burnham, “Coupling coefficients for distributed feedback single- and double-heterostructure diode lasers,” *IEEE Journal of Quantum Electronics,* vol. 11, no. 11, pp. 867-873, 1975.

[86] K. Iwatsuki, K. Hotate and M. Higashiguchi, “Effect of Rayleigh backscattering in an optical passive ring-resonator gyro,” *Applied Optics,* vol. 23, no. 21, pp. 3916-3924, 1984.

[87] P. Marin-Palomo, J. N. Kemal, W. Freude, S. Randel and C. Koos, “OSNR limitations of chip-based optical frequency comb sources for WDM coherent communications,” *arXiv,* vol. 1907.01042, 2019.

Chapter 4

Photonic integrated devices for generation of optical frequency combs

4.1 Introduction

The introduction of several bandwidth-hungry applications such as high-definition video streaming, real-time online gaming and cloud services has resulted in an ever-increasing demand for higher speed optical networks [1]. Advancements in the optical networks should include the different segments of the networks, which includes the core, metro, and the short-reach (access and data centre) networks [2]. Hence, the development of such high-capacity optical networks needs to be realised at a lower cost and power consumption [3].

The need for optical frequency combs and its effective generation was discussed in detail in the last Chapter (Chapter 3). It was established that gain switching in conjunction with external optical injection was an optimum way to realise a multi-carrier transmitter. Several semiconductor laser devices were experimentally characterised for the generation of a GS-OFC. The externally injected GS-OFC inherits the lower RIN and narrower linewidth from the purer master laser used for injection. Moreover, optical external injection results in the enhancement of the MBW, allowing the implementation of higher bit rates.

However, the implementation of external injection with the aid of discrete components can be cumbersome, bulky (occupy a large footprint), and non-ideal in terms of stability. The combination of several optical components in a single chip would offer a compact, lower cost, stable, and more

efficient solution. One way to achieve this systematic result is via photonic integration [5]. Integrating the externally injected GS-OFC can open the door for more potential applications due to the compactness and cost-effectiveness that photonic integration offers.

In this chapter, a systematic detailed experimental characterisation of a multi-section photonic integrated circuit (PIC) is introduced. The capability of this four-section device to be used as a compact externally injected gain switched OFC (multi-carrier) transmitter is demonstrated. Furthermore, the performance of this PIC as a directly modulated transmitter in an OOK communication system is investigated. Some of the learning from the experiments performed on the 4-section PIC is then fed back to an industrial collaborator, which aided them in designing an improved six-section device. The 6-section PIC is characterised and employed as a directly modulated transmitter in an access network.

4.2 Photonic integration

Photonic integration refers to the combination of several optical components on a single chip. A PIC can be defined as a miniaturised photonic circuit that consists of a large number of individual optical components, fabricated side-by-side on a common substrate and wired together to perform a particular function [3]. Miniaturization, higher speed, low thermal effects are typical advantages that PICs offer. In addition, compatibility with existing processing flows allow for high yield, volume manufacturing, and thereby lower prices. Currently, the applications of PICs are quite broad including classical optical communications, sensing, atomic clocks, and quantum networks [4]. It also offers better optical alignment between the components as they are implemented on a single chip [5]. Furthermore, they introduce lower power consumption which contributes to a better overall energy efficiency of the system.

4.2.1 Photonic integrated circuits

Two of the main substrate materials that are used for the fabrication of photonic integrated circuits are InP and Silicon (Si) [6]. Each material has its own distinct properties, qualifying it to be used in a set of desired functions.

Si is an indirect bandgap semiconductor material and a part of the group IV materials [7]. This group of materials are easy to obtain. This allows the mass production of functionally advanced and relatively cheap PICs using it [8]. Furthermore, this group of materials offers low optical loss, which makes it ideal for passive devices such as optoelectronic devices that require special characteristics such as polarization splitting/combining [7].

On the other hand, indium phosphide (InP) is a direct bandgap semiconductor material that belongs to the group III-V materials. It supports the integration of active materials such as lasers and optical amplifiers. Thanks to the direct bandgap, InP manifests excellent electro-optical properties, that allows efficient light generation and detection, light guiding and fast phase modulation [8].

In this work, the focus is on an InP PIC consisting of four electrically insulated sections. The four sections allow us to realise a master-slave configuration that enables optical injection from the master to the slave. As highlighted in Chapter 3, the light emitted by the master laser is injected into the cavity of the slave laser to achieve injection locking. OIL provides various improvements for the slave laser characteristics such as a lower RIN value [9], a narrower linewidth [10], a reduced chirp [11] and an enhanced modulation bandwidth [12].

4.3 Integrated four-section PIC

4.3.1 Device structure

The schematic of the multi-section PIC is shown in Figure 4.1(a). The regrowth-free device is designed and fabricated (by Pilot Photonics Ltd.) using InP as a standard 1550 nm laser. Five strained ($(Al_{0.23}Ga)_{0.3}In_{0.7}As$) quantum wells of 5 nm thickness form the active region. This active region is placed on an n-doped InP substrate. The active region is an intrinsic region that contributes to lasing and optical confinement. ($(Al_{0.23}Ga)_{0.3}In_{0.7}As$) makes an intrinsic semiconductor. An active region with a quantum well increases the quantum efficiency. The thickness of the quantum well is always much lower than the operating wavelength. The number of quantum wells is always in odd multiples (1,3,5). The stress-strain situation caused by variation in doping changes the energy gap of the material and hence varies the emission spectrum. There are in total 22 slots with a depth of 1.395 µm, as shown by the side view of the device in Figure 4.1(b). These slots are used to control the longitudinal mode spectrum to ensure single moded emission. Standard electron beam lithography is used in the fabrication of the slots to provide precise control of the slots' dimensions (width, depth) and location [13]. The total length of the device is ~1.5 mm.

As highlighted earlier, the 4-section PIC makes up two FP lasers, integrated together in a master-slave configuration. Each of the two FP lasers, consists of two electrically isolated sections, with different cavity lengths named gain and reflector sections, as shown in Figure 4.1(c). Both sections of the laser (gain and reflector) share the same active layer and InP substrate. The gain section of each laser is a FP structure that generates and amplifies the light inside the cavity and has an anti-reflection (AR)-coated facet. The reflector section of the laser consists of distributed slots that can be considered as

an active distributed Bragg grating [14]. The multiple uniformly distributed slots in the reflector section act as a filter that enhances one of the longitudinal FP modes and suppresses the other modes of the FP resonance. Hence, it restricts the FP laser to a single mode of the allowed FP cavity modes thereby achieving single longitudinal mode emission [15]. The left facet at the end of the slot's region (reflector section) is high-reflection (HR)-coated. Both reflector sections of the two lasers are etched into the surface ridge waveguide, close to the active region, to provide internal reflections and enable a high SMSR of ~50 dB [13]. Furthermore, they provide improved control of the emission wavelength and the injection power inside the PIC due to the presence of the reflector (grating) section. A 2-section PIC comprising a master and a slave laser was reported in [16].

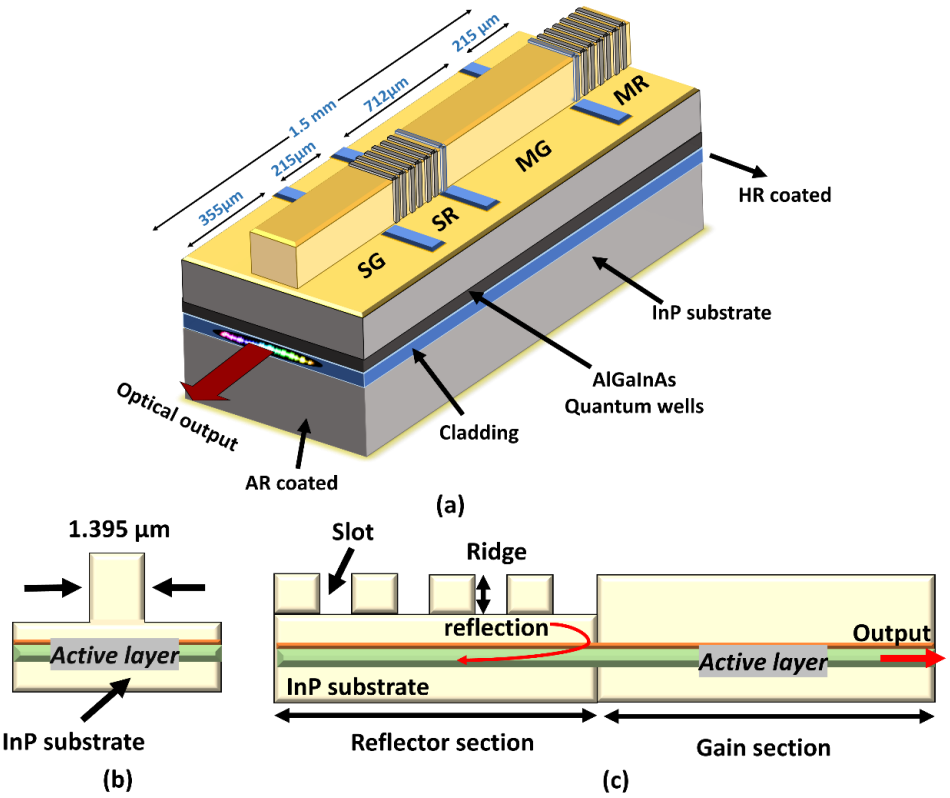

Figure 4.1: (a) InP multi-section photonic integrated device schematic diagram, (b) 2D front (emission) side view of the waveguide structure, (c) 2D view of the waveguide structure of a one FP laser made up of two-sections (gain & reflector) of the 4-section laser, and (d) 7-pin high speed butterfly package of the multi-section.

Although providing enhanced performance in terms of RIN and MBW under the influence of optical injection locking, the device suffers from difficulty of controlling the emission wavelengths of the two lasers. Hence, achieving an injection locking case is hard. By providing input about this issue to the 4-section device designers and manufacturers, the 4-section device was implemented where the reflector (grating) section of each laser provides a better control of the emission wavelength. Hence, achieving an injection locking case becomes a simpler task. Even though the master laser is made up of the master reflector (MR) and the master gain (MG), it is important to point out that the master

laser shares the slave reflector (SR) with the slave laser. This enables a reduction of the overall length of the device, providing better confinement of the total temperature of the PIC as the TEC stabilises the temperature of a smaller area. The length of each section is optimised for its specific functions. The master gain is designed to be the longest of all sections (712 µm), to achieve a low linewidth emission [17]. The slave gain section, on the other hand, is much shorter (355 µm), to ensure a high modulation bandwidth (for direct modulation) [18]. The two reflector sections have an equal length of 215 µm. The electrical isolation between the sections is achieved by separating them with a 2 µm wide etched trench, whose impedance is measured at 2.29 kΩ. The trench is not etched down the InP substrate. The trade-off between optical loss and impedance depends on the etch depth and width of the slot. The doping in the InP substrate only contributes to lowering down the resistance of the laser diode. Too much doping would result in many default which affects the quantum efficiency. On the other hand, not enough doping would result in more losses lowering the output power of the laser.

For ease of use and experimentation, the PIC is encased in a 7-pin, temperature-controlled, fibre pigtailed high-speed butterfly package, as shown in Figure 4.1(d). An RF connector, attached to the SG section, allows for high-speed direct modulation of the device. This package contains a TEC to accurately control the device temperature to ensure stable operation of the device and a 10 $k\Omega$ thermistor for monitoring the temperature. The device temperature is maintained at 20°C throughout all the experimental measurements performed in this chapter to ensure that uniformity and consistency are maintained. As the PIC consists of two distinct lasers, two independent spectral modes, corresponding to each laser, can be generated by the device. A CW spectrum of the master (biased at 35 mA) and slave (biased at 90 mA), operating in single-mode regime, is shown in Figure 4.2(a) (with an OSA resolution of 20 pm). It can be seen that the master laser power is lower than the slave one, this can be attributed to the master laser signal getting lower as it passes through two sections (SG, SR) in its way to be emitted from the output facet. When these two sections are detuned, they do not provide any gain to the master laser. Biasing the device at "bias point 1" listed in Table 4.1 results in achieving the injection locking spectrum shown in Figure 4.2(b). To further confirm the independence of the two lasers, the two independent spectral modes are shown again in Figure 4.2(c), where the OSA is set to a finer resolution of 0.04 pm. The master laser and slave lasers are biased at 40 and 60 mA, respectively. OIL is achieved again at "bias point 2" listed in Table 4.1 and its spectrum is shown in Figure 4.2(d). It is important to note that OIL could be achieved at several other bias points, but only the two listed bias points are highlighted for brevity. The independence of the two spectral modes and the fact that each of the distinct modes originates from a different laser source can be confirmed by calculating the wavelength/frequency difference between the cavity modes.

Figure 4.3(a)&(b) show the optical spectra of the two distinct laser outputs measured using an OSA with a 20 pm resolution (Yokogawa AQ6370). The attenuators are placed on the input of the two different OSAs as a mean of protection from any high-power optical signals.

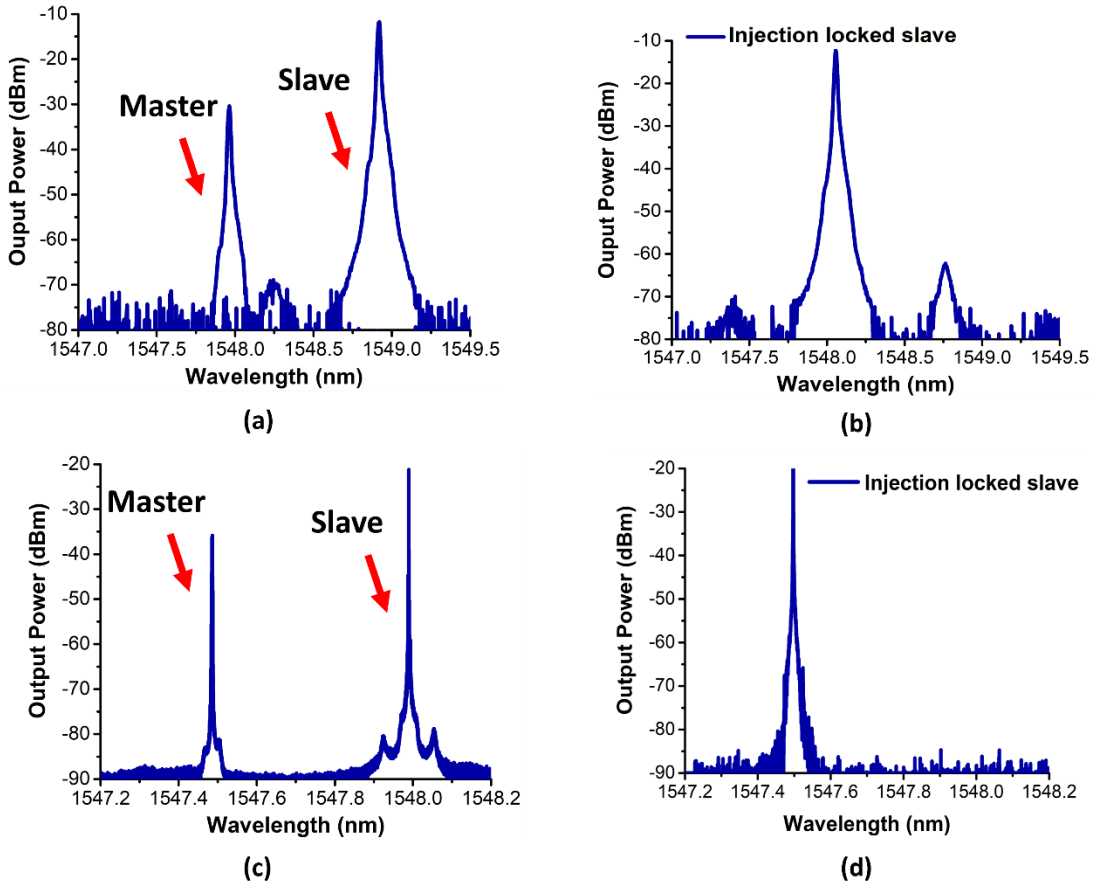

Figure 4.2: (a) Continuous-wave (CW) spectrum of the master (biased at 35 mA) and slave (biased at 90 mA) lasers operating in single-mode operation, (b) PIC output spectrum after OIL is achieved (bias point 1 in Table 4.1). A 20 dB optical attenuator is placed at the input of the OSA (OSA resolution: 20 pm), (c) CW spectrum of the master (biased at 40 mA) and slave (biased at 60 mA) lasers operating in single-mode operation, and (d) PIC output spectrum after OIL is achieved (bias point 2 in Table 4.1). A 30 dB optical attenuator is placed at the input of the OSA for both optical spectra, (OSA resolution: 0.04 pm).

Section	Slave gain	Slave reflector	Master gain	Master reflector
Bias point 1 (mA)	93.7	65.15	34.67	67.65
Bias point 2 (mA)	65	39	54	49

Table 4.1: Bias points for injection locked spectra.

Figure 4.3(a) shows the CW optical spectrum of the slave laser (SG = 80 mA, SR = 40 mA) taken when the master laser is turned off (MG, MR = 0 mA). Within the given OSA resolution, the obtained FSR between the modes ranges between 85 and 100 GHz. A frequency difference of 85 GHz corresponds to a cavity length of 550 µm, which is approximately equal to the length of the slave laser cavity (SG + SR sections) (570 µm). This is calculated using the following formula: $\Delta\nu = c/2nL$, where $\Delta\nu$ is the

FSR, with a refractive index n of 3.2 and a cavity length of L. Figure 4.3(b) shows the CW optical spectrum of the master laser (MG = 80 mA, MR = 8 mA), when the slave laser is biased at transparency (SG = 20 mA, SR = 5 mA). Here, the mode spacing is around 50 GHz, thus corresponding to a cavity length of 937 µm—approximately equal to the master laser cavity length (MG + MR sections) (927 µm). The minor difference between the calculated and given values can be attributed to a small error margin in the measurement.

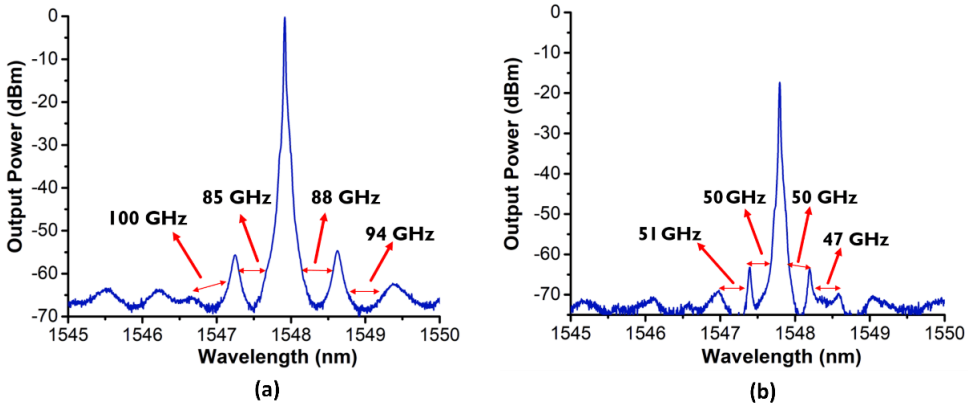

Figure 4.3: (a) Slave laser CW spectrum (master laser is turned off), (b) Master laser CW spectrum (slave laser is biased at transparency). A 20 dB optical attenuator is placed at the input of the OSA for both optical spectra.

Bias condition	Frequency spacing	Calculated cavity length	Actual cavity length
SG=80 mA, SR=40 mA, MG= 0 mA, MR=0 mA	85 GHz	550 µm	SG + SR = 570 µm
SG=20 mA, SR=5 mA, MG= 80 mA, MR=8 mA	50 GHz	937 µm	MG + MR = 927 µm

Table 4.2: Cavity length correspondence calculation.

These results confirm the possibility of achieving independent single-mode emission from each distinct laser. The master laser emission wavelength can then be controlled by varying its bias, and hence can be tuned to achieve OIL. The results obtained are summarized in Table 4.2 below for clarity. The PIC can be operated in an OIL regime by fine-tuning the DC bias applied to the different sections. However, it is important to note that under certain bias points, the PIC portrays operation in a coupled cavity regime. The latter leads to multiple spacings between the modes. It also influences the other sections through a carrier density variation and thereby the refractive index. The presence of the coupled cavity regime is mainly because the two lasers share the same optical waveguide, which leads to multi-cavity effects [19]. The presence of finite electrical isolation between the different sections suggests the possibility of some current leakage between the device sections. This current leakage, even if small, would mean that variation of the bias applied to one section would affect the other one. Increasing the resistance between the section would lower the value of current leakage. However, it would also lead to decreasing of the device quantum efficiency as previously mentioned in this section. Moreover, deep etching can result in a potential damage in the laser waveguide.

4.3.2 Static characterisation

The capability of a laser device to be considered for deployment in next-generation optical networks is determined by the quality of its different characterisation parameters such as the emission wavelength, RIN, SMSR, output optical power, and optical linewidth. A set of various static characterisation procedures is conducted on the PIC to quantify these parameters and to identify the stable regions of operation. In the next section, the dependency of the output spectra of the PIC on the bias values of the different sections is investigated and depicted using contour plots.

4.3.2.1 DC characterisation

Different combinations of DC biases are applied to each of the four different sections of the PIC using a multi-channel current controller (LDC-3900). The output light of the device (emitted by the SG section) is recorded using an OSA with a 20-pm spectral resolution. This allows the extraction of various important parameters such as the power, SMSR and wavelength of the main emission mode. Due to the large number of bias combinations involved, both the current controller and the OSA are driven by an automated Python script, which varies the bias of a specific section for each sweep. The contour plots are generated for both the slave and master lasers of the device.

The first step is to characterise the free-running slave laser. Figure 4.4(a–c) show the power, SMSR, and emission wavelength of the slave laser (main emission mode), as a function of the SG and SR bias currents, respectively. For this test, the master laser is turned off (MG and MR biased at 0 mA) to ignore any of its influence. At these bias configurations, there is no internal optical injection applied to the slave laser. The SG section bias current is varied from 0 to 150 mA, while the SR section bias is varied from 0 to 100 mA. The current limits were chosen from the safe operating conditions of the PIC (specified by the manufacturer).

From Figure 4.4(a), it can be observed that the SG has an average threshold of around 32 mA, when the SR is biased over 20 mA. This threshold value decreases with the increase of the SR bias. In addition, it can be noted that lasing from the SR section can be observed when the SG is biased at values greater than 30 mA and the SR is biased at values greater than 65 mA.

From Figure 4.4(a)&(b), it can be seen that for a single-mode operation (high SMSR > 40 dB), the power of the slave reaches a maximum of 9 dBm. The SMSR contour plot in Figure 4.4(b) allows one to identify the bias currents that result in a high SMSR (dark red regions) as well as the currents at which the device shows multi-mode behaviour (blue and cyan regions). The latter has been confirmed by

observing a bi-modal operation of the slave laser on the OSA. A high SMSR of around $\sim 55 - 60$ dB can be achieved for several bias points.

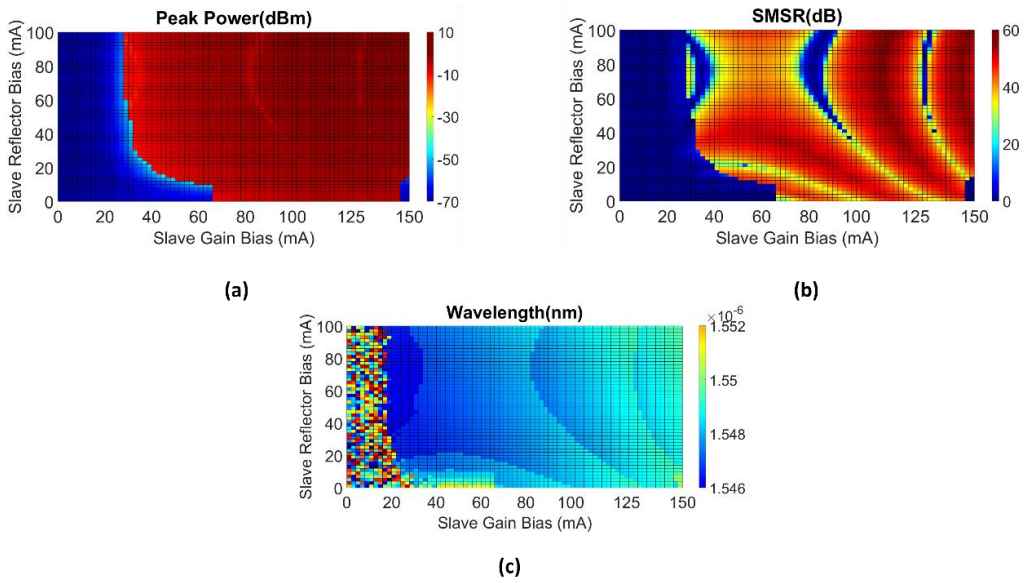

Figure 4.4: Contour plots of varying SG, SR bias currents and observing the following slave laser parameters: (a) Main mode power, (b) SMSR of the output modes of the PIC, and (c) Emission wavelength of the main mode.

Figure 4.4(c) shows the emission wavelength of the slave laser main mode. From the plot, it can be observed that by varying the currents, the wavelength of the slave laser can be tuned gradually over ~2 nm before a mode hop occurs (marked by an abrupt change in colour). The multi-coloured region on the left of the plot corresponds to noise (as captured by the OSA), since for those currents, the laser is biased below the threshold. The gradual variation in the emission wavelength (between the mode hops) is caused by temperature changes due to the Joule effect [20] occurring with the increase in the bias of the SG and SR sections. When the temperature increases, the central emission wavelength of the laser experiences a redshift [21].

The same DC characterisation procedure is applied to the master laser. Here, the slave laser is biased just above transparency (SG = 10 mA, SR = 5 mA) to minimise any interaction between the master and slave lasers. Again, the MG section bias is varied from 0 to 150 mA, while the MR section bias is varied from 0 to 100 mA as per the safe operating conditions of the PIC specified by the manufacturer. The master laser characterisation shows that the MG has an average threshold of ~45 mA (around 13 mA higher than SG threshold), when the MR is biased higher than 20 mA, as depicted in Figure 4.5(a). The higher threshold value can be attributed to the master laser having a longer cavity length. Again, it can be seen that the MR lases only when the MG is biased above 40 mA, as illustrated in the same figure. The master laser SMSR contour plot shown in Figure 4.5(b) manifests a comparable behaviour with that of the slave laser. By careful control of the biases applied to the two sections of the master laser, a SMSR as high as 50 dB can be achieved.

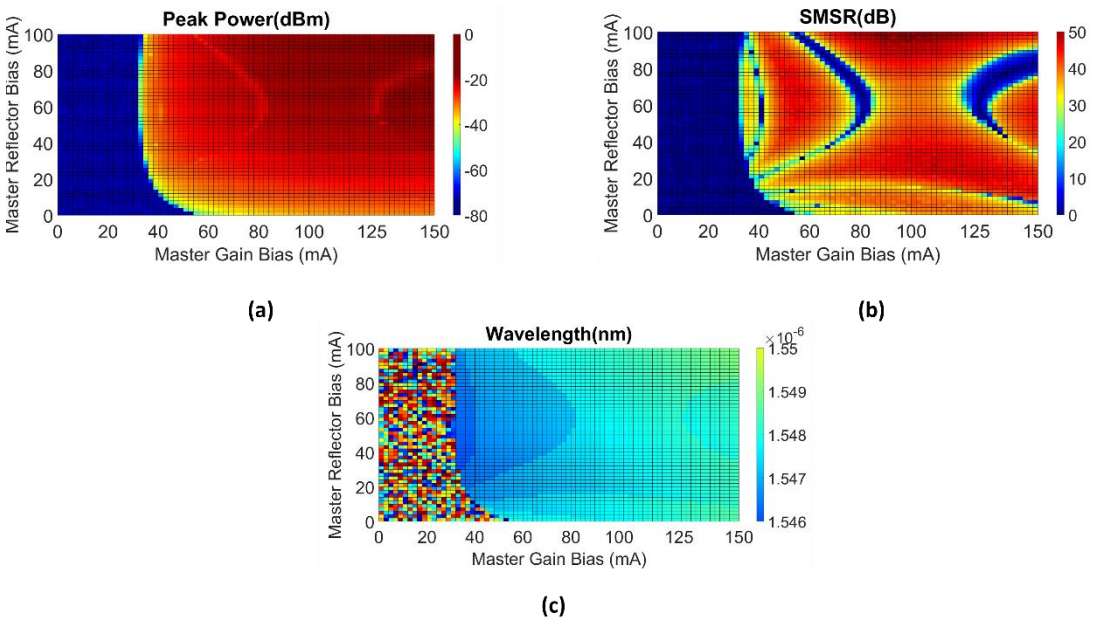

Figure 4.5: Contour plots of varying MG, MR bias currents and observing the following master laser parameters: (a) Power of the main mode, (b) SMSR of the output modes of the PIC, and (c) Emission wavelength of the main mode.

Figure 4.5(c) shows the capability of the master laser wavelength to be gradually tuned over ~1.5 nm, through variation of the bias currents. Mode hopping only takes place for a few points of bias currents where we experience low SMSR. This is due to the two modes having an approximately similar values of gain, which gives a higher probability of transition between different modes in the resonator. Overall, it can be concluded from the different contour plots that a similar behaviour of the master laser and slave laser is obtained with slight variations of power, SMSR, and emission wavelengths values. These plots provide a good understanding of the device behaviour and a means to determine the optimum bias points that will ensure a single-mode emission with high SMSR and high output power. Having carried out a detailed characterization of the operating bias currents, a set of optimum ones are chosen to carry out measurements of the optical linewidth and RIN.

4.3.2.2 Linewidth and RIN measurements

The ever-growing demand for bandwidth is pushing future short-reach networks towards the employment of coherent modulation schemes that combine both amplitude and phase modulation to increase the amount of data being transferred [22]. In such networks employing higher-order modulation formats, optical transmitter parameters such as the linewidth and RIN play an important role in determining the overall system performance. Hence, the linewidth and RIN are characterised to determine the suitability of the proposed PIC to be used in next-generation coherent short-reach networks. In general, characterisation results show that applying on-chip injection from the master laser into the slave laser improves both the linewidth and RIN of the slave laser, as long as the device

is operating at a single-mode regime. This characterisation test has been conducted for many injection locking bias points. However, for the sake of clarity and brevity, the results of only two bias points are shown in this thesis. The two bias points are listed in Table 4.3 below.

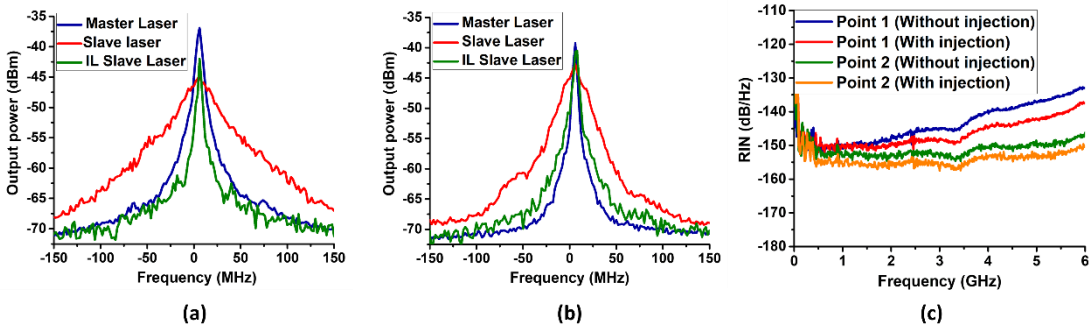

Figure 4.6: Electrical spectra of the measured linewidth of master laser, slave laser and injection-locked (IL) slave laser for (a) Bias point 1 in Table 4.3, (b) Bias point 2 in Table 4.3, and (c) RIN values for bias points 1,2 in Table 4.4 with (red, orange) and without injection (blue, green) from the master laser.

Section	Slave gain	Slave reflector	Master gain	Master reflector
Bias point 1 (mA)	45	58	112	74
Bias point 2 (mA)	97.9	50.98	98	92

Table 4.3: Bias points for linewidth measurements.

The DSH technique with a resolution of 50 kHz, previously explained in detail in Chapter 3 (Section 3.4.2.1) of this thesis, is used to measure the linewidth of the device at these two operating bias points. The linewidth measurements results are presented in Figure 4.6(a)& (b) where the PIC is biased at bias points 1 & 2 respectively. The blue trace shows the master laser linewidth on its own, the red trace shows the slave laser linewidth on its own, and the green trace shows the linewidth of the slave laser injection-locked by the master laser.

From Figure 4.6(a), it is evident that the free-running slave laser has a large linewidth of 8 MHz, which can be ascribed to its short cavity. The long cavity master laser at bias current of 112 mA has a much lower linewidth of 2 MHz. The optical linewidth of the slave laser can be significantly reduced by employing OIL from the lower linewidth master laser. As OIL allows for the transfer of the phase noise characteristics from the master to the slave laser [23], the linewidth of the latter is reduced to 2 MHz, as shown in the same figure. Similar behaviour is shown in Figure 4.6(b), where again the lower linewidth of the master laser (2.7 MHz) was imposed onto the slave laser through OIL. This results in decreasing the large linewidth of the slave laser from 5 MHz to 2.7 MHz. It is important to note that this PIC is a proof-of-concept device and the potential for further improvement exists. Having a shared reflector in the device results in the presence of coupled cavity effects in some bias cases as explained before. Hence, there is a difficulty in tuning of the wavelength of the two different lasers thus obtaining OIL points. Moreover, the master laser possesses a relatively high linewidth which is

inherited by the slave laser in case of OIL. In the later part of this chapter, the second generation of this device will be introduced, which is expected to give an overall improved performance by overcoming some of the challenges encountered in the older PIC. The work on the 4-section PIC presented in this report, has been given as feedback to the manufacturing company in order to be taken in consideration when designing the new PIC.

RIN is another important parameter of an optical transmitter, quantifying the intensity fluctuations of the laser output power. High RIN values (>−120 dB/Hz) can be a limiting factor for the employment of a laser in systems employing intensity modulation schemes especially multi-level formats such as PAM 4/8. The RIN characterisation of the proposed PIC has been carried out using the same method explained previously in detail in Chapter 3 (Section 3.4.2.2). The measurement is conducted for two different bias points listed in Table 4.4 below.

Section	Slave gain	Slave reflector	Master gain	Master reflector
Bias point 1 (mA)	45	58	112	74
Bias point 2 (mA)	100.16	69.7	45.3	87.19

Table 4.4: Bias points for RIN measurements.

Figure 4.6(c) shows the obtained RIN values for bias points “1 and 2” listed in Table 4.4 with and without injection. The obtained averaged value of RIN (DC to 6 GHz) of “bias point 1” in Table 4.4 without injection (blue trace) (both MG and MR biases are set to zero) is −143.4 dB/Hz. Turning the master laser sections on (MG = 112 mA, MR = 74 mA) (red trace) decreases the average RIN to −146.1 dB/Hz. The reduction of RIN value for the injection-locked case can be attributed to the reduction of cavity gain by the injected signal. This reduction also causes the carrier density to deplete, resulting in a decrease in the overall spontaneous emission rate, which in turn reduces the overall RIN of the PIC [24]. A similar reduction in the RIN value is shown also for “bias point 2” listed in Table 4.4 in the same figure. The RIN value obtained without injection (green trace) is −151.6 dB/Hz. This value decreases to −154.3 dB/Hz by turning the master laser on (MG = 45 mA, MR = 87 mA) and applying optical injection (orange trace). The obtained results demonstrate that the integrated device has a relatively low RIN value qualifying it as a potential candidate to be used in direct intensity-modulated short-reach communication networks [25].

Having provided the static characterisation results of the PIC, showing that on-chip optical injection can provide an improvement on both the linewidth and RIN values, the next step is to investigate the dynamic performance of the PIC to determine its usefulness as a directly modulated transmitter and to examine the on-chip optical injection influence on the dynamic characteristics of the device.

4.3.3 Simulation model to support the experimental results

A VPItransmissionMaker™ simulation model, that mimics the InP photonic device, has been built to get a deeper understanding of the behaviour of this complex integrated device. VPItransmissionMaker™ is software that comprises the design, analysis and optimisation of photonic components, systems, and networks. To start with a model that is similar to the device structure, has been established. In this model, the different parameters of each section can be controlled and specified individually. The four different sections were designed to be electrically insulated which is the ideal expected case. Figure 4.7(a) shows the schematic diagram of the simulated device, where the DC bias of each section can be tuned individually. The modelled device length was set to 1.5 mm (imitating the physical device). Moreover, two sections were implemented with gratings to mimic the reflector sections and the other two without gratings to resemble the gain sections.

Figure 4.7(b) shows the simulated output optical spectrum of the device. Two different laser modes are generated when the MR, MG, SR and SG sections are biased at 30, 80, 30 and 60 mA respectively. This clearly shows that there are two different modes, each of them belongs to one laser section. The same behaviour has been demonstrated by the physical device in Figure 4.2(a-c). For further confirmation of partial independence of the two modes, the master section bias was set to zero (MG, MR=0) and one of the modes just disappeared. OIL is achieved through fine tuning of the bias values of the four different, where the master laser drags the slave laser to its wavelength.

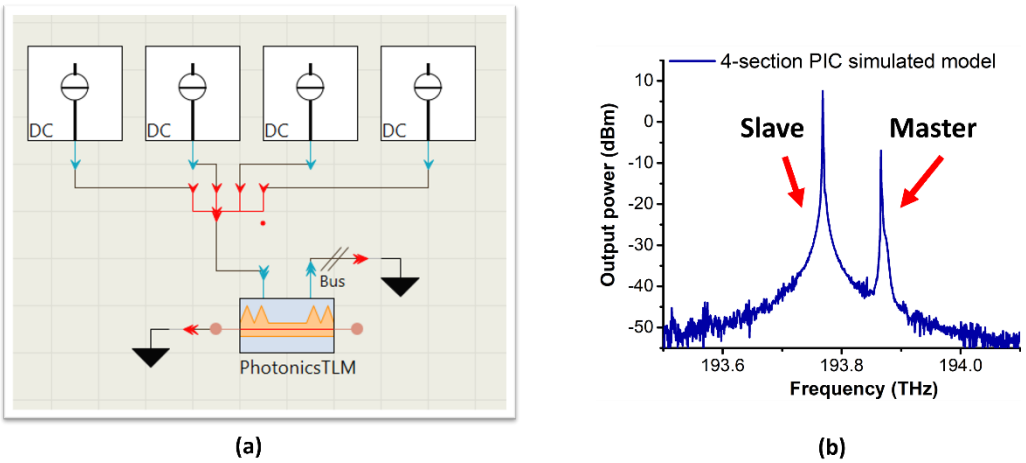

Figure 4.7: (a) VPI schematic structure of the integrated 4-section device, (b) Output optical spectrum of the simulated integrated device.

This is demonstrated in Figure 4.8(a) where the laser is injection locked and single moded. The injection locking of the slave laser is further confirmed by measuring the 3-dB linewidth of the signal to examine the influence of OIL.

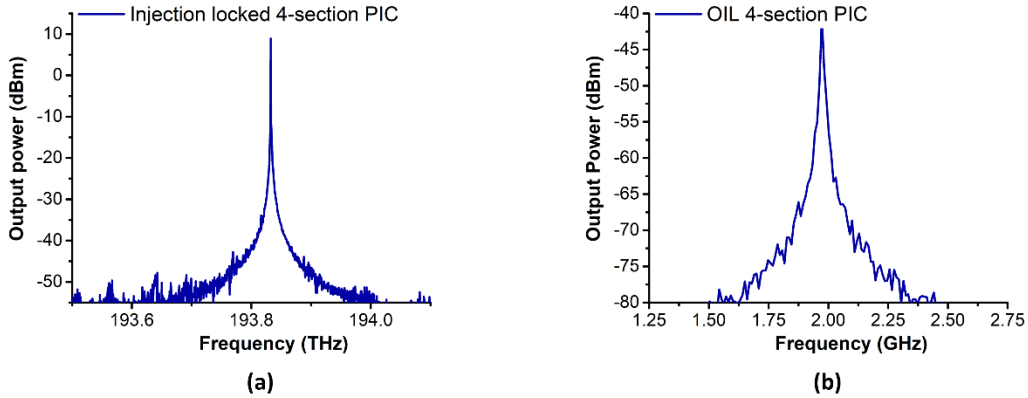

Figure 4.8: (a) Optical spectrum of the simulated device when injection locked, (b) Corresponding RF spectrum of the measured linewidth.

A DSH modelled setup that is similar to the experimental one was employed to measure the linewidth of the laser after applying the injection from the master laser. Figure 4.8(b) shows the generated RF-spectrum where the 3-dB linewidth was found to be 8 MHz when injection locking is achieved. This is the same value specified initially as the master laser linewidth in the device parameters, which proves the transfer of the phase noise characteristics from the master laser into the slave laser by applying

OIL.

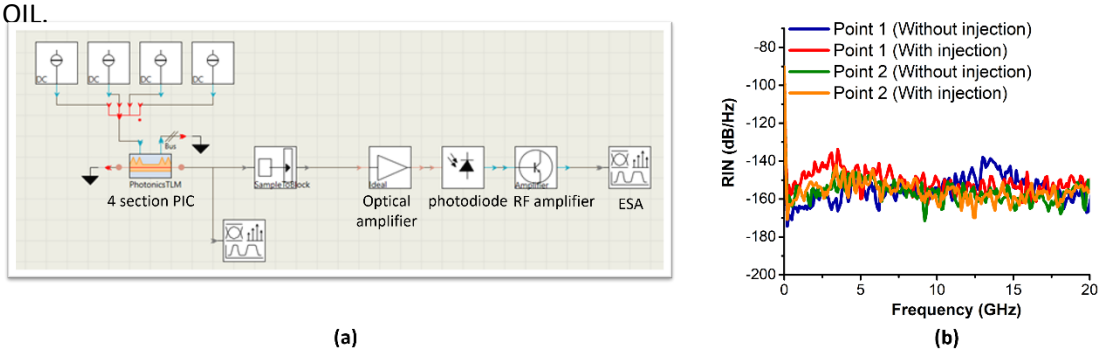

Figure 4.9: (a) Schematic setup diagram for the VPI RIN measurement, (b) Measured RIN (0-20 GHz) for the simulated integrated laser device with and without injection for two different bias points.

Bias point	Condition	Averaged RIN value (0-20 GHz)
Point 1	Without Injection	-151.96 dB/Hz
Point 1	With Injection	-157.38 dB/Hz
Point 2	Without Injection	-154.803 dB/Hz
Point 2	With Injection	-158.21 dB/Hz

Table 4.5: Averaged measured RIN values (0-20 GHz) for two different bias points with and without injection.

RIN measurements are also carried out using the VPI software to examine the impact of the OIL. Figure 4.9(a) shows the setup diagram used to conduct the RIN measurements. It follows the same principle

that has been explained previously in this thesis. The optical output of the integrated laser device is amplified and sent to a photodiode and then the electrical output of the photodiode is amplified again and finally, the output is shown on an ESA.

Figure 4.9(b) shows the electrical spectra of the RIN (0-20 GHz) for two different OIL bias points with and without injection from the master laser. The corresponding table (Table 4.5) shows the averaged RIN values (0-20 GHz) ranging between -151.9 and -158.2 dB/Hz. The results show that the averaged RIN values (0-20 GHz) decreases slightly for both bias points when applying injection from the master laser. This proves that the slave laser inherits the better spectral characteristics (in this case the lower RIN values) from the purer master laser.

The simulated model shows relatively similar characterisation results to the experimental work. This verifies the convenience of this model to be used for further complicated characterisation in the future, which is hard to achieve using the physical device and experimental test beds.

4.3.4 Dynamic characterisation

Direct modulation is a simple and cost-effective technique, where data modulation can be accomplished simply by adding the information signal to the bias current of the laser [26]. One of its main drawbacks is the limited laser bandwidth, which restricts the maximum modulation data rate. Another disadvantage with direct modulation is frequency chirp, where the broadened optical spectrum in conjunction with fibre dispersion, limits the transmission distance [27]. OIL can be implemented to overcome both of these drawbacks, thus increasing the data rates and extending the transmission distances achievable in systems employing direct modulation. As previously discussed in Section 3.4.3 in Chapter 3, Previous reports have shown that external injection can enhance the intrinsic MBW of the laser up to about three times [28]. There are also some studies on how injection locking can be used to significantly reduce the chirp of a directly modulated laser [29].

Hence, any laser transmitter to be used in a direct modulation-based system should be thoroughly characterised to evaluate its dynamic characteristics. The following section focusses on this aspect, in order to evaluate the PIC potential to be used as a transmitter in a short reach OOK system and as an OFC generator.

4.3.4.1 Modulation response measurement

As highlighted above, to evaluate the performance of a PIC as a directly modulated transmitter, its frequency response at different bias conditions should be characterised. We start by measuring the

small-signal frequency response of the PIC as shown in the setup diagram in Figure 4.10. Two measurement scenarios are implemented: with and without optical injection from the master laser.

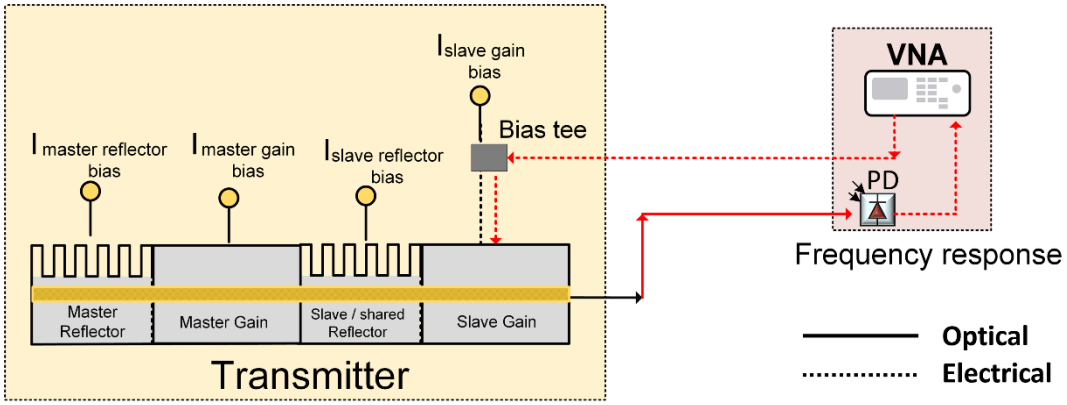

Figure 4.10: Schematic of the setup used for the small signal frequency response measurement.

The master laser is turned off (MG, MR=0) to realise the first scenario where there is no injection. Subsequently, the second scenario (with injection) is carried out experimentally for several injection locking points. However, for the sake of brevity again, we chose two of the optimum bias points for illustration in this report. The two bias points are listed in Table 4.6 below.

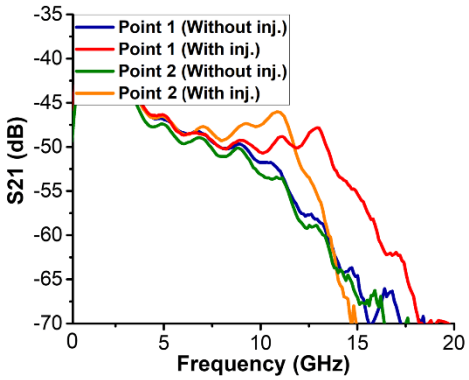

Figure 4.11: Frequency response of the slave laser for the two bias points of the PIC listed in Table 4.6 without (blue, green) and with (red, orange) injection from the master laser.

Section	Slave gain	Slave reflector	Master gain	Master reflector
Bias point 1 (mA)	100.18	69.7	45.35	85.15
Bias point 2 (mA)	98.68	56.15	65.62	87.56

Table 4.6: Bias points for frequency response measurements.

For this measurement, a 50 GHz vector network analyser (HP 8517B) is used to directly modulate the SG section of the device. The frequency of the modulated RF signal is swept from 0.05 to 20 GHz. The optical output of the PIC is split using a 90:10 coupler, where the 90% branch is detected by a 20 GHz photodiode (Discovery DSC30S) and then sent back to port 2 of the network analyser. The other 10% branch is used to monitor the optical spectrum (ensuring single-mode operation) of the device. The measured "S_{21}" parameter (i.e., the frequency response) of the slave laser is shown in Figure 4.11.

The measurement is first carried out for the free-running slave laser biased at “bias point 1” referenced in Table 4.6 without injection (MG, MR = 0) (blue trace) and subsequently for the OIL case (red trace). Figure 4.11 shows that by employing OIL, the 3 dB MBW of the slave can be increased from 9.5 to 14 GHz (45% enhancement). The same measurement is conducted for “bias point 2” in Table 4.6. The slave laser without injection (green trace) shows a MBW (3 dB) of 9.2 GHz. Injection from the master laser improves the modulation bandwidth to 12.1 GHz. The improvement as a result of injection from the master laser enables higher direct modulation rates of the device as well as extends the linearity of the slave laser frequency response. The reduction in non-linearity, as a result of the external optical injection, is important for employment of the device in subcarrier multiplexed, ROF, and/or OFDM systems [30] [16].

4.3.4.2 Direct data modulation and transmission

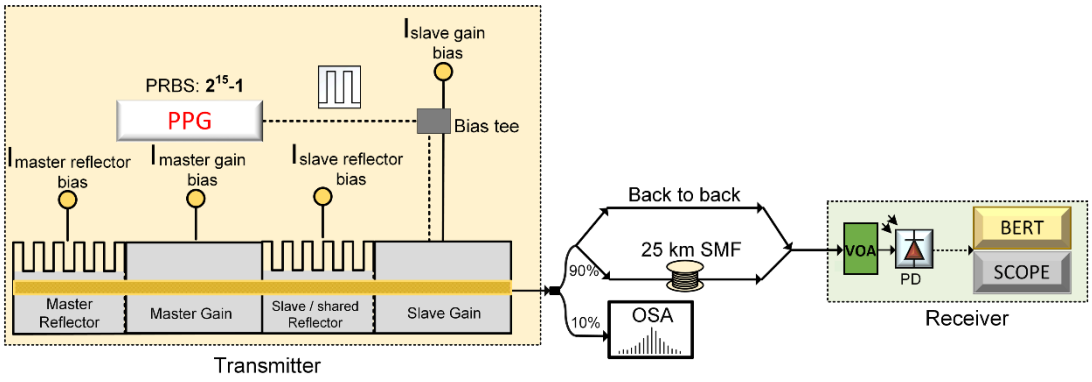

Figure 4.12: Setup used of the PIC employed in a short reach transmission system.

The frequency response measurements have proven the capability of the PIC to handle higher direct modulation rates thanks to the improvement in the 3-dB MBW influenced by the on-chip optical injection. However further validation of this concept is carried out with the aid of a system experiment. Here, the SG section of the PIC is directly modulated with a 10.7 Gb/s OOK data signal after which the modulated signal is transmitted over SMF. Apart from the frequency response enhancement validation, this experiment also highlights the potential of employing such a PIC as a transmitter in a short reach network. The schematic of the experimental setup used is shown in Figure 4.12. A pulse pattern generator (PPG) is used to generate a 10.7 Gb/s pseudo random bit sequence (PRBS) with a length of 2^{15}-1. The data signal is combined with a DC bias of 72.8 mA using an internal bias-tee contained within the device package. The optical output of the device is split using a 90%-10% coupler. The 10% path is connected to a 20 MHz high-resolution OSA, while the 90% path is launched into a 20 GHz PIN photodiode (DSC30S) either back-to-back (B2B) or after transmission over 25 km of SSMF. A VOA is used to vary the received optical power. The photodiode output is connected either to a digital

sampling oscilloscope, to generate eye diagrams (qualitative measurement), or to an error detector, to measure BER of the system (quantitative measurement).

BER results as a function of the received optical power are presented in Figure 4.13(a). The measurements are taken for both the cases when the master laser was turned off (circles) and on (triangles). For the B2B transmission, the injected case has a power penalty of 2 dB with respect to the non-injected one at BER $= 4 \times 10^{-9}$. This penalty can be attributed to the fact that the optical injection reduces the threshold current of a laser, resulting in a degraded extinction ratio (ER) [31] [32]. The reduction in the threshold current of the laser is associated with an increase in the laser slope efficiency. Hence, given that the modulation current is kept constant, the differentiation between the "1" and "0" levels is reduced. Hence, ER is reduced. However, after transmission over 25 km of SSMF, the optically injected laser performs significantly better. The received optical power required to achieve the FEC limit for the injection case is 2 dB lower than that without injection. This can be mainly attributed to a reduction of the chirp due to the applied OIL [33]. For both cases, a BER below the hard decision FEC limit (BER $= 3.8 \times 10^{-3}$) is achieved.

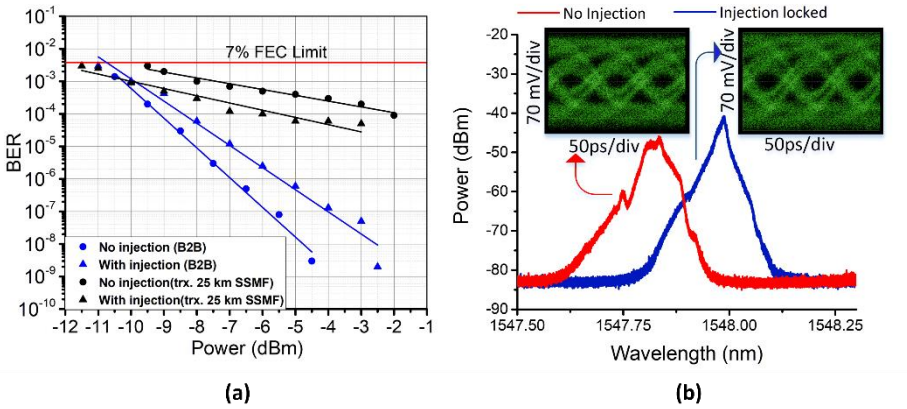

Figure 4.13: (a) BER results for back-to-back (B2B) (blue) and 25 km SSMF transmission distances (black) with and without injection, (b) Optical spectra of the PIC under modulation with injection (blue) and without injection (red); inset: obtained eye diagrams after 25 km SSMF transmission and 0.5 dBm received optical power.

The achieved BER values compare to the current state of art for the short reach networks as even with 25 km SMF transmission, the device hits the 7% FEC limit, that satisfies the requirements of the latest ITU-T recommendation for passive optical networks (ITU-G987). The optical spectra recorded using a 0.04 pm resolution OSA (APEX AP2433B) in Figure 4.13(b) verify the reduction in frequency chirp. The OIL case is represented by the blue line and the non-injected case by the red line. It can be seen that the spectral width of the modulated laser without OIL is significantly broader than the case where is OIL is achieved. The interplay between the fibre chromatic dispersion and this large spectral width (due to higher value of chirp) causes pulse spreading, leading to ISI and resulting in a degraded performance (worse BER). The insets in Figure 4.13(b) shows the recorded eye diagrams at a received optical power of 0.5 dBm for both cases.

The reduced eye-opening for the laser without injection is visible and validates the results of the BER measurements. This experiment clearly shows the positive effect of the optical injection in the performance of the device when employed in a short reach transmission system. The laser MBW is enhanced as an effect of optical injection, allowing the PIC to achieve better BER results when the optical signal is transmitted for 25 km of SMF. Furthermore, the results show a clear reduction in the chirp value as a result of applying optical injection. This reduction also contributes to achieving a better BER.

4.3.5 OFC generation by gain switching the PIC

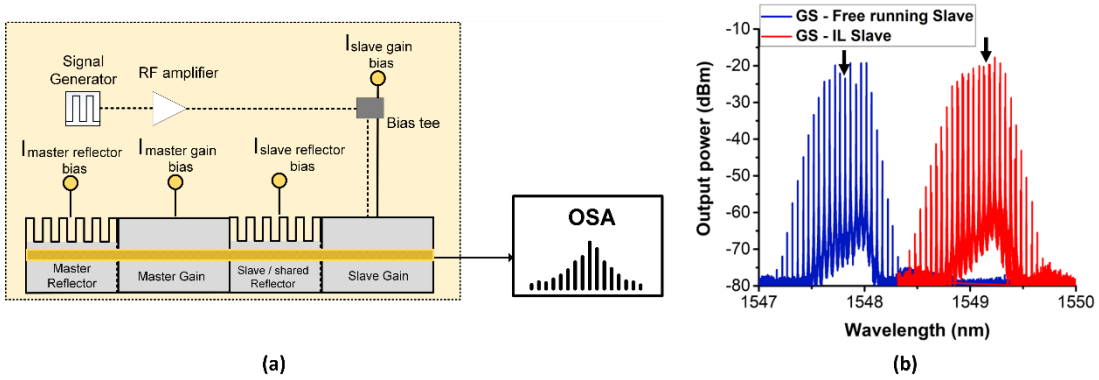

Figure 4.14: (a) Schematic setup diagram of gain switching of the integrated 4-section device, (b) Optical spectrum of the gain switching based OFC of the device with and without injection.

The detailed static characterisation of the PIC has demonstrated its ability to achieve OIL by fine tuning of the bias values of the different sections. Moreover, the dynamic characterisation has shown a sufficient laser MBW, that allows the device to be gain switched at FSR values that follows the ITU-T recommendation (i.e., 6.25 GHz).

Figure 4.14(a) shows the experimental setup diagram used for the gain switching of PIC for the generation of an OFC. Gain switching of the device is achieved by applying an amplified sinusoidal RF signal of ~24 dBm in conjunction with a DC bias, to the SG section. The frequency of the applied RF signal is 6.25 GHz. As aforementioned in Chapter 2, gain switching technique provide simple FSR tunability by varying the frequency of the RF signal from the signal generator. However, in this report, only this FSR is shown for sake of clarity. Initially, the slave laser is biased at (SG = 61.31 mA, SR = 53.32 mA), and the master laser is turned off. This results in the generation of an OFC exhibiting four comb lines within 3 dB from the spectral peak and an OCNR of 45 dB, as illustrated by the blue plot in Figure 4.14(b). As previously shown in the dynamic characterisation, on-chip OIL results in the expansion of the MBW of the device, which in turn results in an enhancement of the spectral characteristics of the

generated OFC. So subsequently, the master laser is turned on in order to examine the effects of OIL. The slave laser bias is kept at the same optimised values, and the master laser bias is optimised to achieve the maximum number of OFC tones at (MG = 74.62 mA, MR = 74.34 mA). Thanks to OIL, the generated OFC now exhibits nine comb lines within 3 dB from the spectral peak and an OCNR of 46 dB as shown by the red plot in Figure 4.14(b). The latter demonstrates that the on-chip OIL results in more than doubling of the number of the OFC lines within 3 dB from the spectral peak. As each of these lines can potentially be used as data carriers, OIL enables an increase of the aggregate data rate that can be carried by a single OFC. However, as the applicability of any laser as a transmitter in a system employing advanced modulation formats depends on its linewidth and RIN, the performance of the generated OFC in terms of these two parameters, needs to be investigated.

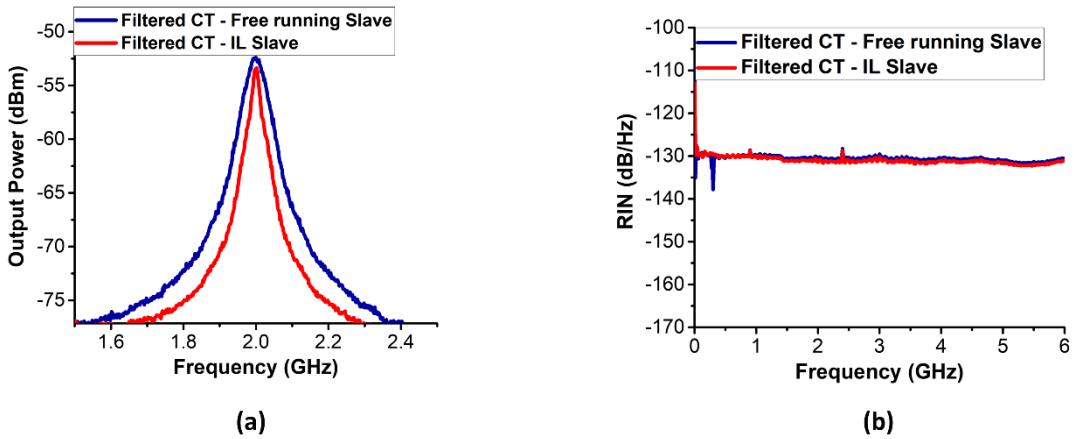

Figure 4.15: (a) RF spectrum of the linewidth of a filtered comb tone (CT) of the case of: the free running gain switched slave (blue) and, injection locked (IL) slave (red), (b) RIN measurement electrical spectra (0-6 GHz) for the filtered comb tone (CT) without (blue) and with (red) injection and the whole optical frequency comb (OFC) without (green) and with (orange) injection.

First, the optical linewidth is characterised, using the DSH technique, with a resolution of 50 kHz. To this effect, the middle comb line (labelled by the black arrow in Figure 4.14(b) is filtered using a bandwidth tunable OBPF (with the minimum achievable bandwidth of 4 GHz) and sent to the DSH setup. The measurement is conducted for two different scenarios: (i) no injection from the master laser (blue plot in Figure 4.15(a), (ii) the OIL case (red plot in the same figure). In the case of no injection, the filtered comb tone exhibits a linewidth of 22 MHz. In the second case, the phase noise characteristics of the master laser are transferred to the slave laser, resulting in narrowing of the linewidth to 13 MHz. Despite this significant linewidth narrowing, the measured linewidth value is still too high for the device to be used with higher-order modulation formats at low baud rates [34]. The OFC tones linewidth broadening compared to the CW laser case is a result of the gain switching process, which brings the laser below threshold and introduces more spontaneous emission noise. An

improvement in the device design is required in order to achieve a master laser linewidth much lower than the current MHz linewidths displayed.

Next, RIN measurements are conducted for a filtered OFC tone and the whole OFC generated by the 4-section device using the same method explained previously in detail in Chapter 3 (Section 3.4.2.2). The RIN measurements (0-6 GHz) of the filtered comb tone for both cases, with and without injection, is demonstrated in Figure 4.15(b). Without injection, the filtered middle OFC tone has an averaged RIN value of -130.5 dB/Hz, as shown by the blue plot in Figure 4.15(b). Applying the OIL (MG = 74.62 mA, MR = 74.34 mA) results in a slight reduction of the RIN of the filtered comb tone to - 131 dB/ Hz, represented by the red plot in the same figure.

4.4 Six-section PIC in a master slave configuration

As mentioned in the previous section, the integrated four section PIC suffers from some drawbacks which may restrain its employment in specific functions. The presence of a shared reflector results in difficulties in the fine control of the emission wavelengths of each individual laser due to the absence of individual Bragg gratings. Moreover, the current leakage between the different sections presents a challenge in the accurate control of bias applied to each section. The obtained results from the 4-section device were fedback to the manufacturing company, which in turn initiated an improvement in the design by introducing a middle VOA section. The latter provides better control of the injection power from the master laser, hence provides a better injection locking conditions and reduction of chirp Hence, the upgraded version of the PIC is introduced and characterised in this section.

4.4.1 Device structure

The schematic diagram of the six-section PIC is shown in Figure 4.16(a). Based on the same general design of the legacy device, the six-section device is fabricated using a standard InP 1550 nm material and it has 5 strained $\mathrm{Al}_{(0.24)}\ \mathrm{Ga} - \mathrm{In}_{(0.71)}\ \mathrm{As}$ quantum wells in the active region on an n-doped In-P substrate. However, it consists of six different sections as opposed to only four sections in the legacy device. The master laser now consists of a long MG section of length 790 µm that is sandwiched between two reflector sections (MR1, MR2) with an equal length of 220 µm. In this case, none of the reflectors are shared among the two lasers. An intermediate VOA section is placed between the slave and the master lasers and has an approximate length of 130 µm. The slave then consists of two different sections, a SG section that can be modulated and has a short length of 215 µm to allow high speed modulation and a SR section of a length of 210 µm. The total length of the device is

approximately 1.78 mm. The main advantage of the new device over the previous 4-section PIC, is the presence of the VOA section. It acts as a means for varying the level of injection from the master laser into the slave laser offering better control of the injection parameters, which is quite crucial. The level of injection can be controlled easily by tuning the bias applied to the VOA section. Furthermore, it acts as an isolation between both lasers, resulting in lowering the level of the current leakage among them. This leads to the achievement of independent control of the master and slave sections, resulting in a better overall enhancement of the performance of the integrated device. In addition to that, the presence of a separate (not shared) two reflector sections belonging to the master laser provides a better control of the master emission wavelength. Hence, easier achievement of injection locking conditions.

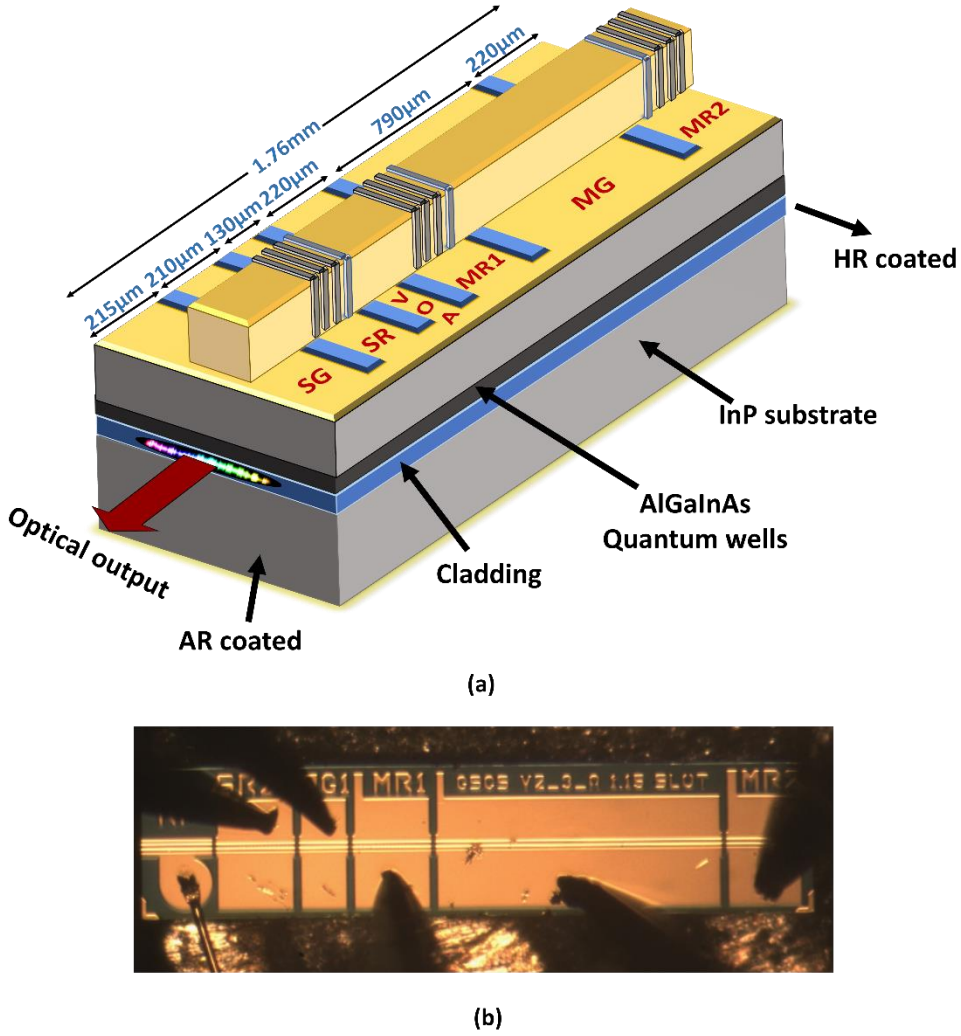

Figure 4.16: (a) Schematic diagram of the InP six-section photonic integrated device, (b) microscopic image of the physical chip with DC probes on each section.

It is important to note that the device tested is a bare chip that is mounted on an RF subcarrier. It is designed with a $50\,\Omega$ coplanar waveguide to support high-speed modulation. Preliminary static characterisation of the slave section shows that it demonstrates a 16Ω dynamic resistance. In order to match the 50Ω matched RF waveguide of the subcarrier, a 34Ω linear surface mount device matching resistance is wire-bonded to the SG section.

For characterisation and testing purposes, the sub-mounted chip is placed on a probe station, where several probes are used to bias each section independently. The temperature of the device is maintained, using a TEC placed under the subcarrier, at 18°C for the characterisation and tests. An AR coated optical lensed fibre is used to couple the light from the output facet of the PIC. The SG section is biased via a high-speed bias tee while the other five sections are DC-biased using a low noise current source. Figure 4.16(b) shows a microscopic photograph of the fabricated chip with each DC probe placed at different sections to allow the individual tuning of each section bias.

4.4.2 Static characterisation

In order to identify the stable regions of operation of the device, L-I curves of the slave laser at different bias values of the reflector section (0, 10, 20, 30, 40, and 50 mA) is shown in Figure 4.17. The SG section bias is varied from 0 to 80 mA in steps of 2 mA.

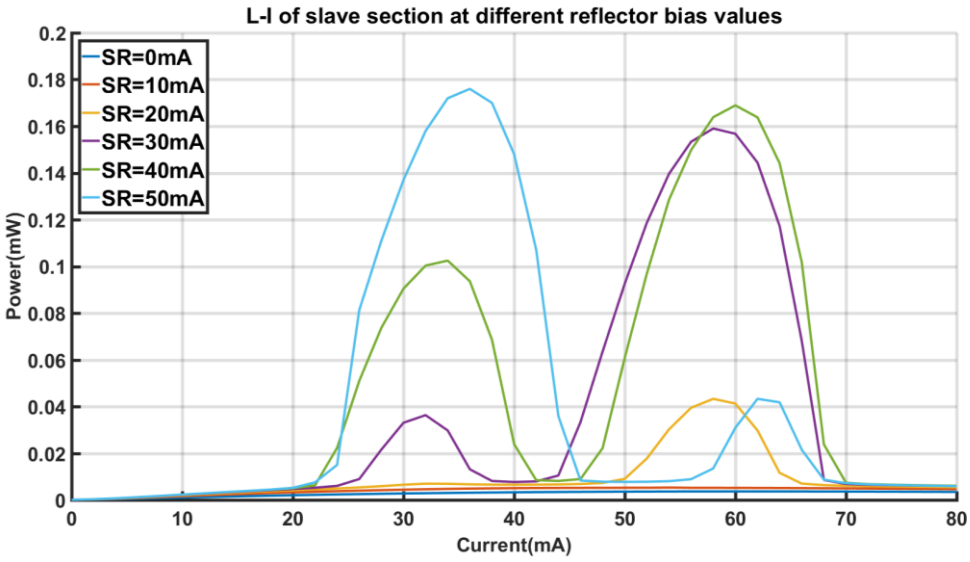

Figure 4.17: L-I curve of the slave laser at different bias values of the SR section.

From the plot, it can be concluded that the slave section only lases when the SR section is biased above 20 mA. When the reflector section is biased below this point, the loss inside the cavity surpasses the

gain and the device is not able to lase. Increasing the slave reflector sections bias results in increasing the value of the bias where the laser curve rolls off as shown in Figure 4.17. At SR bias values of 20 and 30 mA, the device needs a high bias SG value to start lasing. After reaching the 30mA bias level, increasing the reflector section bias results in the increase of the value of the threshold current of the slave laser. The threshold current of the slave laser is 22 and 24 mA for reflectors bias currents of 40 and 50 mA respectively.

Having identified the L-I curve of the device showing the stable operating regions, the next step is to show the independence of the master and slave lasers, and to show the capability of the device to achieve OIL.

Figure 4.18(a) shows the output optical spectrum of both the slave and master lasers of the PIC. It demonstrates the independent lasing of both lasers. The slave laser emits at 1544.5 nm (when it is biased at SR=70 mA, SG=55 mA), while the master lases at 1545.4 nm (when it is biased at MR1=25 mA, MG=45 mA, and MR2=25 mA). The VOA is biased at 10 mA to be in a transparency condition. The emission wavelength of each laser can be tuned by varying the bias current applied to the reflector sections of the corresponding laser. Fine tuning of these bias values leads to the OIL of the device. Figure 4.18(b) demonstrates the OIL condition of the device when the MR1, MG, MR2, VOA, SR, and SG sections are biased at 45, 20, 8.8, 15, 35, and 30 mA, respectively. As previously mentioned, on-chip optical injection provides several enhancements in the laser properties. One of the main advantages of optical injection is enhancement of the MBW of the laser and reduction of the chirp. This will be demonstrated in the next sections, where the frequency response of the device will be measured for both cases, with and without injection. Moreover, the device will be implemented in a short reach transmission system in order to examine the influence of the optical injection on the chirp levels of the device.

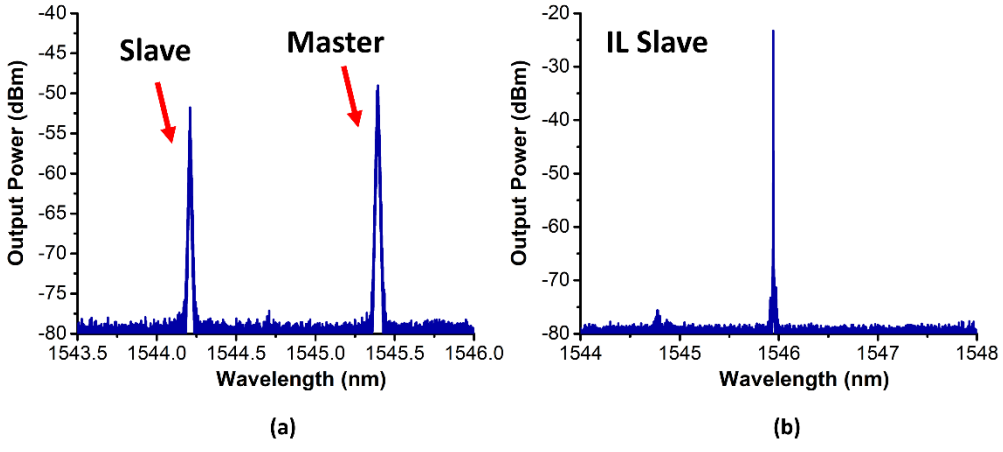

Figure 4.18: (a) CW spectrum of the master (biased at MR1=25 mA, MG=45 mA, MR2=25 mA) and slave (biased at SR=70 mA, SG=55 mA) lasers operating in single-mode operation, (b) Output spectrum after OIL is achieved.

A detailed characterisation of the linewidth and RIN of the device under different bias scenarios is expected to be carried out as a part of the future work on this device.

4.4.3 Dynamic characterisation

4.4.3.1 Modulation response measurement

The frequency response of the integrated laser is measured using different bias configurations to examine the influence of injection from the master laser on the MBW of the slave laser. The same setup as previously shown in Figure 4.10 is used for this purpose, where the small signal modulation signal from the VNA is injected into the SG section of the PIC in conjunction with its DC bias. The first step is to measure the frequency response of the slave laser on its own, using different bias configurations. The SR bias is kept constant at 30 mA, while the SG bias is tuned to 35, 40, 45, and 50 mA respectively. Both the master laser and the VOA sections bias are set to zero. Figure 4.19(a) shows the frequency response of the slave laser of the PIC biased at the aforementioned values.

From Figure 4.19(a), it can be noticed that the slave laser has a limited MBW. The best possible 3-dB MBW that was achieved in this measurement is 2 GHz when the SG is biased at 45 mA. The measurements were conducted for different bias values of the SG and SR sections and no improvements in the 3-dB MBW were achieved.

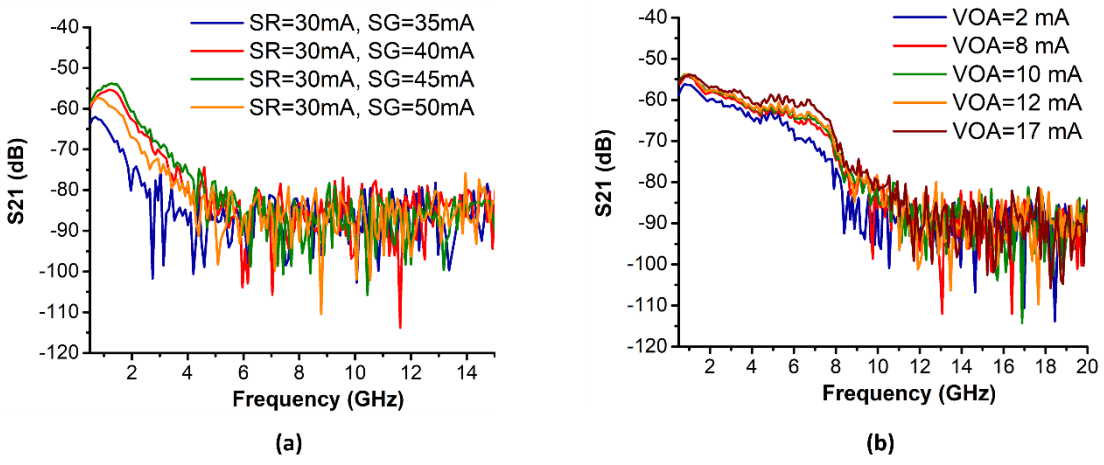

Figure 4.19: (a) Frequency response of the free running slave laser without injection from the master laser at different bias points and (b) Frequency response of the injection locked slave laser for different bias values of the VOA section.

The next step is to turn both the master and VOA sections on, and to examine their influence on the MBW of the slave laser. Figure 4.19(b) shows the laser frequency response at different bias values applied to the VOA section, while keeping the bias values to the other sections constant. The SG, SR,

MR1, MG and MR2 are biased at 35, 30, 44, 60 and 52 mA respectively. The positive influence of the on-chip injection on the frequency response of the laser can be easily noticed from the figure, where a steady increase in the 3-dB MBW is experienced when the VOA bias is increased gradually. Increasing the VOA bias results in lowering of the attenuation of the light injected from the master laser into the slave laser, which thereby improves the MBW of the slave laser. The 3-dB MBW is improved up to ~ 7.5 GHz when the VOA is biased at 17 mA. These results show the importance of having an accurate control on the injection levels from the master laser on enhancing the device performance.

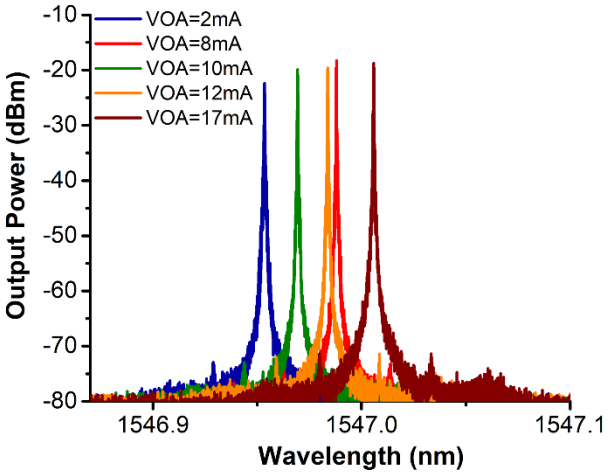

Figure 4.20: Optical spectrum of the injection locked slave laser for different bias values of the VOA section.

This is achieved by the introduction of the new VOA section, in which the injection level can be easily tuned by varying the bias applied to this section. Varying the VOA bias results in a change in the injection level from the master laser. However, it does not affect the emission wavelengths of neither the slave nor the master laser, as was the case in the 4-section PIC. This results in simpler achievement of injection locking. Furthermore, in order to confirm that the PIC was injection locked at different steps of the characterisation process, high resolution (0.2 pm) optical spectra of the different bias configurations were recorded and is shown in Figure 4.20 demonstrating that the PIC has been in OIL condition at different bias values used for the frequency response characterisation.

Having characterised the frequency response and the potential of the device to handle high speed modulation, a short reach transmission system experiment is conducted. The PIC (slave section) is directly modulated with an OOK signal and the modulated signal is transmitted over 25 and 50 kms of SSMF. The positive influence of the on-chip injection on improving the transmission reach (reduction of chirp) and the BER is highlighted.

4.4.3.2 Direct data modulation and transmission

A transmission experiment, mimicking a short reach system, is conducted using the same setup as shown in Figure 4.12, with the only exception that an avalanche photo diode (APD) is now used instead of a pin photodiode. This is mainly due to the nature of the experimental device being a bare chip, which results in high coupling losses leading to lower output levels of power that favours the APD as a photodetector which is able to detect lower power optical signals [35]. A 10.7 Gbit/s NRZ PRBS ($2^{15}-1$) signal with a peak-to-peak amplitude of 2V is used to modulate the SG section of the device using the AC input of a broadband bias-tee. Simultaneously, a DC-bias of 35 mA is applied via the DC input of the bias tee. The OIL bias point used in this system experiment is extracted from the frequency response measurements and is listed in Table 4.7 below.

Section	SG	SR	VOA	MR1	MG	MR2
Bias value	35 mA	30 mA	17 mA	44 mA	60 mA	52 mA

Table 4.7: Six section PIC OIL bias point for system experiment.

The experiment is carried out for three different transmission distances as follow: B2B, 25 and 50 km of SMF. The output results are demonstrated using eye diagrams generated from an oscilloscope, and BER curves calculated using an error detector.

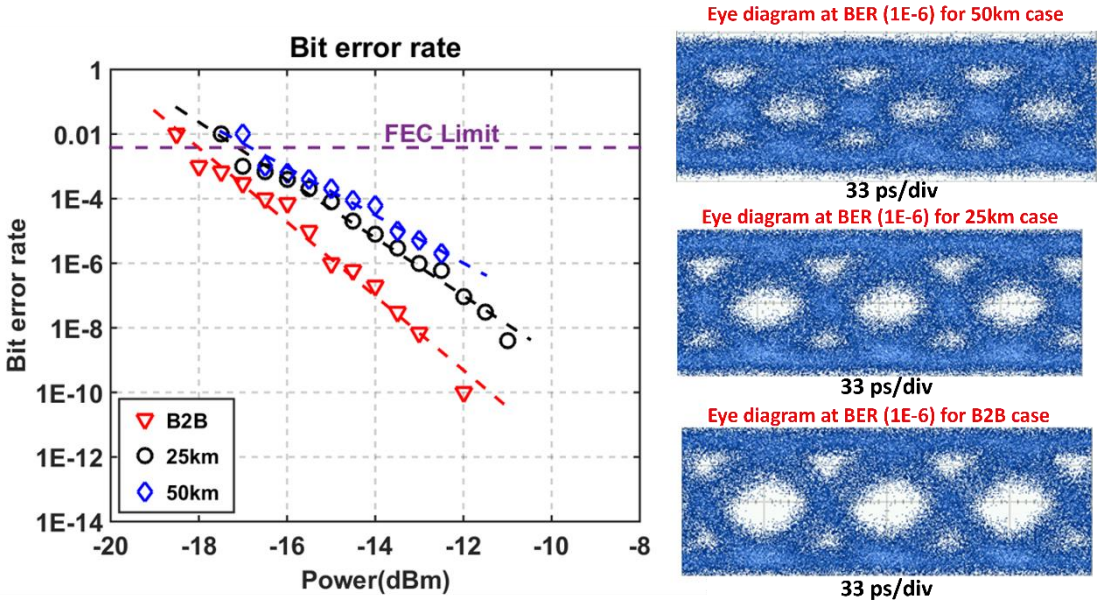

Figure 4.21: (a) BER vs. ROP curves for B2B (red) and after transmission over 25 (black) and 50 km (blue), (b) Corresponding eye diagrams at a BER of $1x1e^{-6}$ for the three different transmission scenarios.

Figure 4.21(a) shows the BER curve versus the received optical power (ROP) falling on the APD. The plot demonstrates that an error free performance (1×10^{-9}) for the B2B case can be achieved at an

ROP of -13 dBm. For the case of transmission over 25 km of SMF, the best achievable BER is 4×10^{-9} for an ROP of -11 dBm, while for the 50 km SMF transmission case, the lowest BER achieved is $1\ x\ 10^{-6}$ at an ROP of -12.5 dBm. In the latter case, this output power is the maximum achievable unamplified value from the device after experiencing approximately 10 dB attenuation due to transmission for 50 km of SMF. The coupled power is limited due to the free space coupling arrangement used in the experiment. It is anticipated that a packaged device would deliver error free performance through the improved coupling and thereby a higher power. It is expected that with higher ROP falling on the APD, the device can achieve an error free transmission even after transmission for 50 km of SMF. However, even at the current output power levels, error free performance at the FEC limit is achieved for the three different transmission scenarios. The power penalty at the FEC limit, with respect to the B2B case, for the 25 and 50 km SMF transmission is 1 dB and 2 dB respectively. Figure 4.21(b) shows three different eye diagrams illustrating the eye openings at different ROPs for the three different transmission scenarios. From the eye diagrams, it can be concluded that as expected, transmission over longer distances causes the eye opening to be smaller due to pulse broadening caused by the chromatic dispersion. However, as mentioned before, in this new PIC, the VOA section is implemented to control the injection levels from the master into the slave laser, which in turn results in a reduction of the introduced chirp levels. An increased chirp would result in a degradation in the achieved BER values [36]. On the other hand, there is a trade-off between chirp and ER. Injecting the slave laser would result in reduction of chirp, but on the same time in a reduction in the extinction ratio due to increase of average optical energy in logic “0”. Decreased ER results in receiver sensitivity degradation due to SNR degradation. Otherwise, decreased chirp improves the transmission distance by reducing the pulse broadening. So, a trade-off exists between increased chirp at higher ER and reduced SNR at lower ER [37]. To further confirm this matter, Figure 4.22 shows a high-resolution optical spectrum of the modulated PIC biased at the bias point listed in Table 4.7, but with varying bias values of the VOA section. The blue plot shows the case when the VOA section is biased at 2 mA, while the red plot shows the case when it is biased at 17 mA (the optimum point for enhancement of the PIC MBW).

It is clear that optimising the VOA bias results in a reduction of the chirp, as a direct result of the on-chip optical injection from the master laser.

The dynamic characterisation and the system experiment conducted using the improved six-section PIC clearly demonstrates the merits of introducing the middle VOA section that is sandwiched between the master and slave lasers. It provides a means of accurate control of the on-chip injection power levels, which with fine optimising, can result in improving the laser MBW and reducing the chirp levels. Furthermore, it balances the trade-off between the reduced chirp and reduced ER. In addition

to that, it provides a way of controlling the injection power without altering the wavelengths of the master or the slave lasers, which enhances the independence of both master and slave lasers. It is important to note that the device used in this work is a proof-of-concept device and was tested as a bare chip that caused some limitations in the nature of tests that could be carried out. A packaged PIC is expected to give a more stable and a better overall performance.

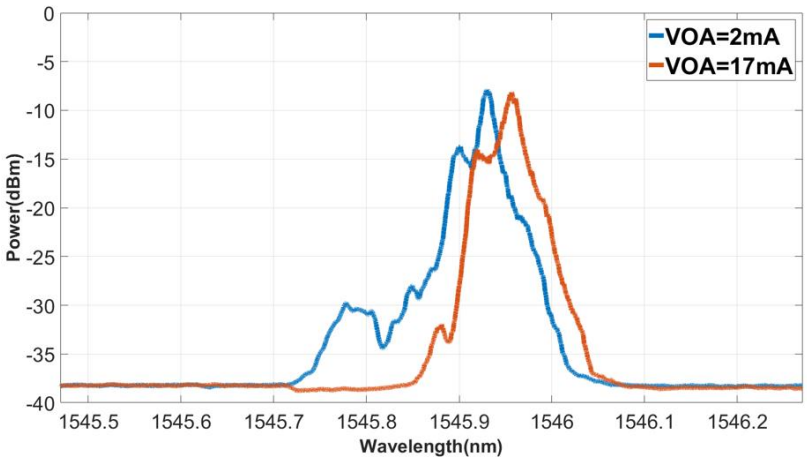

Figure 4.22: Optical spectrum of the modulated injection locked slave laser after transmission for 50 km at VOA section bias value of 2 mA (blue), 17 mA (dark orange).

4.5 Conclusions

Photonic integration provides a more compact, lower power consumption and footprint solution for next generation optical networks. PICs are expected to play an integral role in the development of next generation optical networks. Furthermore, photonic integration facilitates the mass production of various optical components in a single, simple platform, resulting in a decrease in the complexity of optical systems.

In this chapter, two different photonically integrated devices were presented, characterised and investigated to be employed as a transmitter in short reach transmission systems. Furthermore, the 4-section device were gain switched to generate a 6.25 GHz FSR OFC that exhibits 9 comb lines within 3 dB from the spectral peak and an OCNR of 46 dB.

The first device is an InP based PIC which comprises two lasers with different cavity lengths, that are integrated in a master-slave configuration, where the master laser injects its output light into the cavity of the slave laser to improve its characteristics. Different characterisation tests demonstrate the positive influence of the on-chip injection on the slave laser parameters such as the linewidth and RIN. Furthermore, the dynamic characterisation carried out shows that the OIL results in an enhancement of the laser MBW allowing the device to be used as a directly modulated transmitter.

Subsequently, the device is employed as a transmitter in a short reach transmission scenario, where it is directly modulated with a 10.7 Gb/s signal. The signal is transmitted for 25 kms of SSMF, and the positive influence of the on-chip OIL on the BER and the opening of eye diagrams is demonstrated. Subsequently, the device is gain switched to generate an OFC. Again, it is shown that the on-chip OIL results in expansion of the generated comb and an enhancement of its spectral properties.

The second device is an updated version of the 4-section device, where a VOA section is placed between the master and slave lasers to perform several functions. Varying the VOA bias results in a change in the injection level from the master laser. However, it does not affect the emission wavelengths of neither the slave nor the master laser, as was the case in the 4-section PIC. This results in better independence of the two different lasers (master and slave), which leads to simpler achievement of injection locking. Moreover, it acts as an isolation between the two lasers which reduces the coupled cavity effects. The influence of varying the VOA bias on the resultant MBW of the device is investigated, and it is shown that the fine optimising of this bias value can result in enhancement in the 3-dB MBW of the PIC. Again, the PIC is used a directly modulated transmitter in a short reach transmission scenario. It shows an error free performance (below the FEC limit) for a transmission distance of 50 km as a result of the reduction of chirp induced by achievement of better optical injection conditions from the master laser. The latter is achieved due to the presence of the VOA section which allows the accurate control of the injection power without having an influence on the emission wavelengths of the master and slave lasers.

The attractive features of photonic integration in terms of cost and power consumption, supported by the experimental characterisation results presented in this chapter qualifies the two multi-section PICs to be employed as a standalone directly modulated transmitter in next-generation optical short-reach networks. Moreover, it can be employed as a source of OFC generation that can be used also as a multicarrier transmitter for short reach networks applications.

As a next step, it would be great to have the six-section device packaged, to facilitate conducting a full characterisation in terms of linewidth and RIN. Moreover, it would be interesting to gain switch the device to generate an OFC. A detailed comparison between the two different OFCs generated from the two PICs can be compared in terms of bandwidth, flatness, phase noise and RIN of the generated tones.

References

[1] R. Essiambre and R. W. Tkach, “Capacity Trends and Limits of Optical Communication Networks,” *Proceedings of the IEEE,* vol. 100, no. 5, pp. 1035 - 1055, 2012.

[2] C. Kachris and I. Tomkos, “A Survey on Optical Interconnects for Data Centers,” *IEEE Communications Surveys & Tutorials,* vol. 14, no. 4, pp. 1021 - 1036, 2012.

[3] D. Liang and J. E. Bowers, “Photonic integration : Si or InP substrates,” *Electronics Letters,* vol. 45, no. 12, pp. 10-12, 2009.

[4] R. Soref, “The Past, Present, and Future of Silicon Photonics,” *IEEE Journal of Selected Topics in Quantum Electronics,* vol. 12, no. 6, pp. 1678-1687, 2006.

[5] C. Kopp, S. Bernabé, B. B. Bakir, J.-M. Fedeli, R. Orobtchouk, F. Schrank, H. Porte, L. Zimmermann and T. Tekin, “Silicon Photonic Circuits: On-CMOS Integration, Fiber Optical Coupling, and Packaging,” *IEEE Journal of Selected Topics in Quantum Electronics ,* vol. 17, no. 3, pp. 498 - 509, 2011.

[6] M. Ziari, B. Little, M. Kato, P. Evans, S. Chu, W. Chen, J. Hryniewicz, F. Johnson, W. Chen, D. Gill, O. King and D. Welch, “Large scale integration of photonic integrated circuits on indium phosphide and high-index-contrast Si platforms,” in *35th European Conference on Optical Communication*, Vienna, Austria, 2009.

[7] C. R. Doerr, “Integrated Photonic Platforms for Telecommunications: InP and Si,” *IEICE Transactions on Electronics,* vol. 96, no. 7, pp. 950-957, 2013.

[8] R. Piramidowicz, S. Stopinski, K. Lawniczuk, K. Welikow, P. Szczepanski, X. Leijtens and M. Smit, “Photonic integrated circuits : a new approach to laser technology,” *Bulletin of the Polish Academy of Sciences: Technical Sciences,* vol. 60, no. 4, pp. 683-689, 2012.

[9] N. Schunk and K. Petermann, “Noise analysis of injection-locked semiconductor injection lasers,” *IEEE Journal of Quantum Electronics,* vol. 22, no. 5, pp. 642-650, 1986.

[10] H. O. F. Mogensen and G. Jacobsen, “Locking conditions and stability properties for a semiconductor laser with external light injection,” *IEEE Journal of Quantum Electronics,* vol. 21, no. 7, pp. 784-793, 1985.

[11] H. B. S. Mohrdiek and H. Walter, “Chirp reduction of directly modulated semiconductor lasers at 10 Gb/s by strong CW light injection,” *Journal of Lightwave Technology,* vol. 12, no. 3, pp. 418-424, 1994.

[12] T. B. Simpson and J. M. Liu, “Enhanced modulation bandwidth in injection-locked semiconductor lasers,” *IEEE Photonics Technology Letters,* vol. 9, no. 10, pp. 1322-1324, 1997.

[13] M. D. G. Pascual, V. Vujicic, J. Braddell, F. Smyth, P. M. Anandarajah and L. P. Barry, “InP photonic integrated externally injected gain switched optical frequency comb,” *Optics Letters,* vol. 42, no. 3, pp. 555-558, 2017.

[14] Q. Lu, W.-H. Guo, D. Byrne and J. F. Donegan, “Design of Slotted Single-Mode Lasers Suitable for Photonic Integration,” *IEEE Photonics Technology Letters,* vol. 22, no. 11, pp. 787 - 789, 2010.

[15] C. Herbert, D. Jones, A. Kaszubowska-Anandarajah, B. Kelly, M. Rensing, J. O'Carroll, R. Phelan, P. Anandarajah, P. Perry, L. Barry and J. O'Gorman, “Discrete mode lasers for communication applications,” *IET Optoelectronics,* vol. 3, no. 1, pp. 1-17, 2009.

[16] P. M. Anandarajah, S. Latkowski, C. Browning, R. Zhou, J. O'Carroll, R. Phelan, B. Kelly, J. O'Gorman and L. P. Barry, “Integrated Two-Section Discrete Mode Laser,” *IEEE Photonics Journal ,* vol. 4, no. 6, pp. 2085 - 2094, 2012.

[17] H. Wenzel, M. K. M. Radziunas and U. Bandelow, “Semiconductor Laser Linewidth Theory Revisited,” *Applied Sciences ,* vol. 11, no. 13, p. 600, 2021.

[18] E. K. Lau, A. Lakhani, R. S. Tucker and M. C. Wu, “Enhanced modulation bandwidth of nanocavity light emitting devices,” *Optics Express,* vol. 17, no. 10, pp. 7790-7799 , 2009.

[19] J. P. Toomey, D. M. Kane, C. McMahon, A. Argyris and D. Syvridis, “Integrated semiconductor laser with optical feedback: transition from short to long cavity regime,” *Optics Express,* vol. 23, no. 14, pp. 18754-18762, 2015.

[20] K. Pipe, R. Ram and A. Shakouri, “The physics of heat transport in semiconductor lasers,” in *IEEE 18th International Semiconductor Laser Conference*, Garmisch, Germany, 2002.

[21] M. Mahdi, A. Ali, H. Alaa and M. Hussein, “Heat Effects on Data Transmission by Laser Diode and Light Emitted Diode for High Frequency Optical Communication Systems,” *Journal of Nanoscience and Technology,* vol. 2, no. 2, pp. 126-129, 2016.

[22] K. Kikuchi, “Coherent transmission systems,” in *34th European Conference on Optical Communication (ECOC)*, Brussels, Belgium, 2008.

[23] C. L. Tang, “Phase-Locking of Laser Oscillators by Injected Signal,” *Journal of Applied Physics ,* vol. 38, no. 1, pp. 323-324, 1967.

[24] X. Jin and S. L. Chuang, “Relative intensity noise characteristics of injection-locked semiconductor lasers,” *Applied Physics Letters ,* vol. 77, no. 9, pp. 1250-1252, 2000.

[25] H.-K. Lee, J.-H. Moon, S.-G. Mun, K.-M. Choi and C.-H. Lee, “Decision Threshold Control Method for the Optical Receiver of a WDM-PON,” *IEEE/OSA Journal of Optical Communications and Networking ,* vol. 2, no. 6, pp. 381-388, 2010.

[26] S. Kobayashi, Y. Yamamoto, M. Ito and T. Kimura, “Direct Frequency Modulation In AlGaAs Semiconductor Lasers,” *IEEE Transactions on Microwave Theory and Techniques,* vol. 30, no. 4, pp. 428-441, 1982.

[27] R. Maher, K. Shi, P. M. Anandarajah, A. Kaszubowska, L. P. Barry and Y. Yu, “Novel Frequency Chirp Compensation Scheme for Directly Modulated SG DBR Tunable Lasers,” *IEEE Photonics Technology Letters,* vol. 21, no. 5, pp. 340-342, 2009.

[28] L. Barry, P. Anandarajah and A. Kaszubowska, “Optical pulse generation at frequencies up to 20 GHz using external-injection seeding of a gain-switched commercial Fabry-Perot laser,” *IEEE Photonics Technology Letters,* vol. 13, no. 9, pp. 1014-1016, 2001.

[29] G.Yabre, “Effect of relatively strong light injection on the chirp-to-power ratio and the 3 dB bandwidth of directly modulated semiconductor lasers,” *Journal of Lightwave Technology ,* vol. 14, no. 10, pp. 2367-2373, 1996.

[30] C. Browning, K. Shi, S. Latkowski, P. M. Anandarajah, F. Smyth, B. Cardiff and L. P. Barry, “Increased Bit Rate Direct Modulation AMO-OFDM Transmission by Optical Injection Using Monolithically Integrated Lasers,” *IEEE Photonics Technology Letters,* vol. 24, no. 11, pp. 879 - 881, 2012.

[31] Q. T. Nguyen, P. Besnard, L. Bramerie, A. Shen, A. Garreau, O. Vaudel, C. Kazmierski, G.-H. Duan and J.-C. Simon, “Using optical injection of Fabry-Perot lasers for high-speed access in optical telecommunications,” in *SPIE Photonics Europe*, Brussels, Belgium, 2010.

[32] X. Zhao, L. Chrostowski and C. Chang-Hasnain, “Extinction ratio of injection-locked VCSELs,” in *The 17th Annual Meeting of the IEEELasers and Electro-Optics Society (LEOS)* , Rio Grande, PR, USA, 2004.

[33] S. Hwang and J. Tian, “Chirp reduction in directly-modulated semiconductor lasers subject to external optical injection,” in *IEEE LEOS Annual Meeting Conference Proceedings*, Sydney, Australia, 2005.

[34] D. Dhawan and N. Gupta, “Investigation of Tolerable Laser Linewidth for Different Modulation Formats in CO-OFDM Systems,” *Optics and Photonics Journal,* vol. 7, no. 5, 2017.

[35] R. McIntyre, “The distribution of gains in uniformly multiplying avalanche photodiodes: Theory,” *IEEE Transactions on Electron Devices,* vol. 19, no. 6, pp. 703-713, 1972.

[36] Y.-C. Chi, C.-C. Lin, H.-C. Kuo, P.-C. Peng and G.-R. Lin, “Bit-error-rate and chirp analyses of a gain-switching VCSEL based all-optical NRZ-to-RZ converter,” in *International Conference on Photonics in Switching*, Sapporo, Japan, 2008.

[37] G.-Y. Kim and Y.-G. Lee, “The influence of chirp and extinction ratio on directly modulated DFB lasers,” in *4th Pacific Rim Conference on Lasers and Electro-Optics (CLEO/Pacific Rim)*, Chiba, Japan, 2001.

[38] D. F. Welch, F. A. Kish, S. Melle, R. Nagarajan, M. Kato, C. H. Joyner, J. L. Pleumeekers, R. P. Schneider, J. Back, A. G. Dentai, V. G. Dominic, P. W. Evans, M. Kauffman and D. J. H. Lambert, “Large-Scale InP Photonic Integrated Circuits: Enabling Efficient Scaling of Optical Transport Networks,” *IEEE Journal of Selected Topics in Quantum Electronics,* vol. 13, no. 1, pp. 22 - 31, 2007.

[39] Cisco, “Cisco Annual Internet Report (2018–2023) White Paper,” 9 March 2020. [Online]. Available: https://www.cisco.com/c/en/us/solutions/collateral/executive-perspectives/annual-internet-report/white-paper-c11-741490.html. [Accessed May 2021].

[40] J. Baliga, R. Ayre, K. Hinton, W. V. Sorin and R. S. Tucker, “Energy Consumption in Optical IP Networks,” *Journal of Lightwave Technology,* vol. 27, no. 13, pp. 2391-2403, 2009.

[41] D. Dhawan and N. Gupta, “Investigation of Tolerable Laser Linewidth for Different Modulation Formats in CO-OFDM Systems,” *Optics and Photonics Journal,* vol. 7, no. 5, 2017.

[42] M. Li, R. Hu, J. Xia, Q. Yang, X. Xiao, C. Li, X. Li and S. Yu, “Cost-effective coherent PON using silicon Mach-Zehnder modulator and digital carrier regeneration,” *Optics Express,* vol. 23, no. 15, pp. 19799-19805, 2015.

[43] A. Wiberg, P. Perez-Millan, M. Andres, P. Andrekson and P. Hedekvist, “Fiber-optic 40-GHz mm-wave link with 2.5-Gb/s data transmission,” *IEEE Photonics Technology Letters ,* vol. 17, no. 9, pp. 1938-1940, 2005.

[44] T. Koch and U. Koren, “Semiconductor photonic integrated circuits,” *IEEE Journal of Quantum Electronics,* vol. 27, no. 3, pp. 641 - 653, 1991.

[45] B. Pezeshki, D. Thomas and J. S. H. Jr., “Optimization of modulation ratio and insertion loss in reflective electroabsorption modulators,” *Appl. Phys. Lett,* vol. 57, p. 1491, 1990.

[46] C. Browning, K. Shi, S. Latkowski, P. M. Anandarajah, F. Smyth, B. Cardiff and L. P. Barry, “Increased Bit Rate Direct Modulation AMO-OFDM Transmission by Optical Injection Using Monolithically Integrated Lasers,” *IEEE Photonics Technology Letters,* vol. 24, no. 11, pp. 879-881, 2012.

Chapter 5

Gain switching of passive feedback laser for generation of an expanded OFC

5.1 Introduction

Further to the detailed discussion on optical frequency combs and its generation using externally injected gain switched lasers, chapters 3 and 4 focused on the merits of employing photonic integrated circuits to realise the master slave configuration (required to realise external optical injection). In the previous chapter, two different PICs in a master-slave configuration were proposed to be utilised as directly modulated (multi-carrier and short reach) transmitters. The discussion was expanded to include many advantages that such PICs could offer, which included compactness, low cost, and low power consumption. Moreover, the capability of such devices to achieve OIL, to improve the different laser characteristics such as the linewidth, RIN, and frequency response was proved.

In this chapter, another multi-section photonically integrated device is presented. The passive feedback laser (PFL) [1] comprises an active and a passive section, each of which can be biased separately. The passive section reflects a portion of the light emitted by the active section. The power and the phase of the feedback are controlled by the bias of the passive section. As aforementioned in Section 2.3.4.3.2 in Chapter 2, self-seeding provides a simple method to achieve the generation of optimum optical pulse with enhanced spectral

properties. As opposed to the external injection, there is no need for the usage of an external source of injection. A typical external optical injection setup comprises several discrete passive and active components. For the successful realisation of a master-slave configuration, different components such as circulators, polarisation controllers, fibre patch cords, master, and slave lasers are required. Such a setup arrangement consisting of these components would potentially suffer from different sources of instabilities, mainly due to polarisation dependence in case of usage of SMF. PMF based components could have the potential to avoid the polarisation dependence issue. However, the setup will still suffer from temperature variation in the injection path. Moreover, the usage of several discrete components would result in a higher values of insertion loss and an elevated implementation cost.

An alternative solution is the usage of the self-injection technique, where there is no need for an external master laser source. In addition to the aforementioned enhancements in the spectral properties of the laser as a result of the optical injection, self-injection provides more merits in terms of robustness, lower cost and lower footprint.

Experimental and computational results of static and dynamic characterisation of the PFL are highlighted in order to show the influence of the self-seeding signal on different laser characteristics. As the focus of the work proposed is on using such devices for optical frequency comb generation, the device is subsequently gain switched. The generated OFC under different bias and feedback configurations is characterised.

5.2 Self-seeding concept

In Chapter 2, optical injection has been demonstrated to provide enhancement to the spectral properties of the semiconductor lasers. The injected laser would inherit the superior spectral properties of the purer master laser. Using the same general concept, the semiconductor laser can be injected/seeded using its own signal in place of an external laser source. In this case, the laser can be referred to as “self-injected or self-seeded”. Several reports have demonstrated the capability of self-injection to improve the laser spectral properties such as achieving a narrower linewidth or a reduced phase noise [2]. Thus, self-injection can provide the same merits of traditional optical injection employing an external laser source in addition to improving the associated cost and footprint due to the elimination of the external seeding source. Photonic integration of a self-seeding setup in a single chip would provide even a more compact solution. An integrated self-seeding device is a

promising alternative to the OI discrete setup, providing a simpler and cheaper solution that is polarisation independent and has a lower footprint [3]. Previous reports have shown the capability of improving semiconductor lasers intrinsic performance by utilising self-seeding feedback. In [1], the authors demonstrate a significant improvement of the MBW at low-injection currents in a PFL device under the influence of optimised feedback. Furthermore, this improvement allows the achievement of a 40 Gbit/s open eye transmission with an extinction ratio of 6 dB [4]. In [5], the authors demonstrated an enhancement of 57% in the MBW and 9 times reduction in the laser linewidth as a result of an optimised self-optical injection locking.

The operation principle of self seeding has been explained in details in Section 2.3.4.3.2 in Chapter 2

5.3 Passive feedback laser

5.3.1 Device structure

A schematic of the fully integrated PFL is shown in Figure 5.1(a). It is a two-section device comprising a DFB laser and an integrated feedback (IFB) segment. Each of the sections have an independent bias. The IFB section is terminated by a high reflectivity coated facet, which provides a strong feedback signal. Hence, the amplitude and phase of the feedback signal is controlled by the IFB bias current. The DFB section facet is AR coated, which results in the laser power being emitted only from that end as shown in Figure 5.1(a). The total length of the integrated device is 330 µm, with the length of the DFB section being 150 µm and the IFB section being 180 µm.

Figure 5.1(b) shows a photograph of the physical device. It is custom packaged in a 7-pin temperature-controlled butterfly encasing with a high-speed RF connector attached to the active DFB section that allows direct modulation of the device. As in the Figure 5.1, the package is placed on an aluminium mount for ease of handling and experimental characterisation.

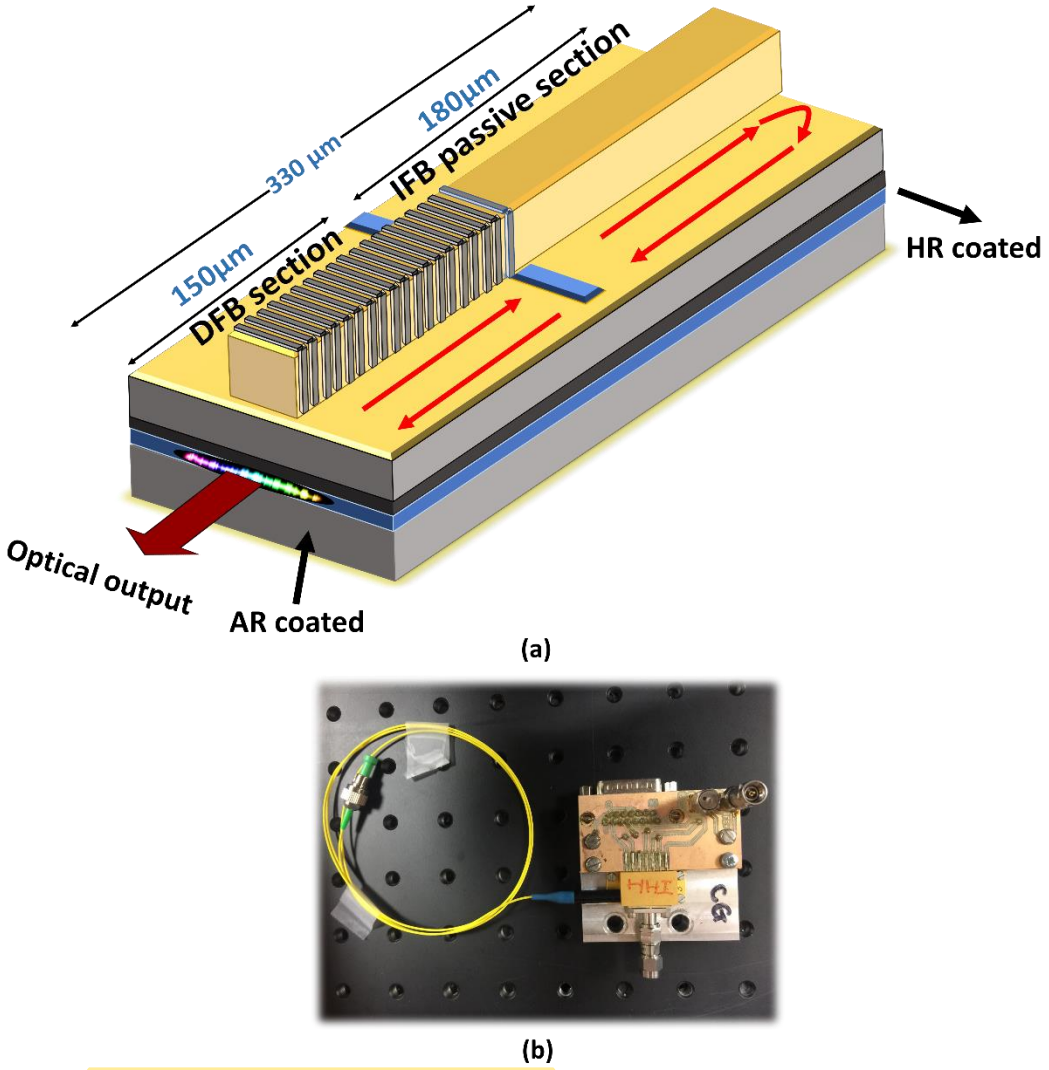

Figure 5.1: (a) Schematic diagram of the PFL, (b) Photograph of the packaged PFL.

5.3.2 Static characterisation

5.3.2.1 Basic characterisation

The initial characterisation, in this section, shows the L-I curve of the device at two different bias scenarios as shown in Figure 5.2(a). When the IFB section is turned off (IFB bias=0 mA), the device exhibits a threshold current of 4.5 mA. Biasing the IFB section at 4.25 mA results in the increase in the threshold value to be 6 mA. The sudden drop in the red plot (IFB biased at 4.25 mA) can be attributed to the low-frequency fluctuation (LFF), in the LFF region, the laser output intensity displays irregular, apparently random, and sudden dropouts as described in [6]. Also, the Figure 5.2(b) shows the output optical spectra of the device obtained when the DFB section is DC biased at 50.3 mA and IFB section current is swept. The device temperature is kept constant at 20°C throughout the different measurements for consistency. The spectra are recorded using a high resolution (20 MHz) OSA. The plot shows

that by varying the IFB section current, there is a change in both the emission wavelength and the output power of the device. As per the analytical analysis in [1], there exist different regions of resonance frequency depending on the phase of the feedback signal. Varying the bias applied to the IFB section would result in variation of the phase. Hence, the resonance frequency is varied causing a change in the emission wavelength. When the IFB section is turned off, the carrier photon resonance (CPR) is dominant. Increasing the bias of the IFB section would result in variation of the signal phase leading to the photon photon resonance (PPR) becoming dominant. The latter causes the variation in the resonance frequency and the emission wavelength. The IFB section bias variation results in moving the DFB mode to a lower wavelength. This behaviour can be compared to the external injection case, where the master laser emission wavelength is detuned from the free-running slave laser wavelength [7]. In that sense, the variation of the bias of the IFB section results in a change in a phase change of the feedback signal. This phase variation causes a variation in the resonance frequency due to the laser entering a region where the PPR is dominant over the CPR causing a frequency detuning of the feedback injection coming from the passive section. This detuning can also be considered as the predominant reason for the improvement in MBW as will be discussed in the device dynamic characterisation section in the latter part of this chapter. The position of the lasing wavelength relative to the feedback spectrum of the reflector section depends on the refractive index difference between both sections, which changes if the carrier densities vary [8].

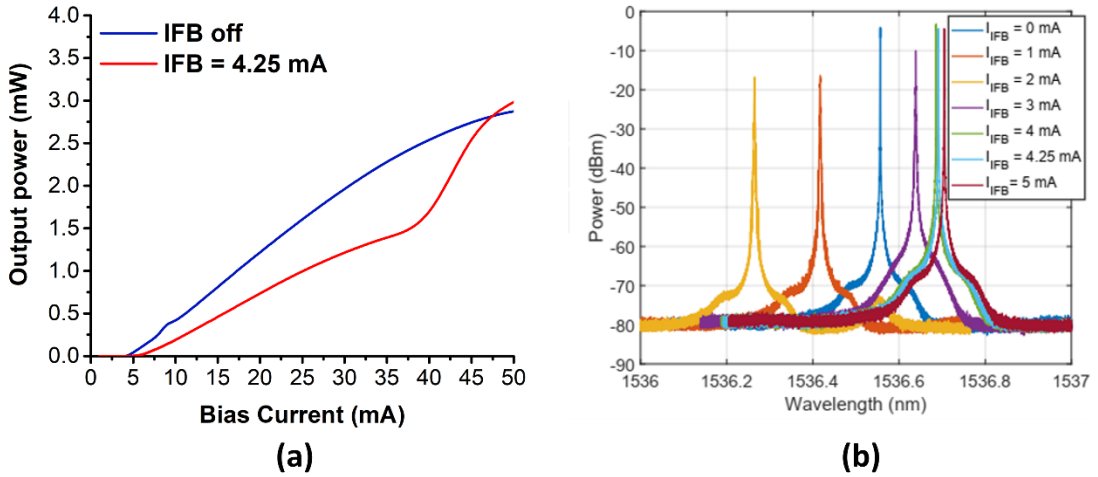

Figure 5.2: (a) L-I curve of the PFL device with the IFB section turned off and biased at 4.25 mA, (b) Optical spectra of the PFL device with the DFB section biased at 50.3 mA while the IFB section bias is tuned from 0 to 5 mA.

The phase and the power of the feedback signal can be easily controlled through varying the bias applied to the IFB section. Depending on the bias applied to the section, the carrier density is varied. Hence, the phase and the strength of the feedback section is varied [9].

Tuning the phase (via varying the bias applied to the passive section can result in a phase that matches the phase of the signal being emitted by the DFB section. This scenario would result in constructive interference with the DFB laser signal [1] improving different intrinsic laser parameters such as laser linewidth, RIN and MBW.

In order to gain a deeper understanding of the behaviour of the device, contour plots of the main mode peak power and emission wavelength versus bias currents of the DFB and IFB sections are generated. A python script is used to automate control on the bias and temperature controller, and the OSA.

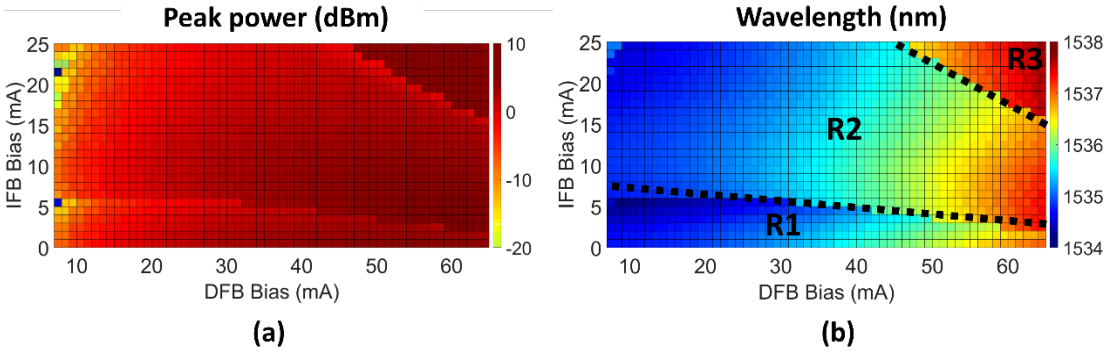

Figure 5.3: Varying DFB and IFB bias values with the resultant contour plots of (a) Peak power of the main mode, (b) Wavelength of the main mode.

Figure 5.3(a)&(b) show the contour plots of the peak power and wavelength of the main mode, as a function of the DFB and IFB bias currents. The presented contour plots provide a clear roadmap for determining the optimum operating bias points for both sections of the device. For the DFB, the bias current is varied from 7 to 65 mA, while for the IFB, it is varied from 0 to 25 mA. The maximum bias limits are as per the recommendations of the manufacturer. In Figure 5.4(a), it can be observed that the DFB has a threshold of ~7 mA, when the IFB bias is set to 0 mA. The threshold value decreases with an increase of the IFB section bias. This can be related to the larger absorption that the light experiences passing through the passive section when it is biased at lower values. This behaviour can be seen across different areas of the contour plot, except for the areas that have an abrupt step change of colour, where two different modes are competing for power.

Figure 5.3(b) allows the identification of three different wavelength regions of the device (marked as R1, R2, and R3 in the plot). The wavelength of the device can be tuned gradually over a ~3.5 nm range (1534 to 1537.5 nm), by varying the bias currents of both sections. In R2, there is a gradual change in the wavelength of the main mode as a result of the temperature changes due to the Joule effect caused by the increase of the bias currents supplied to both sections [10]. On one hand, the increase in bias currents raises the

temperature of the active layer of the laser, which leads to a redshift in the device wavelength [11]. On the other hand, at the region of low currents of DFB (<20 mA) and IFB (<5 mA), increasing the bias on the IFB section results in a raise in the bandgap energy leading to a carrier induced effect on the refractive index of the laser causing a slight blue shift of the wavelength [12]. The temperature effect on the refractive index supersedes the carrier induced effect, which eventually results in a red shift. Mode hopping defined as the temporal variations of the mode powers exhibiting random switching by nonlinear coupling among them [13], occurs in two different regions (R1 and R3) and is marked by the abrupt step change of the colour. In a WDM communication system, the mode hopping can cause power fluctuations and transmission on a different wavelength, which may lead to undesired interference among the different channels, eventually causing a deterioration of the system performance [13]. Hence, the device should not be operated at bias points where mode hopping is experienced. The presented contour plots provide a clear roadmap for determining the optimum operating bias points for both sections of the device, ensuring a single-mode emission, with a high output power and no mode hops.

5.3.2.2 Linewidth and RIN experimental characterisation

Linewidth measurements

Linewidth measurements are conducted on the PFL using the same DSH technique mentioned in Section (3.4.2.1) in Chapter 3 with a 50 kHz resolution.

The first step is to examine the PFL linewidth with the DFB biased using an ITC 502 benchtop laser driver (LD) (with an RMS noise of <1.5µA according to the specifications) and the IFB biased using Thorlabs LDC205C LD (with an RMS noise of <3µA according to the specifications). In Figure 5.4(a), the blue plot represents the case with no feedback (IFB bias = 0 mA) while the red plot represents the case when the IFB is biased at 0.7 mA. With the current controllers / laser drivers used, 0.7 mA is found to be the optimum IFB bias point for obtaining the lowest linewidth relative to any other IFB current. The low output power can be attributed to the low power in the beat tone sent to the photodiode. This is because of the different losses incurred in the different parts of the DSH setup, and it is not relevant to the integrity of the measurements. For the first case where the IFB is biased at 0 mA, the laser has an 8.45 MHz linewidth. For the second case where the IFB is biased at 0.7 mA, the laser linewidth increases to be 21.45 MHz. This result is opposite to what is expected, as the optimised feedback (where there is a phase match between the feedback signal and the laser main signal) should result in the reduction of the laser linewidth as reported by various

research efforts previously conducted [14], [15], [16]. The wider optical linewidth can be attributed to the noise of the LD used to bias the IFB section. It is well known that the noise of the current source contributes to a wider optical linewidth. According to [17] [18], as the current fluctuations are increased, the linewidth shape should tend from the standard Lorentzian to a Gaussian. The rate at which the linewidth increases is according to the square of the fluctuations for low values of standard deviation of the current noise, but as the noise becomes larger, the dependence becomes linear. Hence, this current source (Thorlabs LDC205C) (RMS noise of <3μA) is replaced by an ultra-low noise LD (Koheron DRV110-A-375), with a much lower RMS noise of ~ 265 nA.

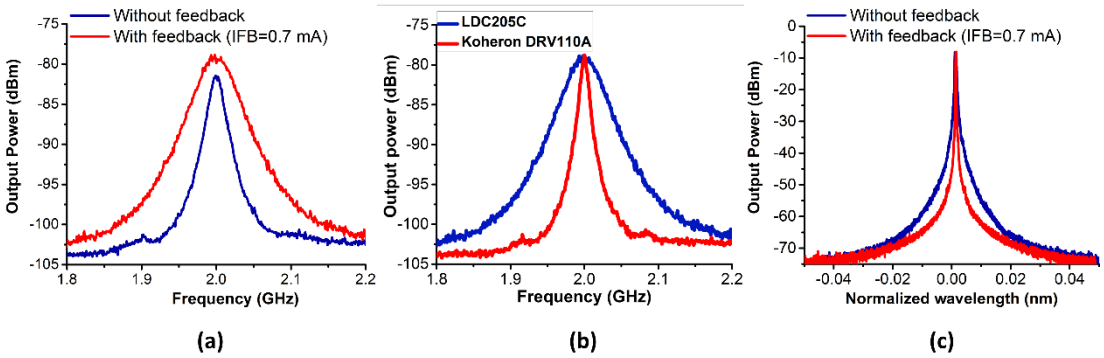

Figure 5.4: (a) PFL linewidth for the DFB biased at 55 mA using ITC 502 laser driver (LD) with the IFB turned off (blue) and biased at 0.7 mA using Thorlabs LDC205C LD (red), (b) PFL linewidth for the DFB biased at 55 mA using ITC 502 laser driver, IFB biased at 0.7 mA using Thorlabs LDC205C laser driver (blue) and Koheron DRV110-A-375 LD (red), and (c) Normalised 0.1 nm span optical spectra for the without (blue) and with feedback (red) cases.

Figure 5.4(b) shows a comparison of the generated linewidth using the two different current sources (LDC205C & DRV110-A-375) on the IFB section while the DFB section uses the ITC 502 LD. The two sections are biased at the same point (DFB = 55 mA, IFB = 0.7 mA). The ultra-low noise LD (DRV110-A-375) generates a much narrower linewidth, of 4.35 MHz as denoted by the red plot in Figure 5.4(b), in comparison to the blue plot in the same figure which shows the 21.45 MHz linewidth due to the other current source (LDC205C). It is evident that there is a significant reduction in the linewidth when the ultra-low noise LD is used. The reason for this is that beside the typical factors determining the linewidth of the laser such as the fraction of the spontaneous emission coupled into the lasing mode, the phase-amplitude coupling factor and the carrier density fluctuations in the cavity, there exists another important factor which is the current noise of the LD. The bias current supplied by this driver is responsible for changing the laser refractive index [19] and consequently, the wavelength of the laser. The noise component of this current translates into lasing frequency fluctuations contributing to the overall measured linewidth [20]. Moreover, the IFB passive section has a higher sensitivity to low frequency noise than the active section, which results in the

broadening of the laser linewidth. This is because there are two main sources of the low-frequency noise: the 1/f noise [20] and the injection recombination shot noise (IRSN) that is particularly present in the passive tuning sections of the laser [21]. In the active sections, the IRSN is usually suppressed by the gain saturation [22]. However, the passive laser sections suffer from refractive index fluctuations, that are generated as a result of the carrier fluctuations not being damped by the radiation carrier interaction [23]. This effect then results in a widening of the laser linewidth that is not dependant on the optical power of the laser [23]. Hence, this is considered as the limiting reason for not achieving a narrow linewidth in the order of kHz using the feedback from the integrated passive section. Moreover, the obtained results suggest that the low frequency noise generated from the laser driver has more impact on the phase noise generated by the IFB section than the photon noise. According to that, we proceed with our measurements, using the ultra-low noise current source to bias the passive section. Figure 5.4(c) shows the output optical spectra of the PFL with the DFB biased at 55.55 mA and the IFB biased at 0 mA (blue) and 0.7 mA (red) plotted on a normalised wavelength axis, with the emission wavelength of the laser, for each biasing point, corresponding to 0 nm. The resulting spectra shown in the figure, clearly show the reduction in the laser linewidth due to feedback. However, the measured linewidth (MHz) is still higher than the expected linewidth (kHz). To have more clarification on this issue and to confirm the possibility of achieving a narrow kHz order linewidth experimentally, we conduct another linewidth measurement of the PFL device using an external loop to affect the self-seeding as shown previously in Figure 5.1. The filter shown in the diagram was not used as the PFL consists of a DFB (single mode) laser.

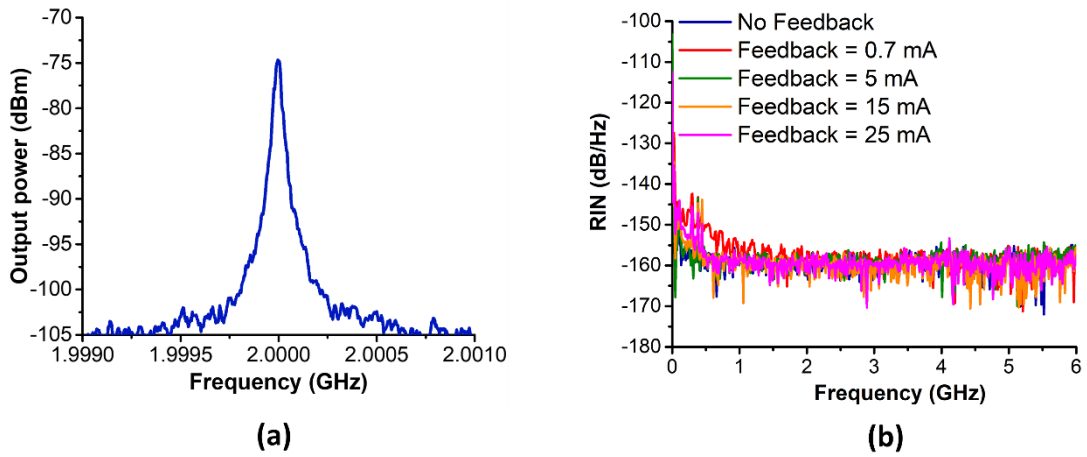

Figure 5.5: (a) PFL linewidth when the device is self-seeded with the aid of an external cavity, (b) RIN values (0-6 GHz) of the PFL with DFB biased at 55.5 mA and IFB biased at 0, 0.7,5,15 and 25 mA.

A tunable optical delay is inserted in the path to optimise the phase of the feedback. The DFB bias is kept constant at 55.55 mA and the IFB is turned off to minimise its influence on the

laser linewidth. Again, the measurements are carried out using the DSH technique, with a resolution of 50 kHz. This time, the measured linewidth of the PFL device under the influence of external self-seeding is 65 kHz as shown in Figure 5.5(a). This value is similar in order of magnitude to what is expected and have been shown in previous reports applying a similar external loop/cavity technique. This result highlights on one hand, the effectiveness of self-seeding in reducing the linewidth of the PFL laser to kHz order, on the other, the significant difference between the feedback from an external cavity and that provided by the integrated passive section. The internal noise generated in the passive section can be considered as the limitation, that is preventing the PFL to have much lower linewidth values (kHz order) when applying the integrated feedback.

RIN measurements

The next step is to measure the RIN of the PFL at different bias scenarios.

IFB Bias point (DFB biased at 55.55 mA)	**Obtained Averaged RIN value (0-6 GHz) (dB/Hz)**
0 mA	-159.281
0.7 mA	-157.44
5 mA	-158.596
15 mA	-159.798
25 mA	-159.021

Table 5.1: Measured averaged RIN values for the PFL (DFB biased at 55.5 mA and IFB bias is varied from 0 to 25 mA).

The RIN is measured using the same setup diagrams and equations, that is previously described in Section 3.4.2.2 in Chapter 3. Figure 5.5(b) shows the obtained RIN of the PFL for the DFB biased at 55.55 mA and the IFB bias at 0, 0.7, 5, 15, and 25 mA respectively. The obtained averaged RIN values (0-6 GHz) for the different bias scenarios are listed in Table 5.1. There is no direct influence of the feedback on the RIN, whose value remains similar except for the lower frequency region (<1 GHz). This can be attributed to the noise of the electronics used in the measuring setup. In all bias scenarios presented, the device generates a low RIN value (<-150 dB/Hz) at frequencies > 1 GHz that qualifies it as a potential candidate to be used in systems employing multilevel intensity schemes [24]. It is important to note that ROF of the laser is higher than the bandwidth of the ESA used. As a result, the noise peak corresponding to ROF does not appear in the RIN measurements plots shown in Figure 5.5(b).

Having examined the effect of the integrated feedback on the generated linewidth and RIN values of the PFL device, the next step entailed the examination of the influence of the

feedback on the frequency response and MBW of the device by conducting a series of dynamic characterisations.

5.3.3 Dynamic characterisation

Direct modulation presents a simpler, lower-cost alternative solution to external modulators which are both bulky, have a high insertion loss, and can lead to a higher cost. Direct modulation is achieved by adding the data signal to the bias current of the laser [25] resulting in an intensity modulation of the laser output power. However, the achievable data rates are limited, due to the intrinsic MBW of the laser which is restricted by the conventional CPR phenomenon [26]. There have been several techniques proposed for extending the MBW. Amongst them, external optical injection has been reported to extend the laser modulation bandwidth by up to three times [27] [28]. PICs implementing on-chip injection through an integrated master-slave configuration have also been reported to extend the MBW of the slave laser [3].

The frequency response of the PFL is measured using the same setup diagram shown in Figure 4.10 in Chapter 4. A RF signal at a power of -10 dBm, with a frequency that is swept between 0.045 to 40 GHz, is generated using a vector network analyser (Agilent Technologies E8363A) and applied to the PFL through the RF connector attached to the DFB section. The output of the laser is then detected using a 50 GHz photodetector (Finisar XPDV21x0R) and connected to port 2 of the VNA to measure the S21 parameter (i.e., the frequency response) of the PFL.

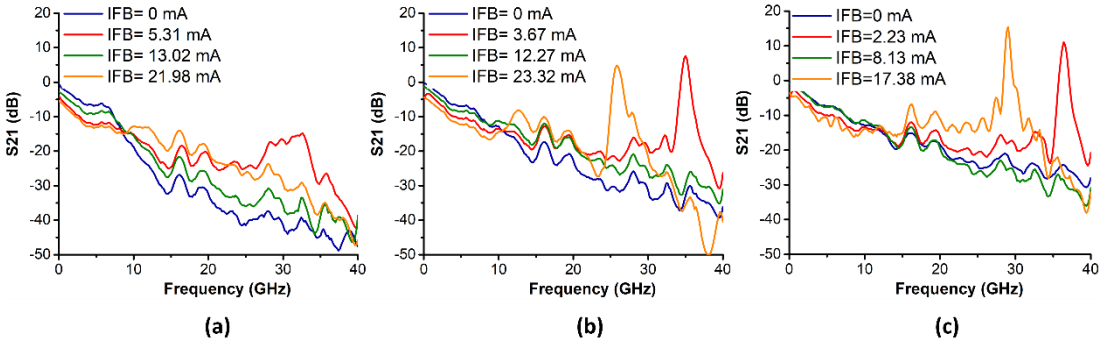

Figure 5.6: Measurements of the PFL's frequency response with the following bias conditions: (a) DFB = 25 mA, IFB = 0, 5.31, 13.02, and 21.98 mA, (b) DFB = 45 mA, IFB = 0, 3.67, 12.27, and 23.32 mA, and (c) DFB = 55 mA, IFB = 0, 2.23, 8.13, and 17.38 mA.

The measurement is performed for three different DFB bias currents: 25, 45 and 55 mA whilst varying the IFB bias at each of the DFB bias currents. Figure 5.6(a-c) show the results together with the values of the IFB currents used. For the DFB bias of 25 mA, the best frequency response featuring a wide ROF peak around 31 GHz, is obtained for an IFB current of 5.31

mA. Beyond that value this peak diminishes, however there is a moderate improvement in the 3-dB MBW of the laser, from 8.2 GHz (minimal feedback with IFB at 0 mA) to 13.9 GHz at IFB of 21.98 mA. For higher DFB biases, the enhancement in the frequency response becomes more pronounced and occurs at higher frequencies (35 GHz for DFB section biased at 45 mA and 36.4 GHz for DFB section biased at 55 mA). The plots also show that as the DBF current is increased, the bias of the IFB section that provides the peak at the higher frequency reduces. This suggests that the peak happens at a certain feedback level: as the bias to DFB section increases so does the output power of the laser. Thus, the same feedback level is obtained at a lower IFB bias. While a laser with such a peaky frequency response is not ideal for application as a directly modulated transmitter, however it is ideally suited for the generation of OFCs using gain switching, which will be investigated in the next sections of this chapter. Gain switching favours the high response (peak) at a given frequency value. On the other hand, direct modulation favours a more linear frequency response curve. Prior to showing the results of gain switching the PFL, a simulation model will be presented to explain and understand the operation of such a laser in more detail.

5.3.4 Simulation model

To gain a better understanding of the impact of the power level and phase shift of the feedback on the performance of the PFL, a simulation model is constructed using VPItransmissionMaker™ software. It consists of an active DFB laser, a reflective coupler and a delay signal link component. The latter is a VPItransmissionMaker™ module (an optical fibre) that controls the time delay, over the feedback path, as shown in Figure 5.7(a).

The value of the phase shift can also be varied through the phase shift parameter implemented in the same component. The simulation parameters used for this model are listed in Table 5.2. They correspond to the physical parameters of the physical device that has been used in the experimental characterisations highlighted earlier in this chapter. The carrier capture time constant and linewidth enhancement factor values were obtained from [1].

First, we measure the L-I curve of the DFB laser, with no feedback. As can be seen from the blue plot in Figure 5.7(b), the stand-alone DFB laser has a threshold of 15 mA. Next step is to apply the feedback signal and to optimise its level (by changing thereflectivity of the coupler) to achieve a reduction in the threshold value [29] [30].

The reduction in the threshold can be attributed to re-injection of optical signal from the feedback path. The red plot in Figure 5.7(b) shows that the minimum threshold of 5 mA is obtained for a feedback level of -10 dBm. Finally, the optical delay in the feedback path is varied and the corresponding effect on the laser LI curve is observed. Setting the delay to 1.15 ps does not cause a change in the threshold current value. However, it slightly increases the slope of the LI curve, as shown by the green plot in Figure 5.7(b). The calculated slopes for the L-I curves of the three cases (no feedback, -10 dBm feedback without and with 1.15 ps delay) are 0.4, 0.38 and 0.42 mW/mA respectively. The 1.15 ps delay corresponds to a cavity length of 175 µm according to the following

equation $t = \frac{2L}{C}$ where t is the time delay that the signal experiences inside the cavity, L is the cavity length and C is the speed of light in the semiconductor material. This particular length is chosen as it corresponds to the length of the IFB section of the physical device used in the experiment. Having decided about the optimum parameters for the simulated model, we now move to measure the linewidth of the simulated model with and without the influence of the feedback.

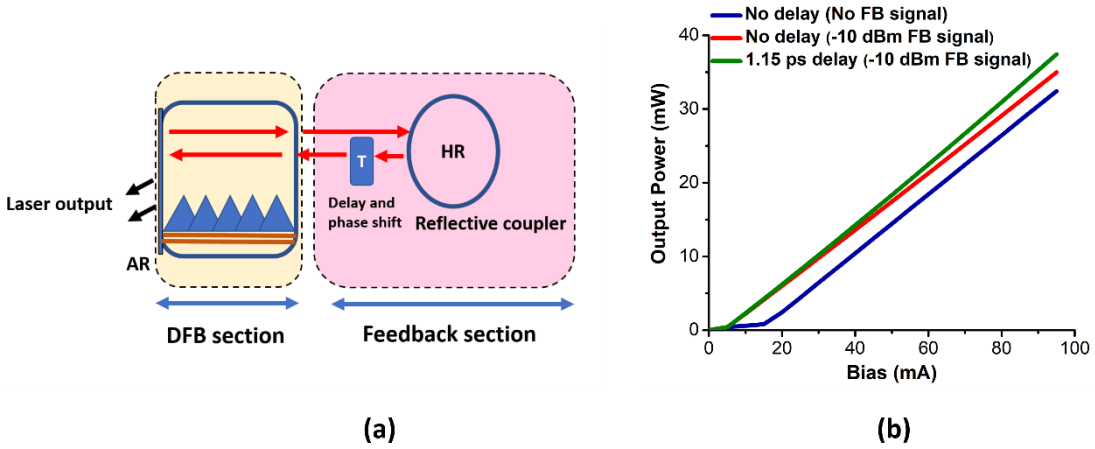

Figure 5.7: (a) Schematic diagram of a PFL VPItransmissionMaker™ simulation, (b) L-I curves of the PFL for: no delay and no feedback (blue), no delay and -10 dBm feedback level (red) and 1.15 ps delay and -10 dBm feedback level (green).

Parameter	Value
DFB section length	160 µm
Active region width	2.5 µm
Carrier capture time constant	20 ps
Linewidth enhancement factor	-4

Table 5.2: Simulation parameters used for the PFL model.

5.3.4.1 Linewidth characterisation using the simulation model

Linewidth measurements, employing the simulation model built, are conducted to examine the effect of varying the delay and phase shift of the feedback on the optical linewidth of the laser. One of the main goals is to calculate the linewidth value for 1.15 ps delay and to check if varying the delay and phase shift will result in obtaining a narrower optical linewidth.

Figure 5.8(a) shows the measured linewidths of the simulated model at different bias values of the DFB, with a -10 dBm feedback signal and without any delay or phase shift applied to it. The linewidths of the laser are measured to be 14.48 MHz, 9.57 MHz, 677.5 kHz for bias values of 25, 50, 75 mA respectively.

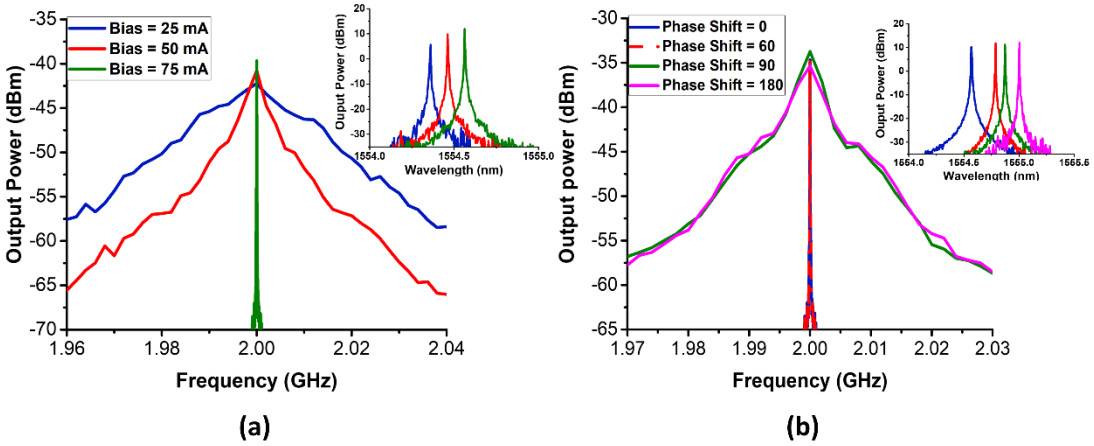

Figure 5.8: Linewidth measurements using the simulation model for: (a) Bias values of 25, 50, and 75 mA of the DFB (inset: optical spectra for the same), (b) Phase shifts of 0°, 60°, 90° and 180° applied to the feedback (inset: corresponding optical spectra).

The linewidth reduction with an increase of bias current is as expected and results from the fact that increasing the gain value leads to a decrease of the linewidth enhancement factor, hence the spectral linewidth [31]. The insets show the corresponding optical spectra for the same bias values. Increasing the bias results in a redshift of the laser emission. This behaviour is similar to the one observed with the physical device as shown previously by the contour plot in Figure 5.3(b). The increase in bias currents raises the temperature of the active layer of the laser, which leads to a redshift in the device wavelength. Next, the impact of varying the delay and phase shift of the feedback on the laser linewidth is investigated. To this effect, the bias current of the DFB is set to 75 mA and the linewidth measurements are conducted again. A narrow linewidth of 35.68 kHz is obtained for a delay varying between 0.98 and 1.2 ps, corresponding to an external cavity of a length between 147-180 µm. The delay is set to

an intermediate value of 1.15 ps which corresponds to the length of the IFB section in the physical device. The linewidth is measured at this particular delay value while varying the phase shift of the feedback. Figure 5.8(b) shows the linewidth results for phase shift values of 0°, 60°, 90° and 180°, giving a linewidth of 31.6 kHz, 120 kHz, 1.82 MHz, and 2 MHz respectively. Increasing the value of the phase shift results in the widening of the laser linewidth. This can be attributed to the phase mismatch between the feedback signal and the laser main signal resulting in the generation of more phase noise and widening of the linewidth. The inset in the figure presents the optical spectra of the laser corresponding to the same values of phase shift. It shows that in addition to degrading the linewidth, the increase in the phase shift value also results in a redshift of the wavelength of the laser. The simulation results show that the optimum parameters to obtain the narrowest linewidth are a 1.15 ps delay and 0° phase shift on the feedback signal.

To conclude, the L-I curves show that with applying feedback, the threshold value decreases due to the re-injection of optical signal to the laser. This is contrary to the results shown in the experimental section. The difference maybe attributed to the fact that the simulation model considers a simple external cavity, while for the experimental case, it is an integrated device with both sections having cavity effects on each other. For the emission wavelength, there is a good agreement between the simulation and experimental results as there is a red shift in wavelength with the increase in bias. Moreover, variation of the laser output linewidth shows a good agreement between the simulation and the experimental cases.

5.3.4.2 Frequency response characterisation using the simulation model

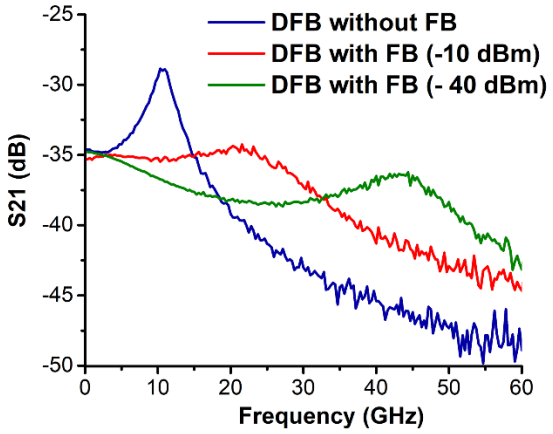

Figure 5.9: Frequency response measurements of the simulated PFL without feedback (blue), -10 dBm feedback (red) and -40 dBm feedback (green).

As previously mentioned, the optical feedback has been shown to have a positive influence on extending the laser MBW [32]. The PFL makes use of the self-seeding technique to benefit from a highly extended MBW stemming from the PPR phenomenon which will be discussed in more detail in the next paragraph [33] [34].

The first step is to examine the effect of the feedback on the MBW of the simulated model of the laser. Without applying any feedback, the DFB section biased at 50 mA has a 3-dB MBW of 16.5 GHz, as shown by the blue plot in Figure 5.9. Applying the feedback with a delay of 1.15ps, 0° phase shift and an initial value of -10 dBm while keeping the DFB section bias at the same value, extends the 3-dB MBW to 32.5 GHz as shown in the red plot in Figure 5.9. Decreasing the feedback power to -40 dBm, further improves the frequency response of the device, with the 3-dB bandwidth exceeding 40 GHz. This can be related to variation of the PPR with varying the optical power that is fedback to the laser. The appearance of this peak is owed to the PPR phenomenon which results in the expansion of the laser MBW to higher values beyond the conventional limits set by the traditional CPR limited by the laser intrinsic MBW [26]. The PPR peak is located at a higher frequency value [35], which is equal to the frequency difference between the two dominant longitudinal modes of the laser [36].

In summary, the simulated frequency response results have a good agreement with the previously shown experimental results. Careful optimisation of the phase shift, delay that the feedback signal experiences during its path in the passive section results in the introduction of the PPR peak in the frequency response curves at values much higher than the traditional CPR peaks. This has a direct influence on extending the laser MBW to a higher value allowing the usage of the laser with much higher data bit rates.

5.3.5 Experimental gain switching of the PFL laser

One of the main challenges facing the gain switching technique is the limited number of the generated OFC tones, as the latter mainly depends on the MBW of the laser. Several techniques have been proposed for the expansion of the gain switching based OFC. In [37], the authors combine two gain switched OFCs and expand them using a phase modulator. This results in the generation of 42 highly correlated OFC lines separated by 6.25 GHz, with an OCNR of over 50 dB. While such a scheme generates a relatively high number of OFC lines, it suffers from high insertion loss and cost due to the employment of a number of lasers and optical components including polarisation controllers, optical delay lines and a phase modulator. Another OFC expansion technique using self-phase modulation effects is shown in [38]. However, this technique also suffers from additional complexity and cost.

Another simple, compact, and cost-effective method for OFC expansion is the use of a photonic integrated device that comprises two lasers, applying in-chip optical feedback technique.

As shown previously, the feedback signal can improve the frequency response of the laser. In this section, the influence of self-seeding on an OFC generated by gain-switching the PFL is examined. The DFB section is gain-switched using a 6.25 GHz sinusoidal RF signal, with an RF power of 23.78 dBm. At first, the DFB section is biased at 50.3 mA and the IFB section is turned off. The generated OFC, shown by the blue plot in Figure 5.10, exhibits 5 lines, within a 4 dB from the spectral peak, with an OCNR of 47 dB (measured at the middle tone). Next, the feedback section bias is turned on and adjusted to achieve an optimum OFC (in terms of best spectral flatness and the largest number of OFC tones).

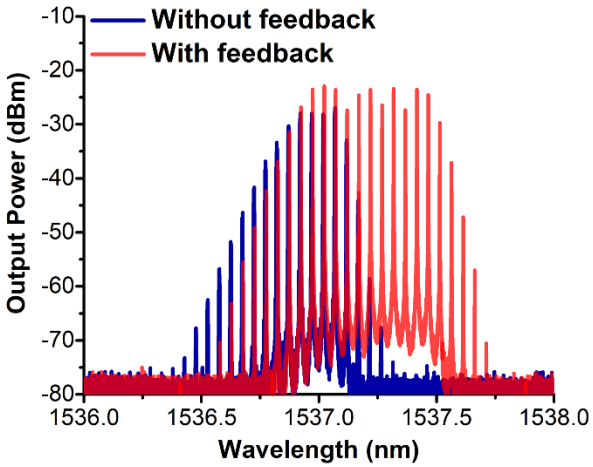

Figure 5.10: Optical spectra of generated OFC from the PFL device, with the IFB turned off (blue), with the IFB biased at 2.87 mA (red).

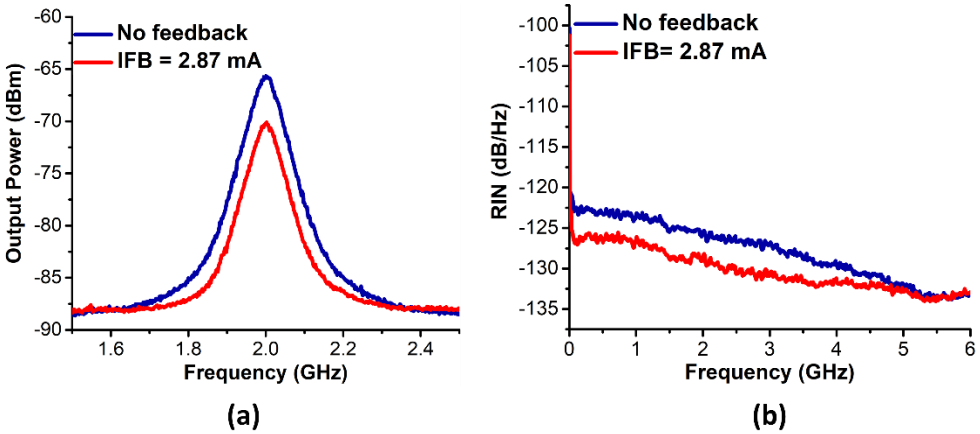

Figure 5.11: (a) Measured linewidth of the middle-filtered OFC tone with the IFB turned off (blue), with the IFB biased at 2.87 mA (red), (b) Measured RIN of the middle filtered OFC tone for the same.

The result, for an IFB current of 2.87 mA, is portrayed by the red plot in Figure 5.10. The expanded OFC exhibits 12 lines within the same 4 dB optical power range (from the peak). The OCNR is measured to be 47 dB. This increased number of tones can be used as

additional data channels from the same device, improving the energy efficiency and reducing the footprint of the multicarrier transmitter.

Next, we examine the effect of the expansion on the quality of the generated comb, by measuring the linewidth and RIN of the individual (filtered) OFC tones. Figure 5.11(a) shows the measured linewidth for the cases of no feedback (IFB bias = 0 mA) (blue plot) and with the IFB section biased at 2.87 mA (red plot). The respective linewidths of the middle OFC tones (tone 0 in both OFCs) for no feedback and with IFB biased at 2.87 mA cases are 21.29 and 22.5 MHz respectively. This shows as a proof of concept that the linewidth of the OFC tone is not affected by the expansion due to the feedback. High linewidth values can be attributed to the LD based noise as previously explained.

RIN measurements are conducted for the same OFC tone and shown in Figure 5.11(b). In this case, applying the feedback does a slight improvement in the RIN value from an original value of -127.4 dB/Hz to be -130 dB/Hz. As mentioned before, the obtained RIN values for both bias scenarios are satisfactory (<-120 dB/Hz) for using the expanded OFC in optical networks employing multi-level intensity modulation schemes.

5.4 Conclusions

In this chapter, a detailed characterisation of a PFL is carried out prior to it being used for the generation of an expanded OFC. A VPItransmissionMaker™ simulation model was presented to give a detailed analysis of the device behaviour under different conditions of the feedback signal. The results show that applying the feedback results in enhancement of the 3-dB MBW values to exceed 40 GHz. Moreover, the feedback results in narrowing the laser linewidth up to 31.6 kHz. Experimentally, by using on-chip optical feedback, a narrow linewidth in order of kHz is not achieved, due to the noise generated from the current source used to bias the passive section. Nevertheless, a linewidth reduction from 8.45 to 4.35 MHz as a result of applying feedback is demonstrated. Moreover, RIN measurements of the device show values as low as -159.7 dB/Hz. Experimental dynamic characterisation of the device demonstrates a remarkable enhancement in the MBW resulting from the PPR phenomenon, which improves the frequency response at certain frequency values due to applying feedback by biasing the IFB section. The experimental results show a general good agreement with the simulation ones. The enhanced MBW results in achieving an expanded gain switched OFC. By careful optimisation of the bias of the two sections, a discernible enhancement of the number of OFC tones within the 4-dB optical power range from 5 to 12 tones is demonstrated. linewidth

measurements of the additional comb tones show no widening due to the expansion and stays almost the same value at 22.5 MHz, while the RIN measurements show a slight improvement in the RIN value from an original value of -127.4 dB/Hz to be -130 dB/Hz.

The improved spectral characteristics as of the optimised in-chip feedback, accompanied by the attractive features of photonic integration such as compactness, cost-effectiveness, lower footprint, and power consumption qualify the device to be used in the next-generation of short-reach optical networks.

References

[1] M. Radziunas, A. Glitzky, U. Bandelow, M. Wolfrum, U. Troppenz, J. Kreissl and W. Rehbein, “Improving the Modulation Bandwidth in Semiconductor Lasers by Passive Feedback,” *IEEE Journal of Selected Topics in Quantum Electronics,* vol. 13, no. 1, pp. 136-142, 2007.

[2] K.-H. Lee, J.-Y. Kim and W.-Y. Choi, “A 30-GHz Self-Injection-Locked Oscillator Having a Long Optical Delay Line for Phase-Noise Reduction,” *IEEE Photonics Technology Letters,* vol. 19, no. 24, pp. 1982-1984, 2007.

[3] M.N.Hammad, A.Kaszubowska-Anandarajah, M. Pascual, P. Landais, P.D.Lakshmijayasimha, G. Jain and P.M.Anandarajah, “Characterization and Direct Modulation of a Multi-Section PIC Suited for Short Reach Optical Communication Systems,” *Photonics,* vol. 7, no. 3, 2020.

[4] J. Kreissl, U. Troppenz, W. Rehbein, T. Gaertner, P. Harde and M. Radziunas, “40 Gbit/s Directly Modulated Passive Feedback Laser with Complex-Coupled DFB Section,” in *33rd European Conference and Exhibition of Optical Communication (ECOC)*, Berlin, Germany, 2007.

[5] M. H. M. Shamim, M. A. Shemis, C. Shen, H. M. Oubei, T. K. Ng, B. S. Ooi and M. Z. M. Khan, “Investigation of Self-Injection Locked Visible Laser Diodes for High Bit-Rate Visible Light Communication,” *IEEE Photonics Journal,* vol. 10, no. 4, p. 7905611, 2018.

[6] Y.Th.Younis, S. K.Musa, S.F.Abdalah, A. K.Ahmed, R.Meucci and K. Naimee, “The rule of bias current of semiconductor laser in chaos communications,” *Results in Physics,* vol. 6, pp. 243-251, 2016.

[7] Z. Liu and R. Slavík, “Optical Injection Locking: From Principle to Applications,” *Journal of Lightwave Technology ,* vol. 38, no. 1, pp. 43-59, 2019.

[8] H. Wenzel, U. Bandelow, H.-J. Wunsche and J. Rehberg, “Mechanisms of fast self pulsations in two-section DFB lasers,” *IEEE Journal of Quantum Electronics,* vol. 32, no. 1, pp. 69-78, 1996.

[9] O. Brox, S. Bauer, M. Radziunas, M. Wolfrum, J. Sieber, J. Kreissl, B. Sartorius and H.-J. Wunsche, “High-frequency pulsations in DFB lasers with amplified feedback,” *IEEE Journal of Quantum Electronics,* vol. 39, no. 11, pp. 1381-1387, 2003.

[10] K. Pipe, R. Ram and A. Shakouri, “The physics of heat transport in semiconductor lasers,” in *IEEE 18th International Semiconductor Laser Conference (ISLC)*, Garmisch, Germany, 2002.

[11] M. Mahdi, A. Ali, H. Alaa and M. Hussein, “Heat Effects on Data Transmission by Laser Diode and Light Emitted Diode for High Frequency Optical Communication Systems,” *Journal of Nanoscience and Technology,* vol. 2, no. 2, pp. 126-129, 2016.

[12] M. Fukuda, T. Mishima, N. Nakayama and T. Masuda, “Temperature and current coefficients of lasing wavelength in tunable diode laser spectroscopy,” *Applied Physics,* vol. 100, pp. 377-382, 2010.

[13] M. Ohtsu and Y. Teramachi, “Analyses of mode partition and mode hopping in semiconductor lasers,” *IEEE Journal of Quantum Electronics,* vol. 25, no. 1, pp. 31-38, 1989.

[14] T. B. Simpson, J.-M. Liu, M. AlMulla, N. G. Usechak and V. Kovanis, “Linewidth Sharpening via Polarization-Rotated Feedback in Optically Injected Semiconductor Laser Oscillators,” *IEEE Journal of Selected Topics in Quantum Electronics ,* vol. 19, no. 4, p. 1500807, 2013.

[15] K. Aoyama, R. Yoshioka, N. Yokota, W. Kobayashi and H. Yasaka, “Optical Negative Feedback for Linewidth Reduction of Semiconductor Lasers,” *IEEE Photonics Technology Letters ,* vol. 27, no. 4, pp. 340-343, 2015.

[16] Y. Zhao, Y. Li, Q. Wang, F. Meng, Y. Lin, S. Wang, B. Lin, S. Cao, J. Cao, Z. Fang, T. Li and E. Zang, “100-Hz Linewidth Diode Laser With External Optical Feedback,” *IEEE Photonics Technology Letters,* vol. 24, no. 20, pp. 1795-1798, 2012.

[17] W. Burkett, B. Lu and M. Xiao, “Influence of injection-current noise on the spectral characteristics of semiconductor lasers,” *IEEE Journal of Quantum Electronics,* vol. 33, no. 11, pp. 2111 - 2118, 1997.

[18] G. P. Agrawal and R. Roy, “Effect of injection-current fluctuations on the spectral linewidth of semiconductor lasers,” *Physical Review A,* vol. 37, pp. 2495-2501, 1988.

[19] G. Duan and P. Gallion, “Drive current noise induced linewidth in tunable multielectrode lasers,” *IEEE Photonics Technology Letters,* vol. 3, no. 4, pp. 302-304, 1991.

[20] M.-C. Amann and R. Hakimi, “Linewidth broadening by $1/f$ noise in wavelength-tunable laser diodes,” *Applied Physics Letters,* vol. 70, no. 12, pp. 1512-1514, 1997.

[21] R. Maher and B. Thomsen, “Dynamic linewidth measurement technique using digital intradyne coherent receivers,” *Optics Express,* vol. 19, no. 26, pp. B313-B322, 2011.

[22] R. Schimpe and W. Harth, “Theory of FM noise of single-mode injection lasers,” *Electronics Letters ,* vol. 19, no. 4, pp. 136-137, 1983.

[23] M.-C. Amann and R. Schimpe, “Excess linewidth broadening in wavelength-tunable laser diodes,” *Electronics Letters,* vol. 26, no. 5, pp. 279-280, 1990.

[24] V. Vujicic, A. P. Anthur, A. Saljoghei, V. Panapakkam, R. Zhou, Q. Gaimard, K. Merghem, F. Lelarge, A. Ramdane and L. P. Barry, “Mitigation of relative intensity noise of quantum dash mode-locked lasers for PAM4 based optical interconnects using encoding techniques,” *Optics Express,* vol. 25, no. 1, pp. 20-29, 2017.

[25] S. Kobayashi, Y. Yamamoto, M. Ito and T. Kimura, “Direct Frequency Modulation In AlGaAs Semiconductor Lasers,” *IEEE Transactions on Microwave Theory and Techniques ,* vol. 30, no. 4, pp. 428-441, 1982.

[26] M. Ahmed and A. Bakry, “Modulation performance of semiconductor laser coupled with an ultra-short external cavity,” *Optics Communications,* vol. 360, no. 1, pp. 52-60, 2016.

[27] P. M. Anandarajah, S. Latkowski, C. Browning, R. Zhou, J. O'Carroll, R. Phelan, B. Kelly, J. O'Gorman and L. P. Barry, “Integrated Two-Section Discrete Mode Laser,” *IEEE Photonics Journal ,* vol. 4, no. 6, pp. 2085-2094, 2012.

[28] M. I. Memon, B. Li, G. Mezosi, Z. Wang, M. Sorel and S. Yu, “Modulation Bandwidth Enhancement in Optical Injection-Locked Semiconductor Ring Laser,” *IEEE Photonics Technology Letters,* vol. 21, no. 24, pp. 1792-1794, 2009.

[29] J. Sigg, “Effects of optical feedback on the light-current characteristics of semiconductor lasers,” *IEEE Journal of Quantum Electronics,* vol. 29, no. 5, pp. 1262-1270, 1993.

[30] J. Osmundsen and N. Gade, “Influence of optical feedback on laser frequency spectrum and threshold conditions,” *IEEE Journal of Quantum Electronics,* vol. 19, no. 3, pp. 465-469, 1983.

[31] E. Kapon, Semiconductor Lasers I Fundamentals, Academic Press , 1999.

[32] M. Ahmed, A. Bakry, R. Al-Tuwirqi, M. S. Alghamdi and F. Koyama, “Enhancing Modulation Bandwidth of Semiconductor Lasers beyond 50 GHz by Strong Optical Feedback for Use in Millimeter-Wave Radio over Fiber Links,” *Japanese Journal of Applied Physics,* vol. 52, no. 124103, 2013.

[33] P. Bardella and I. Montrosset, “A New Design Procedure for DBR Lasers Exploiting the Photon–Photon Resonance to Achieve Extended Modulation Bandwidth,” *IEEE Journal of Selected Topics in Quantum Electronics,* vol. 19, no. 4, p. 1502408, 2013.

[34] J. Reithmaier, W. Kaiser, L. Bach, A. Forchel, V. Feies, M. Gioannini, I. Montrosset, T. Berg and B. Tromborg, “Modulation speed enhancement by coupling to higher order resonances: a road towards 40 GHz bandwidth lasers on InP,” in *International Conference on Indium Phosphide and Related Materials*, Glasgow, United Kingdom, 2005.

[35] M. Dumitrescu, A. Laakso, J. Viheriala, T. Uusitalo, M. Kamp and P. Uusimaa, “Distributed feedback lasers with photon-photon-resonance-enhanced modulation bandwidth,” in *International Semiconductor Conference (CAS)*, Sinaia, Romania, 2012.

[36] T. Uusitalo, H. Virtanen, P. Bardella and M. Dumitrescu, “Analysis of the photon–photon resonance influence on the direct modulation bandwidth of dual-longitudinal-mode distributed feedback lasers,” *Optical and Quantum Electronics ,* vol. 49, no. 46, 2017.

[37] P. D. Lakshmijayasimha, A. Kaszubowska-Anandarajah, E. P. Martin, P. Landais and P. M. Anandarajah, “Expansion and phase correlation of gain-switched optical frequency combs through FWM in an SOA,” in *Optical Fiber Communication Conference (OFC)*, San Diego, California, United States, 2019.

[38] P. M. Anandarajah, R. Maher, Y. Q. Xu, S. Latkowski, J. O'Carroll, S. G. Murdoch, R. Phelan, J. O'Gorman and L. P. Barry, “Generation of Coherent Multicarrier Signals by Gain Switching of Discrete Mode Lasers,” *IEEE Photonics Journal ,* vol. 3, no. 1, pp. 112-122, 2011.

[39] R. Tucker, “High-speed modulation of semiconductor lasers,” *Journal of Lightwave Technology ,* vol. 3, no. 6, pp. 1180-1192, 1985.

[40] J. Tang and K. Shore, “30-gb/s signal transmission over 40-km directly modulated DFB-laser-based single-mode-fiber links without optical amplification and dispersion compensation,” *Journal of Lightwave Technology,* vol. 24, no. 6, pp. 2318-2327, 2006.

[41] M. Akram, C. Silfvenius, O. Kjebon and R. Schatz, “Design optimization of InGaAsP–InGaAlAs 1.55 µm strain-compensated MQW lasers for direct modulation applications,” *Semiconductor Science and Technology,* vol. 19, no. 5, pp. 615-625, 2004.

[42] J. Liu, H. Chen, X. Meng and T. Simpson, “Modulation bandwidth, noise, and stability of a semiconductor laser subject to strong injection locking,” *IEEE Photonics Technology Letters,* vol. 9, no. 10, pp. 1325-1327, 1997.

[43] E. K. Lau, H.-K. Sung and M. C. Wu, “Frequency Response Enhancement of Optical Injection-Locked Lasers,” *IEEE Journal of Quantum Electronics ,* vol. 44, no. 1, pp. 90-99, 2008.

[44] T. Simpson, J. Liu and A. Gavrielides, “Small-signal analysis of modulation characteristics in a semiconductor laser subject to strong optical injection,” *IEEE Journal of Quantum Electronics ,* vol. 32, no. 8, pp. 1456-1468, 1996.

[45] K. Hill and G. Meltz, “Fiber Bragg grating technology fundamentals and overview,” *Journal of Lightwave Technology,* vol. 15, no. 8, pp. 1263-1276, 1997.

[46] F. Grillot, C. Wang, N. A. Naderi and J. Even, “Modulation Properties of Self-Injected Quantum-Dot Semiconductor Diode Lasers,” *IEEE Journal of Selected Topics in Quantum Electronics,* vol. 19, no. 4, p. 1900812, 2013.

[47] T. Komljenovic, L.Liang, R.-L.Chao, J.Hulme, S.Srinivasan, M.Davenport and J. Bowers, “Widely-Tunable Ring-Resonator Semiconductor Lasers,” *Applied Sciences ,* vol. 7, no. 732, 2017.

[48] R. Pillai, E. Garmire and P. Menendez-Valdes, “Relative intensity noise of laser-diode arrays,” *IEEE Photonics Technology Letters,* vol. 3, no. 11, pp. 968-970, 1991.

[49] P. D. Lakshmijayasimha, A. Kaszubowska-Anandarajah, E. P. Martin, P. Landais and P. M. Anandarajah, “Expansion and phase correlation of a wavelength tunable gain-

switched optical frequency comb," *Opt. Express,* vol. 27, no. 12, pp. 16560-16570, 2019.

[50] P. M. Anandarajah, R. Maher, Y. Q. Xu, S. Latkowski, J. O'carroll, S. G. Murdoch, R. Phelan, J. O'Gorman and L. Barry, "Generation of coherent multicarrier signals by gain switching of discrete mode lasers," *IEEE Photonics Journal,* vol. 3, no. 1, p. 112–122, 2011.

Chapter 6

Noise figure and saturation characteristics of multi-section semiconductor optical amplifier

6.1 Introduction

The massive increase in demand for higher internet speed and bandwidth has ignited a tremendous development of the field of optical communications in the last few decades. The growing demand for bandwidth makes the optimum utilisation of the legacy optical fibre infrastructure essential. A possible solution to maximize the use of the existing network resources, is the employment of flexible super channel based optical networks [1]. In such networks, improved spectral efficiency can be achieved by using densely packed channels where the channel spacing could be reduced to 6.25 GHz or even lower. Such a close/tight channel spacing imposes a strict and challenging requirement on the frequency stability of the laser transmitter [2]. An attractive solution that meets these demands, entails the use of an OFC, which has been the major focus of this work. OFCs provide multiple carriers that are intrinsically equidistant in frequency. The precise FSR of a comb enables the reduction of the size of guard bands between data channels, thereby significantly enhancing the spectral efficiency of a network.

While OFCs provide several advantages, they suffer from low comb line power (CLP). This is mainly due to the output power of the laser being shared amongst all the generated comb

tones. This means that the larger number of comb tones that are typically sought after, for employment in optical fibre communication systems, leads to an even lower CLP. It is also important to note that the CLP is worsened by the insertion loss of a passive demultiplexer, required to separate the carriers/comb tones prior to data modulation. As a result, an external optical amplifier is required to enhance the CLP. As aforementioned in Section 1.3.2 in Chapter 1, there exist different types of optical amplifiers. EDFAs is the most commonly used amplifier in optical networks due to their outstanding inherent characteristics in terms of gain. SOAs are an attractive alternative to EDFAs, as they provide several advantages such as their susceptibility for integration, which in turn provides a simpler, lower cost and lower footprint solution.

With the current trend of expanding the optical networks bit rates up to 100 Gbit/s, optical fibre cables are deployed closer and closer to the end user [3]. Thus, low cost and flexible optical components are needed now more than ever for implementation in the optical networks, especially in short reach access networks, where there are more stringent requirements on cost (CAPEX and OPEX). In such scenarios, SOAs offers a versatile, low cost and flexible solution for optical amplification [4]. It possesses two main advantages over other optical amplifiers as discussed previously in chapter 1. Having a similar general structure as a semiconductor laser allows SOAs to lend themselves to photonic integration [5]. Furthermore, they can be used to perform signal processing due to the non-linear effects in the semiconductor medium, which can be availed of if required [6].

The compactness and relatively low fabrication costs of SOAs qualify them as a strong candidate for amplification and transmission extension in short reach optical networks (such as PONs and data centre networks). However, one of the main reasons for SOAs not being used widely is the high NF and the effects of gain saturation at high input optical powers [7].

In this chapter, a photonically integrated multi-section SOA is introduced for tackling the issues of high NF and/or the low saturation power. Depending on the bias configuration applied to the different sections of the device, the carrier density inside the cavity can be tuned which allows the device to be flexible for various functions requiring different specifications. In addition, the proposed SOA can be photonically integrated with other devices. As mentioned above, one of the mains challenges facing gain switched OFCs is the low CLP. An SOA can be used to solve this issue, as it can provide amplification and be integrated with the PICs used for the OFC generation (such as the ones presented earlier in Chapters 4 and 5 of this thesis). Such integrated devices containing both the laser (OFC

generator) and SOA can serve as a reliable transmitter in next-generation short reach optical networks.

6.2 Semiconductor optical amplifiers (SOAs)

6.2.1 Historical development and Operational concept

The historical development of SOA has been closely connected with the development of semiconductor lasers, as both share almost the same structure. The first SOAs were demonstrated in 1964 [8]. Having a very similar structure to the semiconductor FP lasers, SOAs benefited from major improvements when the double heterostructure idea was proposed [9]. The first transmission experiment employing an SOA was conducted in the 1980s [10]. However, the EDFA introduction in the late 80s as a strong competitor for the SOA for in-line amplification have affected the research society interest in the SOAs development [11]. In the 1990s, an SOA that can offer high gain and high saturation power was demonstrated [12]. Since then, SOAs have passed through different phases of development. Like semiconductor lasers, SOAs are mainly based on III-V group semiconductor materials. Starting from the 1990s, the focus was to manufacture SOAs based on InP with InGaAsP active regions [13]. This was mainly driven by the fact that these materials can amplify optical signals in the 1300-1600 nm wavelength range, which is the operation region of choice for optical fibre communications as previously mentioned. Different types of SOAs are currently available in the market as commercial products. Depending on their operation regime, SOAs can be broadly classified into two main categories: FP SOAs, where a semiconductor laser is biased slightly below threshold and used as an SOA in an FP cavity, where the FP cavity is characterised by multiple reflections at the facets with reflectivities [14]. The latter results in the observation of a cavity resonance, leading to undesired large gain ripples in the output gain spectrum. The second category is the travelling wave (TW) SOA, where the oscillations are relatively prevented to create a single pass gain [14]. TW-SOAs have reduced facet reflectivities due to dielectric coatings at the air-semiconductor interface [15]. This results in an output gain spectrum that is both broad and relatively flat. However, the imperfection in the facet coating for some values of wavelengths results in the existence of some cavity resonance.

Figure 6.1 shows a typical structure of an SOA. An electrical bias is injected into the device to achieve optical gain for the injected optical signal. The injected signal is trapped in the active region through the refractive index guiding, where the optical gain occurs [15].

The different characteristics of an SOA depends on various parameters such as the bias current, the injected optical signal level, and the temperature of the device. Moreover, one of the main parameters affecting the properties of the SOA is the structure and dimensions of the active region. SOAs active regions are classified into three main categories: bulk, quantum wells (QWs) and quantum dots (QDs). Bulk SOAs employs a symmetrical waveguide, where a square shaped sub-micron bulk active region is placed in a regrown buried structure [16]. This allows both TE and TM polarisation to have the same confinement factor, due to the rotation symmetry of the active region. An SOA with an active region whose dimensions are significantly greater than the De Broglie wavelength (λ_B) where ($\lambda_B = \frac{h}{p}$, h is Planck's constant and p is the carrier momentum) can be considered as a bulk SOA [15]. This technology provides a large confinement factor and amongst the rest is quite mature.

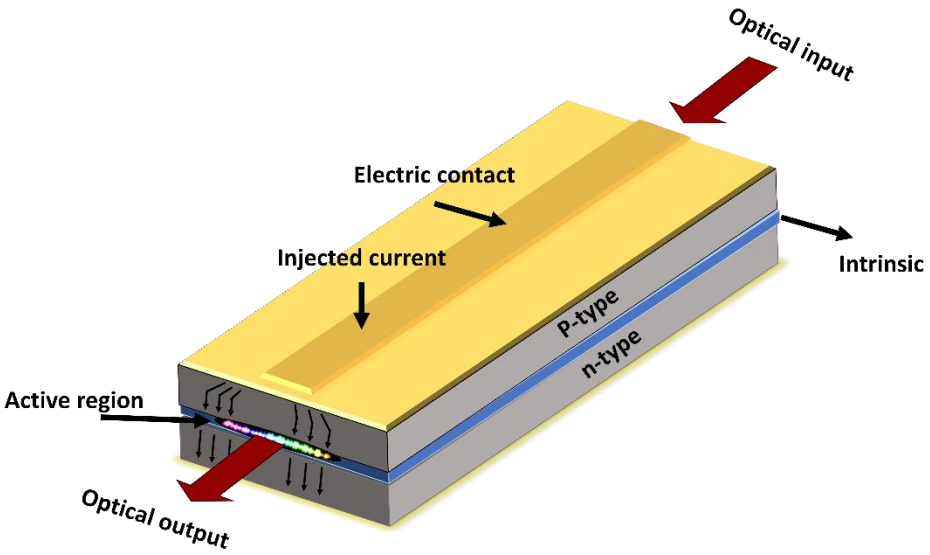

Figure 6.1: Schematic diagram of a typical SOA structure.

A QW SOA has a relatively similar structure to the bulk SOAs, except that the active layer thickness of the former is reduced to the order of 10nm where quantum effects play an essential role [14]. This is done to confine the carriers to two dimensions only, while the third dimension has a scale in the order of λ_B. In QWs SOAs, the profile of the electron density of states is a step function, rather than a random continuous spread of the possible states [17]. This results in the QW SOAs having a broad gain spectrum due to the reduction in the dependency of the gain on the photon energy [18]. The small dimensions of the QW SOAs result in them having a smaller confinement factor than the bulk SOAs. Furthermore, the

threshold current of them is also much lower than that of the bulk SOAs. On the other hand, the saturation output power of the QW-SOA is improved compared to the bulk-SOA as a result of the lower differential gain coefficient.

QD SOAs are tiny semiconductor materials with dimensions in the nm region/order. They provide better gain bandwidth and higher saturation power compared to the QW SOAs [19]. Moreover, they possess a much faster gain dynamics than other types of SOAs [20]. However, QD SOAs are still in the development stages. Improvements in both the quality of the material used and the modal gain of the device would be an important step for consideration of QD SOAs in future applications [21]. In [22], authors demonstrated an ultra-fast QD-SOA- Mach-Zehnder interferometer (MZI)-based XOR gate operating under 1, 2, and 2.5 Tb/s input bit sequences with Q factors of 28.4, 8.8, and 4.9, respectively.

6.2.2 SOA parameters

There exist some main parameters that are used to define the SOA performance and its potential to be used in current optical networks. These parameters depend on different factors such as the SOA structure, fabrication materials used, length of the device etc. This section provides a brief explanation of these parameters.

Optical gain: It can be considered as one of the most important operational parameters of optical amplifiers in general. A typical SOA generates an optical gain, in the active region, when population inversion is reached. The gain parameter can be simply defined as the ratio between the output signal power and the input signal power when it passes through the SOA. The gain in SOAs depends on both the injected signal level and wavelength (related to the gain curve) and can be calculated using the following formula:

$$G = \frac{G_O}{1+(\frac{P}{P_S})} \tag{6.1}$$

where G_O is the small signal gain, P is the input optical power and P_S is the saturation input power (input power at which the gain of the SOA is reduced to half its maximum value). The small signal gain (SSG) can be defined as the highest achievable gain in an optical amplifier. Typically, optical amplifiers can handle a maximum input signal level. When the input signal level is too high and exceeds that maximum value, the amplifier saturates.

Figure 6.2 shows a theoretical representation of a typical gain curve of an SOA versus its output power. At low input levels, the output power is almost equal to the SSG. Increasing the input power would result in depleting the carrier density inside the SOA leading to a

reduction in the gain value. When the gain decreases by 3 dB (half of its maximum value), the corresponding output power value is called the output saturation power ($Psat_{out}$). The relative input power will be called the input saturation power ($Psat_{in}$).

The $Psat_{out}$ is an indicator of the upper limit of an SOA linear operation region. An ideal SOA would have a $Psat_{out}$ value that is as high as possible. Different device parameters define the $Psat_{out}$ value such as the confinement factor, saturation energy and loss coefficient [23].

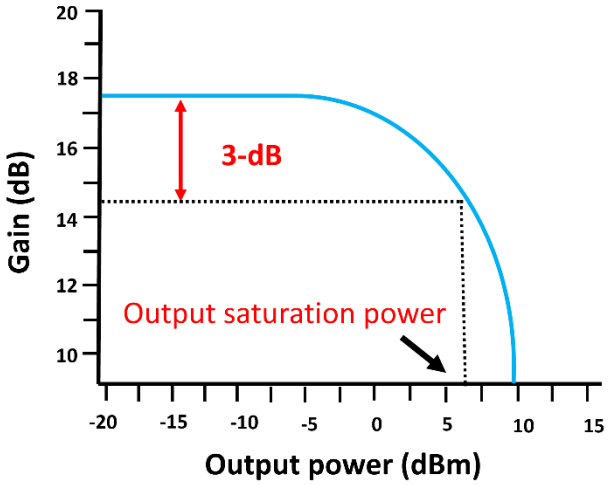

Figure 6.2: Output power of an SOA versus its gain showing the 3 dB saturation point.

Noise figure (NF): Introduction of noise to the input signal during the amplification process is a typical behaviour and portrayed by all amplifiers. The NF is a parameter used to quantify the noise characteristics of an amplifier. The noise in an SOA is mainly contributed by the amplified spontaneous emission (ASE). The NF can be defined as the measure of degradation of the signal to noise ratio (SNR) in a device. It is the ratio of the SNR at the input to the SNR at the output. The degradation of the SNR is because of the amplification process and can be calculated using the following equation:

$$NF = 10 * log_{10}\left(\frac{SNR_{in}}{SNR_{out}}\right) \tag{6.2}$$

There exist other different sources of noise contributing to the overall NF of the SOA such as signal-spontaneous beat noise and spontaneous- spontaneous beat noise and multi-path interference noise (MPI). The signal-spontaneous beat noise arises from the beating between the signal photons and spontaneously emitted photons in the same polarisation as the signal when both are incident on a photodiode. This type of noise depends mainly on the incident signal photon density, which means that it increases at high input signal powers to the SOA. On the other hand, spontaneous-spontaneous beat noise is caused by the beating among the

different frequency components of the spontaneous emission within the same state of polarisation. It also manifests itself during the detection process in the photodiode. Finally, MPI is caused by multiple reflections during the input signal path in the SOA cavity. With the lack of an optical isolator at the output of the SOA, ASE can be reflected back into the cavity of the SOA, which can in turn causes an increase in both signal-spontaneous and spontaneous- spontaneous beat noises. Thus, an optical isolator can be used to prevent back reflections into the SOA cavity. In this case, the source of MPI would be the reflectivity of the cavity facets, which is typically low in the case of TW- SOAs and can be neglected.

The NF is known to be one of the main limiting factors of the wide use of SOA especially in comparison to EDFAs. The latter can have NFs as close as possible to the quantum limit of 3 dB. One of the main contributions, listed later in this chapter, is the use of a multi-section (MS) SOA. Such an MS-SOA, where the NF can be enhanced by the accurate control of the bias applied to each SOA section, is characterised and shown to be capable of operating with reduced NFs or increased saturation powers. Such operation is achieved through better control of the carrier density distribution along the amplification medium.

Non-linear effects: It starts to arise when the SOA is in the saturation regime and the input signal power is high. It causes a deterioration of the linear signal transmission and amplification. There exist different types of non-linear effects in an SOA such as patterning effect and channel cross talk. Patterning effects are a direct result of the finite gain recovery time, and they can result in difficulties related to differentiation between the transmitted bits. Channel cross talk, on the other hand is a limitation of the number of the transmitted channels that can be amplified simultaneously in WDM applications. Channel cross talk can be defined as the phenomenon when a signal in a single transmission channel has an undesired effect or interference on another transmission channel [24]. Although these non-linear effects are undesirable for linear transmission systems, they can be advantages for specific functions. The SOA can be used in different applications of wavelength conversion [25] [26] and optical switching [27] [28] when it is forced to operate in the saturation regime. These applications include and are not limited to cross and self-phase modulation, and four wave mixing. The SOAs implemented for these functions should be designed to have a low saturation power to enhance the functionality of non-linear effects.

Polarisation sensitivity: The inherent polarisation sensitivity is considered as one of the major limiting factors of the SOAs when compared to EDFAs [29]. This is due to the fact that the SOA is made of a polarisation sensitive waveguide structure while the EDFA is an optical fibre-based system which is polarisation insensitive. Depending on the dimensions of the SOA

waveguide, the confinement factors for the TE and TM modes are not equal, thus they experience different values of gain. Furthermore, the antireflective coatings used to suppress the resonance in the cavity can also result in more polarisation sensitivity. To solve this, the SOA cavity can be designed and manufactured to have a symmetrical waveguide and eliminate most of the differences in the confinement factor values. The introduction of a strain in the active region during the fabrication process is another well-known method of reduction of polarisation sensitivity. This is mainly done by creating a lattice mismatch between the semiconductor layers which can be used to favour one polarisation mode over the other, resulting in an overall balanced gain over the two polarisation modes. Another method that can be used to overcome the polarisation sensitivity issue is to use ridge waveguides. The main advantage here is that it does not require epitaxial regrowth which makes it simple to realise. Moreover, the control of the waveguide width is not as critical as for a square-shaped active region. The presence of the ridge above the active region guides the signal in the horizontal direction, while in the vertical direction, the signal is directed by the double hetero layers structure [30].

6.2.3 Comparison with other optical amplifiers

Optical amplifiers can be divided into two main categories. Firstly, the fibre amplifiers, which are typically based on doping of rare earth materials such as Erbium, Praseodymium and Thulium or to make use of the stimulated Raman or Brillouin scattering. The second category is the amplifiers based on the non-fibre waveguides such as SOAs.

The main advantages of the first category are the polarisation insensitivity, the low reflectivities at interfaces, high gain and output power, slow gain dynamics (allowing the amplification of multiple channels without the occurrence of crosstalk effects), and low NF. On the other hand, their operation requires the presence of a pump laser, which results in a larger footprint and a higher cost. Furthermore, fibre based optical amplifiers do not lend themselves to photonic integration.

SOAs on the other hand provide the cost efficiency, versatility, and the possibility of photonic integrability with other optical components to form a PIC. Moreover, they are compact and electrically pumped which alleviates the need for the use of a large size laser pump. Furthermore, they can provide a broad optical bandwidth and can operate in multiple bands. The latter allows the amplification of optical signals outside the C-band. This is due to the reason that the SOA active material can be optimised to provide gain in a wide variety of bands. When used in the nonlinear regime, SOAs can perform functional applications such as

all-optical signal processing because of their strong nonlinearities and their fast gain dynamics. However, for linear amplification functions SOAs show worse performance than EDFAs in terms of NF and saturation power [31].

Generally, for long haul optical networks, where a high gain, low NF amplifiers are required, fibre amplifiers are widely employed. However, for access and short reach networks, the requirements are more relaxed on the optical amplifier performance and the cost becomes one of the most critical features. Such a requirement makes the SOAs an attractive candidate. However, the high NF and the low saturation power of SOAs needs to be tackled prior to their employment in short reach networks. This work examines the reduction of the NF and increment in the saturation power by using a MS-SOA. The MS-SOA is fully characterised and employed in a short reach system. The system experiment conducted mimics the use of a single comb tone (using a semiconductor tunable laser) that is intensity modulated. The work reported in this chapter shows that a PIC comprising a comb source and an MS-SOA would be an attractive transmitter source that can deliver high power multi-carrier tones for employment in short reach networks.

6.3 Multi-section SOA

As mentioned above, two main limitations of SOAs preventing them from being widely used in optical fibre communications systems are the (relatively) high NF and low output saturation power. The MS-SOA is introduced to overcome both limitations. In an MS-SOA, the carrier density distribution within the device active region can be controlled easily by the shaping of the carrier density profile [32]. An MS-SOA typically comprises electrically isolated semiconductor-based gain sections, which can be DC biased independently, allowing for the individual control of the carrier density within each of those sections. The most attractive feature of the MS-SOA is its ability to cater for different applications by allowing dynamic change of the device parameters by simply changing the bias configurations applied to its different sections. Hence, the MS-SOAs can be implemented for different applications. Some demonstrations that use the MS-SOA include an ultrafast pico-second all optical signal processing in an MZI based on an MS-SOA [33] and a remote modulator that enables a 36-dB optical budget for colorless operation at 2.5 Gb/s over 45-km SSMF for Hybrid WDM/TDM-PON Architecture [34].

6.3.1 Control of noise figure in an MS-SOA

In a standard (single section) SOA cavity, the carrier density within the active region can vary even when the device is supplied with a constant bias. This is due to the influence of the ASE or the input optical signal which result in the depletion of the carriers. The NF at any point in the active region can vary as a result of the local carrier density distribution affecting the total NF of the SOA. However, if one were to take advantage of this concept by building a MS-SOA and controlling the bias on each section (carrier density distribution), to take advantage of each section's NF.

An abstraction of an MS-SOA entails it to be considered as a chain of amplifiers stacked together (continuous chain of different optical amplifiers) in a single device. This abstraction then makes the calculation of the total NF much easier.

Consider a chain of four different amplifiers as shown in Figure 6.3. Each amplifier has its own different gain and noise resulting in a different NF value for each of the amplifiers.

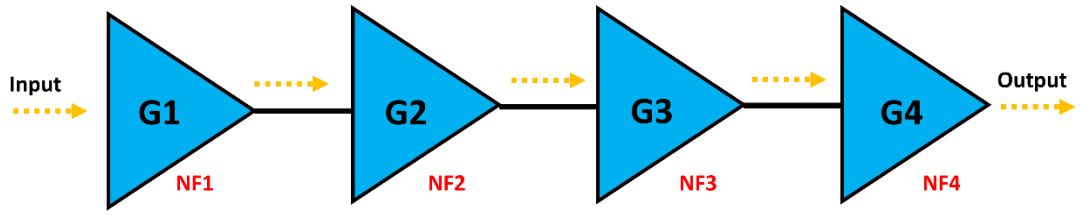

Figure 6.3: Chain of four amplifiers showing their respective gain and noise figures.

The following equation can be used to calculate the total NF of the whole amplifier chain [35]:

$$NF_{total} = NF_1 + \frac{NF_2}{G_1} + \frac{NF_3}{G_1 G_2} + \frac{NF_4}{G_1 G_2 G_3} \tag{6.3}$$

where G_n is the gain of the amplifier "***n***". From the equation, it is clear that the amplifier placed as the first one in the chain is the one that contributes the majority of the noise to the system. This concept can be explained easily, as the noise generated by the first amplifier will go through the other amplifiers in the chain and get amplified by each one of them. Each successive term in the equation is divided by an additional factor G, where G is the multiplication of the gain of each of the previous amplifiers in the chain. Hence, by using this concept in a cascaded system, one can place a low noise amplifier first. It is important to note that all the terms used in the equation are linear and not logarithmic. If this same concept is applied to the MS-SOA, where each section can be considered as a discrete amplifier in the chain, then an accurate control of the total NF of the device can be achieved by controlling

the NF to each section. The overall NF of the MS-SOA device can be reduced by creating a carrier density profile where the input section of the MS-SOA has a low NF.

The NF of an amplifier is directly proportional to the population inversion factor, which in turn is inversely proportional to the level of the carrier density in the active region [36] according to the following equations:

$$NF = 2\, n_{sp} \frac{(G-1)}{G} + \frac{1}{G} \tag{6.4}$$

$$n_{sp} = \frac{N_c}{N_c - N_0} \tag{6.5}$$

where $\boldsymbol{n_{sp}}$ is the population inversion factor, $\boldsymbol{G}$ is the gain, $\boldsymbol{N_c}$ is the active region carrier density and N_0 is the carrier density at transparency.

Hence, to achieve a low NF in a particular section, the carrier density (the electric bias applied) in that section should be kept at a high level. On the other hand, if the bias applied is constant and limited to a given value, the output section should be kept at a low level of current. Firstly, the ASE generated from the input sections would experience lower amplifications as they go through the different sections of the MS-SOA on their path to the output section. This would mean that the portion of the ASE reflected from the output facet back into the SOA would be very little and can be neglected. Finally, and most importantly, the level of the ASE generated from the output sections would be reduced with a lower bias value due to the lower carrier density value. Both factors result in the generation of an overall lower ASE level on the output signal.

6.3.2 Control of output saturation power in an MS-SOA

The saturation intensity (intensity where saturation occurs) in an SOA is inversely proportional to the spontaneous carrier lifetime "$\boldsymbol{\tau}$" [37] [38]. Hence, to increase the output saturation power of the SOA, the value of the spontaneous carrier lifetime has to be reduced. The latter is defined as the average time it takes carriers in the conduction band to recombine with holes in the valence band through a spontaneous process [36]. It is well known that in a semiconductor device, the total recombination rate is directly proportional with the carrier density [39]. Hence, the spontaneous carrier lifetime is inversely proportional to the carrier density as indicated by the following equation [39]:

$$\tau = \frac{N}{R(N)} = \frac{1}{A+BN+CN^2} \quad (6.6)$$

where $\boldsymbol{R(N)}$ is the total recombination rate, $\boldsymbol{N}$ is the carrier density, $\boldsymbol{A, B\ and\ C}$ are the non-radiative, radiative, Auger recombination coefficients respectively.

Increasing the supplied bias results in increasing the carrier density, which in turn results in an indirect increase in the saturation power as a result of improving the saturation intensity. Nevertheless, in physical devices, the current supplied to the SOA is typically limited by the manufacturer's specifications. In this case, the bias configuration for achieving a higher output saturation power should be opposite to that of achieving a low NF. This is due to the input optical signal being increased exponentially in magnitude as it passes through the SOA because of the amplification process. input optical signal keeps increasing until it converges to the saturation intensity value. The saturation intensity at any one point in the SOA waveguide, therefore, needs to be tailored to reflect the intensity of the signal being amplified at that point [36]. As previously demonstrated, to increase the saturation intensity, the carrier lifetime needs to be reduced by increasing the carrier density. This means that a higher carrier density (higher applied bias) will be needed at the output facets of the SOA, where the input optical signal has experienced more amplification. It is important to note that the decrease of the spontaneous carrier lifetime along the propagation direction is the key to keeping the saturation intensity higher than the intensity of the propagating signal ensuring a higher output saturation power.

The following sections in this chapter will be dedicated to experimental demonstrations of reducing the NF and subsequently increasing the output saturation power, using an integrated MS-SOA. This demonstration is achieved by employing the MS-SOA in a short reach communication system experiment employing OOK and PAM-4 modulation formats.

6.3.3 Device structure

The schematic of the MS-SOA is shown in Figure 6.4(a). The device is a prototype and custom designed by III-V lab. It consists of four equal length sections (S1, S2, S3 and S4). Note that the concept could be demonstrated with the aid of two or more sections. The MS-SOA is a bulk InP/InGaAsP SOA, angled and AR coated, with a length of approximately 1mm. It has an angled facet to prevent back reflections into the device.

Four different electrodes are used for current injection into the four sections. Each section has an approximate length of 250 µm. The chip can be accessed (optically) from both sides

(S1 and S4) which allows the injection of the optical signal into it and the extraction of the amplified output signal from the other side. A 10 µm slot in the ridge provides electrical isolation between the different contacts. The resistance between the different sections is measured to be 355 Ω between S1 and S2, 365 Ω between S2 and S3, and 355 Ω between S3 and S4. The large resistance leads to a reduction in the carrier diffusion. The waveguide is slightly flared at the facets such that an area of the facet is increased. As per the manufacturer's recommendation, the bias supplied to each section should be limited to 100 mA and the total current supplied for the whole device should not exceed 300 mA at a given instant. This prevents the overheating of the device that could lead to the deterioration in its performance (faster ageing).

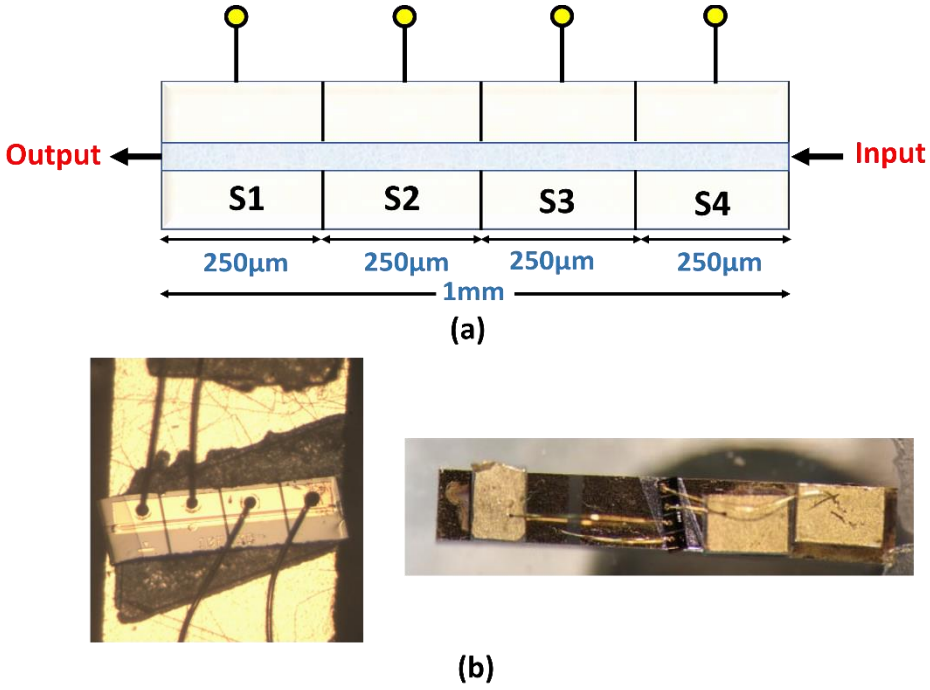

Figure 6.4: (a) schematic diagram of the 4-section MS-SOA, (b) a photograph of the chip under the microscope showing how it is wire bonded to gold contact plates and mounted on a sub carrier.

Figure 6.4(b) shows a microscopic photograph of the MS-SOA chip. As can be seen from the picture, the device has four different sections where each section is wire bonded to a separate gold contact for ease of use and experimentation. A common ground pad is shared by the four sections. Having a separate electric contact on each section allows them to be DC biased independently. All experiments described in the next few sections of this chapter had the 4 sections biased by a multi-channel current controller which allowed the independent biasing of each section. As discussed before, the multi-contact design of this MS-SOA provides a high degree of flexibility. The MS-SOA can generate a lower NF if the input sections are biased higher than the output sections as discussed before in Section 6.3.1. On the other hand, a higher output saturation power can be achieved from the device using the same total

DC bias value, but by inverting the DC bias condition to have the output sections supplied by a higher DC bias than the input sections.

To allow access from both of sides of the chip, the device is placed on a bespoke printed circuit board (PCB). The four contacts are wire bonded to connection points on the PCB to permit simple connectivity to the bias sources. Figure 6.5(a) shows a microscopic photograph of the chip glued to the top of the PCB. The PCB is then placed on an Aluminum plate, which is placed on another copper plate that has a TEC beneath it to ensure that the temperature is kept stable while operating the device. Figure 6.5(b) shows a photograph of the experimental setup used for characterising the MS-SOA chip. The plates holding the PCB and the MS-SOA chip are screwed to a big Aluminum block, which has two heat sinks, on both sides, glued to it using thermal paste. The function of the heat sinks is to increase the heat flow away from the device during its operation. Two tapered v-groove fibre holders are each placed on a 3-axis manual precision stage for accurate control of the fibre alignment with the MS-SOA chip. As shown in Figure 6.5(b), two lensed ended fibres are used on both sides of the chip to inject the input optical signal into the MS-SOA and to retrieve the amplified output signal from the output facet. All the components are placed on a honeycomb optical breadboard in order to reduce the vibration, which affects the coupling of the fibres at both ends of the chip.

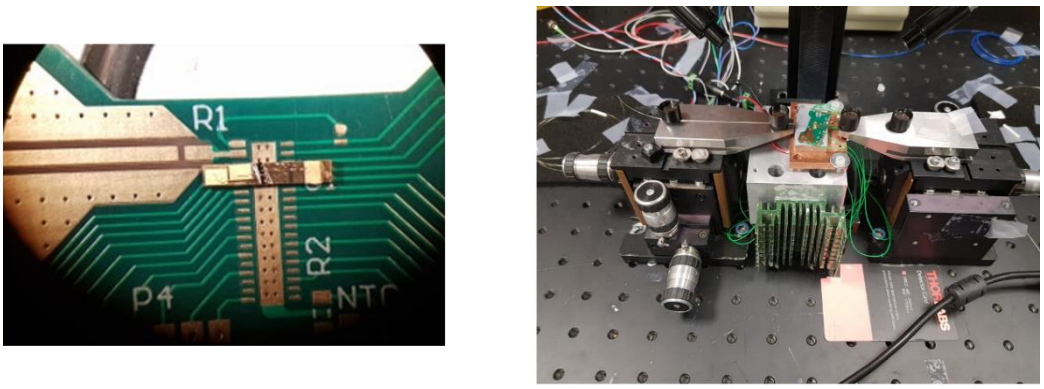

Figure 6.5: (a) A photograph of the MS-SOA mounted on a specially designed PCB, (b) a photograph of the setup used for the static characterisation of the device.

6.3.4 Static characterisation

The experimental characterisation is conducted to examine the performance of the SOA under the influence of different bias configurations.

The first step in the static characterisation is to look at the ASE noise curve of the MS-SOA at different bias configurations. This test is conducted to see the effect of varying the bias configuration supplied to the different sections of the MS-SOA on the output ASE noise. Figure 6.6(a) shows the optical spectrum of the output of the MS-SOA under three different bias configurations without applying an input signal to it. The ***first*** bias configuration is when all the sections are biased at 70 mA, in this case the MS-SOA can be considered to act as a single section SOA as the same bias is supplied to all the four sections. The ***second*** bias configuration entails biasing the input sections higher than the output sections at the following values: (S1 = 40, S2 = 60, S3 = 80, and S4 = 100 mA) where S4 is the input section while S1 is the output section. Finally, the ***third*** bias configuration is opposite to the second one (output sections biased higher than the input sections) at the following values (S1 = 100, S2 = 80, S3 = 60, and S4 = 40 mA). It is important to note that the total bias of the MS-SOA is kept constant at 280 mA for all of the three bias configurations in order to ensure consistency. As can be seen from the figure, there is a slight change in the shape of the ASE spectrum for the different bias configurations especially for the region that lies between 1450 and 1525 nm.

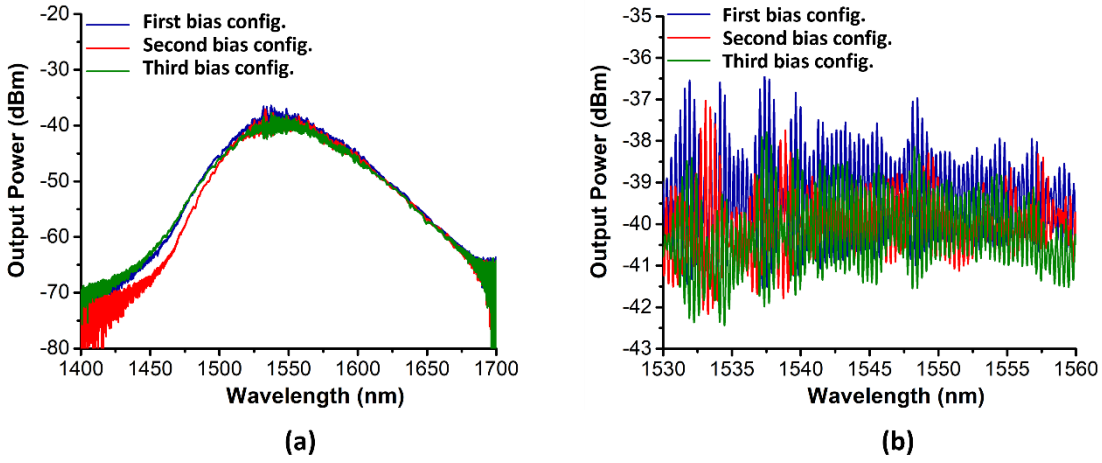

Figure 6.6: (a) Optical spectrum of the ASE noise curve of the MS-SOA biased at three different conditions, (b) Zoomed in optical spectrum (30 nm) of the ASE noise curve of the MS-SOA showing the FP ripples.

The second bias configuration (input sections bias > output sections bias) show a relatively lower ASE noise at this region. This follows the analysis shown previously in Section 6.3.1 where a lower NF should be expected when the output sections are biased higher than the input ones. Figure 6.6(b) shows a zoomed-in version of the ASE noise curve on a 30 nm span for the three bias configurations. The ripples in the figure for the different bias configurations do not exceed 4 dB peak to peak. These FP ripples are caused by the residual facet reflectivity.

The next step is to examine the behaviour of the MS-SOA when injected with an optical signal. For that purpose, a wavelength tunable laser is used, where both the emission power and wavelength can be varied. The first phase entailed studying the effect of varying the injection power while keeping the injected laser wavelength constant at 1527.6 nm. This particular wavelength has been chosen as the difference in the ASE noise curve for the different bias configuration is more obvious for the lower wavelength region. Also, the lowest wavelength that the used tunable laser can reach is 1527.6 nm. It is important to note that for all the upcoming measurement, a 3-dB fixed optical attenuator has been placed at the input port of the OSA (for protection). Moreover, the coupling losses between the device facets and the lensed fibres from both sides are estimated to be 6 dB. This will be taken account of in the different calculations of power and NF.

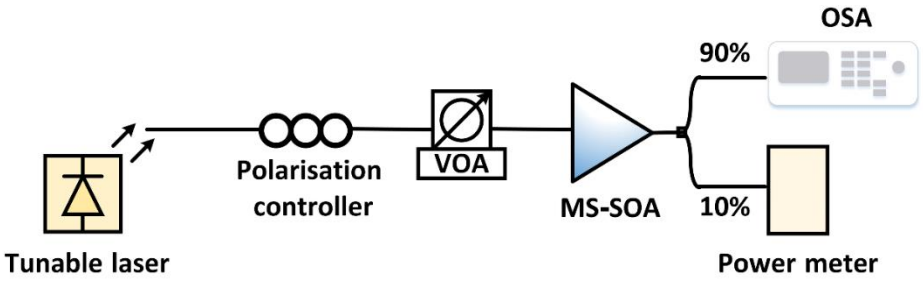

Figure 6.7: Experimental setup of light injection from a tunable laser into the MS-SOA.

Figure 6.7 shows the experimental setup used to realise the injection of an optical signal into the MS-SOA. The output of a wavelength tunable laser is fed to a PC, which has a vital role in synchronising the injection signal polarisation with that of the SOA cavity. A VOA is placed after the PC to control the injected power level into the MS-SOA. The output of the MS-SOA is then fed to a 90%-10% coupler where the 90% is sent to a 20 pm high resolution OSA and the 10% is fed to an optical power meter for power monitoring purposes.

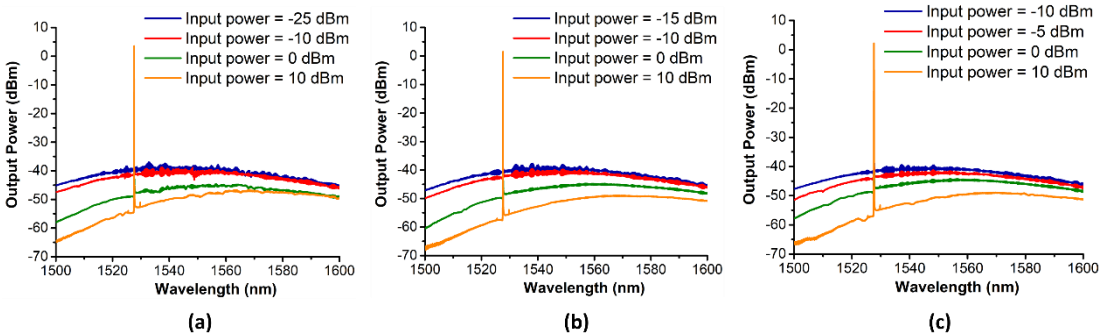

Figure 6.8: Optical spectra of the MS-SOA output when injected with a CW optical signal at different injection levels and biased in: (a) First condition, (b) Second condition, and (c) Third condition.

Figure 6.8(a) shows the MS-SOA output spectrum, when it is biased with the first bias condition (all sections are biased at 70 mA) and injected with a CW optical signal at different

optical power levels ranging from -25 to 10 dBm. From Figure 6.8(a), it can be seen that when the injected optical signal power is increased, the output noise level decreases and the peak power increases, which result in an increase of the output OSNR value. Furthermore, the FP ripples are being suppressed with higher injection powers due to the carriers being consumed by the amplification process. Table 6.1 below gives the exact measured values of the output peak power, noise level and NF for different injection power levels when applying the first bias condition.

Input Power (dBm)	Output peak power (dBm)	Noise level (dBm)	NF (dB)
-25	-20.45	-39.85	13.03
-15	-6.85	-39.88	9.73
-10	-2.66	-41.35	8.88
-5	0.01	-44.22	8.25
0	1.57	-48.17	7.61
5	2.89	-48.95	7.15
10	3.56	-53.43	6.76

Table 6.1: Measured output peak power, noise level and NF for different input power levels when the MS-SOA is biased at the first condition.

Figure 6.8(b) shows the MS-SOA output spectrum when the MS-SOA is biased in the second bias configuration (the input sections bias > the output sections bias with a total SOA bias value of 280 mA). Table 6.2 indicates measured values of the different parameters mentioned previously when the MS-SOA is biased at the second bias condition. Figure 6.8(b) and Table 6.2 demonstrate a similar trend to the first bias conditions.

Input Power (dBm)	Output peak power (dBm)	Noise level (dBm)	NF (dB)
-15	-6.61	-40.78	9.55
-10	-2.7	-42.49	8.73
-5	-0.45	-45.13	8.13
0	0.67	-49.04	7.59
5	1.1	-53.01	7.17
10	1.51	-56.51	6.81

Table 6.2: Measured output peak power, noise level and NF for different input power levels when the MS-SOA is biased at the second bias condition.

Figure 6.8(c) and Table 6.3 show the same characterisation procedure as the two previous cases but for the third bias condition (output sections bias > input sections bias). Again, the same overall behaviour is demonstrated with a slight difference in the value of the parameters.

Input Power (dBm)	Output peak power (dBm)	Noise level (dBm)	NF (dB)
-10	-3.32	-41.76	8.9
-5	-0.29	-43.74	8.27
0	1.38	-47.99	7.62
5	1.77	-51.97	7.19
10	2.18	-55.79	6.82

Table 6.3: Measured output peak power, noise level and NF for different input power levels when the MS-SOA is biased at the third bias condition.

Table 6.4 gives a direct comparison of the output values of the three parameters (output peak power, noise level and NF) for the three different bias configurations when the MS-SOA is injected with an optical signal at powers of -5 and -10 dBm respectively.

Injection power (dBm)	Bias condition	Output peak power (dBm)	Noise level (dBm)	NF (dB)
-10	1	-2.66	-41.35	8.88
	2	-2.7	-42.49	8.73
	3	-3.23	-41.76	8.9
-5	1	0.01	-44.22	8.25
	2	-0.45	-45.14	8.13
	3	-0.29	-43.74	8.27

Table 6.4: Comparison of the measured output peak power, noise level and NF for an optical signal input at powers of -5 and -10 dBm input power levels under the three different bias

From the results shown in the table, it can be concluded that the second bias condition yields the lowest NF at both optical injection powers of -10 and -5 dBm. Considering that the input signal OSNR is constant for the three different bias conditions (as the injection level is the same), the second bias condition can be interpreted to be delivering the best NF relative to the other two bias conditions. On the other hand, the third bias condition gives a slightly worse NF than the first bias condition, where the device is considered as a single section one. These findings agree with the analysis done before and proves that optimisation of the bias applied to the different section of the MS-SOA would give a better NF.

The next step involved measuring the NF when injecting the MS-SOA with an optical signal at different wavelengths. Figure 6.9 shows the measured NF at different injection wavelengths starting from 1530 to 1560 nm (tuning step of 5 nm) for the three different bias configurations. The input signal level is kept constant -5 dBm for all the cases. It is clear that at the second bias condition (input section bias > output section bias), the NF is lower than the two other bias conditions at the different values of injection wavelengths. This again confirms that the accurate control of the bias applied to the different sections of the MS-SOA

can result in reducing the generated NF figures. It is important to note that this experiment is a proof of concept. The generated NF are relatively high due to different experimental reasons. The device is not packaged which results in occurrence of fluctuations. Moreover, the temperature control of a bare chip is more complicated than a packaged device which. It is important to note that these issues contribute to resultant fluctuations and difficulties in the stable performance of the device as a direct result of the fluctuations.

The second static characterisation carried out is the output saturation power of the MS-SOA when DC biased at the three different bias conditions mentioned above. The same setup diagram shown in Figure 6.7 is used to extract required data from the generated optical spectra.

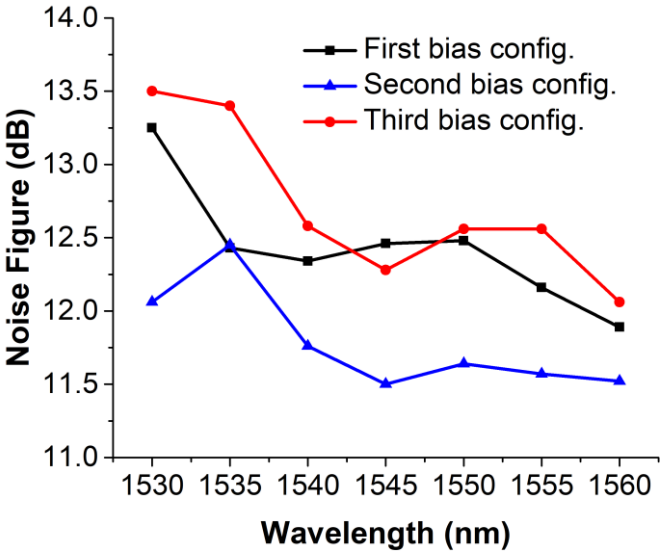

Figure 6.9: Noise figure values of the MS-SOA when injected with an optical signal at different wavelengths and biased in the three different bias configurations.

Figure 6.10(a) shows the injected optical power into the SOA versus the generated gain. Bias configurations 1, 2 and 3 are presented using black, blue, and red colours respectively in the plot. The coupling losses are considered in the calculation of the injected power into the SOA. The gain is calculated in linear scale using the following formula:

$$G = \frac{P_{out}}{P_{in}} \tag{6.7}$$

In the logarithmic scale, this translates to

$$G_{dB} = P_{out}\,(dBm) - P_{in}(dBm) \tag{6.8}$$

The input saturation power is defined as the injection power where the gain goes 3 dB below its initial maximum value. At this level, the MS-SOA gain is half its maximum value. As per Figure 6.10(a), the three bias configurations (1, 2, and 3) have an input saturation power of -

9.5 dBm, -12.5 dBm and -8 dBm. The third bias configuration (output sections bias > input sections bias) has the highest input saturation power. This result agrees with the analysis presented earlier in Section 6.3.2.

Figure 6.10(b) shows the output amplified optical power from the SOA versus the generated gain. Again, bias configurations 1, 2 and 3 are presented using black, blue, and red colours respectively in the plot. The output saturation power is defined as the output power where the gain goes 3 dB below its initial maximum value. First, second and third bias configurations have an output saturation power of 2.52 dBm, 0.7 dBm and 3.25 dBm respectively. Here again, the third bias configuration gives a higher output saturation power confirming the validity of the previous analysis.

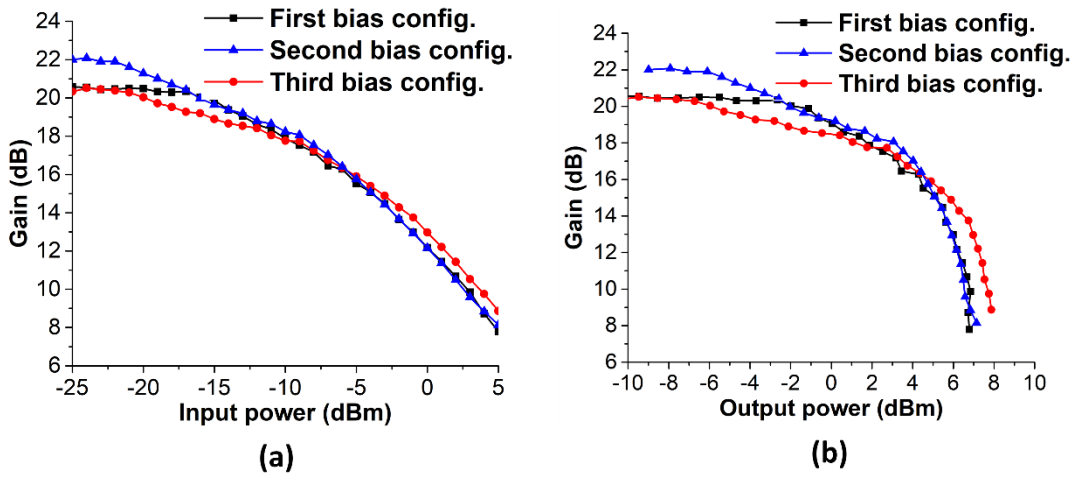

Figure 6.10: (a) Input power injected into the MS-SOA versus its gain for the three different bias configurations, (b) Output power of the MS-SOA versus its gain for the three different bias configurations.

In this section, the accurate control of the bias supplied to each section of the MS-SOA has been shown to enhance the MS-SOA performance according to the required function. The NF can be reduced when the input sections are biased higher than the output sections. Conversely, when the output sections are biased higher than the input sections, a bigger output saturation power value is obtained. This proves the functionality and the flexibility that the MS-SOA can provide.

Having demonstrated the capability of the MS-SOA to be operated in a low NF or high output saturation power mode, the next step involves validating this behaviour of the MS-SOA in a short reach transmission system. Two different experiments were performed for this validation: i) the MS-SOA used as an optical amplifier in a system where an OOK signal is transmitted over 25 km of SMF and ii) the MS-SOA used as an optical amplifier in a system where a PAM-4 signal is transmitted over 10 km of SMF.

It is important to note that these experimental demonstrations were carried out using a wavelength tunable laser as the light source. The single tone (CW light) was used to mimic a tone filtered from an OFC. The main reason was due to the lack of an appropriate (bandwidth and spectral resolution) filter that could filter out a single tone from the OFC with an adequate suppression of the other tones. In addition, the filters available were all passive, which would have made it quite difficult to control the temperature and thereby maintain the stability.

6.3.5 OOK system experiment

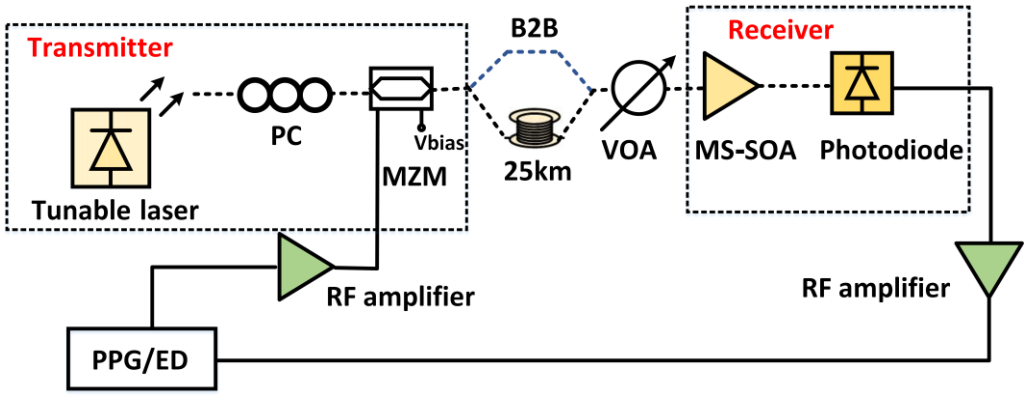

Figure 6.11: Experimental setup where the MS-SOA is used as a pre-amplifier in an OOK system.

Depending on the required function in the optical network, the SOA can be employed either as a booster, in-line or a pre-amplifier. In this system experiment, the MS-SOA will be employed as a pre-amplifier, where it will be placed directly before the PD in the receiver part of the system. This is to make sure maximum possible power is falling on the photodetector and to amplify the signal after the attenuation it experiences during its path through the 25 km SMF. Figure 6.11 shows the experimental setup used. A semiconductor wavelength tunable laser (ID photonics Cobrite DX-1) is used to generate a 7 dBm single moded optical signal at a wavelength of 1527.6 nm. This signal passes through a PC before being sent to a MZM that is biased at 2.35 V (corresponds to the quadrature point of the MZM). The PC function is to adjust the polarisation of the laser signal before going through the MZM. A 10 Gb/s NRZ signal with PRBS length of 2^{15}-1, generated by a PPG, is amplified by a data driver and used to drive the MZM. The modulated optical signal is then transmitted directly (B2B) and subsequently over a 25 km long link of SMF. A VOA is used to control the optical power falling on the receiver (ROP). The receiver consists of the MS-SOA and a 20 GHz PD. The output from the PD is then amplified and sent to an error detector (ED) to measure the BER as a function of the ROP.

Figure 6.12(a-c) show the BER as a function of the ROP for the three different bias cases in the two scenarios: B2B and transmission over 25 km SSMF. For the B2B scenario (shown separately in Figure 6.12(a) for sake of clarity), it is clear that the second bias configuration gives better figures of BER. The first and the third bias configurations have a power penalty of 0.5 dB, 1 dB respectively at a BER of 1×10^{-9} in comparison with the second bias configuration.

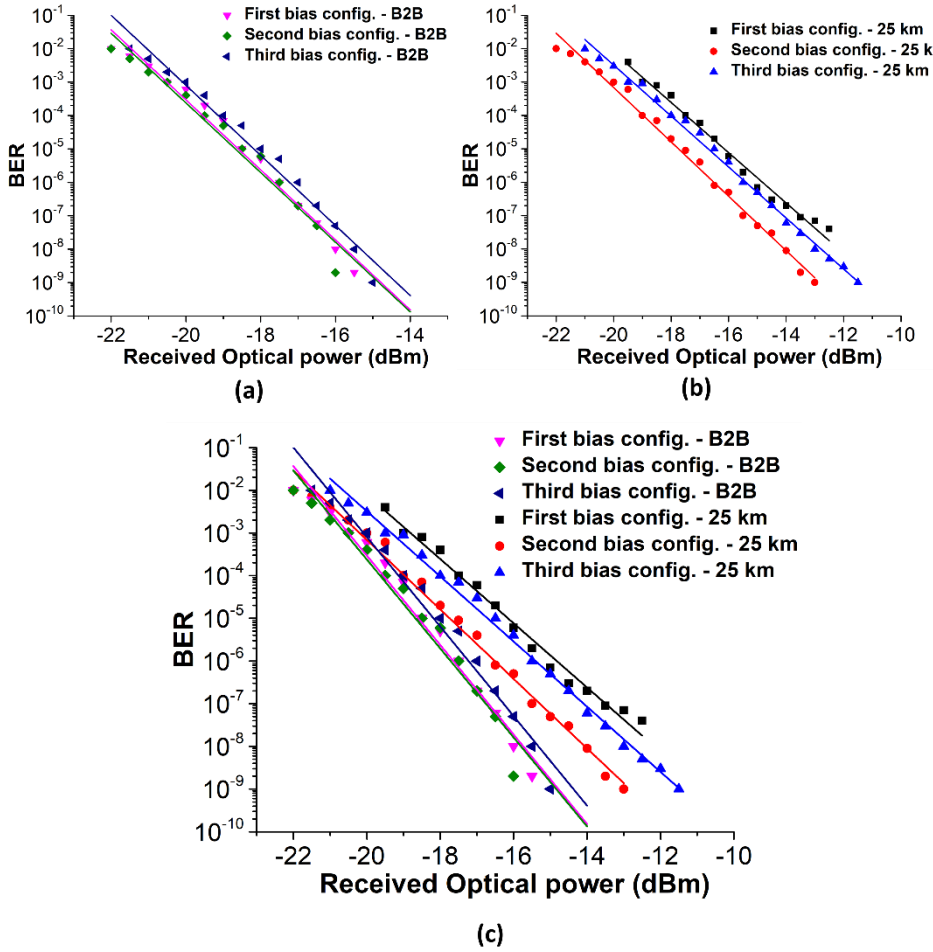

Figure 6.12: BER results for: (a) B2B for the three different bias configurations (magenta, green, navy), (b) 25 km transmission for the three different bias configurations (black, red, blue), and (c) combined B2B for the three different bias configurations (magenta, green, navy) and 25 km transmission for the three different bias configurations (black, red, blue).

This corresponds to the earlier finding (in the characterisation section), where the second bias configuration has been shown to have the lowest NF with respect to the two other bias configurations. This same behaviour is observed in the case of the 25 km transmission (shown in Figure 6.12(b) for sake of clarity), where the second bias configuration gives the best BER in comparison to the other two bias configurations. The performance of the system when the MS-SOA is biased in third bias configuration is degraded and suffers a power penalty of 1.5 dB in comparison with the second bias

configuration (referenced at a BER of 1×10^{-9}). For the first bias configuration case, a BER of 1×10^{-9} is not achieved and the trend line indicates a bigger penalty.

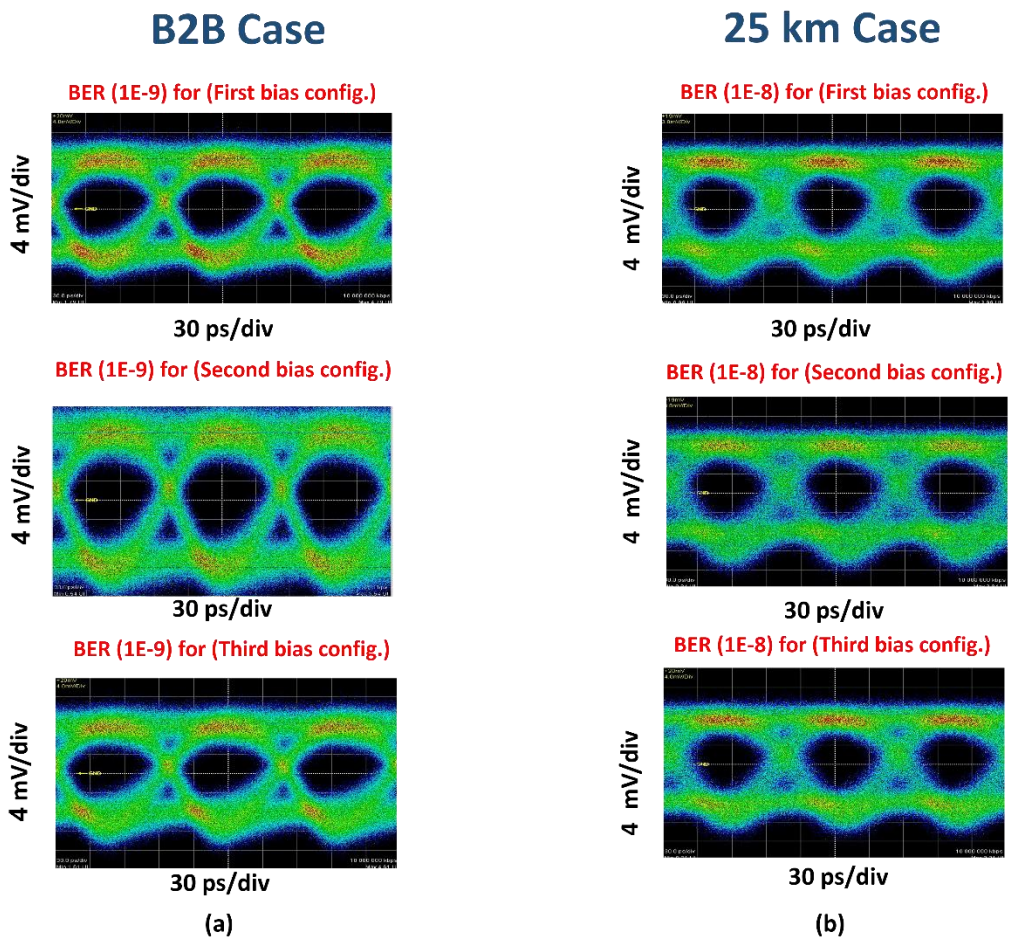

Figure 6.13: Eye diagrams for: (a) B2B case for the three different bias conditions, (b) 25 km transmission case for the three different bias conditions.

In order to visualise the difference in the MS-SOA performance in the transmission system for the three different bias configurations qualitatively, eye diagrams are taken for each bias condition at different BER values. For sake of brevity, only two sets of eye diagrams are shown. Figure 6.13(a) shows a comparison between the B2B eye diagrams for the three different bias cases at a BER of 1×10^{-9}. Figure 6.13(b) shows the eye diagrams for the same bias conditions at a BER of 1×10^{-8} after being transmitted over 25 km of SMF. For the B2B case (shown in Figure 6.13(a)), It is clear that the eye for the second bias condition is better than the eyes corresponding to the other bias conditions in terms of eye opening and the eye tilt. For the 25 km SMF transmission case (shown in Figure 6.13(b)), again the eye diagram of the second bias configuration is better than the other eyes corresponding to the two other bias conditions in terms of the tilt and the noise generated in the “0“ and “1“ levels.

This system experiment has confirmed that the bias configuration with the output sections of the MS-SOA biased higher than the input sections gives a better BER performance than the two other bias configurations. Hence, this result validates the findings from the initial discussion in Section 6.3.1. This proves that an MS-SOA with an optimised bias would deliver better performance than a single-section SOA in terms of low NF. Hence, it can be concluded that such MS-SOAs, in comparison to single section SOAs, could be used to boost the power of filtered tones from an OFC with less degradation in the performance of the system (generating an overall lower NF).

For further investigation of the MS-SOA performance as an amplifier in a short reach optical network, a PAM-4 system experiment is conducted. The main motivation for this experiment, is to highlight the bigger penalty with the use of an SOA that exhibits a high NF. In other words, one expects an SOA with a higher NF to incur a bigger penalty with PAM-4 (multi-level) modulation format than in the OOK format.

6.3.6 PAM-4 system experiment

Growth in video delivery and other high bandwidth services, especially between data centres continue, to increase. In long haul networks, coherent transmitters and receivers are used to support transmitting modulation formats such as QPSK and 16-QAM in conjunction with polarisation multiplexing. However, such transceivers are costly, relatively bulky, and consume higher amounts of power. A major motivation of operators looking to cater for the high-capacity demand in and out of the data centres, is to keep the cost-per-bit low while reducing the power and space requirements. Hence, in order to increase the capacities of data centre interconnects/networks (DCI/Ns) at the cost, module footprints and power necessary, direct-detection formats such as PAM-4 and discrete multi-tone (DMT) have been extensively studied and employed [40] [41] [42].

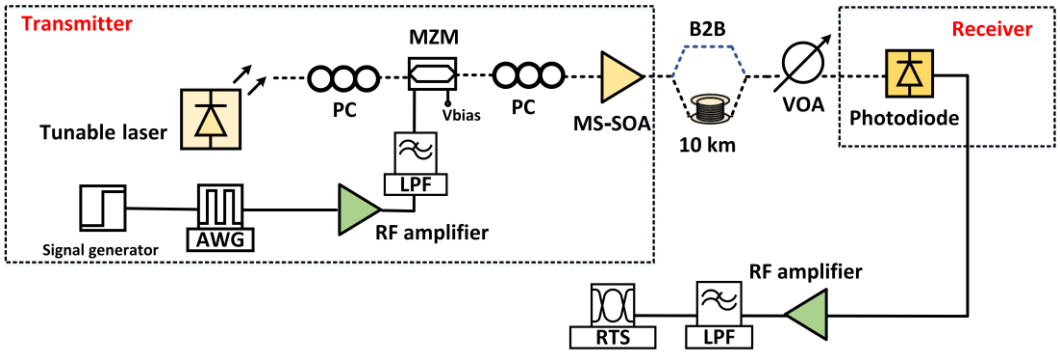

Figure 6.14: Schematic of the experimental setup of a PAM-4 experiment employing the MS-SOA as a booster amplifier.

Figure 6.14 shows the experimental setup used for the PAM-4 system experiment involving the MS-SOA. A 5 GHz sinusoidal signal generated by a signal generator is used to clock an FPGA based AWG (Micram VEGA AWG). The PAM4 signal is synthesised offline in Matlab and generated using the AWG operating at 20 GSa/s. The signal is occupying a bandwidth of 5 GHz, thus giving a data rate of 10 Gbps. The signal is then amplified using a 12 GHz data driver and sent through a low pass filter (LPF) with a 3-dB bandwidth of 7.46 GHz that smooth the sharp edges created by the discrete levels in the output of the digital to analog (DAC) system. These sharp edges imply the presence of high frequency components superimposed on the fundamental. The high frequency components account for the quantization distortion. In the frequency domain, quantization distortion errors are aliased within the Nyquist band and appear as discrete spurs in the DAC output spectrum [43]. Moreover, the LPF is used to block the noise generated by the RF amplifier. Moreover, the LPF removes the clock leakage or harmonics at higher frequencies greater than 5 GHz. The amplified and filtered PAM-4 signal is then sent into the MZM (biased at 2.62V) to be used as a modulation signal for the optical carrier. The optical carrier is provided by a single mode tunable laser with a 7.5 dBm output power and emission wavelength of 1530 nm. The CW signal passes through a PC before being injected to the MZM for polarization optimization (as highlighted in the OOK experiment). The optical output of the MZM is then sent through a polarization controller before being coupled into the MS-SOA. In this setup, the latter is employed as a booster amplifier. In the OOK system experiment presented in Section 6.3.5, the MS-SOA was employed as a pre-amplifier. For the PAM-4 experiment, it was decided that the MS-SOA would be employed as a booster amplifier in order to test it in a new configuration. In this case, the MS-SOA is part of the transmitter section and is expected to boost the optical signal before transmission through the SMF.

The modulated and amplified optical signal is then transmitted directly (B2B) and subsequently over a 10 km long link of SSMF. A VOA is used to control the optical power falling on the receiver (ROP). The receiver consists of a 20 GHz PD. The RF output of the PD is then amplified and filtered by passing the received signal through a data driver (bandwidth of 12 GHz) and a LPF (3-dB bandwidth of 7.46 GHz). The signal is then sent either to a scope to capture the eye diagrams or to an RTS for measuring the BER (performed offline in Matlab (the code was developed by a postdoctoral member of PSSL). Figure 6.15(a) shows the BER versus the ROP for the B2B case. In all of the three different bias configurations, the MS-SOA portrays a BER that is better than the hard-decision FEC limit ($3.8 \text{ x } 10^{-3}$) (portrayed by the golden horizontal line in Figure 6.15(a) and Figure 6.16(a)).

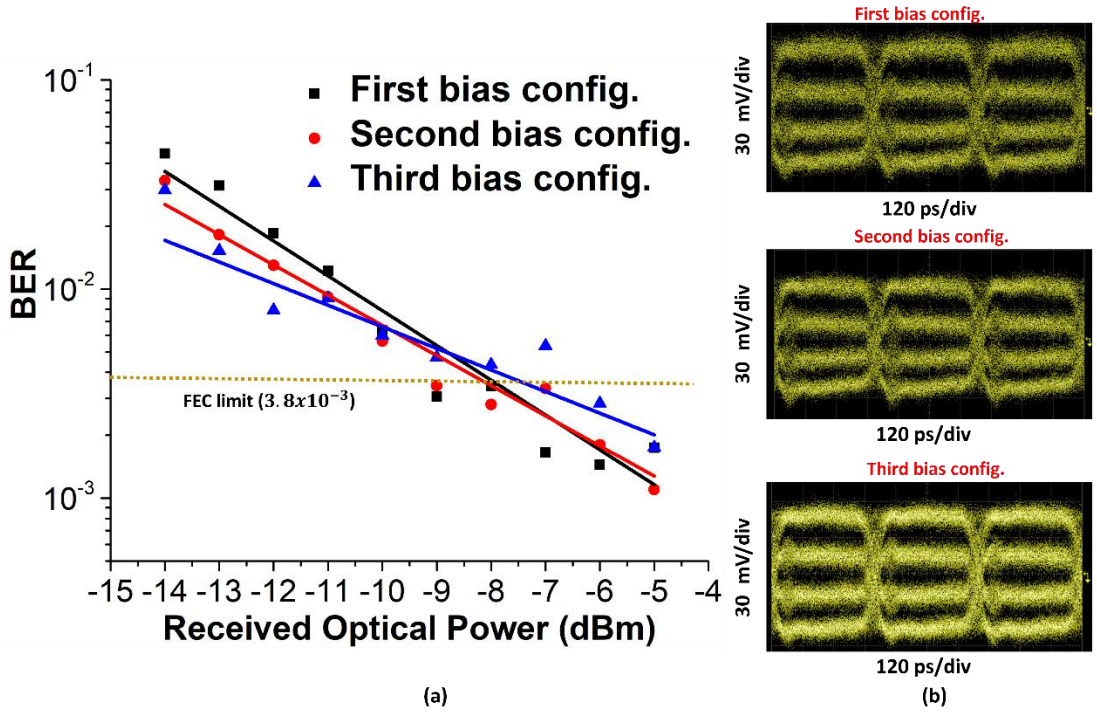

Figure 6.15: Experimental results for the B2B scenario of the: (a) BER versus ROP for the three different bias conditions, (b) Corresponding PAM-4 eye diagrams at the output of the MS-SOA for the three different bias conditions.

The second bias configuration has a relatively better BER performance than the first and third bias configurations (at a reference BER of $2 \text{ x } 10^{-3}$). This implies that the device is showing a similar performance to the OOK transmission case where the second bias configuration shows a better BER than the two other bias conditions due to the reduced NF. This again follows the findings of the discussion shown in Section 6.3.1. Figure 6.15(b) shows the corresponding eye diagrams at the output of the MS-SOA for the three bias configurations. For the different bias configurations, the optical signal injected into the SOA power is kept constant at 7.5 dBm and the wavelength constant at 1530 nm. The eye diagrams also show that the second bias configuration has a slightly wider eye opening than the two other bias conditions, which confirms the better BER performance shown in Figure 6.15(a) confirming the validity of the previous findings in the BER of both the OOK and the PAM-4 experiments. Having completed the B2B scenario, the next step entailed carrying out a system performance measurement after transmitting the modulated signal over a 10 km SSMF span.

Figure 6.16(a) demonstrates the measured BER versus the ROP for the 10 km transmission case. Again, the three different bias configurations portray a BER that is better than the FEC limit. As in the B2B case, the second bias configuration shows a slightly better performance than the first and third bias configurations (at a reference BER of $2 \text{ x } 10^{-3}$). The corresponding eye diagrams for the three bias configurations are shown in Figure 6.16(b).

Here again, the second bias configuration gives a slightly wider open eye than the other two bias configurations confirming that the NF generated by the MS-SOA when biased at the second configuration would translate to a better performance.

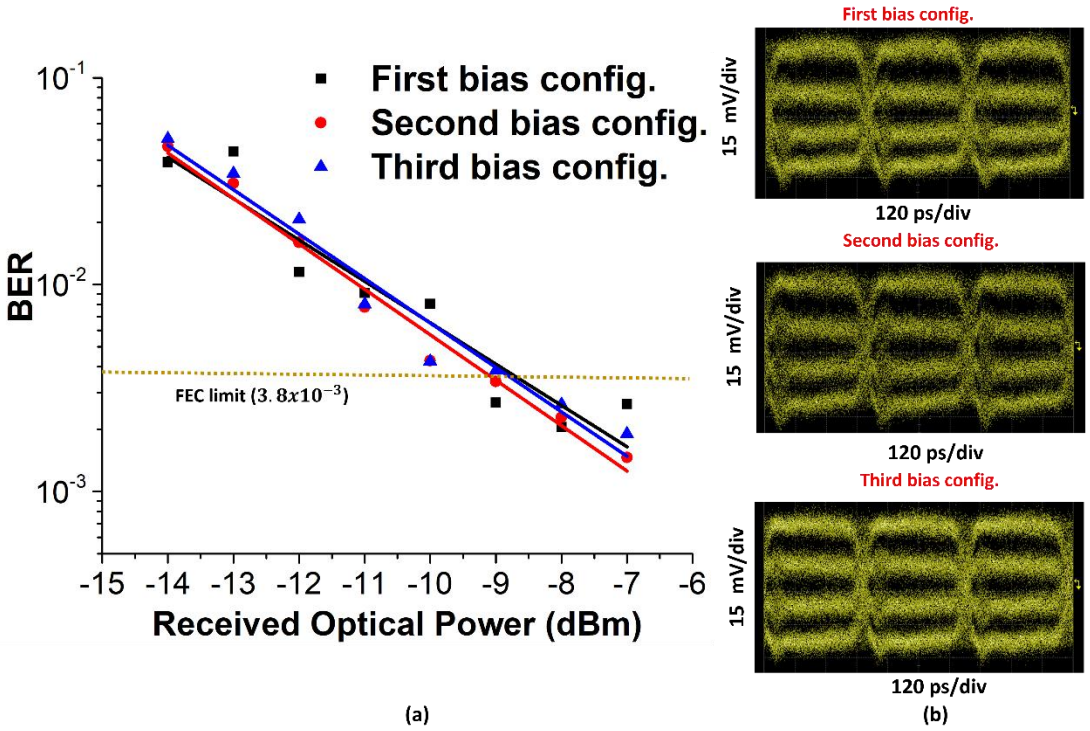

Figure 6.16: Experimental results for the 10 km transmission scenario (a) BER results of the three different bias conditions, (b) corresponding PAM-4 eye diagrams at the output of the MS-SOA.

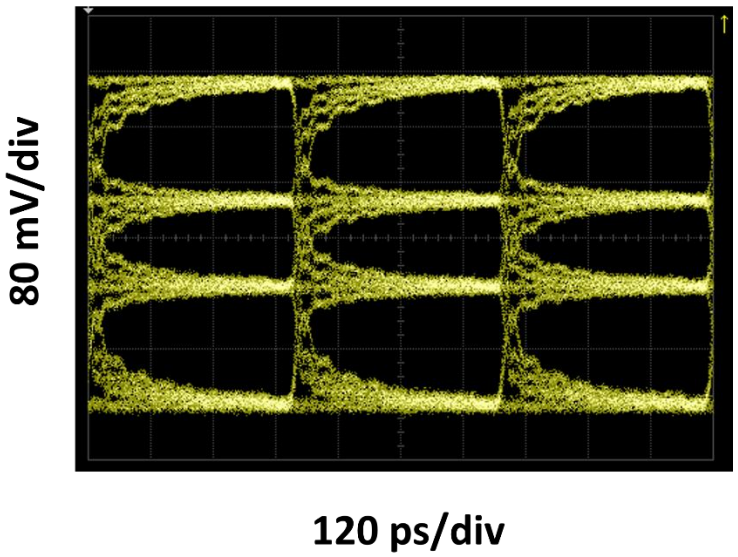

Figure 6.17: AWG output eye diagram.

It is important to note again that the device is a proof-of-concept, and the experimental environment was not ideal as the device is not packaged. Moreover, there was an issue with the AWG used in the experiment, as the generated PAM-4 signal had a poor quality in terms of noise and distortion due to a problem in the input clock causing a

poor input OSNR which in turn affected the quality of the measurements. The distorted output eye diagram from the AWG is shown in Figure 6.17. The eye opening is not symmetrical on the left and right sides. Moreover, noise is affecting the rising edge in the eye. Unfortunately, due to the limited time frame, this issue was not resolved as the AWG has to be sent to the manufacturer for inspection and repair in order to have a symmetrical eye opening in the output of the AWG. It is anticipated that with a better-quality PAM-4 signal, the generated results of the MS-SOA would be better.

6.4 Conclusions

In this chapter, a photonically integrated MS-SOA device is proposed, which offers a flexible control of different parameters such as the NF and the output saturation power. The device consists of four different electrically isolated sections, where each section can be biased individually. By varying the bias configuration applied to the device, the NF can be reduced or conversely the output saturation power increased. The experimental characterisation of the device revealed that biasing the output sections higher than the input section would result in achieving a lower NF. Furthermore, the device is implemented in two different short reach transmission scenarios employing OOK and PAM-4 modulation formats. The experimental results of these two experiments show that the lower NF achieved by optimising the bias configuration of the device would result in achieving a better BER performance. It is expected that the device can even give better performance when it is packaged.

Being manufactured of semiconductor materials, the MS-SOA provides the capability of photonic integration with other optical components. Hence, an MS-SOA can be integrated with the multicarrier transmitter to amplify the generated OFC tones. This would result in overcoming the low output power issue of the gain switched OFCs in a simple and a cost-effective method. Having an integrated device that can generate high quality and high-power multi-carriers would serve as an attractive candidate for transmitters in next-generation short reach optical networks.

References

[1] A. D. Ellis, M. Tan, M. A. Iqbal, M. A. Z. Al-Khateeb, V. Gordienko, G. S. Mondaca, S. Fabbri, M. F. C. Stephens, M. E. McCarthy, A. Perentos, R. Maher, S. Sygletos and P. Bayvel, "4 Tb/s Transmission Reach Enhancement Using 10 × 400 Gb/s Super-Channels and Polarization Insensitive Dual Band Optical Phase Conjugation," *Journal of Lightwave Technology,* vol. 34, no. 8, pp. 1717 - 1723, 2016.

[2] I. Tomkos, S. Azodolmolky, J. Solé-Pareta, D. Careglio and E. Palkopoulou, "A tutorial on the flexible optical networking paradigm: State of the art, trends, and research challenges," *Proceedings of the IEEE ,* vol. 102, no. 9, pp. 1317-1337, 2014.

[3] R. Soref, "The Past, Present, and Future of Silicon Photonics," *IEEE Journal of Selected Topics in Quantum Electronics ,* vol. 12, no. 6, pp. 1678-1687, 2006.

[4] M. O'Mahony, "Semiconductor laser optical amplifiers for use in future fiber systems," *Journal of Lightwave Technology ,* vol. 6, no. 4, pp. 531-544, 1988.

[5] L. Stampoulidis, D. Apostolopoulos, D. Petrantonakis, P. Zakynthinos, P. Bakopoulos, O. Zouraraki, E. Kehayas, A. Poustie, G. Maxwell and H. Avramopoulos, "Enabling Tb/s Photonic Routing: Development of Advanced Hybrid Integrated Photonic Devices to Realize High-Speed, All-Optical Packet Switching," *IEEE Journal of Selected Topics in Quantum Electronics,* vol. 14, no. 3, pp. 849-860, 2008.

[6] J. Zhang, J. Wu, C. Feng, K. Xu and J. Lin, "All-Optical Logic or Gate Exploiting Nonlinear Polarization Rotation in an SOA and Red-Shifted Sideband Filtering," *IEEE Photonics Technology Letters,* vol. 19, no. 1, pp. 33-35, 2007.

[7] A. Crottini, F. Salleras, P. Moreno, M.-A. Dupertuis, B. Deveaud and R. Brenot, "Noise figure improvement in semiconductor optical amplifiers by holding beam at transparency scheme," *IEEE Photonics Technology Letters ,* vol. 17, no. 5, pp. 977-979, 2005.

[8] F. Arecchi and R. Bonifacio, "Theory of optical maser amplifiers," *IEEE Journal of Quantum Electronics,* vol. 1, no. 4, pp. 169-178, 1965.

[9] G. P. Agrawal and N. K. Dutta, Semiconductor Lasers, Springer US, 1993.

[10] H. Ghafouri-Shiraz, Fundamentals of Laser Diode Amplifiers, Wiley, 1996.

[11] R. Mears, L. Reekie, I. Jauncey and D. Payne, "Low-noise erbium-doped fibre amplifier operating at 1.54μm," *Electronics Letters ,* vol. 23, no. 19, pp. 1026-1028, 1987.

[12] C. Holtmann, "Polarization insensitive semiconductor optical amplifiers in InGaAsP/InP for 1.3{mü}m wavelengths exploiting bulk ridge-waveguide structure," ETH Zürich, Zürich, Switzerland, 1997.

[13] Q. Wang and A. K. Dutta, Semiconductor Optical Amplifiers, World Scientific Publishing, 2006.

[14] P. Urquhart, Advances in Optical Amplifiers, IntechOpen, 2011.

[15] M. J. Connelly, Semiconductor Optical Amplifiers, Springer US, 2002.

[16] F. Girardin, G. Guekos and A. Houbavlis, "Gain recovery of bulk semiconductor optical amplifiers," *IEEE Photonics Technology Letters,* vol. 10, no. 6, pp. 784-786, 1998.

[17] Y. Arakawa and A. Yariv, "Quantum well lasers--Gain, spectra, dynamics," *IEEE Journal of Quantum Electronics ,* vol. 22, no. 9, pp. 1887-1899, 1986.

[18] S. Park, R. Leavitt, R. Enck, V. Luciani, Y. Hu, P. Heim, D. Bowler and M. Dagenais, "Semiconductor optical amplifier for CWDM operating over 1540-1620 nm," *IEEE Photonics Technology Letters ,* vol. 17, no. 5, pp. 980-982, 2005.

[19] A.V.Uskova, E.P.O'Reilly, M.Laemmlin, N.N.Ledentsov and D.Bimberg, "On gain saturation in quantum dot semiconductor optical amplifiers," *Optics Communications,* vol. 248, no. 1-3, pp. 211-219, 2005.

[20] P. Borri, W. Langbein, J. Hvam, F. Heinrichsdorff, M.-H. Mao and D. Bimberg, "Ultrafast gain dynamics in InAs-InGaAs quantum-dot amplifiers," *IEEE Photonics Technology Letters ,* vol. 12, no. 6, pp. 594-596, 2000.

[21] T. Akiyama, M. Sugawara and Y. Arakawa, "Quantum-Dot Semiconductor Optical Amplifiers," *Proceedings of the IEEE,* vol. 95, no. 9, pp. 1757-1766, 2007.

[22] A. Rostami, H. B. A. Nejad, R. M. Qartavol and H. R. Saghai, "Tb/s Optical Logic Gates Based on Quantum-Dot Semiconductor Optical Amplifiers," *IEEE Journal of Quantum Electronics ,* vol. 46, no. 3, pp. 354-360, 2010.

[23] K. Carney, R. Lennox, R. Maldonado-Basilio, S. Philippe, F. Surre, L. Bradley and P. Landais, "Method to improve the noise figure and saturation power in multi-contact semiconductor optical amplifiers: simulation and experiment," *Optics Express,* vol. 21, no. 6, pp. 7180-7195, 2013.

[24] K.-C. Syao, K. Yang, X. Zhang, L.-H. Lu, L. Katehi and P. Bhattacharya, "Investigation of adjacent channel crosstalk in multichannel monolithically integrated 1.55 /spl mu/m photoreceiver arrays," *Journal of Lightwave Technology ,* vol. 15, no. 10, pp. 1888-1894, 1997.

[25] M. Matsuura, N. Kishi and T. Miki, "All-optical wavelength conversion with large wavelength hopping by utilizing multistage cascaded SOA-based wavelength converters," *IEEE Photonics Technology Letters ,* vol. 18, no. 8, pp. 926-928, 2006.

[26] G. Contestabile, N. Calabretta, M. Presi and E. Ciaramella, "Single and multicast wavelength conversion at 40 Gb/s by means of fast nonlinear polarization switching in an SOA," *IEEE Photonics Technology Letters,* vol. 17, no. 12, pp. 2652-2654, 2005.

[27] J. Kurumida, T. Morita, Y. Tatara, H. Uenohara and K. Kobayashi, “Fast all-optical switching for label-payload separation with a 1×2 SOA-MZI switch by asymmetric control light,” in *Photonics in Switching*, San Francisco, CA, USA, 2007.

[28] S. Zsigmond, H. Furukawa and N. Wada, “Scalability study of SOA based optical switch for optical packet networks,” in *International Conference on Photonics in Switching*, Pisa, Italy, 2009.

[29] S. Philippe, A. L. Bradley, B. Kennedy, F. Surre and P. Landais, “Experimental Investigation of Polarization Effects in Semiconductor Optical Amplifiers and Implications for All-Optical Switching,” *Journal of Lightwave Technology,* vol. 26, no. 16, pp. 2977-2985, 2008.

[30] L. Occhi, “Semiconductor optical amplifiers made of ridge waveguide bulk InGaAsP/Inp,” ETH Zürich, Zürich, Switzerland, 2002.

[31] S. Shimada and H. Ishio, Optical Amplifiers and their Applications, Wiley, 1994.

[32] R. Lennox, K. Carney, R. Maldonado-Basilio, S. Philippe, A. L. Bradley and P. Landais, “Impact of bias current distribution on the noise figure and power saturation of a multicontact semiconductor optical amplifier,” *Optics Letters,* vol. 36, no. 13, pp. 2521-2523, 2011.

[33] C. Crognale and A. D. Giansante, “All-Optical Picosecond Signal Processing in a M-Z Interferometer Based on a Multi-Section Semiconductor Optical Amplifier,” in *IEEE Global Telecommunications Conference (GLOBECOM)*, New Orleans, LA, USA, 2008.

[34] G. d. Valicourt, D. Make, J. Landreau, M. Lamponi, G. H. Duan, P. Chanclou and R. Brenot, “High Gain (30 dB) and High Saturation Power (11 dBm) RSOA Devices as Colorless ONU Sources in Long-Reach Hybrid WDM/TDM-PON Architecture,” *IEEE Photonics Technology Letters,* vol. 22, no. 3, pp. 191-193, 2010.

[35] D. Baney, P. Gallion and R. Tucker, “Theory and Measurement Techniques for the Noise Figure of Optical Amplifiers,” *Optical Fiber Technology,* vol. 6, pp. 122-154, 2000.

[36] K. Carney, “Investigation of In-Situ Parameter Control in Novel Semiconductor Optical Amplifiers,” Dublin City University, Dublin, Ireland, 2012.

[37] Y. Yamamoto, S. Saito and T. Mukai, “AM and FM quantum noise in semiconductor lasers - Part II: Comparison of theoretical and experimental results for AlGaAs lasers,” *IEEE Journal of Quantum Electronics ,* vol. 19, no. 1, pp. 47-58, 1983.

[38] P. Berger, M. Alouini, J. Bourderionnet, F. Bretenaker and D. Dolfi, “Dynamic saturation in semiconductor optical amplifiers: accurate model, role of carrier density, and slow light,” *Optics Express,* vol. 18, no. 2, pp. 685-693, 2010.

[39] G. Agrawal, Long-Wavelength Semiconductor Lasers, Netherlands: Springer , 1986.

[40] J. Wei, T. Rahman, S. Calabrò, N. Stojanovic, L. Zhang, C. Xie, Z. Ye and M. Kuschnerov, “Experimental demonstration of advanced modulation formats for data center

networks on 200 Gb/s lane rate IMDD links," *Optics Express,* vol. 28, no. 23, pp. 35240-35250, 2020.

[41] B. Teipen, N. Eiselt, A. Dochhan, H. Griesser, M. Eiselt and J.-P. Elbers, "Investigation of PAM-4 for extending reach in data center interconnect applications," in *17th International Conference on Transparent Optical Networks (ICTON)*, Budapest, Hungary, 2015.

[42] C. a. D. Comparison for 100 Gb/s PDM-DD Short Reach Optical Communication System Transmission Performance with PAM4, "Comparison for 100 Gb/s PDM-DD Short Reach Optical Communication System Transmission Performance with PAM4, CAP16 and DMT," in *Conference on Lasers and Electro-Optics Pacific Rim (CLEO-PR)*, Hong Kong, China, 2018.

[43] S. Babani, A. Bature and M. I. Faruk, "comparative study between fiber optic and copper in communication link," *International Journal of Technical Research and Applications,* vol. 2, no. 2, pp. 59-63, 2014.

[44] M. Castro, D. Thomason and M. K. Bacle, "Transatlantic Fiber Optics," [Online]. Available: https://sites.google.com/site/bit4554fiberoptics/home. [Accessed 10 8 2021].

[45] T. Akiyama, H. Kuwatsuka, T. Simoyama, Y. Nakata, K. Mukai, M. Sugawara, O. Wada and H. Ishikawa, "Nonlinear gain dynamics in quantum-dot optical amplifiers and its application to optical communication devices," *IEEE Journal of Quantum Electronics,* vol. 37, no. 8, pp. 1059-1065, 2001.

[46] S. Zhu, L. Huang and Y. Chen, "Gain spectrum control in multi-electrode semiconductor optical amplifiers," in *SPIE Proceedings Volume 7278, Photonics and Optoelectronics Meetings (POEM) Fiber Optic Communication and Sensors*, Wuhan, China, 2008.

[47] H. Ono, M. Yamada, T. Kanamori, S. Sudo and Y. Ohishi, "1.58-/spl mu/m band gain-flattened erbium-doped fiber amplifiers for WDM transmission systems," *Journal of Lightwave Technology,* vol. 17, no. 3, pp. 490-496, 1999.

[48] T. Yamatoya and F. Koyama, "Optical preamplifier using antireflection-coating-free semiconductor optical amplifier with signal-inverted ASE," *IEEE Photonics Technology Letters ,* vol. 15, no. 8, pp. 1047-1049, 2003.

[49] H. Ibach and H. Lüth, Solid-State Physics An Introduction to Principles of Materials Science, Berlin, Heidelberg: Springer, 2003.

Chapter 7

Conclusions and future work

7.1 Conclusions

The increasing demand for new services and the growth of broadband applications (video on demand, interactive multimedia, teleconferencing etc.) has fuelled a great interest and a colossal amount of research effort into high-capacity transmission systems. How service providers can be assured of being able to process and transport an increasing volume of traffic with this unprecedented growth in data and internet traffic is a commonly asked question. Currently there are a few choices available. One would be to install more fibre although this proves to be very expensive. Furthermore, this idea brings out a lot of redundancy regarding the available bandwidth offered by optical fibres. Another solution to the question raised above, is to use higher speed electronic devices, which means that one has to use the most advanced technologies that is neither established nor cost efficient. A potential solution that is attractive entails the use of optical multicarrier transmitters.

Next generation optical networks that will offer flexibility and high capacity would benefit from a reliable, high quality multi-carrier optical transmitter. Gain switched OFCs that are injected either externally injected or self-seeded can be considered as attractive and promising candidates for this purpose. This versatile multi-carrier optical source provides several advantages such as flexibility, and cost efficiency.

In this thesis, a detailed computational and experimental investigation of characterising different laser structures to generate gain switched OFCs with enhanced spectral properties

is presented. This is done with a distinctive focus on enhancing the operating parameters of the lasers which influence the generated gain switched OFC. The main parameters of interest that have been focussed on are the OFC bandwidth, spectral flatness, phase noise and intensity noise. Several laser structures and the variation of some laser parameters have been characterised using simulation models and experimental work. The experimental work was extended in verification of employing these optical sources in next generation short reach optical networks.

The following section highlights the main computational and experimental contributions that this thesis offers.

Study and characterisation of the effects of some vital laser parameters and operating conditions for the generation of a gain switched OFC with enhanced spectral characteristics

In chapter 2, an OFC has been presented as an attractive transmitter solution for next generation optical networks. Different parameters that determine the quality of the generated OFC are discussed in detail. A comparative study showing the pros and cons of the different OFC generation techniques are presented, which then leads to the motivation behind the choosing of the technique of gain switching. Hence, special focus and a discussion on the operating principles of gain switching is included. Subsequently, optical injection is shown to be a complementary process to gain switching. Simulations results are provided to demonstrate the enhancement that optical injection has on the properties of the generated gain switched OFC. Moreover, the simulation model serves as a mean of understanding and investigating the influence of different physical laser parameters on the laser output. This contributes to improving the overall performance of the laser by optimising some of the vital laser parameters.

In chapter 3, the theoretical and computational findings are verified experimentally. Several types of lasers such as an FP, DFB, and VCSEL are gain switched to generate an OFC. The operating parameters of these lasers are characterised and optimised in order to generate a gain switched based OFC with enhanced characteristics such as larger bandwidth, flatness and low phase noise and RIN of the generated tones. As with the simulation model, external optical injection (with a low noise and spectrally pure master laser) of the gain switched lasers is shown to result in the enhancement of different spectral properties of the OFC. These OFC enhancements include larger bandwidth, flatness, higher OCNR, lower phase noise, and lower RIN. Then, two different VCSELs are characterised, and their operation parameters are optimised in order to generate an OFC. Applying external optical injection to the gain

switched VCSEL has been shown to double the number of generated OFC tones (3 to 6 tones). Moreover, it shows an enhancement of the OCNR value of these tones (∼40 dB to ∼55 dB). The phase noise investigation on the OFC tones after applying external injection demonstrates that there is a reduction of the linewidth of the tones (∼234 kHz reduced to 14 kHz) inherited from the lower phase noise of the master laser. In addition to that, the OFC tones have been shown to have a relatively low averaged RIN value of -130 dB/Hz. In the same chapter, the VCSEL polarisation dynamics are investigated and utilised to generate two OFCs in the two orthogonal polarisations. The experimental results presented in this chapter supports the simulation results reported in the previous chapter. Both the experimental and the simulation results reported in this work contributes to optimising the laser operating conditions to generate a gain switched OFC with enhanced spectral characteristics (larger bandwidth, better flatness and lower phase noise and RIN).

Photonic integrated circuits

With the advent of next-generation optical networks, optical sources that provide lower cost, lower footprint and lower power consumption are required. In chapter 4, a novel PIC structure that realises on-chip OIL is presented. It is a four-section device that comprises two lasers and arranged in a master-slave configuration allowing for the achievement of simple OIL through injection from the master laser into the slave laser. Static and dynamic characterisation of the device are conducted and presented in detail. The OIL is shown to improve various parameters of the device including the linewidth, RIN, and MBW. Applying on-chip OIL while the device is gain switched results in the expected increase in the number of generated OFC tones (4 lines to 9 lines within a 3-dB spectral window). The integrated chip is then employed as a directly modulated transmitter in a 10.7 Gb/s OOK system. Improvement of all the above-mentioned parameters accompanied by reduction of the generated chirp leads to an improvement in the system performance. Specifically, the ROP required to achieve the FEC limit is 2 dB lower (reduction in power penalty) for the injection case in comparison to the one without injection. A VPItransmissionMaker™ simulation model has been developed, and its results are presented to back up the findings of the experimental work. A good degree of resemblance between both the experimental and simulation findings is shown.

Based on the studies and characterisation, an upgraded version of the 4-section PIC is designed and fabricated. This 6-section PIC also comprises two lasers arranged in a master-slave configuration but with the addition of a VOA section and independent reflector sections. The six electrically insulated section PIC addresses some of the issues associated

with the 4-section device. This includes difficulties in the control of the injection power from the master laser and the independence of the two laser sections.

Experimental results show that optimisation of the VOA section bias can improve the 3-dB MBW of the slave section. The improvement in all the previously mentioned parameters and the MBW is verified by employing the device as a directly modulated transmitter in a 10.7 Gb/s NRZ OOK system. The modulated signal is transmitted over 25 and 50 km of SSMF to show that the injection can be used to reduce the deleterious effects of direct modulation induced chirp. With reduction of chirp, the device achieves a BER of 4×10^{-9} for an ROP of -11 dBm for 25 km SSMF transmission, while for 50 km transmission case, the lowest BER achieved is 1×10^{-6} at a ROP of -12.5 dBm. The main contribution in this chapter was to fully understand the behaviour of this particular type of PICs employing in-chip injection to achieve OIL. The results reported as a result of characterisation of the 4-section device has opened the road for development of the next generation (6 section device) which tackles some of the main issues that were facing the initial version such as the accurate control of the injection power and the individual emission wavelengths of the two lasers.

In chapter 5, an integrated PFL is presented, which introduces another type of on-chip optical injection. In this case, the device comprises individually biased active and passive sections. Depending on the bias of the latter, the phase of the feedback signal is controlled. A feedback signal that is synchronised in phase with the original signal results in the improvement of the laser spectral properties. A VPItransmissionMaker™ simulation model is built to study the effect of varying the feedback level and phase on the laser output. Optimising the feedback signal phase and power led to the reduction of the linewidth (677.5 kHz reduced to 31.6 kHz). Furthermore, it results in the improvement of the 3-dB MBW to exceed 40 GHz which is more than double the initial value obtained with no optimisation of the feedback signal. Similar findings are reported experimentally, where the linewidth of the laser decreases to be 4.35 MHz (almost half its initial value) with the optimised feedback. The decrease in the linewidth value is proved to be limited by the low noise generated from the current controller used to bias the passive section. Moreover, the experimental dynamic characterisation of the device shows the enhancement in the values of the 3-dB MBW up to 32.5 GHz and the ROF peak frequency values as a result of the PPR effect. Finally, gain switching the device shows a discernible enhancement of the number of OFC tones within the 4-dB spectral window from 5 to 12 tones in case of applying optimised feedback from the passive section. This chapter contributes to characterisation of an integrated PFL to generate an expanded gain switched OFC through optimising the bias of the feedback section in order to adjust the phase delay

of the feedback signal to be synchronised constructively with the phase of the laser main signal.

In chapter 6, a four-section SOA is presented as a simple cost-effective solution for amplifying optical signals that lends itself to photonic integration. One of the main challenges facing gain switched based OFC is the relatively low power of its tones. MS-SOA can be used as an attractive solution to tackle this issue and to amplify the low powered OFC tones. Furthermore, MS-SOA susceptibility for integration provides more advantages in terms of lower power consumption, lower footprint, and cost efficiency. In the MS-SOA characterised in this work, the four sections can be biased separately, which allows the flexible configuration of the device to achieve either a low NF or a high output saturation power. Experimental work is conducted where the modulation of an OFC tone is mimicked. The experiment is carried out using a tunable laser output as the optical source to be amplified. Experimental results show that biasing the output sections higher than the input sections would result in achieving a lower NF. An opposite bias configuration would result in a higher output saturation power. These experimental findings agree with the theoretical and analytical explanation presented earlier in Chapter 6. Eventually, the device is employed to amplify the tunable laser optical signal in two different short reach transmission scenarios employing OOK and PAM-4 modulation formats. The multifunctionality of the device accompanied by its permissiveness to photonic integration qualifies it to be implemented as an attractive optical component for next-generation short reach optical networks.

7.2 Future work

The research in this thesis has presented a detailed overview of the characterisation of different laser structures and the optimisation of their operating parameters for the generation of OFCs (gain switched). Taking into consideration my contributions to the field presented in this work and the current state of the art, there could be additional avenues that could be exploited and can be detailed as follow:

- In chapter 2, a Matlab model describing the semiconductor laser dynamics based on rate equation was introduced with an emphasis on phase noise by including the Langevin force term. The model can be customised to have the capability of being easily integrated VPItransmissionMaker™. The model can be then used to construct different types of optical systems and sub-systems in VPItransmissionMaker™, which gives the ability to study the direct effect of different laser parameters on the

performance of the optical source being implemented in a simulation of a real-life scenario of an optical system.

- In Chapter 3, two different VCSEL structure were introduced for generation of an OFC through gain switching. Moreover, external optical injection has been shown to improve the different OFC parameters generated through gain switching VCSEL_2 device. The device can be further improved by having the TEC integrated in the laser package, which will give better control on the device temperature ensuring more stability on the device temperature. Furthermore, a PIC that contains both the VCSEL and another VCSEL acting as a master laser and used as an optical injection source can be designed and manufactured, which will give many advantages in terms of functionality, practicality, cost-effectiveness. The polarisation dynamics of VCSEL_2 device can be further studied by characterising the influence of varying the polarisation direction of the applied optical injection on the generated OFC parameters. It is expected that with careful optimisation of the direction of the polarisation of the injection signal and trying to match it with the polarisation of the main VCSEL signal, the generated OFC can be further expanded.
- In chapter 4, two multi-section PICs were introduced. The 4-section device has been fully characterised, used as an optical transmitter in a 25 km OOK transmission experiment and gain switched to generate an OFC. The influence of the additional VOA section has been studied for the 6-section device. After that, the latter has been used in a 50 km OOK transmission experiment. Both devices can benefit from better packaging which is expected to deliver overall better performance when the devices are employed as directly modulated optical transmitters. It would be interesting to conduct a fully detailed characterisation of the 6-section device under the influence of different bias scenarios. Moreover, another interesting study will be to gain switch the device and characterise the generated OFC. A direct comparison between the generated OFCs out of the two different devices would be an attractive study case.
- In chapter 5, a PFL was introduced, which is another integrated device. The device was fully characterised and its operating parameters optimised to generate an expanded OFC. The future work can entail integrating the PFL device with a demultiplexer, where an OFC can be generated and its tones demultiplexed using the same integrated device. This would result in providing a much simpler, more cost-effective solution for next-generation short reach optical networks. Furthermore, the device can also comprise electro-absorption modulators after each de-multiplexed

tone to provide independent data modulation. Moreover, the PFL based gain switched OFC can be employed in an elastic optical network with coherent detection.

- In chapter 6, a multi section SOA was introduced for optical amplification applications in short reach optical networks. The device has been characterised using an optical signal from a tunable laser. As a next step, it would be interesting to characterise the performance of the SOA to amplify the various tones of a gain switched OFC. Moreover, as the SOA lends itself to photonic integration, a new integrated device that comprises both the OFC source and the multi-section SOA would be an attractive multi-functional compact device that can be used in short reach and data centre networks. Finally, it would be great to get the multi-section SOA packaged to improve its coupling and overall performance and compare it with a typical single section SOA in order to benchmark it.

Eventually, I would like to conclude that I believe that the contributions presented in this work is beneficial to both the gain switching and OFCs research fields and there is a lot of promise in it. Even though, the work is not exhaustive, there is novelty. A wide array of devices has been covered in this work going through parameters, characterisation techniques and reporting interesting results to be used for the optimisation of OFCs to be used in next generation networks.

List of Publications

The following is the list of publications included in this work.

A.1 Referred Journal Papers

1. **Mohab N. Hammad**, Eamonn P. Martin, M. Deseada Gutierrez Pascual, Prajwal D. Lakshmijayasimha, Gaurav Jain, Pascal Landais, Jules Braddell, Prince M. Anandarajah, "*Compact gain switched optical frequency comb generator for sensing applications,*" Journal of Physics: Conference Series; vol. 1289, 1, Jul 2019, doi:10.1088/1742-6596/1289/1/012048.
2. **Mohab N. Hammad**, Aleksandra Kaszubowska-Anandarajah, M. Deseada Gutierrez Pascual, Pascal Landais, Prajwal D. Lakshmijayasimha, Gaurav Jain, Prince M. Anandarajah, "*Characterization and Direct Modulation of a Multi-Section PIC Suited for Short Reach Optical Communication Systems,*" Photonics, vol.7(3), pp. 55, 2020, doi: 10.3390/photonics7030055.
3. **Mohab N. Hammad**, Prajwal D. Lakshmijayasimha, Aleksandra Kaszubowska-Anandarajah, Prince M. Anandarajah, "*Photonically integrated gain-switched lasers for optical frequency comb generation,*" Microwave and Optical Technology Letters, vol. 63 (8), pp.2219-2226, 2021, doi: 10.1002/mop.32880.
4. **Mohab N.Hammad**, Eamonn P.Martin, Aleksandra Kaszubowska-Anandarajah, Syed T. Ahmad, Pascal Landais, Prince M.Anandarajah, "*Characterization of a passive feedback laser for generation of an expanded optical frequency comb,*" Optics & Laser Technology, 2022 (Submitted)
5. Prajwal D.Lakshmijayasimha, Aleksandra Kaszubowska-Anandarajah, Eamonn P.Martin, **Mohab N.Hammad**, Pascal Landais, Prince M.Anandarajah, "*Characterization of a multifunctional active demultiplexer for optical frequency combs,*" Optics & Laser Technology, vol. 134, pp. 106637, 2021, doi: 10.1016/j.optlastec.2020.106637.

A.2 Refereed Conference Papers

1. **Mohab N. Hammad**, Abhishek Anchal, Sean O'Duill, Pascal Landais, Aleksandra Kaszubowska-Anandarajah and Prince M. Anandarajah, "*Multi-Section Semiconductor Optical Amplifiers for Data Centre Networks*," 2018 20th International Conference on Transparent Optical Networks (ICTON), Bucharest, Romania, 2018, pp. 1-1.
2. **Mohab N. Hammad**, Eamonn P. Martin, M. Deseada Gutierrez Pascual, Prajwal D. Laksmijayasimha, Gaurav Jain, Pascal Landais, Jules Braddell, Prince M. Anandarajah, "*Compact Gain Switched Optical Frequency Comb Generator for Sensing Applications*," International Conference on Spectral Line Shapes (ICSLS), Dublin, Ireland, 2018.
3. **Mohab N. Hammad**, Eamonn P. Martin, Prajwal D. Lakshmijayasimha, Aleksandra Kaszubowska-Anandarajah, Pascal Landais, and Prince M. Anandarajah, "*Optimum optical frequency comb generation via externally injection of a gain switched VCSEL,*" Conference on Lasers and Electro-Optics (CLEO), San Jose, CA, USA 2019, paper SM4N.6.
4. **Mohab N. Hammad**, Gaurav Jain, Aleksandra Kaszubowska, Prince M.Anandarajah, Pascal Landais, " *Characterisation of a novel InP photonic integrated circuits for direct modulation applications*," 2019 21th International Conference on Transparent Optical Networks (ICTON), Angers, France, 2019.
5. Prajwal D. Lakshmijayasimha, **Mohab N. Hammad**, Christian Blumm, Alvaro Moscoso-Martir, Florian Merget, Jeremy Witzens, J. van de Belt, Prince M. Anandarajah, Aleksandra Kaszubowska-Anandarajah, "*Reconfigurable Microring Resonator-Based Optical Transmitter for Elastic Optical Networks,*" 2018 20th International Conference on Transparent Optical Networks (ICTON), Bucharest, 2018, pp. 1-3.doi: 10.1109/ICTON.2018.8473998.
6. Ankit Sharma, **Mohab N. Hammad**, Aleksandra Kaszubowska-Anandarajah, Gaurav Jain, Michael Wallace, Jules Braddell, Frank Smyth, Prince M. Anandarajah, "*A six-section photonic integrated transmitter with chirp control for transmission reach extension,*" 2021 27th International Semiconductor Laser Conference (ISLC), Potsdam, Germany, 2021, doi: 10.1109/ISLC51662.2021.9615884.
7. **Mohab N. Hammad**, Eamonn P. Martin, Syed T. Ahmad, Aleksandra Kaszubowska-Anandarajah, Prince M. Anandarajah, Pascal Landais, " *Characterisation of a novel InP photonic integrated circuits for direct modulation applications*" 2020 22nd International Conference on Transparent Optical Networks (ICTON), Bari, Italy, 2020, doi: 10.1109/ICTON51198.2020.9248698.

8. **Mohab N. Hammad**, Eamonn P. Martin, Syed T. Ahmad, Aleksandra Kaszubowska-Anandarajah, Prince M. Anandarajah, Pascal Landais "*Generation of an enhanced optical frequency comb using a gain-switched integrated passive feedback laser,*" 2021 Photonics Ireland, Dublin, Ireland, 2021.
9. Manas Srivastava, **Mohab N. Hammad**, Syed T. Ahmad, Ankit Sharma, Aleksandra Kaszubowska-Anandarajah, Pascal Landais, and Prince M. Anandarajah, " *Noise Figure and Saturation Characteristics of Multi-section Semiconductor Optical Amplifier for Data Center Networks,*" Conference on Lasers and Electro-Optics (CLEO), San Jose, CA, USA 2022.